Plasma Membrane Dynamics in Immune Signalling



Falk Schneider

Pembroke College
University of Oxford

This dissertation is submitted for the degree of
Doctor of Philosophy

Trinity term 2019

Abstract

The cellular plasma membrane encloses all mammalian cells and is a heterogeneous structure organised on small length- and short timescales. Separation from the exterior milieu allows non-equilibrium processes and renders the membrane the first point of contact in cell-cell interactions or the first line of defence in cell-pathogen encounters. Unravelling the mechanisms contributing to the dynamic membrane architecture offers the opportunity to shed light on one of the biggest mysteries of cell biology: How do structure and organisation emerge from a seemingly chaotic and fluid plasma membrane? This thesis describes the development and application of new fluorescence microscopy-based methods to understand the nature of membrane heterogeneity, such as compartmentalisation to facilitate receptor engagement. Taking snapshots of cellular processes using imaging techniques yields detailed insights into the static structure of the cells, yet overlooks fast and transient interactions, which are increasingly recognised as drivers of molecular organisation. In this work, imaging and spectroscopy approaches are used together to show that molecular diffusion dynamics can serve as a readout for membrane heterogeneity. A combination of super-resolution stimulated emission depletion (STED) microscopy and fluorescence correlation spectroscopy (FCS) is employed to obtain dynamic information at the nano-scale and developed further to measure the diffusion behaviour of lipids and proteins in living cells and model membrane systems across space at sub-diffraction resolution. Special emphasis is given to the evaluation of new detection equipment allowing flexible, robust, and easy-to-perform measurements. Additionally, a novel analysis pipeline based on confocal FCS is introduced to enable advanced diffusion measurements in live cell membranes with conventional equipment. Finally, the developed approaches are exploited to elucidate the organisation of a crucial T-cell signalling protein, the Src-kinase Lck, in model membrane systems as well as in live resting T cells and during their activation.

Declaration

I hereby declare that except where specific references to the work of others are given, the contents of this thesis are original and have not been submitted in whole or in part for consideration for any other degree or qualification in this, or any other university. This dissertation is my own work and contains nothing which is the outcome of work done in collaboration with others, except as specified clearly in the text and in the following:

- The Jurkat and JCaM T cells with reconstituted Lck-eGFP and/or Lck-SNAP were prepared and kindly provided by Dr. Mafalda Santos and Mr. Edward Jenkins.
- The optical tweezers set-up (PicoTweezers) was kindly provided by Ionovation (Dr. Andy Sischka) and the experiments were performed at the University of Osnabrück (Germany) in the lab of Prof. Michael Hensel.
- Access to the set-up used for the high count rate FCS experiments (SP8 FALCON) was kindly provided by Leica Micorsystems in Mannheim (Germany).
- The simulations on pSTED-FCS were initiated in collaboration with Dr. Dominic Waithe.
- The mathematical framework for the analysis of the sFCS data was developed in collaboration with Dr. Marco Fritzsche.

Falk Schneider
October 2019

Acknowledgements

First and foremost, I would like to thank my supervisor, Christian Eggeling, for welcoming me to the lab starting with a small internship project in 2014. This experience completely changed the way I saw life, microscopy and diffusion. Thank you for the opportunity to return to the lab afterwards for doing a PhD, for pushing me to new discoveries, for all the support and freedom to explore the world on conferences and workshops. Finally, I want to thank Christian for all the countless beers and discussions during our pub meetings - vielen Dank, Boss!

Second, I want to express my deepest gratitude to my day-to-day supervisor, Erdinc Sezgin, who became the greatest friend and mentor to me. All I know about lipids and membranes can ultimately be traced back to him and I hope he enjoyed our successful (and less successful) projects as much as I did. I wish him all the best for his new independent position and I am sure he is gonna achieve magnificence.

I would like to thank my co-supervisor, Simon J. Davis, who keeps on trying to put our quantitative microscopy to good use in immunology and from whom I learned invaluable lessons about T cells, science, writing, and life. Also many thanks to his lab, especially to Mafalda Santos, who never stops believing I could eventually learn some biology and who supported all my efforts relentlessly.

An immense thank you to Marco Fritzsche, who became also a mentor and dearest friend to me. Thanks for working with me (even though we basically solved everything overnight), for all the discussions, all the fun evenings and all the advice.

I am thankful for the support and valuable feedback from my thesis committee members, transfer and confirmation of status examiners: Omer Dushek, Vincenzo Cerundolo, Michael L. Dustin and Sergi Padilla-Parra. Thanks for bearing with me.

I am grateful to the Wolson Imaging Centre, which made most of this work possible and is a unique place to do imaging-based research. Thanks for keeping it running to Esther Garcia, Pablo Hernandez Varas, Jana Koth and B. Christoffer Lagerholm. I would like to acknowledge Chris in particular, who became a great friend to me. Thanks for all the emergency help, out-of-hour experiments and out-of-work activities.

Dominic Waithe, as king of correlation, who made me really understand what's going on, earned my special thanks for getting me started to think quantitatively and critically and teaching me the value of simulations.

To all the past and present members of the Eggeling and Fritzsche labs I owe a huge thanks, without you I would have never survived this experience. You made this journey possible and so much fun. It is amazing to do science with friends. Keep on celebrating every little success and never forget about the 3 pm tea time. In particular, I want to thank Liliana Barbieri, who became a dear friend to me, who I can always rely on, and talk to (even though she never quits talking...), Silvia Galiani, who always will be my optics guru, Huw Colin-York, who is the greatest resource of information and an amazing discussion partner, Tess Stanly, who was the soul of the Eggeling lab and still keeps us all going, Katharina Reglinski, who was my fellow German, kept the schedule right and enlightened us with cheese cake, Dilip Shrestha, who never stops thinking critically and out of the box, Pablo Carravilla, who emerged in instance from a short scientific visitor to the greatest friend, Iztok Urbancic, who became an irreplaceable friend and FCS believer, Dunja Urbancic, who finally brought some biology to the lab, Mathias P. Clausen, who left the lab too early, but will always be the one to have taught me fitting of FCS data first, Francesco Reina, who sat next to me for four years as an outstanding companion and kept me sane, and Aurelien Barbotin, who is the best conference mate and joined the FCS believers.

I want to thank the ones who make science in the building physically possible. Thank you Malcolm Shepherd, Manoj Sondhi, Renata Sojka, Elizabeth Stevens, Alastair Waugh, Matt Husband, Keith Bourne, Jacek Lasocha, and Anne Farmer for keeping the the WIMM and the HIU rolling.

I would like to acknowledge Jörg Enderlein and his lab, Narain Karedla, Sebstian Isbaner, Jan Thiart, Alexey and Anna Chizhik in Göttingen, who all became dear to me and taught me a great deal about microscopy during my Master thesis and finally let me go to Oxford.

I would like to thank Julia Roberti, Frank Hecht and Giulia Ossato, who made a fun collaboration with Leica Microsystems possible.

I am grateful for the good friends in the WIMM and WIMM Graduate Student Association, who created a welcoming and positive atmosphere to thrive and to endeavour all the hard and difficult times. Thanks for always being there to Martyna Lukoseviciute, Ioanna Rota, Bryan Adriaanse, Merve Aksöz and Ivan Fereirra. With all this great people in science (and all the ones I forgot) it feels like doing a PhD in a community, which is just amazing.

I would have given up many times without the support of my family and friends back home in Germany, who believed in me and were a safe haven to reboot any time - many thanks, especially to my parents, Torsten and Petra, and my sister, Sina. You guys are the best.

List of DPhil publications

The results, techniques and data presented in this thesis have partially been communicated before:

Published manuscripts

12. "Nanoscale dynamics of cholesterol in the cell membrane"
K. Pinkwart, **F. Schneider**, M. Lukoseviciute, T. Sauka-Spengler, E. Lyman, C. Eggeling, E. Sezgin **Journal of Biological Chemistry** 294(34):12599-12609 (2019)

11. "Measuring nanoscale diffusion dynamics in cellular membranes with super-resolution STED– FCS"
E. Sezgin, **F. Schneider**, S. Galiani, I. Urbancic, D. Waithe, B.C. Lagerholm, C. Eggeling **Nature Protocols** 14, 1054-1083 (2019)

10. "Nanoparticles Can Wrap Epithelial Cell Membranes and Relocate Them Across the Epithelial Cell Layer"
I. Urbancic, M. Garvas, B. Kokot, H. Majaron, P. Umek, H. Cassidy, M. Skarabot, **F. Schneider**, S. Galiani, Z. Arsov, T. Koklic, D. Matallanas, M. Ceh, I. Musevic, C. Eggeling, J. Strancar **Nano Letters** Aug 8;18(8):5294-5305 (2018)

9. "Statistical Analysis of Scanning Fluorescence Correlation Spectroscopy Data Differentiates Free from Hindered Diffusion"
F. Schneider, D. Waithe, B.C. Lagerholm, D. Shrestha, E. Sezgin, C. Eggeling, M. Frtizsche **ACS Nano** 12 (8), pp 8540–8546 (2018)

8. "Nanoscale Spatiotemporal Diffusion Modes Measured by Simultaneous Confocal and Stimulated Emission Depletion Nanoscopy Imaging"
F. Schneider, D. Waithe, S. Galiani, J. Bernardino de la Serna, E. Sezgin, C. Eggeling **Nano Letters** Jul 11;18(7):4233-4240 (2018)

7. "Capturing resting T-cells: The perils of PLL"
A.M. Santos, A. Ponjavic, M. Fritzsche, R. A. Fernandes, J. B. de la Serna, M. J. Wilcock, **F. Schneider**, I. Urbancic, J. McColl, C. Anzilotti, K. A. Ganzinger, M. Aßmann, D. Depoil, R. J. Cornall, M. L. Dustin, D. Klenerman, S. J. Davis, C. Eggeling, S. F. Lee **Nature Immunology** Mar;19(3):203-205, (2018)

6. "Optimized processing and analysis of conventional confocal microscopy generated scanning FCS data"
D. Waithe, **F. Schneider**, J. Chojnacki, D. Shrestha, J. B. de la Serna, C. Eggeling **Methods** 2018 May1;140-141:62-73 (2017)

5. "Polarity-Sensitive Probes for Superresolution Stimulated Emission Depletion Microscopy"
E. Sezgin, **F. Schneider**, V. Zilles, I. Urbancic, E. Garcia, D. Waithe, A. S. Klymchenko, C. Eggeling **Biophysical Journal** 113, 1321–1330, (2017)

4. "Diffusion of lipids and GPI-anchored proteins in actin-free plasma membrane vesicles measured by STED-FCS"
F. Schneider, D. Waithe, M. P. Clausen, S. Galiani , T. Koller, G. Ozhan, C. Eggeling, E. Sezgin **Molecular Biology of the Cell** Vol. 28 no. 11 1507-1518, (2017)

3. "Dissecting the actin cortex density and membrane-cortex distance in living cells by super-resolution microscopy"
   M.P. Clausen, H. Colin-York, **F. Schneider**, C. Eggeling, M. Frizsche **Journal of Physics D: Applied Physics** 50, 064002, (2017)

2. "Reorganization of lipid diffusion by the myelin basic protein as revealed by STED nanoscopy"
   O. Steshenko, D. Andrade, A. Honigmann, V. Mueller, **F. Schneider**, E. Sezgin, S.W. Hell, M. Simons, C. Eggeling **Biophysical Journal** 110(11), 2441-2450, (2016).

1. "A comparative study on fluorescent cholesterol analogs as versatile cellular reporters"
   E. Sezgin, F.B. Can, **F. Schneider**, M.P. Clausen, S. Galiani, T.A. Stanly, D. Waithe , A. Colaco, A. Honigmann, D. Wüstner, F. Platt, C. Eggeling **Journal of Lipid Research** 57(2), 299-309, (2016).

Manuscripts in preparation

2. "High photon count rate super-resolution fluorescence fluctuation spectroscopy"
   F. Schneider, P. Hernandez-varas, B. C. Lagerholm, D. Shrestha, E. Sezgin, M. J. Roberti, G. Ossato, F. Hecht, C. Eggeling, I. Urbancic
   Pre-print available at: https://www.biorxiv.org/content/10.1101/783639v1?rss=1

1. "Actin-mediated control of lymphatic receptor LYVE-1 mobility and hyaluronan binding in lymphatic vessel endothelium"
   T.A. Stanly, M. Fritzsche, S. Banerji, D. Shrestha, **F. Schneider**, D. Jackson, C. Eggeling

Acronyms

BIC	Bayesian Information Criterion.
cdf	Cumulative Distribution Function.
cpm	count per molecule.
CW	Continuous Wave.
DRM	Detergent Resistant Membrane.
FCCS	Fluorescence Cross-Correlation Spectroscopy.
FCS	Fluorescence Correlation Spectroscopy.
FLCS	Fluorescence Lifetime Correlation Spectroscopy.
FLIM	Fluorescence Lifetime Imaging.
FRAP	Fluorescence Recovery After Photobleaching.
FRET	Förster Resonance Energy Transfer.
FWHM	Full Width at Half Max.
GFP	Green Fluorescent Protein.
GPI-AP	GPI-ancored protein (GPI=Glycosylphosphatidylinositol).
GPMV	Giant Plasma Membrane Vesicle.
GSD	Ground State Depletion.
GUV	Giant Unilamellar Vesicle.
ICS	Image Correlation Spectroscopy.
iMSD	image Mean Square Displacement.
IS	Immunological Synapse.
iSCAT	Interferometric Scattering.
ITAM	Immuno-receptor Tyrosine-based Activation Motif.
LIESS-FCS	Line Interleaved Excitation Scanning STED-FCS.
LSM	Laser Scanning Microscope.
MIET	Metal Induced Energy Transfer.
MLE	Maximum Likelihood Estimation.
MSD	Mean Square Displacement.
NSOM	Near-Field Scanning Optical Microscopy.
PALM	Photoactivated Localisation Microscopy.
pdf	Probability Distribution Function.
pFCS	point Fluorescence Correlation Spectroscopy.
PSF	Point Spread Function.
RICS	Raster Image Correlation Spectroscopy.
sFCS	scanning Fluorescence Correlation Spectroscopy.
SIM	Structured Illumination Microscopy.
SLB	Supported Lipid Bilayer.
SLM	Spatial Light Modulator.
SMLM	Single Molecule Localisation Microscopy.
SNR	Signal to Noise Ratio.
SPT	Single Particle Tracking.
sSTED-FCS	scanning STED-FCS.
STED	Stimulated Emission Depletion.
STICS	Spatio-Temporal Image Correlation Spectroscopy.
STORM	Stochastical Optical Reconstruction Microscopy.
svFCS	spot-variation FCS.
TCR	T-Cell Receptor.
TCSPC	Time Correlated Single Photon Counting.
TIRF	Total Internal Reflection Fluorescence.

Contents

Abstract I

Declaration II

Acknowledgements III

List of DPhil publications V

Acronyms VII

1 Introduction and Outline 1

2 Background 3

2.1 Biomembranes: From the cellular plasma membrane to artificial model membrane systems . . . 3

2.1.1 Concepts of plasma membrane organisation . . . 3

2.1.2 Model membrane systems . . . 6

2.1.3 Plasma membrane organisation in T cell signalling . . . 7

2.2 Optical microscopy and spectroscopy to dissect cellular organisation . . . 9

2.2.1 Optical (super-resolution) fluorescence microscopy . . . 9

2.2.2 A brief overview on STED microscopy . . . 11

2.2.3 Fluorescence microscopy based techniques to study dynamics in cells 13

2.2.4 FCS and STED-FCS . . . 15

3 Aims and Objectives 21

4 Materials and Methods 22

4.1 Cell lines and tissue culture . . . 22

4.2 Fluorescent labelling of cells . . . 23

4.3 Transfections . . . 23

4.4 GPMVs . . . 23

4.5 GUVs . . . 26

4.6 SLBs . . . 26

4.7 Coverslip preparation for T-cell experiments . . . 26

4.8 Calcium imaging . . . 27

4.9 Microscopy and spectroscopy . . . 28

4.10 Fitting of (s)FCS data . . . 30

4.11 STED-FCS . . . 32

4.12 Simulations . . . 33

4.13 Statistical analysis of sFCS data . . . 35

4.13.1 Evaluation of sFCS Histograms . . . 35

4.13.2 Model selection and histogram fitting quality . . . 38

5 Results 42

5.1 Measuring dynamics at high-photon count rates . . . 42

5.1.1 High count rate FCS in solution . . . 43

5.1.2 Application of high count rate FCS to measurement in cells . . . 49

5.1.3 STED-FCS at high count rates . . . 51

5.1.4 Summary high count rate FCS . . . 58

5.2 Nano-scale diffusion dynamics in an actin-free system 59
5.2.1 Diffusion in artificial and cell-derived vesicles 59
5.2.2 Diffusion in cells and GPMVs 63
5.2.3 Monte Carlo simulations on diffusion modes investigated by STED-FCS 69
5.2.4 Summary nano-scale dynamics in cells and actin-free systems 72
5.3 Spatially resolved diffusion modes: LIESS-FCS 74
5.3.1 Simultaneous acquisition of confocal and STED sFCS data 76
5.3.2 LIESS-FCS measurements in living cells 82
5.3.3 Summary LIESS-FCS for Drat imaging 87
5.4 Statistical analysis of confocal sFCS reveals hindered diffusion 90
5.4.1 Simulations and sFCS data on free diffusion 91
5.4.2 Statistical analysis allows for the disclosure of hindered diffusion . . 96
5.4.3 Model selection with Maximum Likelihood Estimation 100
5.4.4 Applications of the sFCS analysis pipeline 101
5.4.5 Further considerations for sFCS experiments 107
5.4.6 Summary sFCS statistical analysis 116
5.5 Applications in immune signalling 117
5.5.1 The quest for a resting state 117
5.5.2 Elucidating diffusion dynamics in T cells 120
5.5.3 Summary dynamics in T cells 132

6 Discussion and Future Work **135**
6.1 Novel techniques to investigate diffusion dynamics 135
6.2 Deciphering the diffusion dynamics in the plasma membrane of living cells 140

7 Conclusions **148**

References **167**

1 Introduction and Outline

Every mammalian cell is enclosed by a plasma membrane which serves as a semi-permeable boundary to the surrounding medium and as a reaction platform composed of thousands of different types of lipids and proteins [1–4]. The plasma membrane is known to be heterogeneously organised over a wide range of temporal and spatial scales ranging from nanometres to micrometres and nanoseconds to tens of seconds, respectively [5–7]. Fascinatingly, short lived, nano-scale interactions and the heterogeneous membrane organisation contribute to its functions, to the point that the membrane should be pictured as much more than a disorganised fluid [3, 8]. Deciphering the details of membrane organisation will allow us to understand signalling mechanisms, biophysical limits of life, dysregulations and ultimately a variety of diseases.

In human immunology, the plasma membrane plays a vital role as it displays the first point of contact when immune cells interact with their target cells such as antigen-presenting cells or pathogens [9]. Thus, organisation and regulation of activating and inhibitory molecules, initiating or stopping the immune response, right at the plasma membrane became a very vivid area of research [10–12]. Over the past years, the advances in microscopy have started to offer new avenues to investigate the plasma membrane organisation in immune cells [13]. This thesis aims to evaluate and provide new tools based on optical microscopy and spectroscopy to further advance this research. Spectroscopic methods are of particular interest, as it becomes increasingly clear that diffusion, short lived interactions and transient organisation may be the key factors defining the membrane structure [5, 14].

The next Chapter of the thesis, Chapter 2, will set the stage for the presented work. First, biomembranes and concepts of their organising principles will be explained, reviewed and then related to T-cell biology. Next, optical microscopy and spectroscopy will be introduced as these represent the main tools used throughout this work. Main emphasis lies on the introduction of super-resolution microscopy and Fluorescence Correlation Spectroscopy (FCS) to investigate membrane organisation by measuring dynamics. After describing the current state of the literature, the Aims and Objectives of the thesis will be outlined in Chapter 3.

Chapter 4 presents the Materials and Methods used for the investigations. This includes cell lines, chemicals and procedures used to prepare the samples as well as the microscopy set-ups employed. Most importantly, the data processing, fitting and analysis are described in detail. Some of the analysis pipelines and simulations were developed as part of this thesis.

Chapter 5 represents the Results chapter and is divided into five parts. First, the use of FCS at high photon count rates is investigated using novel detection equipment that allows for the first time accurate measurements above the conventional detection limit of 1 MHz at a commercial instrument. This enables more flexible and less biased measurements in biological systems.

Next, super-resolved FCS experiments on actin depleted plasma membrane vesicles are presented, which reveal the overwhelming effect of the cytoskeleton on the diffusion behaviour of membrane components. Additionally, the vesicles allow the investigation of active (ATP dependent) versus passive processes.

In the third part of the Results, the measurements are advanced from acquisitions at a single point to recordings at multiple points across space (along µm sized lines), as it became more and more clear that spatial heterogeneity in live cells can cause artefacts. As a remedy, an approach is presented to quasi-simultaneously acquire super-resolved and confocal dynamics in many locations, which may resolve some of the controversies, for example, on GPI-ancored protein (GPI=Glycosylphosphatidylinositol) (GPI-AP) organisation.

The fourth part of the Results is dedicated to a new analysis pipeline based on statistics of large sets of FCS data, which allows for insights into the nano-scale diffusion behaviour on a standard confocal Laser Scanning Microscope (LSM). This is convenient, as no special dyes or equipment are required for the measurements, but the downside is that spatial information are neglected. Therefore, it offers a complementary approach to STED based methods and facilitates the experiments, for example, when screening for promising conditions. It has been used to confirm some of the findings based on STED recordings in the previous Results Sections using different dyes or varying experimental conditions.

In the final, fifth, part of the Results, the aforementioned approaches are applied to mea-

surements on immune cells, specifically T cells, where the organisation of the membrane-bound kinase Lck is investigated in resting versus activating cells and in cell-derived vesicles as a thermodynamic equilibrium state.

Chapter 6 represents the general Discussion, which sets the newly developed methods in the context of other available techniques, and discusses shortcomings and advantages. The data themselves are discussed in detail in Chapter 5 right away. The second part of the discussion is dedicated to the biological findings and implications of the results. The thesis is summarised in Chapter 7.

2 Background

This thesis is about the elucidation of the dynamics and heterogeneity of molecules in the plasma membrane of living cells and about improving the technology to approach their investigation. In this Chapter, I will provide a general introduction to the concepts of biomembrane organisation and its involvement in T-cell activation. In the second part of this chapter, I will introduce optical (super-resolution) microscopy and spectroscopy as the methods of choice to study cellular plasma membrane organisation and dynamics.

2.1 Biomembranes: From the cellular plasma membrane to artificial model membrane systems

Biomembranes are structures composed of amphiphilic lipid molecules forming a 4 to 7 nm thick bilayer with hydrophobic core and hydrophilic edges [15, 16]. These simple structure can be extended to infinite complexity by adding proteins, various types of (modified) lipids and associated structures such as the glycocalix or the cytoskeleton. The plasma membrane is crucial for cellular processes and is even believed to have enabled the development of life by separation of a reaction room from the exterior milieu [5, 17].

2.1.1 Concepts of plasma membrane organisation

The elucidation of the organising principles of the plasma membrane of living (mammalian) cells is ongoing research for decades. Our understanding of the membrane organisa-

tion has evolved over the past years, yet many old concepts remain integral part of current models.

A first comprehensive attempt to describe the plasma membrane organisation, the fluid mosaic model, was already suggested in 1972 by Singer and Nicolson and is depicted as cartoon in Figure 1 A. Singer and Nicolson proposed that the membrane is a viscous fluid made of a phospholipid matrix with embedded mobile, meaning laterally diffusing proteins (peripheral or integral), and appreciated a big heterogeneity in protein content and function. They considered the membrane to be at thermodynamic equilibrium and thus, the long-range organisation (micron scale) was proposed to be random with short-range interactions thought to be likely. The fluid mosaic model remains the standard model for membrane organisation, but has been extended widely.

Already the fluid mosaic model, assuming lateral thermodynamic equilibrium, allowed for the possible asymmetry of membranes meaning that certain lipids and proteins are enriched in concentration either on the cytoplasmic side (inner membrane leaflet) or on the outside of the cell (outer membrane leaflet), controlled by restricted rotational diffusion [1, 18]. Yet, how exactly (lipid) membrane asymmetry is regulated and maintained remains under investigation [19].

Based on short range interactions of lipids and proteins, the formation of functional domains, the so-called lipid rafts, has been suggested in 1997 by Simons and Ikonen. The model arises from the fact that certain membrane components such as sterols (especially cholesterol) and sphingomyelin can only be extracted with harsh detergents and may therefore form platforms in membranes, termed Detergent Resistant Membranes (DRMs) [20, 21]. This idea is supported by the phenomenon of phase separation in lipid membranes in which saturated lipids and cholesterol can form large (micron sized) ordered domains (the so called liquid ordered, L_o-phase) and segregate from unsaturated lipids forming the liquid disordered, L_d-phase [22, 23]. This phenomenon has been observed in model membrane systems and depends on temperature and composition (see below section 2.1.2). The raft concept had a big impact on the field of membrane biology [24] and many molecules have been suggested to be associated with rafts such as signalling proteins like Lck or LAT [25, 26], GPI-APs [27, 28], or (glyco-)lipids such as GM1 [29, 30]. However,

the existence, exact nature and function of raft structures is heatedly debated [5, 7, 31].

Another component, which has been added to membrane complexity in the last decade, originated from the (ultra-fast) study of diffusion within plasma membranes. Kusumi and co-workers detected compartmentalisation of the membrane and proposed the "picket and fence" model [32, 33]. They envision the membrane not as a continuous fluid (as in the fluid mosaic model), but rather divided into areas by the cortical actin cytoskeleton (the fences), which are bound to integral membrane proteins (the pickets). This results in long range hindrance in diffusion. The impact of the actin cytoskeleton on membrane organisation has since then been acknowledged multiple times [5, 34–36] and even been incorporated in an updated version of the fluid mosaic model by Nicolson himself [2] (depicted in Figure 1 B). On the other side of the membrane, components of the extracellular matrix may also interact with and influence the membrane, for example, through the glycocalix [2, 6].

Finally, the protein content of the membrane needs to be acknowledged. As mentioned above, the membrane is often pictured as lipid matrix (continuous fluid), but more and more evidence emerges suggesting that only a very little area of the membrane is actually composed of free and mobile lipid and that the membrane is crowded with proteins (containing lipid shells, more like a protein lipid composite material) [4, 6, 24, 37]. This implies that the membrane (of living cells) behaves collectively rather as a gel than a liquid in terms of compressibility and flow [38]. Thus, the crowding together with the lipid complexity and lipid-protein interactions may modulate the plasma membrane organisation crucially [31, 39, 40].

Overall, our understanding of the plasma membrane is constantly evolving and is still far from completion. However, we more and more appreciate heterogeneity on various length scales and may need to consider that not a single comprehensive model can explain everything [7]. Figure 1 illustrates the impressive evolution of the fluid mosaic model over the years. I am curious to see, how future investigations will elucidate differences between cell types, metabolic state or age and if that will reveal even more complexity.

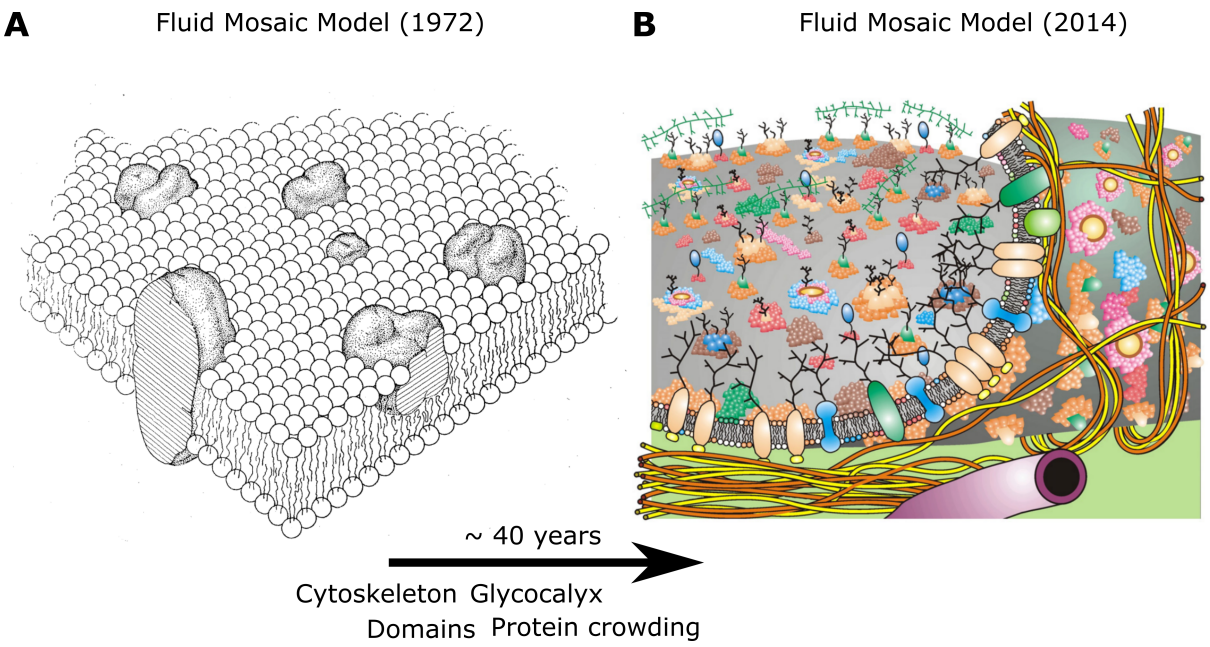


Figure 1: Membrane organisation: The evolution of the fluid mosaic model. **A**: The fluid mosaic model sees the membrane as a continuous fluid composed of a lipid matrix and embedded proteins with no long range order. Adapted from [1]. **B**: The fluid mosaic model after 40 years of membrane research, revised by Nicolson himself, incorporates more layers of complexity and heterogeneity and accounts for non-random (non-equilibrium interactions). Adapted from [2]. Some of the most important modifications to the original model are pointed out below the arrow.

2.1.2 Model membrane systems

The previous section highlighted the enormous complexity and heterogeneity of the plasma membrane of living cells. Hence, membrane research developed many model membrane systems of different and even tunable complexity to address questions like membrane organisation or diffusion within the membrane. As some of them will be used throughout this work, I review the most important ones.

Many may say (model) membrane research started with Benjamin Franklin's famous observation that a spoon full of oil can cover a pond, from which he ultimately calculated the cross section of a lipid with surprising accuracy [41, 42]. In this case, of course, only a monolayer was observed. Building on that, the research on monolayers was developed further by Langmuir and others later on [43].

The first actual bilayer models were probably synthetic liposomes treated with detergent and investigated with electron microscopy [44]. Liposomes became attractive membrane models for studies on fission and fusion as well as prerequisites to prepare Supported Lipid Bilayers (SLBs) [45, 46].

SLBs were a major step toward mimicking flat lateral membranes [23] which became,

as described above, more famous with the discovery of the phase separation phenomenon. Supported membranes are planar, but artefacts may be introduced due to the support (especially when mobility is investigated as the substrate may interact with the lipid headgroups in the membrane or the probe) [47–49]. Thus free-standing model systems like Giant Unilamellar Vesicles (GUVs) emerged [50]. GUVs are also an excellent model to observe phase separation and measure partitioning of dyes (the preference for L_o- or L_d-phase) [21, 51, 52].

All the aforementioned model systems are artificial and can compose only of a limited complexity [21]. Giant Plasma Membrane Vesicles (GPMVs) are an alternative, cell-derived, model system. They are membrane blebs containing almost all the lipids and proteins of the cellular membrane at thermodynamic equilibrium (only restricted lipid asymmetry, difference in lipid composition between inner and outer leaflet of the membrane) [53, 54]. This model system gained popularity due to its potential to show phase separation. This provided evidence that phase separation could exist in the living cell [55] and allowed to measure partitioning of lipids and proteins in these complex membranes [51]. Generally, the observed trend in partitioning is similar to GUVs, but the degree of separation is reduced [54].

The use of model membrane systems is not limited to the investigation of general membrane properties, but has been adapted to observe cell-bilayer interactions, for example, of immune cells with certain proteins presented on the bilayer [56, 57] or by reconstituting a whole array of proteins to determine their organisation [58]. These planar systems have recently been advanced to mimic 3D interaction of cells with GUVs [59]. All these examples represent only the tip of the iceberg of a whole new field of bottom-up biology [60]. Additionally, lipid encaged compounds either in vesicles or micelles (single layer of lipids) are widely used in drug-delivery and medical applications [61].

2.1.3 Plasma membrane organisation in T cell signalling

T cells are an integral part of the adaptive immune response involved in preventing the invasion of pathogens [9]. The response starts with the recognition of antigens presented by a target cell. For example, dendritic cells can process foreign proteins and present

digested peptides on their surface (via the so-called MHC complex) to activate T cells [9]. On the T cell side, the T-Cell Receptor (TCR) recognises the presented antigen and the molecules on the T-cell surface undergo reorganisation which ultimately leads to the formation of a close contact called Immunological Synapse (IS), characteristic for full T-cell activation [62, 63].

The nature and mechanism of the first events in T-cell activation are heavily debated [63]. The key players are certainly the TCR, the kinase Lck and the phosphatase CD45. The first step in activation, the so-called T-cell triggering, is characterised by phosphorylation of the tyrosines on the TCR's Immuno-receptor Tyrosine-based Activation Motifs (ITAMs) by Lck and subsequent calcium flux from the ER into the cytoplasm [63]. In the resting state the phosphatase CD45 keeps the TCR in the inactive (unphosphorylated state). How all of this is concerted is described by various competing models.

In the **kinetic segregation** model the highly expressed phosphatase CD45 suppresses triggering in the resting state [64]. CD45 has a large extracellular domain and once a T cell engages with a target cell, it is physically excluded from the contact zone, leaving the kinase Lck, which is anchored to the inner leaflet, to phosphorylate the TCR [65]. Ultimately, the time a TCR molecule resides in a so-called close-contact governs net phosphorylation, consequently triggering, and is determined by the interaction of TCR and target MHC [66].

Another proposed mechanism is **TCR-aggregation** or -clustering where for example the cross-linking of multiple receptors leads to trans-autophosphorylation [67]. Additionally, it has been suggested that clustering of TCR during activation drives it into lipid rafts, resulting in the formation of efficient signalling platforms [68–70].

Other models suggest that the T-cell triggering is mediated by **conformational changes** of the TCR upon ligand engagement [71, 72]. One popular example is the potential association of the intracellular TCR-tail with the negatively charged inner leaflet of the plasma membrane [73], despite that occurrence and functional relevance have been convincingly questioned [74].

All the aforementioned models and mechanisms are further complicated as they are likely coupled to other cellular events like actin cytoskeleton rearrangements [75–77]. This

work focusses on the role and reorganisation of Lck as one part of this complex mechanism. Lck is a particular interesting molecule because it drives T-cell activation as main kinase. Additionally, Lck is a lipid-modified (palmitoylated at two sites as well as N-terminally myristoylated) membrane associated molecule and thus interesting for the field of membrane biophysics [78–80]. It has been reported to have an affinity for the DRM and L_o-phase and thus it has been suggested to be a raft-associated protein. However, related experimental findings are controversial and probably depend on cellular state [25, 81]. Another debated aspect is the differential organisation of Lck in activated versus resting T cell. Lck has been proposed to be pre-organised, meaning pre-clustered, in the resting state with an increase upon activation (causing slowed down diffusion) [12, 82, 83], but it has also been reported to be randomly distributed in the resting T-cell [84] or mainly controlled by raft-association [85]. Revisiting this controversy is one of the aims of this thesis.

2.2 Optical microscopy and spectroscopy to dissect cellular organisation

Traditionally, biological research relies on robust biochemical assays. However, over the past decades optical microscopy has become more and more important in the field of biomedical sciences following the principle of "seeing is believing" [86]. The recent advancements in conventional and super-resolution optical microscopy and the commercialisation of cutting-edge technology, now enable us to take biological applications further to unforeseen regimes [14, 87, 88]. The achievements of these breakthroughs in optical microscopy have been acknowledged with the Nobel Prize in Chemistry in 2014 [89]. In this Section, I will briefly describe the principles behind optical super-resolution microscopy and spectroscopy as well as their application to decipher membrane organisation.

2.2.1 Optical (super-resolution) fluorescence microscopy

The size of cells is on the order of micrometre and the size of molecules is on the order of nanometre. Thus, observing these structures with the bare eye is deemed impossible. Microscopy is an indispensable tool for the observation of cellular and sub-cellular features.

The visualisation of these objects is enabled by the magnification provided by focussing and collecting light through optical elements such as lenses [90]. The lower limit for the observation of small structures is given by the diffraction of light. Since smaller structures diffract light at higher angles and the lenses (specifically the microscope objective lenses) have finite dimensions, this limits the resolution to d_{Abbe} (diffraction limited spot size) in optical microscopy (often approximated as half of the wavelength λ) [91, 92]:

$$d_{\mathrm{Abbe}} = 0.5\frac{\lambda}{\mathrm{NA}_{\mathrm{obj}}} \tag{1}$$

The numerical aperture of the objective, $\mathrm{NA}_{\mathrm{obj}}$, in fact, depends on the refractive index of the immersion medium and the maximum opening angle of the focussing lens. To circumvent this limit several super-resolution methods have been devised based on different strategies.

One group of super-resolution techniques relies on dye photoswitching, meaning turning fluorescence on or off. Within this group one can differentiate between Single Molecule Localisation Microscopy (SMLM) based approaches such as Photoactivated Localisation Microscopy (PALM) or Stochastical Optical Reconstruction Microscopy (STORM) and fluorescence depletion-based approaches like Stimulated Emission Depletion (STED) and Ground State Depletion (GSD) [87, 93]. Due to its importance for this work, the STED approach will be reviewed in more detail below (see section 2.2.2).

The SMLM approaches are usually using widefield microscopy, meaning they are camera-based, and thus relatively cost-effective and easy to implement. They utilise photoswitching of fluorescent dyes either by photo(de)activation (optically) or by reagent (chemically) induced blinking. The super-resolved imaging relies on the fact that stochastically only few isolated molecules are emitting in one frame. Subsequently, these emitters can be accurately (sub-diffraction precision) localised by fitting the emission events in each frame with a 2D-Gaussian curve. Accumulating thousands of images with many localisations allows to reconstruct the super-resolved image [94, 95]. A particularly elegant way of achieving single emitters at a time is the (DNA)-PAINT approach where the fluorescent probes are quickly exchanged and thus the molecule, or structure of interest, can be imaged for prolonged acquisition times without photobleaching [96, 97]. The SMLM

methods often use fixed samples and require long acquisition times, which makes their application to fast cellular dynamics and reorganisation less suitable [98]. Nevertheless, successful live-cell applications have been reported [99, 100].

Another group of super-resolution imaging techniques is the family of Structured Illumination Microscopy (SIM)-based methods, which show at least a twofold improvement in resolution (in contrast to the previously mentioned approaches with in principle unlimited spatial resolution improvement) [101, 102]. These techniques rely on the superimposition of spatially modulated excitation, which creates low frequency patterns from higher order (smaller scale) structures. Since the final image and the spatially modulated input are known, a Fourier-space reconstruction and deconvolution yield a super-resolved image [103]. The inherent live-cell compatibility makes it attractive for biomedical imaging with moderate acquisition speed [104] and has received impressive further advancements [105].

The above mentioned methods initially improved the lateral (x,y) resolution only and suffered from no optimisation in resolution in axial (z) direction due to the elongation of the Point Spread Function (PSF) along this optical axis. Recently, however, solutions to improve axial resolution have been reported [106, 107].

2.2.2 A brief overview on STED microscopy

STED microscopy was conceptualised and experimentally realised at the end of the last century [108, 109] and, subsequently, successfully applied in cell biology [110]. As mentioned above, its working principle relies on reversible photoswitching of fluorescent molecules in the usually confocal excitation spot, which is achieved by stimulated emission depletion [108]. Figure 2 A illustrates how the overlay of an excitation beam with a spatially modulated depletion beam can generate an effective sub-diffraction observation spot.

In most modern applications a STED microscope is based on a confocal LSM. A simplified scheme for a two-colour implementation is shown in Figure 2 B. In addition to the excitation beam(s) a red-shifted high-power STED laser is inserted. Most importantly, the spatial intensity distribution of the depletion beam is not Gaussian, but usually shaped into a doughnut (i.e., intensity distribution with a central zero) by either a vortex phase plate or a Spatial Light Modulator (SLM) [111, 112]. The fluorescence depletion at the

periphery of the observation spot can be achieved either by a pulsed or a Continuous Wave (CW) laser illumination. The only fluorescing molecules will, therefore, be in the centre of the depletion doughnut. The depleted fluorescence is red-shifted and removed by emission filters, also removing scattered STED light. The effective resolution d_{STED} scales with the incident STED power according to:

$$d_{\mathrm{STED}} = \frac{d_{\mathrm{Abbe}}}{\sqrt{1 + A\frac{I_{STED}}{I_S}}} \tag{2}$$

where $A > 0$ is a geometrical factor for the STED beam shape, I_{STED} is the STED laser power and I_S is the saturation power of the dye [14, 92]. From Equation 1 the resolution seems unlimited and is indeed just governed by the fluorescent dye photophysics. For example, using nano-crystal vacancies resolutions of less than 10 nm were experimentally achieved [113], but the reported values of resolution in (living) cells have so far been limited to about 40 - 50 nm [93, 114].

The wavelength of the STED beam should be on the high-wavelength end of the emission spectrum of the dye to deplete (Figure 2 B). This ensures that no cross-excitation from the STED beam occurs, which would cause immediate photobleaching, and also shifts the high STED laser power to a spectral range where biological samples only absorb minimally. Fluorescence in the centre of the doughnut occurs as usual (transition from electronic ground state, S_0, to excited state, S_1, and spontaneous fluorescence after fast vibrational energy release, Figure 2 B). Note that an unwanted absorption of the depletion light may also occur in the excited state, leading to photobleaching, and that the excited state absorption spectrum may differ from the ground state excitation spectrum [93]. This aspect posed initial obstacles to the use of Green Fluorescent Protein (GFP) for STED microscopy [115].

The fast data acquisition with STED microscopy makes it an attractive tool for live-cell imaging. It is debatable how much photodamage, cytotoxicity, is caused by the use of the high STED laser powers [105, 116, 117]. However, it has been shown to be feasible when adopting photodamage controls and fast beam scanning [118, 119]. STED microscopy has been advanced and combined with many other techniques such as Förster Resonance Energy Transfer (FRET) [120], Fluorescence Lifetime Imaging (FLIM) [121], or for this

work most importantly FCS [122] (see below, section 2.2.4).

More recently, the basic principles of the SMLM techniques and STED have been combined, yielding a technique termed MINFLUX, which has been reported to reach spatial precisions of a few nm [123] below 1 ms localisation time [124]. The technique has already been applied to fast particle tracking in bacteria and single molecule movements and may yield new complementary data to the ones obtained with super-resolved STED-FCS (see below).

Limiting factors of STED microscopy (not only on living systems) may be the the rather slow scanning speed, the photophysics of the dyes and the photodamage which may occur through even slight absorption of the STED light [14, 119]. Ultimately, STED microscopy provides a convenient, direct way to circumvent the diffraction limit and get a glance at the length scales which matter for molecular interactions.

2.2.3 Fluorescence microscopy based techniques to study dynamics in cells

Super-resolution imaging is a very helpful tool to understand spatial organisation and to outline interactions of molecules in their biological context. However, living systems are dynamic and information on rapid changes and transient interactions can be overlooked by taking still images. Thus, studying dynamics and molecular diffusion in cells and live-cell plasma membranes has become a vivid field of research. Three main branches of fluorescence microscopy based techniques (and their advancements) are widely employed to decipher molecular diffusion dynamics: Fluorescence Recovery After Photobleaching (FRAP), Single Particle Tracking (SPT) and FCS. I will briefly introduce the former two and then continue with a detailed review on FCS and the advancement STED-FCS, since these techniques are the main focus of this work.

In FRAP a large (micron-sized) region of interest is bleached and the fluorescence recovery is observed over time (see Figure 3 A). Molecular movements, such as diffusion or directed motion, replenish the fluorescence in the initially bleached volume. Thus, the rate of fluorescence recovery is directly related to the underlying dynamic processes [125]. FRAP can be performed on a widefield or confocal microscope [126, 127]. Uniquely, this technique provides information on the immobile fraction of particles [128]. Unlike FCS or

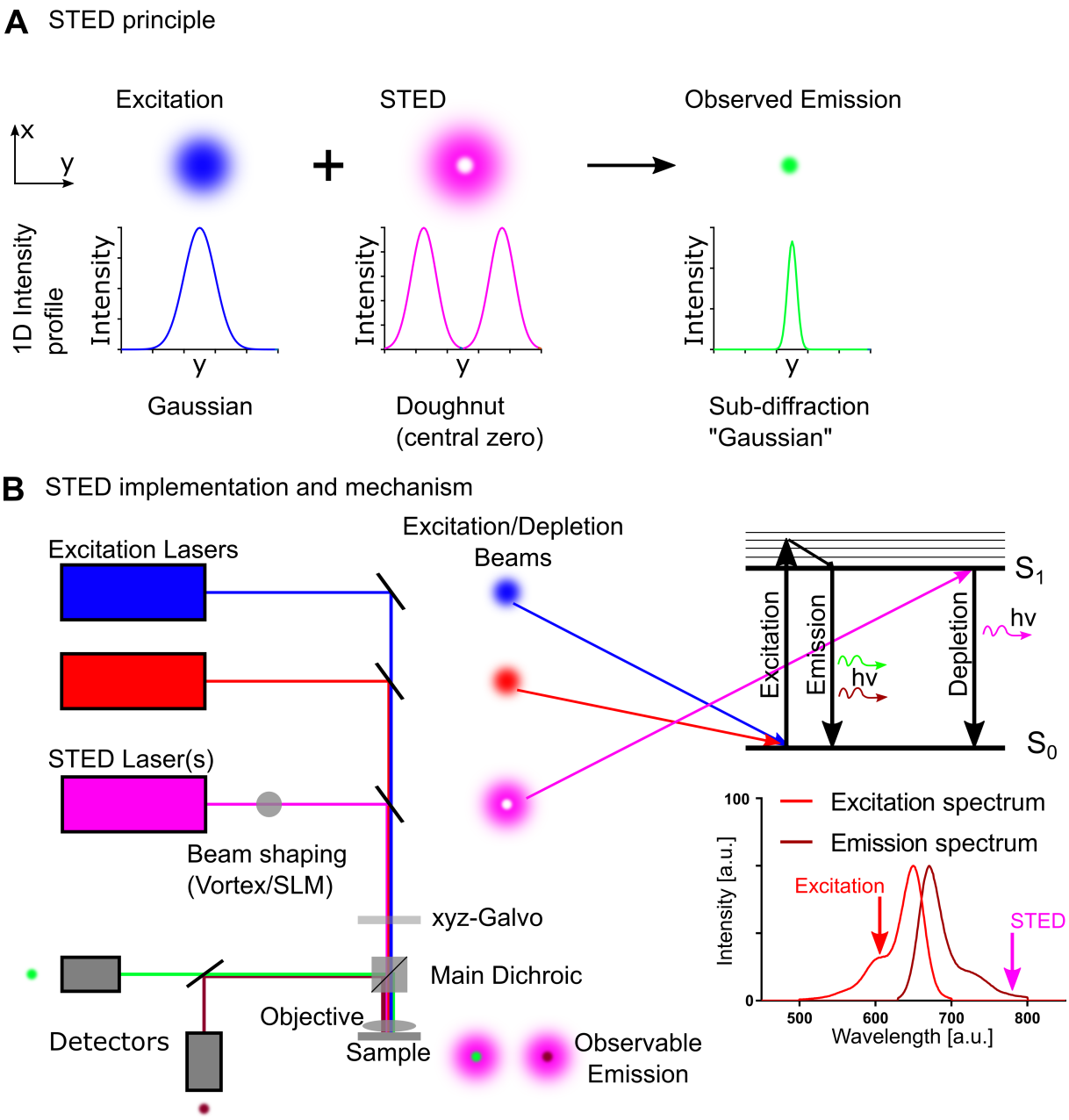


Figure 2: Working principle and implementation of STED **A**: Overlay of a Gaussian-shaped excitation laser (blue) with a doughnut-shaped (with local zero intensity in the centre) depletion laser (magenta) results in an effective sub-diffraction sized observation spot from which emission is collected (green). **B**: Main components of a simple two-colour STED-LSM (left) and photophysical working principle (right). STED beam and excitation lines are combined and sent to the sample, fluorescence is cleaned up (dichroic mirror and filters) and split onto detectors. The STED beam acts on fluorophores in the excited state (S_1) and depletes the fluorescence everywhere but in the centre of the beam (right, top). In this two-colour implementation the same STED beam is used on both excitation lines. In the S_1-state molecules can still emit fluorescence ($h\nu$) and return to the ground state (S_0). The generic excitation and emission spectra (right, bottom) indicate the STED beam being red shifted with regards to emission peak to avoid cross-excitation.

SPT, FRAP is reporting on bulk dynamics and not a single molecules sensitive technique. Nevertheless, fitting the fluorescence recovery with respective models yields, for example, the diffusion or reaction timescale, τ_{FRAP} [125].

In SPT (principle depicted in Figure 3 C) a large field of view is observed (can be several tens of microns) usually with a camera-based system (widefield or TIRF) and either scattering or fluorescent probes are used to tag molecules of interest [129]. Very high frame rates of up to several kHZ have been reached using fluorescence [33] and fast Interferometric Scattering (iSCAT) microscopy offers even higher temporal resolution [130]. In SPT, in general, an image sequence is acquired and the positions of various single particles followed over time (determining their position every frame). Data analysis involves particle localisation, error estimation, trajectory analysis and often Mean Square Displacement (MSD) analysis. The MSD displays the averaged, squared distance which a particle travels in each dimension at different time intervals (frames). If the MSD increases linearly with the lag time (time respective to start of the track), the diffusion is Brownian (free) with a diffusion coefficient of D_{SPT}. If the diffusion is hindered (the molecules undergo some kind of interactions or are restrained within an area, see below), the MSD plot will deviate from linearity. These so-called diffusion modes describe not only the rate of diffusion (diffusion time or diffusion coefficient) but also how a molecule moves [129]. SPT is limited by how many particles can be observed at a time, how precisely they can be localised (signal-to-noise ratio), how large the tag for detection has to be and how fast the camera acquisition is [36, 129–131].

2.2.4 FCS and STED-FCS

In FCS intensity fluctuations at a given spot in space are observed using a confocal microscope (see Figure 3 C for illustration). These fluctuations, transient changes in the fluorescence intensity, can arise from a variety of phenomena and report on, for example, diffusion, triplet-state kinetics, binding/unbinding kinetics or blinking [126]. Temporal autocorrelation analysis of the fluctuation signal allows to reveal the underlying processes. Fitting the resulting autocorrelation curve with appropriate models enables the deduction of parameters such as the average transit time through the observation volume, τ_{D}, or the

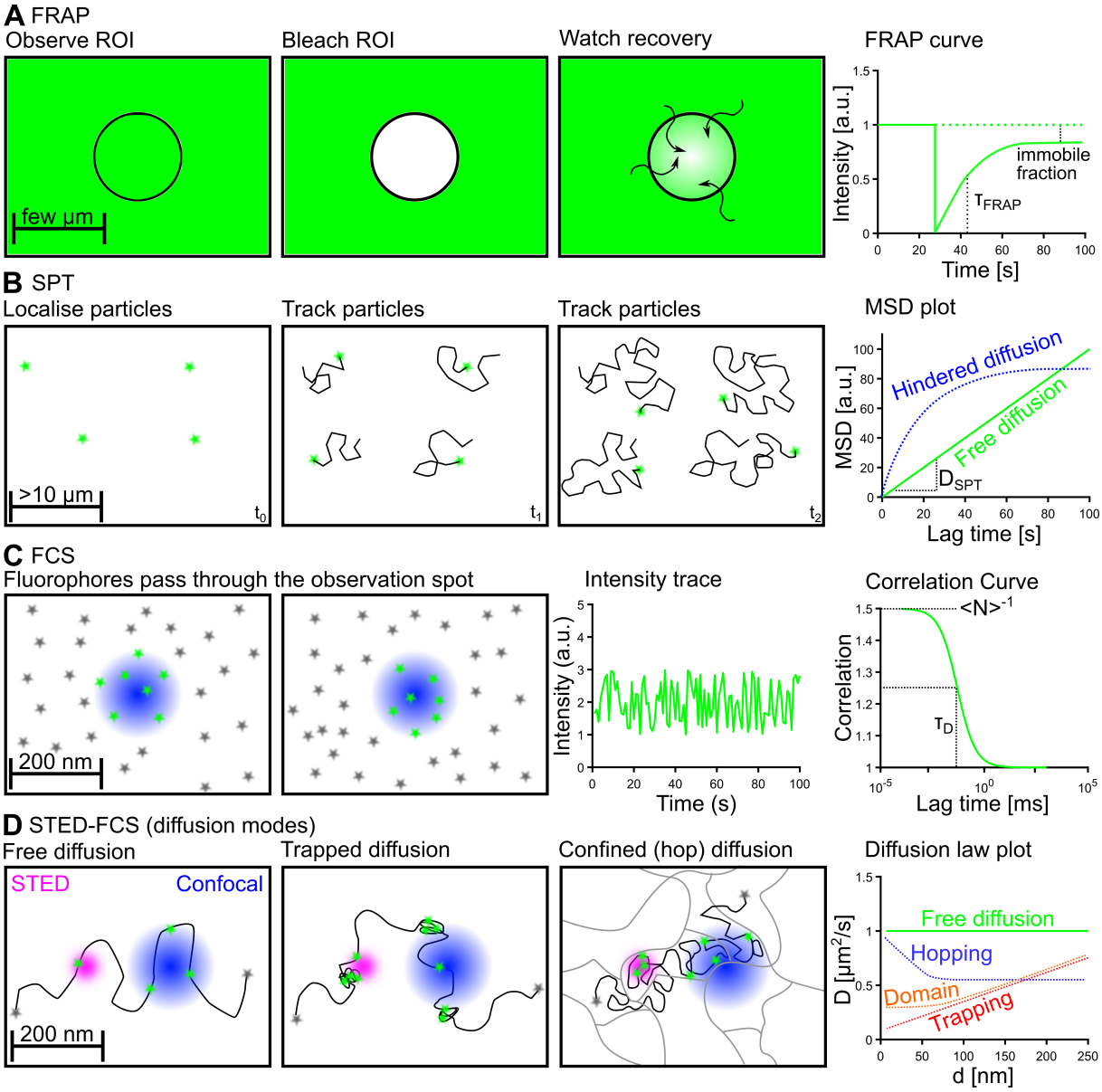


Figure 3: Techniques to explore diffusion dynamics. **A**: In FRAP an area of interest (ROI) is bleached (no green fluorescence) and the recovery observed. By integrating the intensity for each acquired frame, a FRAP curve as shown on the right can be obtained. One can extract the diffusion timescale τ_{FRAP} as well as the immobile fraction. **B**: In SPT single particles (fluorescent molecules or scatterers, green stars) are localised in every frame and followed over time (t_0, t_1,t_2 etc.). From their movements trajectories (black tracks) can be build up and the MSD calculated. Plotting the MSD against the lag time (time relative to begin of track) allows to determine the diffusion coefficient D_{SPT} and the diffusion mode (free diffusion, green, or hindered diffusion, blue). **C**: In FCS the confocal observation spot (blue) is fixed at one location and the transits of fluorescent molecules (stars) are recorded over time yielding intensity fluctuations. By subjecting the intensity time trace to autocorrelation analysis a correlation curve is obtained, from which the average transit time τ_{D} can be extracted. FCS data yield also information on average number of molecules in focus ($\langle N \rangle$) and molecular brightness (cpm). **D**: In STED-FCS, data are acquired with confocal observation spot (blue) as in FCS, but than compared to FCS data acquired with observation spots of different sizes, apparent resolutions, d (STED, magenta, only one STED observation spot size is shown). The obtained apparent diffusion coefficients D can then be plotted against d. For free diffusion D shows no dependence on d but for nano-scale interactions like trapping or confinement a clear dependence is expected red which is referred to as hindered diffusion (dashed lines in the diffusion law plot on the right).

molecular brightness [126, 132].

FCS has been developed about 50 years ago to decipher rotational and lateral diffusion dynamics [133–136] and has since evolved into an important and easy-to-use tool for biological research [137] to investigate diffusion in living cells and synthetic systems in 3D (e.g., cytoplasm or nucleus [138]) and 2D (model or cellular membranes [5, 19]). Over the years FCS has been subject to many technical advancements and the most striking was probably the introduction of confocal optics, a pinhole, which limits the collected emission to an observation volume of roughly 1 fL [126, 139]. As the pinhole rejects out-of-focus light, the zero-lag point in the correlation curve depicts the inverse average number of particles in focus ($G(0) = \langle N \rangle^{-1}$). This conveniently allows for concentration measurements as well as insights into molecular brightness [126]. This in turn allows to determine oligomerisation states [140]. Another step forward represents the combination of FCS with line-scanning of the fluorescence excitation spot (like on LSM), which results in multiple FCS measurements along the scanned line, termed scanning Fluorescence Correlation Spectroscopy (sFCS), and which also allows for spatial correlation [141, 142]. The idea of spatially (or spatio-temporally) correlating pixels has generated a whole array of techniques spearheaded by Image Correlation Spectroscopy (ICS) and Spatio-Temporal Image Correlation Spectroscopy (STICS) on camera-based systems and Raster Image Correlation Spectroscopy (RICS) as well as sFCS on LSM-based set-ups [143–146]. sFCS offers the opportunity to make use of the spatial context (e.g., acquire in the equatorial plane of cells or vesicle and align intensity traces) or to exploit the large statistics [141, 147–149]. Note that all these techniques sacrifice temporal resolution, losing the sub-microsecond timescale, to spatially resolve millisecond dynamics ,which correspond, though, to the timescale of interest for membrane dynamics [14, 148]. The idea of STICS was developed further and has yielded other camera-based FCS approaches using lightsheet or Total Internal Reflection Fluorescence (TIRF) illumination, where a FCS curve for every camera pixel is obtained [150–153]. Binning these pixels into larger areas allows to observe the diffusion at different length scales. This is a concept adapted from single point spot-variation FCS (svFCS) in which the confocal observation spot is stepwise increased by under-filling back aperture of the objective [154, 155]. These techni-

ques disclose the so-called FCS diffusion law by plotting the apparent diffusion coefficient or FCS transit time against the observation spot size or area (apparent resolution). By comparing the obtained results with the known diffusion law for freely diffusing molecules, the underlying, diffusion behaviours can be inferred [155–159]. This is analogous to SPT, as described above, and can reveal hindered diffusion on different length scales. An alternative analysis approach has recently been developed and is called image Mean Square Displacement (iMSD) [160, 161], wherein the STICS function is used and approximated with a Gaussian curve. The variance of that fitted distribution is treated equally to the MSD in SPT [158]. Hence, it is possible to distinguish diffusion modes [158] and, by binning a full field of view in smaller regions of interest, even a diffusion mode map across the whole cell can be determined [161]. For short temporal lags iMSD may provide information beyond the diffraction limit [162], the resolution, however, for this and all the aforementioned techniques is limited by the standard optics.

To actually acquire diffusion data on the relevant length scales FCS has been combined with STED super-resolution microscopy yielding STED-FCS [122, 163]. Following the idea of confocal svFCS, diffusion modes were determined in the membrane of live cells, for the first time allowing, an actual glance at molecular diffusion hindrances [122, 159, 164]. The concept of STED-FCS is depicted in Figure 3 D. For a freely diffusing molecule, probing the diffusion does not depend on the length scale (i.e., large confocal or small STED obervation spot), but as soon as hindrance occurs (such as nano-scale interactions or confinement), the diffusion coefficient changes with the observation spot size d (throughout this work also referred to as apparent resolution). Any type of diffusion behaviour which is not Brownian, free diffusion (i.e., any anomaly, any dependence of the diffusion coefficient on the observation spot size) will be referred to as hindered diffusion. Exemplary forms of hindered diffusion as observed by STED-FCS are outlined below and shown in the diffusion law plot in Figure 3 D. For trapped diffusion (transient halts in the diffusion path), a decrease in apparent diffusion coefficient and for hop diffusion (confinement within a permeable mesh) an increase (Figure 3 D, middle and right, respectively) is observed at smaller spot sizes obtained at higher STED laser powers [36, 122]. Domain diffusion (i.e., transient incorporation of the probe into an immobile area of radii $<$50 nm in which

its diffusion coefficient changes significantly) appears initially similar to trapping, but the D(d) dependence levels off towards smaller d [14, 164, 165]. Accordingly, the term domain diffusion does not refer to the diffusion of a domain itself, but rather describes the diffusion of a probe in presence of immobile, penetrable domains. Experimentally, STED-FCS has for example shown that fluorescent lipid analogs of phospholipids diffuse freely within the plasma membrane of living cells, while fluorescent sphingolipids resulted in trapped diffusion depending on cholesterol content and actin cytoskeleton integrity [122, 159].

Similarly to FCS, STED-FCS has been combined with fast beam scanning to collect spatial information on diffusional heterogeneities [166, 167] or to obtain self-calibrated measurements (i.e., observation spot size calculated by spatio-temporal correlation from the same measurement without the need of an additional control experiment) [168]. Using scanning STED-FCS (sSTED-FCS), for instance, revealed that the trapping of SM may be caused by specific, spatially localised, interactions in so-called hot-spots [166]. Some of the early results from STED-FCS were taken critically, as it was hard to verify them independently by other techniques. Yet, only Near-Field Scanning Optical Microscopy (NSOM)-FCS, where a near-field scanning prope with a small aperture is employed [169], or the use of nano-antennas to confine the observation area plasmonically [170, 171] could reach similar resolutions to STED-FCS in live cells and reassuringly confirmed the STED-FCS findings [14]. Other than that, STED-FCS has been widely applied, for example, to elucidate diffusion of lipids and proteins on sub-diffraction sized objects such as viruses or small vesicles [172, 173], to decipher Ras-diffusion modes in cancer cell membranes [174], or to investigate the role of lipid partitioning and phase separation on membrane domain formation and diffusion [47, 51, 175–177].

Technically, STED-FCS has benefited from various other advancements like pair-correlation analysis [178], combination with RICS [179], or TIRF illumination [180]. Although STED-FCS was first implemented for solution measurements [163], the success of the method came with restricting the observation to a 2D membrane plane [122], as out of focus light negatively affects the amplitude and signal-to-noise ratio in simple STED-FCS implementations. Recently however, several ways such as lifetime-based intensity filtering [181], new fitting models for the correlation curves [182, 183], or adaptive optics [184]

have been introduced to enable 3D-STED-FCS measurements (e.g., in the cytoplasm of cells). This work focusses mainly on the application of FCS-related methods to membrane dynamics.

3 Aims and Objectives

The overall aim of this thesis is to use and advance FCS-based methods to reveal membrane heterogeneity in live cells by measuring diffusion using super-resolution STED and conventional confocal microscopy. Performing super-resolved measurements on diffusion dynamics poses a technical challenge already in model systems. In this work, I try to apply and adapt the current and further developed methodologies to enable measurements on plasma membrane organisation during T-cell activation, which is a crucial part of the immune response. Such measurements require thus far unavailable experimental flexibility and robustness, high temporal and spatial resolution, and a large dynamic range to reveal the relevant processes non-invasively. To this end, I wanted to:

- Increase flexibility in FCS-based experiments on cells using novel detection equipment allowing for high photon count rates.
- Use GPMVs as a an actin-free plasma membrane model system to study diffusion dynamics at thermodynamic equilibrium and in the absence of an organised cytoskeleton.
- Enable the spatial assessment of nano-scale diffusion modes in the cellular plasma membrane using STED microscopy.
- Make these diffusion mode measurements accessible to more researchers by developing a complementary approach based on standard LSMs.
- Apply the developed techniques to a more complex biological system and decipher the diffusion dynamics and organisation of the kinase Lck in resting and activating T cells.

Ultimately, I aim to expand the available toolkit of fluctuation based techniques for the application to challenging biological questions.

4 Materials and Methods

In this Chapter, I present the materials and methods used throughout the work. This includes cell lines, chemicals, description of the optical microscope set-ups and the data analysis pipelines.

4.1 Cell lines and tissue culture

All cell lines were grown at 37 °C and 5 % CO_2. PtK2 cells were maintained in Dulbecco's Modified Eagle's medium (DMEM; Sigma-Aldrich) supplemented with 16 % fetal bovine serum (FBS; Sigma-Aldrich) and 1 % *L*-Glutamine (Life Technologies).

CHO-K1 cells were grown in DMEM/F12 (Lonza) supplemented with 10 % FBS and 1 % *L*-Glutamine. HeLa and HEK 293T cells were maintained in DMEM, 10 % FBS, 1 % *L*-Glutamine.

For GPMV production, the adherent cell lines were seeded on 35 mm Petri dishes and for microscopy experiments they were seeded on 25 mm round coverslips (# 1.5 glass) placed in 35 mm Petri dishes. The cells were grown for 1-3 days to reach a confluency of 75 % before the experiments were performed. Note that for the GPMV production from HEK cells, the dish was treated with sterile poly-*L*-lysine (PLL) for 5 minutes first.

All T-cell lines were cultured in Roswell Park Memorial Institute (RPMI) 1640 Medium (Sigma Aldrich) which was supplemented with 10 % FBS, 1 % *L*-Glutamine, 10 mM HEPES (4-(2-hydroxyethyl)-1-piperazineethanesulfonic acid) and 1 % Penicillin/Streptomycin. Jurkat and JCaM1.6 cells as well as the adherent cell lines were obtained from ATCC. T-cells stably expressing Lck-eGFP were made by viral transduction by Dr. Mafalda Santos and Edward Jenkins (Davis Lab) and kindly provided for the experiments. I distinguish between JCaMs with reconstituted Lck-eGFP (JCaM Lck-eGFP), Jurkat cells with knocked-out and reconstituted Lck-eGFP (Jurkat Lck-KO Lck-eGFP) and Jurkat cells with additional Lck-eGFP (Jurkat Lck-eGFP). For microscopy experiments T-cells were taken from the tissue culture flask treated or labelled as desired (see below) and dropped onto the glass bottom of a 8-well IBIDI chamber.

4.2 Fluorescent labelling of cells

All labelling of cells with fluorescent lipid analogs and dyes was performed in Leibovitz 15 medium (L15) for 5 to 15 minutes (see Table 1 for details on concentrations

and Figure 4 for the structural diagrams of the used lipid analogs and dyes). After two washes the cells were imaged immediately. Note that T cells were preferably labelled at 37 °C while shaking at 400 rpm in an Eppendorf shaker. T cells were washed by spinning down for 2 minutes at 2200 rpm and resuspending in warm L15. Labelling of Halo- or SNAP-tagged proteins (with 0.1-1 mM ligand) was performed in full medium at 37 °C for 30 minutes and 2 washes were performed in L15.

4.3 Transfections

Transfections were performed according to the manufacturer's protocol of the transfection reagent. For PtK2 cells Lipofectamine 3000 (Thermo Fisher), for CHO-K1 and HeLa cells Turbofect (Thermofisher) have been used. The LYPD6 plasmids were obtained from Gunes Ozhan and described in [27], the GPI-SNAP plasmid was a kind gift from Stefan Hell's lab, the GPI-eGFP and GPI-RFP plasmids were provided by Kai Simons.

4.4 GPMVs

GPMVs derived from adherent cells were produced as described in [54]. Briefly, cells were washed with GPMV-buffer (10mM HEPES, 150 mM NaCl and 2 mM $CaCl_2$, pH 7.4) and then incubated for 2-4 h at 37 °C in GPMV-buffer supplemented with 25 mM paraformaldehyde (PFA)/1-25 mM 1,4-dithitreithol (DTT) or 1-5 mM N-ethylmaleimide (NEM). High concentrations of the vesiculating agents were only used for experiments were phase separation was desired, which could further be enhanced by cooling or addition of deoxycholic acid (DCA) 1-500 µM [185].

GPMVs derived from suspension cells (T cells) were prepared according to [186] with slight modifications. The Lck-eGFP cells were treated with 25 mM PFA in addition to 5 mM NEM to improve GPMV yield.

GPMVs were immobilised using a biotin streptavidin system [164]. For this purpose, after harvesting, the GPMVs were incubated with 0.2 $\frac{\mu g}{mL}$ DSPE-PEG-biotin (Avanti Polar

Lipids) for 1.5 h. To remove excess biotinylated lipid the GPMV preparation was spun down at 10,000 rpm for 15 min in a table top centrifuge, 90 % of the supernatant removed and replaced by fresh buffer. The treated GPMVs were dropped on glass (25 mm coverslips or IBIDI 8-well chamber) previously coated with a 1:5 mixture of bovine serum albumin (BSA) and biotinylated bovine serum albumin (bBSA, both obtained from Sigma Aldrich) at a total concentration of 1 $\frac{\text{mg}}{\text{mL}}$ for 1.5 h, thoroughly washed and incubated with 200 $^{\text{ng}}/_{\text{mL}}$ streptavidin (Life Technologies) for another 1.5 h. After 20 minutes of incubation, the GPMVs were immobile and stable for hours. This method is preferred for gentle GPMV immobilisation without disturbing membrane dynamics, especially, when measurements need to be performed in the bottom membrane. For fast and crude immobilisation also PLL coated surfaces (15 minutes at room temperature) can be used [187], but may disturb diffusion dynamics especially in the bottom membrane.

Labelling of GPMVs with fluorescent lipid analogs was performed after formation and DSPE-PEG-biotin incorporation by directly adding the dye at concentrations ranging from 0.1 - 4.0 $\frac{\mu\text{g}}{\text{mL}}$ (see Table 1 for details). Note that Abberior STAR RED is interchangeably used with KK114.

Table 1: Overview of lipid analogs and dyes used to label cell and artificial membranes

Lipid analog / dye	Manufacturer	Concentrations used to label		
		Cells	GPMVs $[^{\mu\text{g}}/_{\text{mL}}]$	GUVs
Atto647N-DPPE	Atto-Tec	1	0.1	0.05
Atto647N-SM	Atto-Tec	1	0.2	0.05
Atto647N-DOPE	Atto-Tec	1	0.14	0.05
Atto647N-(H)-GM1	Custom Synthesis Guenter Schwarzmann (Bonn)	2	0.4	0.005
Abberior STAR RED -DPPE	Abberior	-	0.1	0.1
Abberior STAR RED -PEG-Cholesterol	Abberior	1	-	-
TopFluor-Cholesterol	Avanti Polar Lipids	1	0.1	0.05
TopFluor-DPPE	Avanti Polar Lipids	2	0.1	0.01
TopFluor-SM	Avanti Polar Lipids	1	0.1	0.01
Atto488-DOPE	Atto-Tec	1	0.12	0.01
FastDiO	Sigma Aldrich	-	0.1	0.05

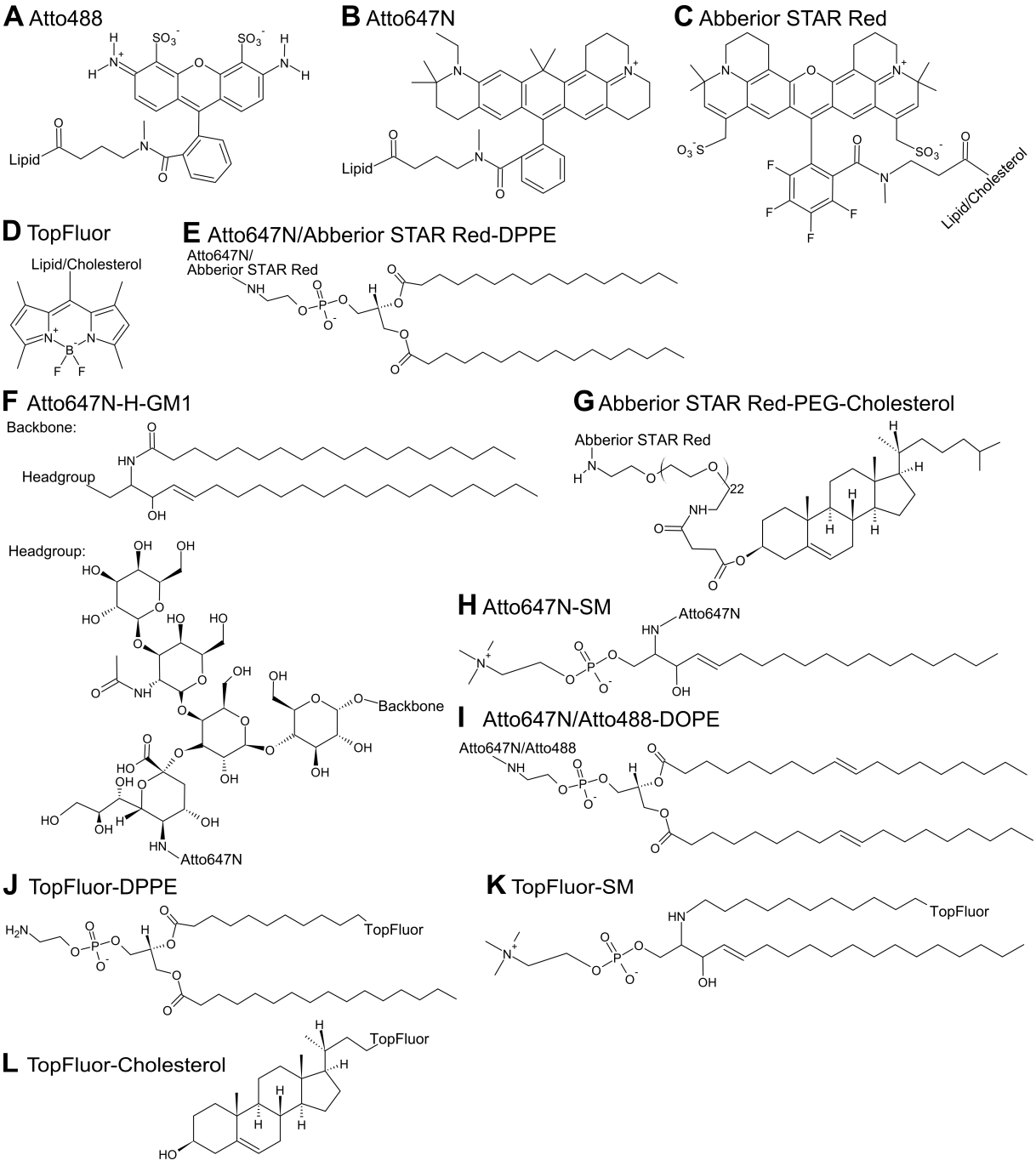


Figure 4: Structural diagrams of the utilised fluorescent lipid analogs. **A-D**: Fluorescent dyes and where they are attached to a lipid or sterol structure. **E-L**: Lipid and sterol analogs and where they are attached to the respective fluorophore. **A**: Atto488 adapted from [188]. **B**: Atto647N adapted from [122]. **C**: Abberior STAR Red (also referred to as KK114) adapted from [166, 189]. **D**: TopFluor adapted from [190]. **E**: Atto647N/Abberior STAR Red-DPPE labelled at the headgroup adapted from [122, 189]. **F**: Atto647N-H-GM1 broken down into ceramide backbone (top) and oligosaccharide headgroup labelled at the sialic acid (bottom) adapted from [122, 191]. **G**: Abberior STAR Red-PEG-Cholesterol labelled at the headgroup including a PEG linker adapted from [166]. **H**: Atto647N-SM tail labelled (acyl replacement) adapted from [122]. **I**: Headgroup labelled Atto647N/Atto488-DOPE adapted from [122]. **J**: Acyl labelled TopFluor-DPPE adapted from [190]. **K**: Acyl labelled TopFluor-SM adapted from [190]. **L**: Tail labelled TopFluor-Cholesterol adapted from [190]. For information on concentrations for labelling and manufacturers see Table 1.

4.5 GUVs

GUVs were prepared using a function generator and electroformation [192]. Briefly, a lipid mix with a total concentration of 1 $\frac{\text{mg}}{\text{mL}}$ of for example DOPC (1,2-dioleoyl-sn-glycero-3-phosphocholine, Avanti Polar lipids) in chloroform was spread on platinum wire and dried. The lipid film on the wire was dipped into a 300 mM sucrose solution and exposed to an AC electrical field of 10 Hz at 2 V for 1 h, followed by 30 minutes at 2 Hz (2 V) in custom-made Teflon chambers. The GUVs were handled carefully (i.e., only using cut tips). All experiments with GUVs were performed in phosphate buffered saline (PBS) in BSA coated glass bottom chambers (IBIDI). The coating of the glass was performed by incubation of 1 $\frac{\text{mg}}{\text{mL}}$ BSA followed by thorough washing. GUVs were labelled in reaction tubes prior to adding them onto the glass coverslips (see Table 1 for details).

4.6 SLBs

SLBs were prepared by spincoating lipid solution onto hydrophilic coverslips [193, 194]. The coverslips were treated and cleaned with piranha acid (1:4 H_20_2 : H_2SO_4) for at least 2 hours and washed with copious amounts of distilled water, in which they could be stored for about a week. Prior to usage the coverslips were plasma cleaned for 10 s.

Spincoating of lipid solutions with total lipid concentration of 1 $\frac{\text{mg}}{\text{mL}}$ (in a 1:2 mix of methanol and chloroform) was performed for 45 s at 3200 rpm. The resulting lipid film was hydrated with SLB buffer (containing 150 mM NaCl, 10 mM HEPES at pH 7.4) and washed multiple times to remove multilamellar structures. For point Fluorescence Correlation Spectroscopy (pFCS) pure DOPC bilayers were prepared, whereas for sFCS measurements often 50 mol% cholesterol (Avanti Polar Lipids) was used. Prior to spincoating, the lipid mix was doped with fluorescent lipid analogs, namely Abberior STAR RED-DPPE or Atto488-DOPE (using varying molar ratios from 1:500 to 1:50,000).

4.7 Coverslip preparation for T-cell experiments

To evaluate the effect of different surface coatings on T-cell activation IBIDI 8-well glass bottom chambers were coated with different proteins or PLL. IgG (Jackson Immuno) was coated over night at 4 °C at 50 $\frac{\mu\text{g}}{\text{mL}}$. After washing with PBS and L15 the coverslips

were ready to use as IgG control or further functionalised with the activating anti-CD3 antibody, OKT3 (prepared in-house by Alastair Waugh) at 10 $\frac{\mu g}{mL}$ for 2 h at room temperature. After washing with L15, the slides were used and not stored. PLL and BSA coating were preformed similarly as for GUVs and GPMVs (see sections 4.4 and 4.5, respectively), but washing was performed with L15.

For experiments on resting T-cells, coverslips (WillCo glass bottom dishes) were coated gradually with decreasing concentration of a hydrogel (CyGel, BioStatus/Abcam). The first layer consisted of 100 % CyGel and was baked for 5 minutes at 65 °C. The second layer consisted of 50 % CyGel (in L15, premixed at least for 24 h) and baked for 3 minutes at 65 °C. As last layer 25 % CyGel has been used. The last layer did not solidify entirely. Note that CyGel is liquid at lower temperatures (below 4 °C) and polymerises reversibly at higher temperatures. Thus, all pipetting was preformed quickly and with a cooled dish.

For microscopy experiments the T cells were carefully dropped into the chamber or well. In the case of the hydrogel, adding small amounts of L15 (at room temperature) allowed the cells to enter the gel and slowly sink towards the coverslip.

4.8 Calcium imaging

Calcium imaging was used to determine T-cell activation (T-cell triggering). Calcium release from the ER is one of the first events in early T-cell signalling. About 10^6 cells (eg. Jurkat or JCaM) were spun down in a table top centrifuge (2000 rpm, 90 s) and resuspended in supplement free RPMI, which got 1 to 1 mixed with HBS containing 1.25 mM probenecid (AATBioquest) and 25 $\frac{\mu g}{mL}$ Fluo4-AM (Thermofisher) final concentrations. The cells were incubated for 20 min in the dark at room temperature and then washed three times with HBS containing 2.5 mM probenecid. The cells could be used over the course of 1 h and experiments were performed in prewarmed HBS. Calcium data (time lapses) were analysed either by hand in FIJI [195–197] or in Matlab by using the software package CalQuo [198, 199].

4.9 Microscopy and spectroscopy

The data for this thesis were acquired on three different microscopes: A Zeiss 780 LSM inverted microscope (Carl Zeiss), a Leica SP8 STED with fast lifetime contrast (FALCON, Leica Microsystems), and a customised Abberior STED microscope (Abberior).

The **Zeiss 780** was used for confocal imaging, pFCS and sFCS measurements. It was equipped with a 40× C-Apochromat NA 1.2 W Corr FCS objective which allowed deep imaging and FCS. All fluorescence was collected on the hybrid detectors (GaAsP-detectors, Channel S) after passing appropriate emission filters. All sFCS data were acquired in photon counting mode and most imaging data were acquired in integration mode (gain of 800). For the measurements either a 488 dichroic or a 488/594/633 MBS was used and the pinhole set to 1 AU. Fluorescence was excited with a 488 nm Argon laser or a 633 nm He-Ne laser. For any FCS measurements or quantitative imaging the focal volume was calibrated using fluorescent solutions of Alexa Fluor 488 or Atto655 in water (each at 10 nM). The correction-collar was set to maximise the counts per molecule and the pinhole aligned using the built-in routine. The microscope was equipped with an incubator allowing measurements at room temperature or at 37 °C as indicated. For cooling and phase separation of GPMVs a Peltier element was used as described in [54]. Confocal sFCS was performed by exploiting the line scan option. 52 pixels (zoom of 40, resulting 100^2 nm^2 per pixel) were acquired at maximum scanning speed (3.94 µs pixel dwell time and 2081 Hz line frequency) for the maximum of 10^5 lines resulting in measurement durations of about 48 s. All files were saved as .lsm5-files. All pFCS was performed with the built in routine. Measurements lasted typically 10 s and data were saved as .fcs-files.

The **Leica SP8 FALCON** (located at Leica Microsystems in Mannheim, Germany) was used for confocal and STED measurements comparing high and low photon count rates. It was equipped with a HC PL APO 100×/1.40 Oil objective and a HC PL APO 86×/1.20 Water objective with motorised correction collar (motCORR) optimised by the internal routine ("set corr ring") for every sample. The oil-immersion objective was used for bottom membrane and SLB measurements, whereas the water-immersion objective was used for solution and top-membrane measurements. For fluorescence excitation the

tunable white light laser (WLL, Koheras SuperK) was employed with clean-up filters to obtain 488 nm and 633 nm. For STED a pulsed 775 nm infrared laser was used. Fluorescence was collected through appropriate notch filters onto the internal hybrid single-molecule detectors (HyD-SMDs). Data post-processing was performed with the LAS-X SMD module and data exported as Excel-sheets.

The **Abberior STED** is a customised RESOLFT microscope which was used for STED imaging, point STED-FCS and scanning STED-FCS (as well as for the during this thesis developed LIESS-FCS, see below) measurements and is described in detail in [88, 112]. Briefly, it is equipped with a 100× UPlanSApo/1.40 objective (Olympus) and two diode lasers for fluorescence excitation (PicoQuant) pulsing at 488 nm and 633 nm. Fluorescence is collected through appropriate emission filters onto two detectors (MPDs). The detectors are connected to a hardware correlator card (Flex02-08D, correlator.com). For depletion a tunable Mai Tai infrared laser (Newport) pulsing at 80 MHz was used and set to 780 nm or 755 nm emission wavelength. All parts of the microscope, except for the correlator card, could be operated via the ImSpector software (Abberior Instruments). Typical acquisition times for pSTED-FCS measurements were 10 - 15 s and data were saved as correlated files (.sin-files). sFCS and sSTED-FCS measurements were much longer and saved as .msr-files. sFCS was performed using the xt-scan option in ImSpector and the scanner calibration optimised for fast scanning. For line interleaved acquisitions, the line step function was exploited and the data stream split alternatingly in confocal and STED sFCS data. Typically sFCS and LIESS-FCS experiments were performed using orbital scanning with pixel dwell times of 10 µs and scanning frequencies of about 3 kHz for 30 s - 180 s. In Imspector the line length and pixel size were set to 1 to 3 µm 100 nm/px (for confocal sFCS) and 40 nm/px (for sSTED-FCS and LIESS-FCS), respectively. Note that for an orbital scan the line length depicts the diameter of the scanned circle.

For all FCS and sFCS experiments the excitation power was below saturation of the respective fluorophore (1 - 10 µW at the objective's back aperture) unless indicated otherwise. The STED powers ranged from 0 to 140 mW.

4.10 Fitting of (s)FCS data

pFCS and pSTED-FCS data obtained from the Leica SP 8 FALCON were processed (e.g., time gated, chopped or corrected for photobleaching), fitted with the LAS-X SMD module (Leica Microsystems) and exported to Excel for further analysis. pFCS and pSTED-FCS data obtained from the Zeiss 780 and Abberior STED were processed and fitted using the FoCuS_point software [200]. sFCS, sSTED-FCS and LIESS-FCS data were processed and fitted using the FoCuS_scan software [148]. The data is read in as intensity carpet and needs to be correlated provided the pixel dwell time and scanning frequency is known. The software allows for correction of initial bleaching by cropping and photobleaching correction by local averaging or fitting of an additional exponential decay. Usually, the first few seconds of a measurement were cropped off and the longest possible averaging window chosen to correct for photobleaching.

Correlated curves, auto correlation values $G(\tau)$, (obtained on any of the described microscopes) were fitted to models of the generic form

$$G(\tau) = G(0) \cdot (G_D(\tau) \cdot G_T(\tau)) + O_{ff} \tag{3}$$

where the correlation G at given lag time τ can be described by the correlation amplitude $G(0)$ (at zero lag time) which relates inversely to the average number of particles in focus ($G(0) = \langle N \rangle^{-1}$), the diffusive process(es) $G_D(\tau)$, the photophysics (e.g. triplet state(s)) $G_T(\tau)$ and the correlation offset O_{ff}.

The term for the diffusive process for a particle moving in 3D is given as

$$G_{3D}(\tau) = (1 + (\frac{\tau}{\tau_D})^{\alpha})^{-1} \cdot (1 + \frac{\tau}{AR^2 \cdot \tau_D})^{-\frac{1}{2}} \tag{4}$$

where τ_D is the transit time of a molecule through the observation volume (often also denoted as diffusion time), α is the anomaly factor and AR the aspect ratio between long and short axis of the Gaussian observation volume (often also denoted as structural parameter).

$G_D(\tau)$ for particles diffusing in 2D like in a membrane of a cell is:

$$G_{2D}(\tau) = (1 + (\frac{\tau}{\tau_D})^{\alpha})^{-1} \tag{5}$$

The anomaly factor α was fixed to 1 for dyes freely diffusing in solutions or bilayers, but allowed to float between 0.7 and 1.05 when anomaly was expected (e.g when observing nanoscale diffusion of SM in a cellular membrane). For confocal sFCS data the α-value given the Signal to Noise Ratio (SNR) was usually fixed to 1.

In a special case, not a Gaussian shaped observation spot, but an elliptical one was assumed (binning of sSTED-FCS data, see chapter 5.3.1) where the diffusive process is given by

$$G_{2D,ell}(\tau) = (1 + \frac{\tau}{\tau_{D,x}})^{-\frac{1}{2}} \cdot (1 + \frac{\tau}{\tau_{D,y}})^{-\frac{1}{2}} \tag{6}$$

where the diffusion times along the different axis $\tau_{D,x}$ and $\tau_{D,y}$ are independent. $\tau_{D,x}$ was obtained from fitting data with a Gaussian observation profile and then fixed. Thus only $\tau_{D,y}$ was a fitting parameter.

In another special case (hop diffusion investigated by statistical analysis, see section 5.4.5), a model for two diffusing species has been used, as suggested earlier for confined diffusion investigated with a camera-based FCS approach [201]:

$$G_{2D,2species}(\tau) = \left(A_1 \cdot \frac{1}{(1 + \tau/\tau_{D,1})} + A_2 \cdot \frac{1}{(1 + \tau/\tau_{D,2})} \right) \tag{7}$$

where A_1 and A_2 are the amplitudes of the diffusing species with the respective transit times $\tau_{D,1}$ and $\tau_{D,2}$.

In contrast to data obtained from sFCS, due to the fast sampling rate of pFCS and pSTED-FCS data, one or multiple triplet states can contribute to the overall correlation term ($G(\tau)$). To describe the triplet dynamics the following exponential model was assumed:

$$G_T(\tau) = 1 + \left(\frac{T_T}{1 - T_T}\right) \exp\left(-\frac{\tau}{\tau_T}\right) \tag{8}$$

where τ_T denotes the characteristic triplet time and T_T the triplet fraction. Typical values used for different dyes were 5 µs for Abberior STAR RED and Atto647N or 40 µs

for eGFP. Note that for Atto647N a second dark state with a relaxation time of 100 µs can be observed in the cell membrane of living cells, as pointed out in [202].

The FoCuS software packages allow for fitting of bootstrapped data, which provides better fits and accurate error estimations as well as SNR estimation (based on $SNR = {G(\tau)}/{var(G(\tau))^{0.5}}$, [148]). This was often employed for sFCS data.

As a measure for quality of curve fitting the residuals displayed in the FoCuS_scan software were used [148]. For the evaluation of the fitting and data quality of the high count rate FCS data a normalised residuals mean squared displacement (nRMSD) was calculated up to the fitted transit time:

$$nRMSD = \frac{\sqrt{N_{\tau_D}^{-1} \sum_{i=1}^{i=N_{\tau_D}} (data_i - fit_i)^2}}{G(0)_{\text{fit}}} \tag{9}$$

The nRMSD value was normalised to the fitted amplitude $G(0)_{\text{fit}}$ and represents the mean squared difference of the fit for the i-th correlation point fit_i for every (i-th) data point $data_i$ including only the values from the fitting minimum (1 µs) up to N_{τ_D}, where the data point equals the fitted transit time τ_D. This ensures a robust assessment of the noise and excludes a bias from fitted data showing an offset. The nRMSD as a quality measure is visualised in Figure 6 C. The reason for this procedure was that the data were processed and fitted (using the same models as described above) in the LAS-X software from Leica Microsystems. All data were exported to Excel for further analysis.

4.11 STED-FCS

STED-FCS data were obtained either on the Abberior STED microscope or the Leica SP8 FALCON. STED and STED-FCS performance were checked and calibrated before starting a measurement session, as outlined in detail in [14]. Briefly, using fluorescent 20 nm Crimson Beads (Thermo Fisher) embedded in Mowiol (Sigma Aldrich) spatial and temporal alignment of the STED microscope were checked. Confocal imaging of the beads yields the confocal Full Width at Half Max (FWHM), d_{conf}, of the microscope's PSF. This value is needed to calculate the FWHM, $d_{STED,i}$, the apparent resolution at arbitrary STED powers i. By performing a FCS experiment on an SLB with freely diffusing lipid

analog the $d_{STED,i}$ can be inferred using the following relationship:

$$d_{STED,i} = d_{confocal} \cdot \sqrt{\frac{\tau_D(STED,i)}{\tau_D(confocal)}} \tag{10}$$

With $\tau_D(STED,i)$ as transit time at given STED power i and $\tau_D(confocal)$ as transit time in confocal mode. Using the FWHM, d, at given STED power (also referred to as apparent resolution) and the respective transit time $\tau_{D,d}$, the apparent diffusion coefficient, $D(d)$, for different observation spot sizes can be calculated and used to plot the STED-FCS diffusion law $D(d)$ versus d (apparent resolution) [122, 159, 164].

$$D(d) = \frac{d^2}{8 \cdot ln(2) \cdot \tau_{D,d}} \tag{11}$$

Often the ratio of the diffusion coefficient at a given STED power (or resolution) and the confocal diffusion coefficient can be indicative of the diffusion mode and is called D_{rat}-value, given by:

$$D_{rat} = \frac{D_{d,STED}}{D_{confocal}} \tag{12}$$

This is used to plot the diffusion modes over space in LIESS-FCS measurements. Note that as a calibration sample also freely diffusing dyes in GUVs or GPMV have been used to mimic SNR in the actual sample as closely as possible.

4.12 Simulations

Monte Carlo simulations to generate molecular tracks with different diffusion modes and sampling by FCS variants were generated in Python and Cython. These simulations have been performed in collaboration with Dominic Waithe and resulted in the GitHub nanosimpy repository (https://github.com/dwaithe/nanosimpy) [164].

In pFCS (after generation of the molecular tracks, see below) the intensity traces were simulated by passing the diffusion tracks through a Gaussian shaped observation spot (of variable diameter for diffusion mode determination). This results in an intensity trace of the simulation "acquisition time" (typically between 10 and 60 s). The intensity was sampled every 1 - 20 µs (time steps) in the centre of the simulation area.

In sFCS the intensities were sampled along a line of multiple observation spots (30-52 pixels) with given scanning frequencies ranging from 500 - 3500 Hz, as indicated. The obtained intensity carpets were saved as .tiff-files. The time steps (for the track generation) were for numerical reasons equal to the pixel dwell time (3.94 µs for sFCS and 10 µs for LIESS-FCS simulations). Generation of the molecular tracks was similar for pFCS and sFCS, but the pFCS simulations were performed in a circular area, whereas the sFCS simulations were performed in a rectangular box to accommodate for the sFCS line (which was in every case 1 µm away from the boundaries).

In the case of free diffusion, the molecular tracks were simply generated by a random walk, where the step size (at every time step) scales with the input diffusion coefficient (sampled from a normal distribution). The simulation was performed on a circular area and once a particle reached a boundary, it was wrapped around to the other side of the simulation area. FCS data were acquired in the centre of the simulation to avoid boundary effects.

Hindered (non-Brownian) diffusion was simulated using different approaches. Firstly, trapped diffusion was simulated using the model of molecular complex formation (or stochastic trapping model) [203], where every molecule at every time step needs to be evaluated. They have a probability of being trapped p_{trap} and a probability of untrapping p_{untrap} (if they are trapped the diffusion coefficient is set to 10^{-10} $\frac{\mu m^2}{s}$, being practically immobile). Note that free diffusion is obtained when $p_{trap} = p_{untrap} = 0$.

Hop diffusion (diffusion with area confinement) was simulated by first randomly seeding points, performing a Voronoi transform and thus obtaining a meshwork (with average meshsize L given as $\sqrt{(area)}$ depending on simulation area and number of seeded points) [36]. This spatial hopping map was superimposed with the simulation box and, whenever a particle hit a boundary it was evaluated to pass on into a new compartment with a probability of p_{hop} or remain within the same compartment $(1 - p_{hop})$. Note that free diffusion is obtained when $p_{hop} = 1$.

Only for pFCS a domain diffusion model was explored as well. 20 nm sized domains were randomly distributed covering about 50 % of the simulation area (the domains were not allowed to overlap). Similarly to the hopping model, once a particle hits a domain

boundary it could pass on (with a given probability p_{domain}), but then it diffused with a third of its initial diffusion coefficient inside the domain. Another probability test with the same p_{domain} was performed for leaving a domain. The values for p_{domain} were chosen similarly to the values for $p_{trap} = p_{untrap}$, since this model was devised as an alternative to explain trapped diffusion behaviour.

The obtained intensity traces or carpets were then correlated (using a multi-tau algorithm [204]) and the obtained correlation curves fitted with FoCuS_point or FoCuS_scan, as described above (section 4.10).

4.13 Statistical analysis of sFCS data

The statistical analysis of sFCS data as a method to reveal hindered diffusion was developed during my D.Phil work [187]. The analysis is split into the fitting of the histograms and the model selection. Ideally, the model would be selected solely based on the data and the best fit found by histogram fitting.

4.13.1 Evaluation of sFCS Histograms

The conceptual basis for the analysis is the observation, that sFCS data of freely diffusing molecules, when histogrammed, are lognormally distributed. This is a result of the sampling bias due to the comparably slow scanning frequency (as outlined in the Results, Section 5.4.1) [148].

For the analysis of a sFCS experiment the raw data (intensity carpets) were analysed and fitted with the FoCuS_scan software, as described above in Section 4.10. Large sets of fitting parameters, most importantly the transit times, were saved into Excel-sheets and loaded into MATLAB (MathWorks) for further analysis. All fitting was performed with custom written scripts using built-in MATLAB functions.

The transit times were histogrammed into equally spaced bins using MATLAB's histogram function. Unrealistically large transit times (e.g., caused by bleaching) were removed by applying a cutoff-value. The histograms were computed as linear histograms (Probability Distribution Functions (pdfs)) and normalised as pdf. Additionally, the histogram was computed as Cumulative Distribution Function (cdf) and normalised as cdf. Finally,

the natural logarithms of the transit times were calculated and the resulting data histogrammed. In that case, lognormally distributed data fall then onto a Gaussian (Normal) distribution [205]. To obtain accurate fits, these three data representations were fitted with the respective analytical form of the probability distribution function. For analysis and fitting of histogrammed data, all midpoints of the histogram bars were extracted and subjected to fitting with the following functions. The linear form of the lognormal function (further denoted as subscript to the function $slogn, lin$) is given as:

$$f_{sLogn,lin}(X_{lin}|\mu,\sigma) = \frac{1}{X_{lin}\sigma\sqrt{(2\pi)}} \exp -\frac{(\ln(X_{lin}) - \mu)^2}{2\sigma^2}, \tag{13}$$

with two characteristic parameters μ and σ as well as the histogrammed data in linear form X_{lin} .

The single cumulative Lognormal function, $f_{sLogn,cum}(X_{cum}|\mu,\sigma)$, is defined as:

$$f_{sLogn,cum}(X_{cum}|\mu,\sigma) = \frac{1}{2} + \frac{1}{2}\mathrm{erf}\frac{(\ln(X_{cum}) - \mu)}{\sqrt{2}\sigma}, \tag{14}$$

where erf denotes the error function and X_{cum} the data in the cumulative form. The third, logarithmic and final representation of the single Lognormal function $f_{sLogn,log}(X_{log}|\tilde{\mu},\tilde{\sigma})$ is given as a Normal distribution:

$$f_{sLogn,log}(X_{log}|\tilde{\mu},\tilde{\sigma}) = \frac{1}{\tilde{\sigma}\sqrt{2\pi}} \exp \frac{-(X_{log} - \tilde{\mu})^2}{2\tilde{\sigma}^2} \tag{15}$$

As described above, when the linear data X_{lin} are lognormally distributed, the logarithm $X_{log} = \ln(X_{lin})$ is normally distributed with the slightly modified parameters $\tilde{\mu} = \mu + \frac{1}{2}(\sigma^2 - \sigma^4)$ and $\tilde{\sigma} = \sigma^2$.

The fitting strategy was to first evaluate the cumulative histogram, extract the fitting parameters μ and σ, then transfer them as initial guesses to fitting the logarithmic representation (allowing only 20 % variation of the fitting parameters), and finally fitting the linear representation with the same strategy. Ultimately, that allows the determination of two parameters by three fits.

For a freely diffusing molecule, the exponential μ-value is closely related to the transit time τ_D ($\tau_D = \exp\mu$). Thus, to evaluate the fitting performance (on simulated data,

see section 5.4.1) a value recovery metric was defined as $\frac{\tau_{D,in}-\tau_{D,out}}{\tau_{D,in}}$, where $\tau_{D,in}$ is the input transit time (from the simulations) and $\tau_{D,out}$ is the output transit time (recovered transist time) from either averaging or fitting with the above described approach.

It turned out that sFCS data for molecules undergoing hindered diffusion and probed by sFCS do not result in a lognormal distribution of the transit times. For instance, molecules undergoing trapped diffusion (short-lived interactions at specific spots resulting in transient halts, see the trapping model for simulations Section 4.12) measured by sFCS yield a double lognormal distribution, *dlogN*, as a second component separates in time. Also in this case, the fitting functions in the three representations can be defined as follows:

$$\begin{aligned} f_{dLogn,cum}(X_{cum}|\mu_1,\sigma_1,\mu_2,\sigma_2,A) =& A\cdot(\frac{1}{2}+\frac{1}{2}\cdot\mathrm{erf}\frac{(\ln(X_{cum})-\mu_1)}{\sqrt{2}\sigma_1})+ \\ & (1-A)\cdot(\frac{1}{2}+\frac{1}{2}\cdot\mathrm{erf}\frac{(\ln(X_{cum})-\mu_2)}{\sqrt{2}\sigma_2}) \end{aligned} \tag{16}$$

$$\begin{aligned} f_{dLogn,log}(X_{log}|\tilde{\mu}_1,\tilde{\sigma}_1,\tilde{\mu}_2,\tilde{\sigma}_2,A) =& A\cdot(\frac{1}{\tilde{\sigma}_1\sqrt{2\pi}}\exp\frac{-(X_{log}-\tilde{\mu}_1)^2}{2\tilde{\sigma}_1^2})+ \\ & (1-A)\cdot(\frac{1}{\tilde{\sigma}_2\sqrt{2\pi}}\exp\frac{-(X_{log}-\tilde{\mu}_2)^2}{2\tilde{\sigma}_2^2}) \end{aligned} \tag{17}$$

$$\begin{aligned} f_{dLogn,lin}(X_{lin}|\mu_1,\sigma_1,\mu_2,\sigma_2,A) =& A\cdot(\frac{1}{X_{lin}\sigma_1\sqrt{(2\pi)}}\exp-\frac{(\ln(X_{lin})-\mu_1)^2}{2\sigma_1^2})+ \\ & (1-A)\cdot(\frac{1}{X_{lin}\sigma_2\sqrt{(2\pi)}}\exp-\frac{(\ln(X_{lin})-\mu_2)^2}{2\sigma_2^2}), \end{aligned} \tag{18}$$

where A is a weighting factor of the two Lognormal distributions represented by μ_1, σ_1 and μ_2, σ_2, respectively.

The described analysis relies on fitting the raw sFCS data first, usually as simple as possible, using a single component FCS-model for one diffusive component and an offset: Equations 3 and 5. For the analysis of sFCS histograms for data from molecules undergoing hindered hop diffusion, a more complicated model with two diffusing components had to be assumed (Equation 7), as suggested previously [201]. Not in every spatial location two diffusing populations can be observed, thus the data were post-processed. Only curves, where the second component contributed more than 10 % to the fit (Equation

7, A_1 or A_2), were accepted. With these processed data at hand, the histograms displayed a combination of a lognormal and an exponential function, which could be fitted as described for the other functional forms. The three representations are given as:

$$\begin{aligned} f_{LognExp,cum}(X_{cum}|\mu_1,\sigma_1,\mu_2,A) =& A\cdot(\frac{1}{2}+\frac{1}{2}\cdot\mathrm{erf}\frac{(\ln(X_{cum})-\mu_1)}{\sqrt{2}\sigma_1})+ \\ & (1-A)\cdot(1-\exp\frac{-X_{cum}}{\mu_2}) \end{aligned} \tag{19}$$

$$\begin{aligned} f_{LognExp,log}(X_{log}|\tilde{\mu}_1,\tilde{\sigma}_1,\tilde{\mu}_2,A,C) =& A\cdot(\frac{1}{\tilde{\sigma}_1\sqrt{2\pi}}\exp\frac{-(X_{log}-\tilde{\mu}_1)^2}{2\tilde{\sigma}_1^2})+ \\ & (1-A)\cdot(\frac{-1}{\mu_2}\cdot X_{log}+\ln(\frac{1}{\mu_2}))+C \end{aligned} \tag{20}$$

$$\begin{aligned} f_{LognExp,lin}(X_{lin}|\mu_1,\sigma_1,\mu_2,A) =& A\cdot(\frac{1}{X_{lin}\sigma_1\sqrt{(2\pi)}}\exp-\frac{(\ln(X_{lin})-\mu_1)^2}{2\sigma_1^2})+ \\ & (1-A)\cdot(\frac{1}{\mu_2}\cdot\exp\frac{-X_{lin}}{\mu_2}), \end{aligned} \tag{21}$$

where A is a weighting factor for the two distributions with μ_1, σ_1 for the Lognormal and μ_2 for the exponential, respectively. C is an offset. Note that for the analysis of hopping, a cutoff value was applied to remove values beyond the resolution limit of sFCS (in this case <1 ms and >300 ms).

4.13.2 Model selection and histogram fitting quality

From fitting the transit time histograms, the fitting residuals can be obtained. These are indicative of the appropriateness of a certain model (just qualitatively, by visual inspection). The normalised residuals were calculated for every point i according to:

$$Residuals_i = \frac{(y_{data,i}-y_{fit,i})}{\sqrt{(y_{fit,i})}}, \tag{22}$$

with $y_{data,i}$ as the i-th y-value extracted from the histogram at the i-th bin, and $y_{fit,i}$ as the i-th recalculated y-value using μ and σ from the fit (for example, with the data at point i in the linear histogram $X_{lin,i}$). Note that the residuals for the sFCS fits were normalised to the square root of the respective value to account for the increasing error with increasing transit time in lognormally distributed data.

As a single number for residual evaluation, the Goodness of Fit value was calculated

according to:

$$Goodness\ of\ Fit = \sum_{i=1}^{n} \frac{(y_{data,i} - y_{fit,i})^2}{y_{fit,i}} \tag{23}$$

This allows by fitting a single data set with multiple models (or input parameters for the same model) to compare the overall improvement, but is not statistically meaningful. Thus, for model selection a different approach, a Maximum Likelihood Estimation (MLE) based evaluation, was performed to fit the linear representation for the different lognormal functions. The MLE provides estimators, $\hat{\mu}_{1,2}$ and $\hat{\sigma}_{1,2}$, which should match the values obtained from histogram fitting. Additionally, when the MLE converges, the optimised maximum likelihood vector is obtained, which can be used for Bayesian Information Criterion (BIC) analysis. The BIC value is a statistical measure of how well data are represented by a model. The lowest BIC value indicates the best model given the data. Note that the BIC evaluation applies a penalty for the introduction of more fitting parameters. For example, if two models fit the data equally well, but one of them has more free parameters, this model will have a higher BIC (not the preferred model). In the first instance, transit time histograms are evaluated for being Gaussian, single lognormal (free diffusion) or double lognormal (trapped diffusion). The log-likelihood functions were derived according to [206] and are given as:

$$\begin{aligned} \ln \mathcal{L}_{Gauss}(\mu, \sigma^2) = &\sum_{i=1}^{n} \ln f_{Gauss}(x_i|\, \mu, \sigma^2) = \\ &- \frac{n}{2} \ln(2\pi) - \frac{n}{2} \ln \sigma^2 - \frac{1}{2\sigma^2} \sum_{i=1}^{n} (x_i - \mu)^2 \end{aligned} \tag{24}$$

$$\begin{aligned} \ln \mathcal{L}_{sLogn}(\mu, \sigma^2) = &\sum_{i=1}^{n} \ln f_{sLogn,lin}(x_i|\, \mu, \sigma^2) = \\ &- \frac{n}{2} \ln(2\pi\sigma^2) - \sum_{i=1}^{n} \ln(x_i) - \frac{\sum_{i=1}^{n} \ln(x_i)^2}{2\sigma^2} + \frac{\sum_{i=1}^{n} \ln(x_i)\mu}{\sigma^2} - \frac{n\mu^2}{2\sigma^2} \end{aligned} \tag{25}$$

$$\begin{aligned} \ln \mathcal{L}_{dLogn}(\mu_1, \sigma_1^2, \mu_2, \sigma_2^2, A) = &\sum_{i=1}^{n} \ln f_{dLogn,lin}(x_i|\mu_1, \sigma_1^2, \mu_2, \sigma_2^2, A) = \\ -\frac{n}{2} \ln(2\pi) + \sum_{i=1}^{n} (-\ln(x_i)) + &\sum_{i=1}^{n} \ln(A\sigma_1^{-1} \exp(-\frac{(\ln(x_i) - \mu_1)^2}{2\sigma_1^2}) + \\ &(1 - A)\sigma_2^{-1} \exp(-\frac{(\ln(x_i) - \mu_1)^2}{2\sigma_1^2})) \end{aligned} \tag{26}$$

x_i represents the single transit times from the sFCS fits, not the bins from the histograms (y_i). Notably, the maximum likelihood estimation, using the above double lognormal expression, is numerically very unstable. For practical calculations the following equation incorporating a second weighting factor B, which does not depended on A was used. Consequently, for the BIC calculation six fitting parameters were assumed:

$$\begin{aligned}\ln \mathcal{L}_{dLogn_{AB}}(\mu_1, \sigma_1^2, \mu_2, \sigma_2^2, A, B) = \sum_{i=1}^{n} \ln f_{dLogn,lin_{AB}}(x_i|\mu_1, \sigma_1^2, \mu_2, \sigma_2^2, A, B) = \\ -\frac{1}{2}\ln(A+B) - \frac{n}{2}\ln(2\pi) + \sum_{i=1}^{n}(-\ln(x_i)) + \\ \sum_{i=1}^{n} \ln(A\sigma_1^{-1}\exp(-\frac{(\ln(x_i)-\mu_1)^2}{2\sigma_1^2}) + B\sigma_2^{-1}\exp(-\frac{(\ln(x_i)-\mu_1)^2}{2\sigma_1^2}))\end{aligned} \tag{27}$$

Practically, instead of maximising the log-likelihood vector, the negative log-likelihood values were minimized with the built-in MATLAB solver fmincon. The next step of the analysis was to feed the minimised value (the resulting negative log-likelihood vector) into the aicbic function also provided by MATLAB. To calculate the BIC values correctly, also the number of free fitting parameters was provided: Two for Gaussian and single Lognormal and six for the double Lognormal. The Matlab routine provides the BIC value which is the basis for the model selection.

In a second instance, the analysis can be expanded to deal with hop diffusion (note that a different data pre-processing strategy, as described above, is necessary). The log-likelihood function for a combination of Lognormal and Exponential distributions is given by:

$$\begin{aligned}\ln \mathcal{L}_{LognExp}(\mu_1, \sigma_1^2, \mu_2, A) = \sum_{i=1}^{n} \ln f_{LognExp,lin}(x_i|\mu_1, \sigma_1^2, \mu_2, A) = \\ \sum_{i=1}^{n} \ln(A \cdot x_i^{-1}(\sigma_1^2 2\pi)^{-1/2}\exp(-\frac{(\ln(x_i)-\mu_1)^2}{2\sigma_1^2}) + (1-A)\cdot\mu_2^{-1}\exp(-\frac{x_i}{\mu_2}))\end{aligned} \tag{28}$$

As mentioned above, calculating the BIC and choosing the model with the lowest value as best model is common practice. However, it is also possible to statistically compare the models to evaluate how good a given model is. For this reason, the relative likelihood

(RL) values for given models were used and are defined as:

$$RL_{\mathrm{i}} = \exp\left((BIC_{\mathrm{min}} - BIC_{\mathrm{i}})/2\right), \tag{29}$$

where RL_{i} is the relative likelihood value for the i-th model with the the i-th BIC value (BIC_{i}) compared to the most likely model with the lowest BIC (BIC_{min}) [131, 207, 208]. This strategy of combining goodness of fit and RL value analysis enables to objectively decide, whether in a given sample free or hindered diffusion is observed and to fit the histograms accurately.

5 Results

The Results chapter is divided into multiple parts. First, I am going to address general issues of performing quantitative imaging and spectroscopy in living cells and demonstrate how novel detection equipment can be beneficial. Next, I will introduce GPMVs as a model system to perform (super-resolution) spectroscopy, and evaluate the influence of the cortical actin cytoskeleton organisation on the nano-scale diffusion behaviour of membrane constituents. Building on the super-resolved spectroscopy results, I will introduce Line Interleaved Excitation Scanning STED-FCS (LIESS-FCS) as a novel tool to spatially resolve diffusion modes. As an alternative method, which does not rely on STED, to disclose hindered diffusion dynamics, I introduce the statistical analysis of sFCS data. Finally, in the last part of the Results all the aforementioned methods are applied to measurements on T-cell activation, specifically to shed light on the diffusion dynamics and organisation of Lck. A discussion goes along with the presented data and a general discussion, placing the developed methods in a broader context and evaluating the biological findings, follows after the Results chapter.

5.1 Measuring dynamics at high-photon count rates

As outlined before, FCS has become a widely applied tool to measure the diffusion dynamics of molecules in synthetic/artificial and living systems all across the areas of chemistry, physics and biology to infer interactions, reactions and molecular organisation. One major limitation of conventional FCS is the photon count rate regime at which it is usually operated. Standard combination of detector and electronics limits the detection to maximum photon streams of about 1 MHz (far below 1 photon per excitation pulse). This is a problem when measuring highly heterogeneous systems like, for example, living cells, where the expression of (fluorescently tagged) proteins can vary from cell to cell or from condition to condition (pM to µM concentrations) resulting in different intensities. Standard instrumentation is limited to measuring dim cells or varying the excitation laser power, which both introduces potential bias. STED-FCS can be a remedy by reducing the count rate, when decreasing the observation spot size, which is commonly employed to measure the nano-scale diffusion law. At high STED laser powers, this can result in

very low photon counts, which limit signal-to-noise ratio as well as applicability. Increased confocal countrates could be of great benefit to STED-FCS measurements, since higher count rates would remain after fluorescence depletion.

Although FCS is a fluorescence fluctuation based technique, there is no obvious reason not to work at high photon counts (high concentrations). Experimentally, it has been validated up to about 100 nM concentrations with standard equipment [209] and µM concentrations using plasmonic effects or custom-built detector banks [210, 211].

In this Section, I explore recent commercially available equipment which can detect photon streams of more than 80 MHz. In this particular case, I got access to a Leica SP8 STED set-up equipped with the so called FALCON module (fast lifetime contrast) at Leica Microinstruments (Mannheim, Germany). Briefly, this recently developed equipment makes use of sensitive hybrid detectors, coupled with fast FPGA electronics with very short dead times. Gigahertz sampling of the photon stream with a pattern matching algorithm allows for the fast and accurate photon detection. Using this new microscope, this part of the thesis is dedicated to evaluate the applicability, advantages, and disadvantages of high count rates for FCS.

5.1.1 High count rate FCS in solution

To gain first insights into the the performance of FCS at high count rates, solution measurements of the fluorescent dye, Atto655, in PBS were performed. The count rates were increased by either increasing the concentration of the dye (we employed a range from 500 pM to 1 µM) or by varying the excitation laser power.

Figure 5 A and B present intensity time traces recorded at various count rates. The conventional detection barrier imposed by the standard electronics is quickly surpassed in both cases, as indicated by the red dashed line at count rates of 1 MHz. The data were normalised to the mean and replotted in Figure 5 C and D for better comparison. The fluctuations at low concentrations are very high, which manifests in a big variance of the trace. At 1 µM concentration (Figure 5 C, yellow) almost no change in normalised intensity is observed. When increasing the count rate through higher laser powers, the fluctuations are less effected. The count rates scale with concentration and excitation po-

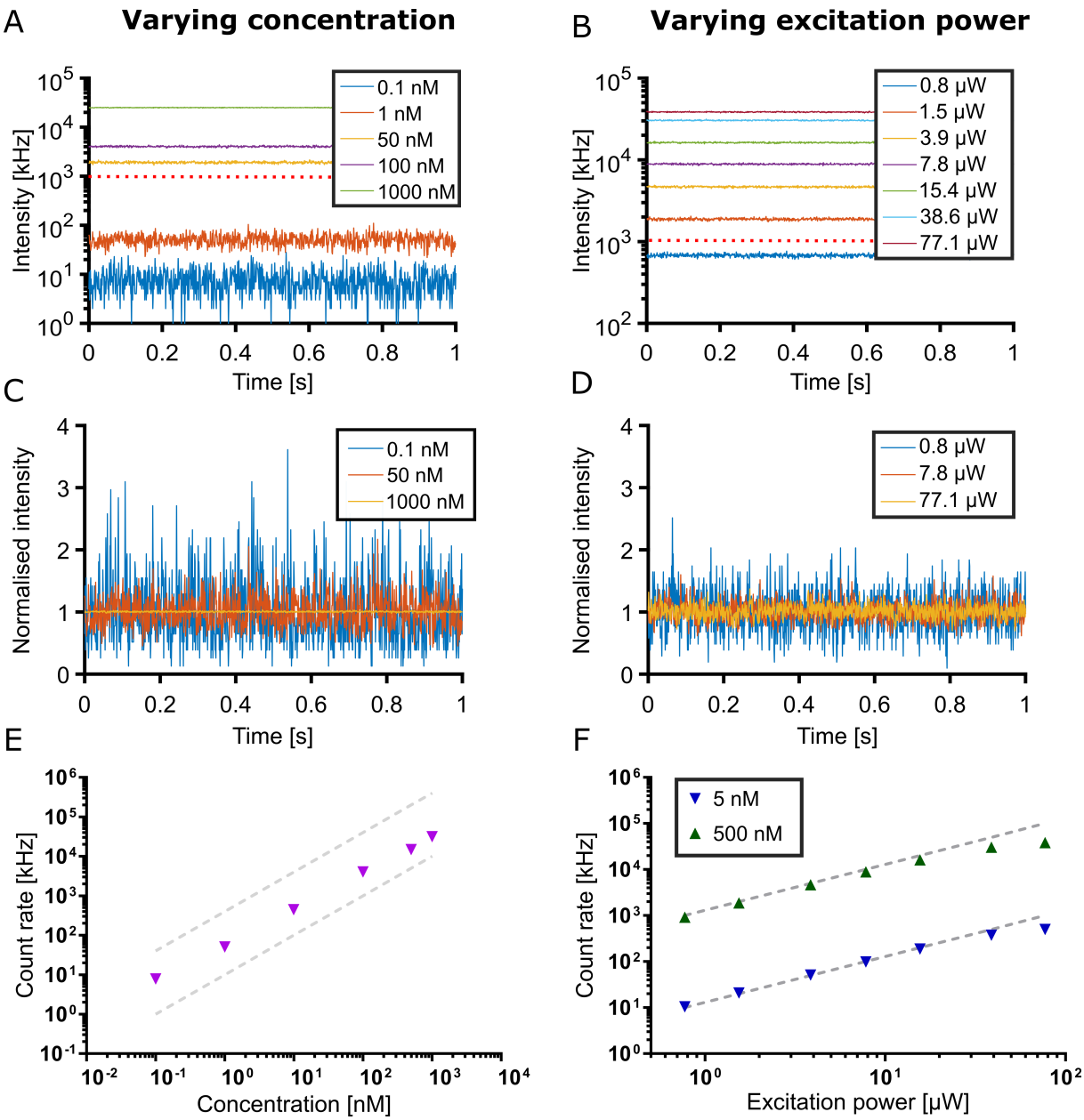


Figure 5: Acquiring high count rate intensity traces of Atto655 by either increasing concentration (left) or excitation laser power (right). **A**: Exemplary raw intensity traces of Atto655 at varying concentrations with constant excitation power. The dashed red line indicates a count rate of 1 MHz (which is the conventional detection limit). **B**: Raw intensity traces of Atto655 (500 nM) at varying excitation powers (red dashed line represents the conventional detection limit of 1 MHz). **C**: Normalised intensity time traces of Atto655 at three different concentrations (resulting in differenet count rates, see Panel A). **D**: Normalised intensity time traces of Atto655 (5 nM) at three different excitation laser powers (resulting in different count rates, see Panel B). **E**: Obtained average count rate versus concentration of Atto655 obtained at constant excitation power of 15.4 µW. **F**: Obtained average count rates of Atto655 at 5 nM (blue triangles) and 500 nM (green triangles) at increasing excitation laser powers. The dashed lines show a linear relationship and are plotted for guidance.

wer up to very high values, where saturation and non-linear effects such as self-quenching or photon re-absorption may impact strongly, (Figure 5 E and F). As the acquisition intensity (raw intensity arriving at the detector) is usually the limiting factor in FCS experiments, most of the remaining data of this Section are presented against count rate rather than concentration or laser power.

The high and low count rate intensity traces were correlated and the auto-correlation curves (FCS curves) obtained. Two examples are given in Figure 6. By increasing the concentration 100-fold the FCS curves appear still very similar, although with vastly different amplitudes (compare colour coded left and right y-axis in Figure 6 A). The curve for the high concentration scatters more. For increasing excitation power (Figure 6 B), the amplitudes do not change, but again a big difference in data scatter was observed. To quantify data quality consistently, I use a measure called nRMSD (normalised residuals mean squared displacement, see Materials and Methods Section 4.10). The magnitude of the residuals is normalised to the correlation amplitude in order to be able to compare data of different concentrations. As already apparent from Figure 6 A, the data vary most at lag times smaller than the transit time ($\tau < \tau_D$). Additionally, for long lag times bleaching, sample drift, duration noise and other factors contribute to the curve quality. Thus, only short lag time points were taken into account for nRMSD calculation. Figure 6 C demonstrates the nRMSD approach and the strategy for assessing data quality by compareing two data sets of different quality (by varying laser power). A smaller nRMSD value indicates better data quality, in this case, for the data acquired at high laser power.

Consistent with literature and theoretical predictions, the brightness (in this work interchangeably used with count per molecule (cpm)) is the major driver of improvement in data quality [135, 212, 213]. The brightness is a function of the excitation laser power, experimental conditions and photophysical properties of the studied fluorescent dye (or protein). Measured values of cpms for three different probes (Atto655, KK114 and Crimson Beads) are shown in Figure 7 A and govern the differences in nRMSD in Figure 7 B.

With the nRMSD value as measure for data quality, the performance of FCS at different count rates (from changing concentration or excitation laser power) was assessed for a

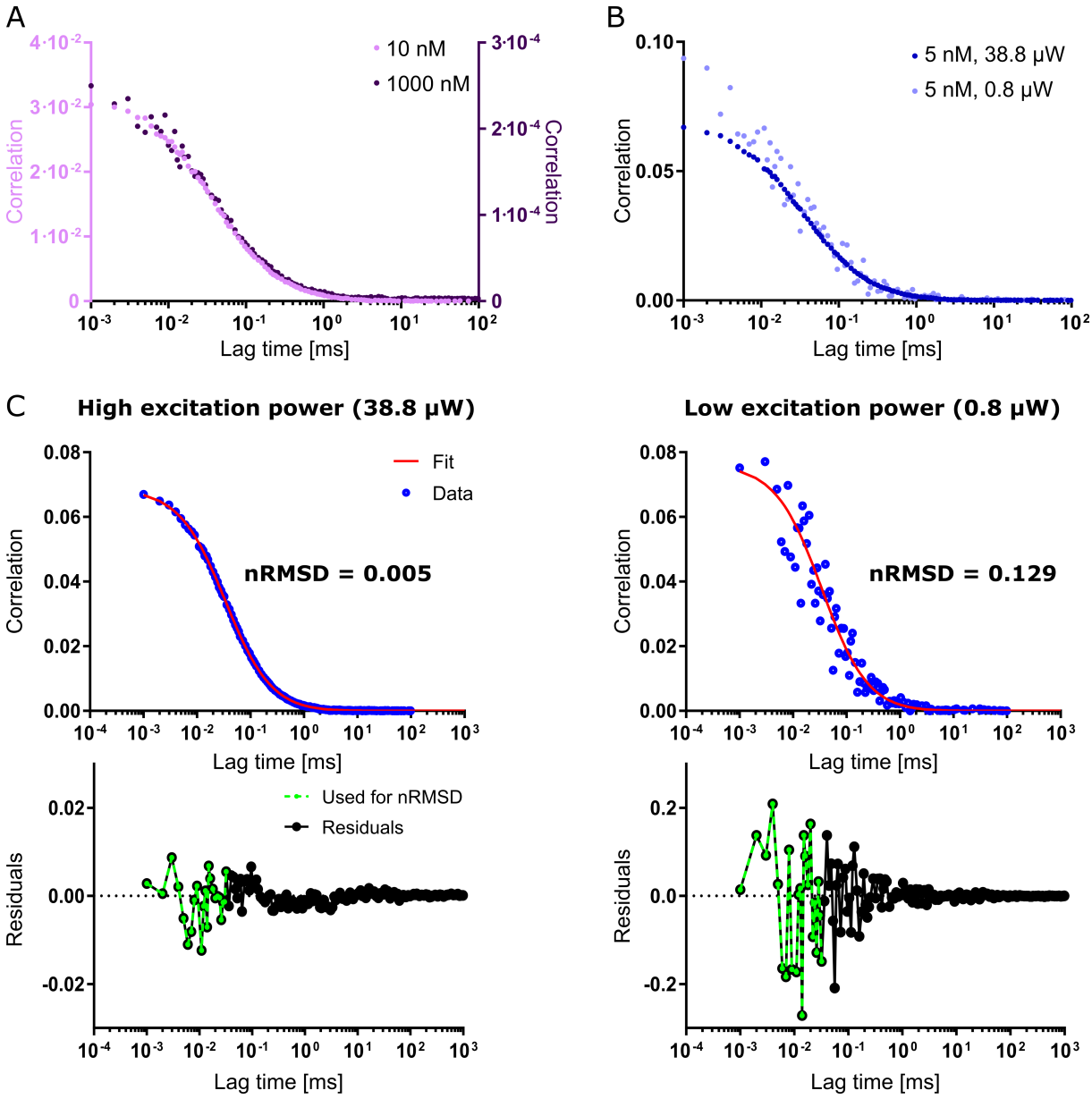


Figure 6: FCS curves and evaluation of data quality. **A**: FCS curves of Atto655 in PBS at 10 nM (light purple) and 1000 nM (dark purple). To accomodate for the different amplitudes the y-axes are colour coded as indicated. **B**: FCS curves of Atto655 (5 nM) at different excitation laser powers (38.8 µW, dark blue and 0.8 µW, light blue). **C**: nRMSD evaluation of the curves shown in B. The FCS data (blue) are fitted with a 3D diffusion model (red line, see Materials and Methods section 4.10). From the fitting residuals (bottom panels) up to the transit time (indicated in green) the normalised residuals mean square displacement is calculated. The curve on the right is worse (noisier) than the one on the left which is quantified by the nRMSD value displayed next to the curves (lower value nRMSD value, better data).

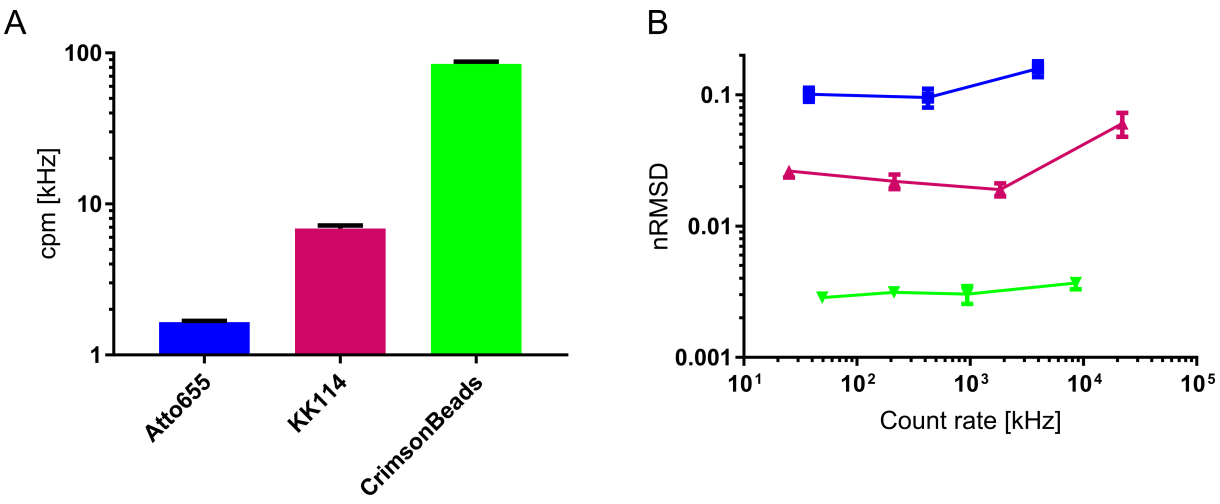


Figure 7: The data quality as measured by nRMSD depends on molecular brightness. **A**: Brightness (cpm) extracted from FCS measurements at constant laser power for three different probes: Atto655, KK114 and CrimsonBeads. **B**: nRMSD versus count rates (changed by increase in concentration of Atto655, blue, KK114, red, or CrimsonBeasds, green) shows that the data quality is not majorly influenced by the count rate but rather governed by the corresponding brightness given in Panel A.

large set of diffusion data on Atto655 dye in solution. Figure 8 A and B depicts the nRMSD changes with increasing count rate. The nRMSD is rather stable against changes in concentration once the count rate is above 10 kHz, which indicates no advantage, but also no disadvantage in increasing the number of molecules. Signal deterioration is only observed for count rates larger than 10 MHz. Changing the excitation laser power has a more dramatic effect on data quality. Note that the nRMSD for a higher concentrated sample (higher count rate) does not have a better signal quality. Furthermore, in this case the best data quality is obtained at rather low concentration (5 nM), with high excitation power (40 µW).

From fitting the autocorrelation curves, the transit times are obtained. They are invariant against increasing count rates due to concentrations (Figure 8 C) and the correlation amplitude drops almost linearly, as expected. Similar behaviour has been observed when increasing the laser power (Figure 8 D), but in this case, the transit times for lowest count rates exhibit some deviations and towards high laser powers the transit times drop, which could be attributed to bleaching. Additionally, the correlation amplitude for the highest excitation power (highest count rate) drops notably probably due to saturation effects.

Nonetheless, these measurement demonstrate clearly that FCS experiments at count rates above the conventional limit of 1 MHz at least up to 10 MHz are possible and can

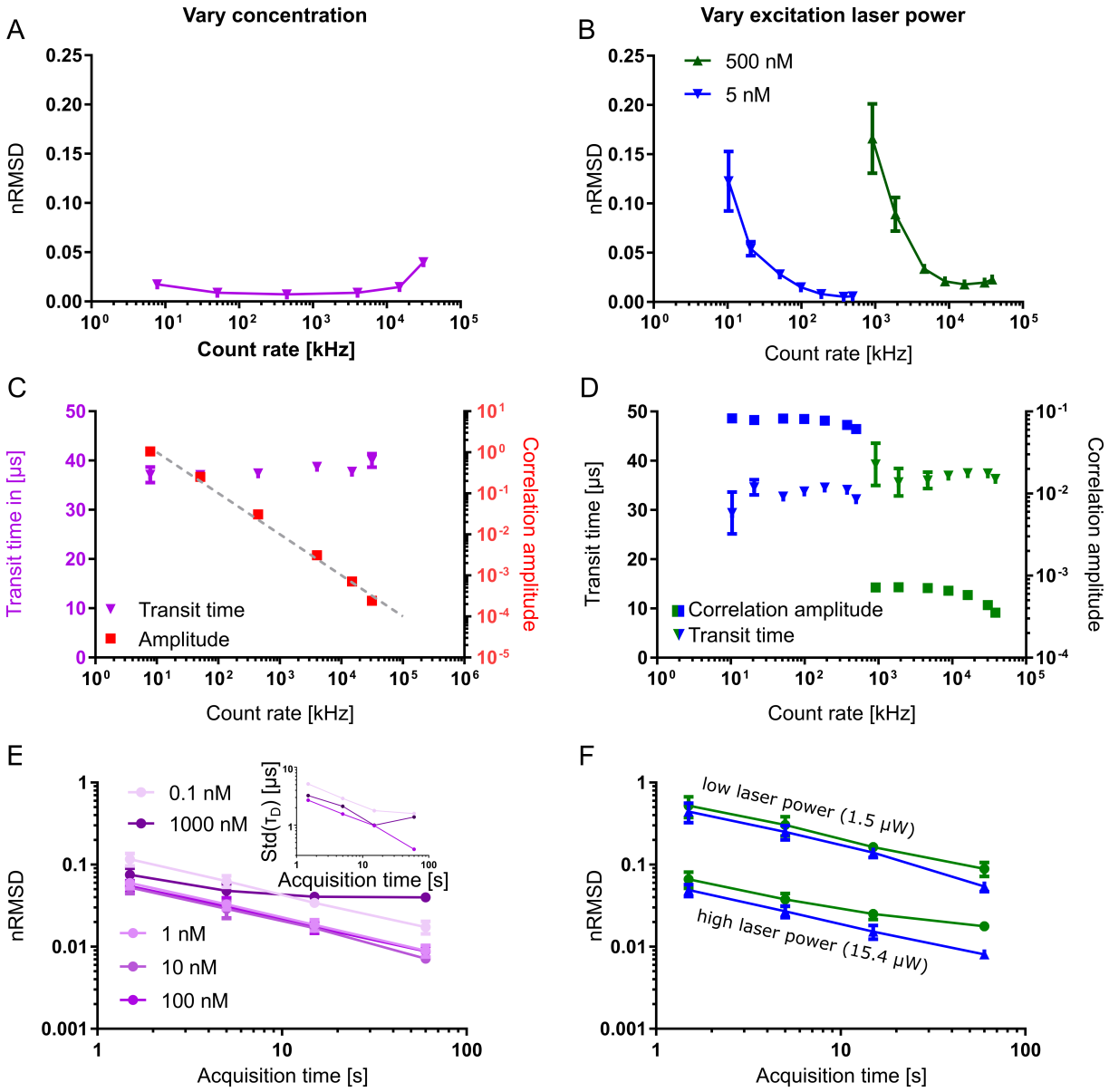


Figure 8: Quantification of fitting results from high count rate FCS experiments on Atto655 diffusion in solution (PBS). Left panels increasing count rates by increasing concentration, right panels by increasing excitation laser powers. **A**: nRMSD against count rate. Signal degradation is only observed for the highest count rate. **B**: nRMSD versus count rates (changing excitation power) for Atto655 at 5 nM (blue) and 500 nM (green). Higher count rate results in improved data quality (lower nRMSD). **C**: Transit time and correlation amplitude against count rate (varying concentration). Dashed grey line indicates linear relationship and is plotted for guidance. **D**: Transit time and correlation amplitude against count rate (varying excitation power). **E**: nRMSD versus acquisition time. Intensity traces of Atto655 were chopped to various shorter acquisition times, correlated and fitted. The nRMSD values decrease with increasing acquisition time. The inset shows standard deviation of the transit time (Std(τ_D)) calculated from three measurements (three repetitions) of different concentrations (0.1 nM, 100 nM and 1000 nM) versus acquisition time. The standard deviations follow the same trend as the nRMSD values. **F**: nRMSD values against acquisition times for Atto655 at 5 nM and 500 nM concentration and at 1.5 or 15.4 µW excitation laser power. At the same acquisition time much better data quality can be reached by increasing the laser power.

yield reliable results. One possible application could be to measure for shorter acquisition times and obtain the same data quality as longer measurements. This would be an advantage when measuring in highly heterogeneous cellular systems or when charactering reaction dynamics. Figure 8 E shows that the nRMSD drops with acquisition time and that the influence of the concentration is rather small. Interestingly, the lowest (0.1 nM) and highest (1 μM) concentrations both have poor nRMSD values, indicating the range where FCS seems to work most reliably. Notably, the inset implies that the standard deviations of the transit times, for three concentrations (0.1, 100 and 1000 nM), correlate with the nRMSD values. Thus, the nRMSD can also be seen as an error indicator for the transit times. To make use of shorter measurement times, the excitation laser power should be increased. In Figure 8 F the nRMSD versus the acquisition time for 5 nM and 500 nM concentration of Atto655 at high (15.4 μW) and low (1.5 μW) excitation powers is plotted. Notably, with low excitation power even for long acquisition times the data do not reach the same nRMSD values as the curves acquired at higher excitation power.

5.1.2 Application of high count rate FCS to measurement in cells

One aim of this project was to increase applicability and ease-of-use of FCS for measurements on living cells. As discussed above, cellular systems can be very heterogeneous and display a variety of expression levels of proteins of interest. Endogenous protein levels can vary multiple orders of magnitude (imagine a rare transcription factor versus a housekeeping protein like actin). In the previous paragraphs, I showed that FCS measurements at high count rates are possible and fairly reliable. This should enable unbiased measurement in living cells. To validate this, cytoplasmic GFP was expressed in HeLa cells and diffusion measurements were performed at constant laser power.

Figure 9 A shows a typical confocal image of cells transfected with a fluorescent protein. The fluorescence intensity of GFP varies drastically from cell to cell. In conventional FCS experiments, only dim cells could be measured or the excitation laser power had to be reduced. This either limits the analysis to a subset of the cell population (biasing the result) or, if the laser power is reduced, changes the signal-to-noise ratio and required acquisition times for reliable measurements. Both makes cell-to-cell comparisons difficult.

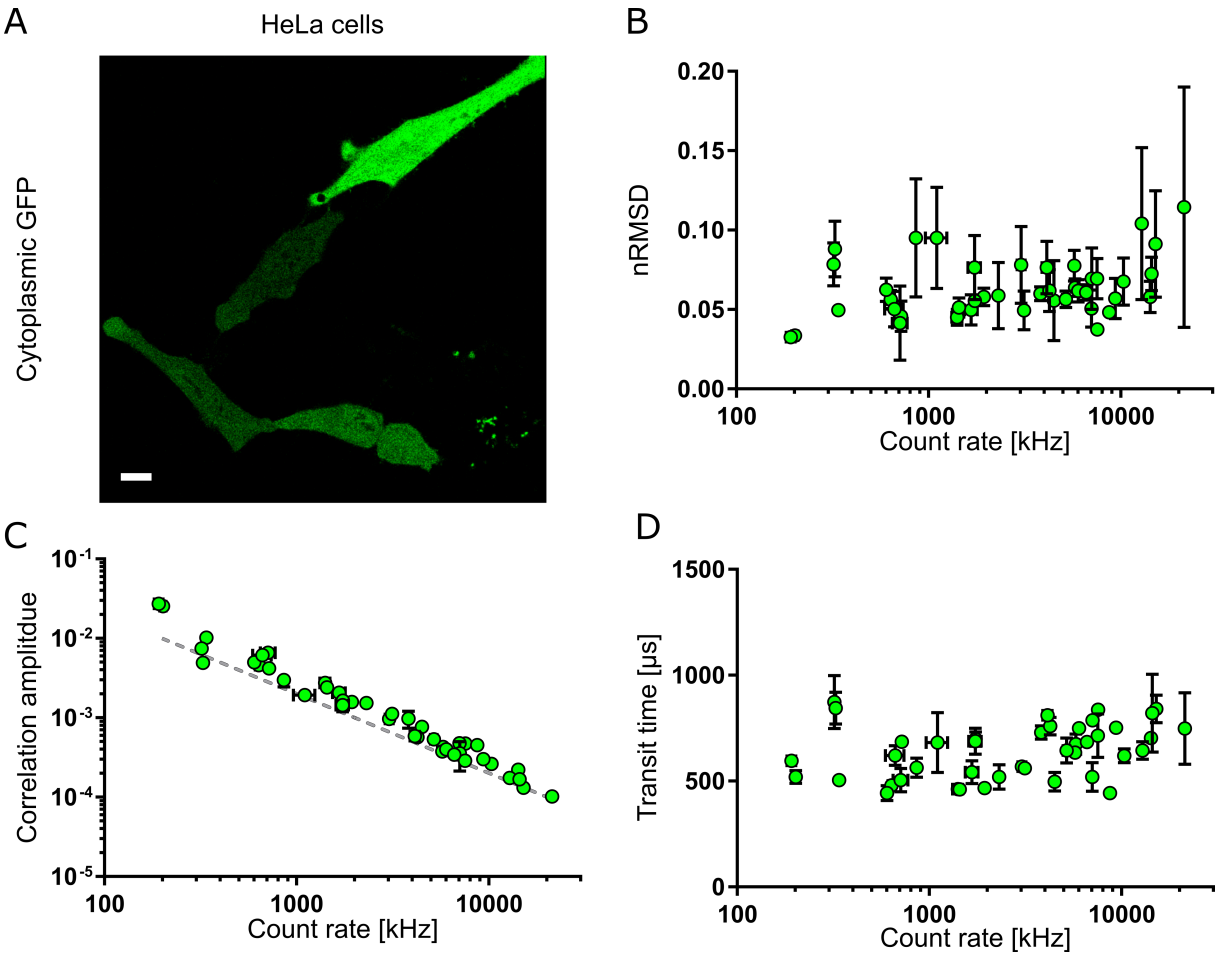


Figure 9: FCS measurements on GFP diffusion in the cytoplasm of HeLa cells. **A**: Confocal image of HeLa cells expressing varying amounts of green fluorescent protein (GFP). Scale bar is 10 µm. **B**: nRMSD values (signal quality) obtained from fitting the correlated data plotted against the acquisition count rate. **C**: The correlation amplitude (inverse number of particles) drops with increasing counts meaning that the higher counts are caused by higher expression levels of fluorescent protein. The grey dashed line is plotted for guidance and represents a linear relationship in the log-log plot. **D**: Transit times against acquisition count rates. The standard deviations increase ($>$ 10 MHz). Every dot represents the average of three measurements on one cell, error bars are standard deviations. Measurements were acquired for 15 s at constant excitation laser power of 0.6 µW.

Using the latest electronics, FCS data with constant excitation power were acquired, fitted and the data quality assessed by the nRMSD value (Figure 9 B). Up to a count rate of 10 MHz reliable data (low nRMSD values) could be recorded, and the nRMSD values do not follow a trend with the count rates demonstrating the dynamic range for FCS measurements. The increased count rates are indeed caused by varying expression levels, as the correlation amplitude (inverse number of molecules in focus) drops almost linearly with the acquisition count rate (Figure 9 C) covering a range of protein concentrations from roughly 0.01 to 5 μM. Finally, the transit times for GFP in HeLa cells extracted from the FCS fits (Figure 9 D) showed no trend over the wide range of acquired count rates (expression levels), meaning the expression level did not influence the viscosity of the cytoplasm by crowding. Additionally, there seem to be no concentration depended interactions or slow-downs. The standard deviations of the transit times, in fact, correlate with the nRMSD values as measure for data quality, as predicted from the solution measurements (Figure 8 E, inset).

Notably, in these experiments (three different sets of transfections) the majority of the data points was acquired at count rates above 1 MHz, even at relatively low excitation power (0.6 μW, far below GFP saturation). In conventional experiments most of these data points would have been ignored or acquired at lower laser power scarifying data quality.

5.1.3 STED-FCS at high count rates

When performing STED-FCS experiments, the fluorescence intensity is naturally reduced by depletion in the periphery of the observation spot, which enables measurements of diffusion dynamics on scales smaller than the diffraction limit (see Section 2.2.4 for detailed description).

The diffusion data at very high resolution (observation spot sizes $<$50 nm) are often hampered by low signal-to-noise ratio, since just very few molecules remain in the focus and cause very few photons to be detected. Hence next, the performance of STED-FCS using high count rates (in confocal and resulting increased count rates in STED) was evaluated on SLBs, similarly to point FCS on solution data in the previous paragraphs.

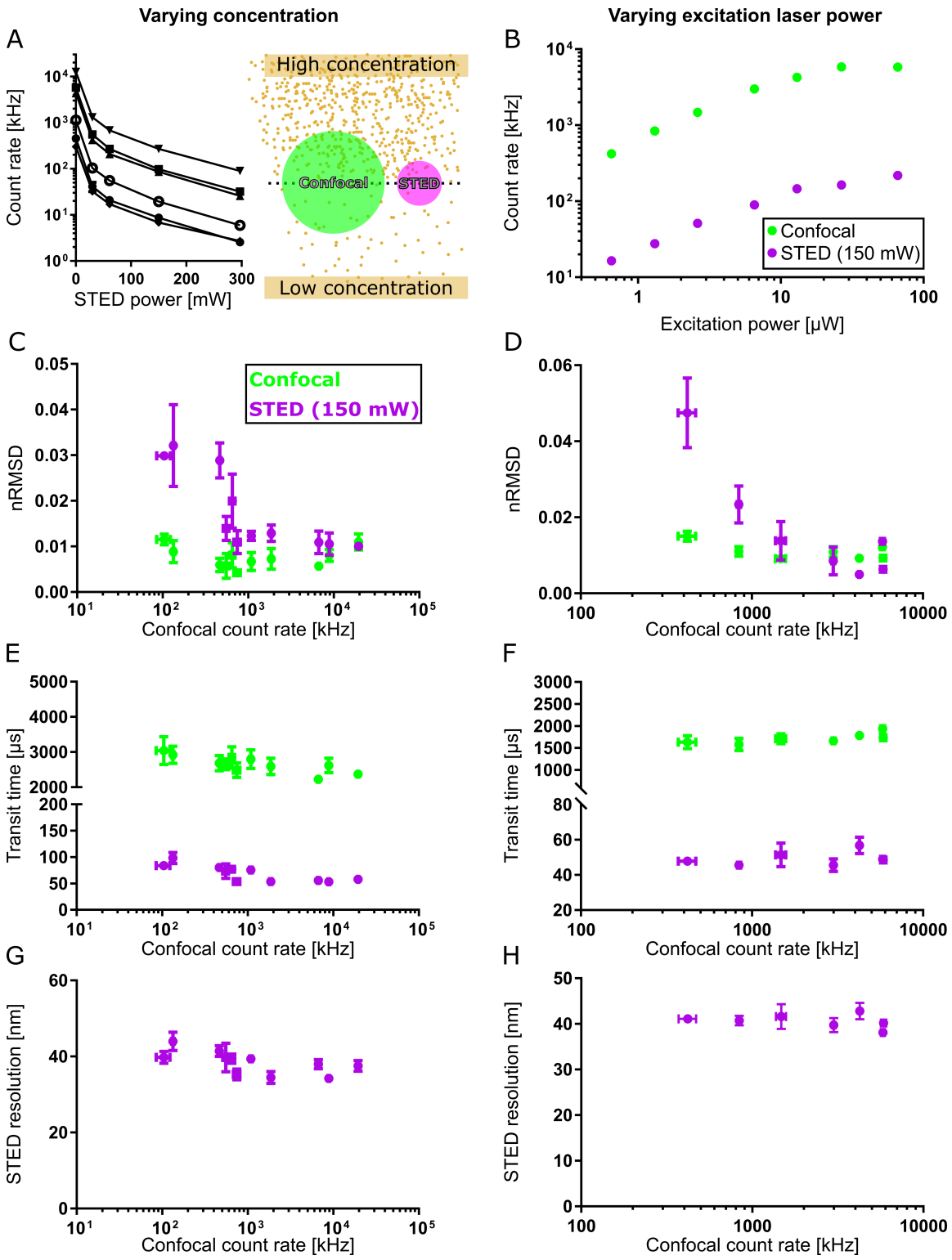


Figure 10: Performing STED-FCS at high (confocal) counts rates. All experiments shown are on SLBs composed of DOPC doped with KK114-DPPE at different concentrations (left panel) or different excitation powers (right panel) to vary acquisition count rates. **A**: Reduction in count rate of SLBs by increasing STED power (left) and cartoon depicting the advantage of high concentrations for STED-FCS experiments (right). **B**: Intensities in confocal and STED (150 mW depletion power) upon change in excitation power. **C**: nRMSD values at different acquisition count rates in confocal and STED caused by changes in concentration or **D**: Changes in excitation power. **E**: Confocal and STED transit times at different count rates caused by either varying concentration or varying excitation power **F**. **G**: Apparent resolution (calculated from confocal and STED (150 mW) measurements) at count rates varied by concentration or excitation power **H**. Mean and standard deviation of at least three measurements are shown.

The counts have either been increased by changing the concentration of labelled lipid analog diffusing within the SLB or by increasing the excitation laser power. Figure 10 A highlights the drop in fluorescence intensity for multiple SLBs upon depletion. Depending on the concentration, the confocal intensity was higher or lower, but dropped in similar manner upon STED exposure. The benefit of a large number of molecules in depletion based experiments, is illustrated in the cartoon on the right of Figure 10 A. Alternatively, the laser power has been increased to obtain higher count rates (Figure 10 B). Note that saturation of the dye only begins to occur at relatively high excitation laser powers (>30 μW) similarly in confocal and STED. For simplicity, only data for one STED power (150 mW depletion power) are shown, the results obtained for other depletion powers follow the same trends. The utilised STED laser reach up to 300 mW power, but the obtained resolutions were not much higher. To ultimately minimise photodamage by the STED laser, the measurements in living cells were limited to confocal and 150 mW STED power acquisitions (see below).

The data quality was estimated using the nRMSD value for measurements in confocal and STED mode (Figure 10 C and D changing concentration or excitation, respectively). In both cases the nRMSD values in confocal improved only marginally with count rates, but the quality of the STED data is massively improved as soon as 1 MHz (conventional detection limit) of confocal acquisition count rate was surpassed. However, the higher data quality in STED (and confocal) has only little impact on the transit times which stay constant (Figure 10 E and F). A similar behaviour was observed for the apparent resolution, which is calculated based on the transit times in confocal and STED (see Materials and Methods section 4.11, compare Figure 10). This may seem surprising as the data quality is better and the data quality (i.e., nRMSD) as well as standard deviations of the transit times correlate (Figure 8, E inset), but that should only result in smaller error bars for the resolution and not in improved resolution. It is actually reassuring that in a model membrane system the same apparent STED resolution can be obtained regardless of the excitation power (even above saturation) and of the concentration of molecules. The improved signal-to-noise ratio at high count rates is surely advantageous when performing live cell STED-FCS measurements, as this ensures more robust results

and enables shorter measurement times.

The application of the novel high count rate approach to live-cell STED-FCS measurements was checked next. As an example HeLa cells were labelled with KK114-PEG-Cholesterol, which got quickly incorporated into the plasma membrane. Figure 11 A shows confocal images of the plasma membrane at the basal (bottom), mid (equatorial) and apical (top) plane of the cells. KK114-PEG-Cholesterol has been indicated before to be diffusing freely in the bottom membrane of PTK2 cells and to cause high count rates [166]. At the bottom membrane of the HeLa cells a lot of internal structures were observed, thus the STED-FCS measurements were performed in the apical membrane of the cells (typical locations for measurements indicated in the apical plane by the yellow arrows in Figure 11). Conveniently, the provided microscope was equipped with a high-NA water-immersion objective (with motorised correction collar), allowing for this type of measurements. Note that the resolution was reduced due to less STED power (125 mW) using a water-immersion objective. STED-FCS calibration (top membrane of immobilised GPMVs using the same probe) yielded an apparent resolution of about 100 nm.

The quality of the live cell FCS curves (nRMSD values, Figure 11 B) improved in STED and confocal, as predicted from the SLB measurements before. Note that the absolute signal quality is only about 20 % worse in the live cells. Using the calibration and the transit times in the HeLa cells, the diffusion coefficients in STED and confocal were calculated (Figure 11 C). The data scatter broadly, but the average diffusion coefficient is very similar indicating free diffusion, which is consistent with the previously published report [166].

The presented experiments establish how powerful the new equipment to perform FCS and STED-FCS experiments at high count rates can be. Since FCS is a correlative technique, it is not too surprising that high count rates do not automatically allow very short measurement times. The technique relies on temporal averaging and simply the convergence of the correlation function. That has been indicated using simulations before [214], but is experimentally verified here.

The performed analysis of high count rate (STED)-FCS data relied on the accurate time tagging of photons. It must be noted that for time integrated FCS (for example using a

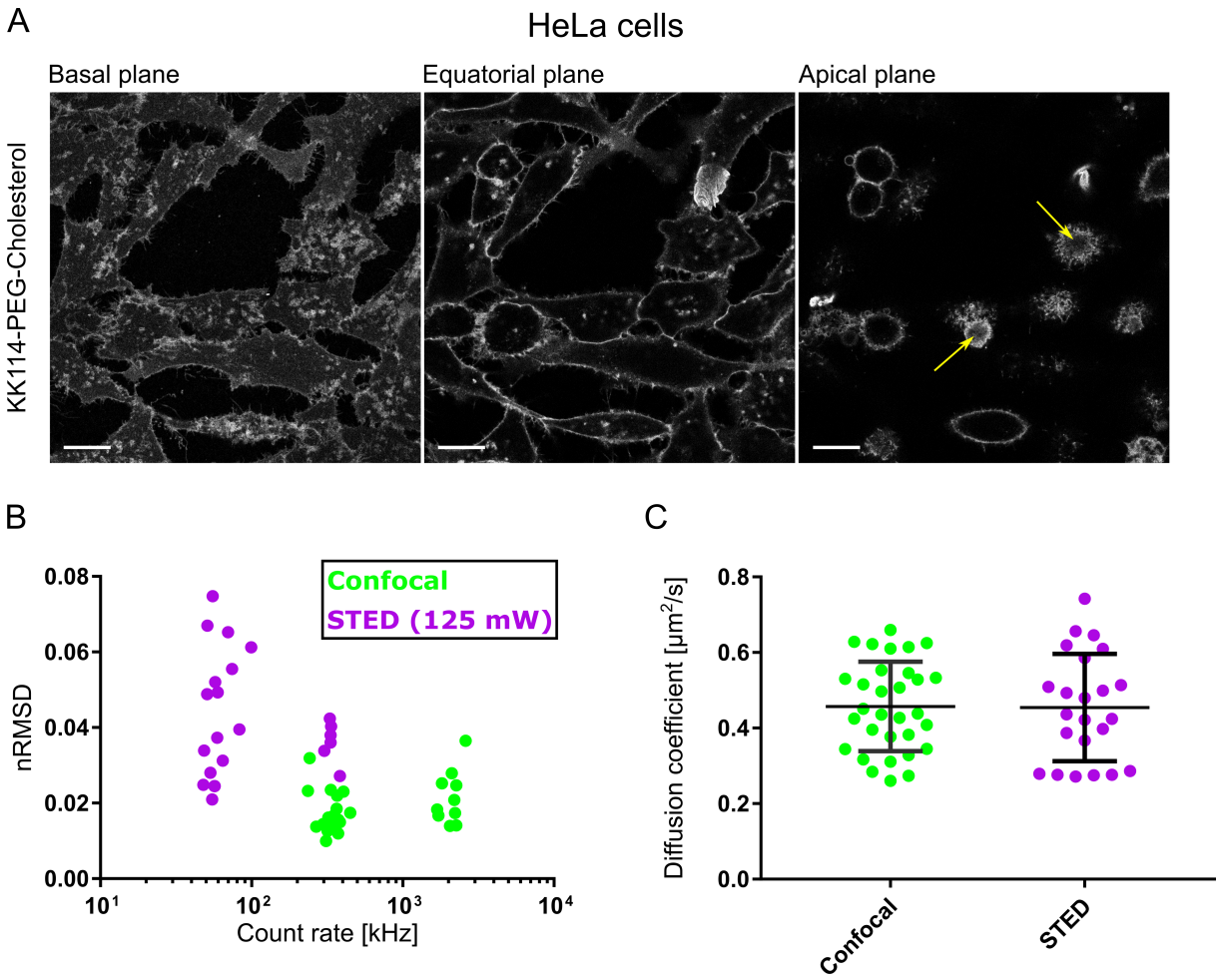


Figure 11: STED-FCS at high count rates in living cells. The plasma membranes of HeLa cells were labelled with fluorescent KK114-PEG-Cholesterol and the diffusion measured in the apical (top) membrane. **A**: Confocal images of the basal, equatorial and apical planes of several HeLa cells. The cells have varying heights but two cells in the centre of the image show top membranes which were typically chosen as locations for multiple pSTED-FCS measurement (indicated by the yellow arrows). Scale bars are 10 µm. **B**: nRMSD values obtained from FCS experiments in the top membranes of HeLa cells. The counts shown are actual acquisition counts (not only confocal counts). **C**: Diffusion coefficients in confocal and STED mode (125 mW depletion power, corresponding to a resolution of 100 nm) appear very similar and indicate free diffusion of the fluorescent probe. Every dot represents one FCS measurement in one cell. Bars are mean value and standard deviation. Acquisition time and excitation laser power were constant at 15 s and 2.3 µW, respectively.

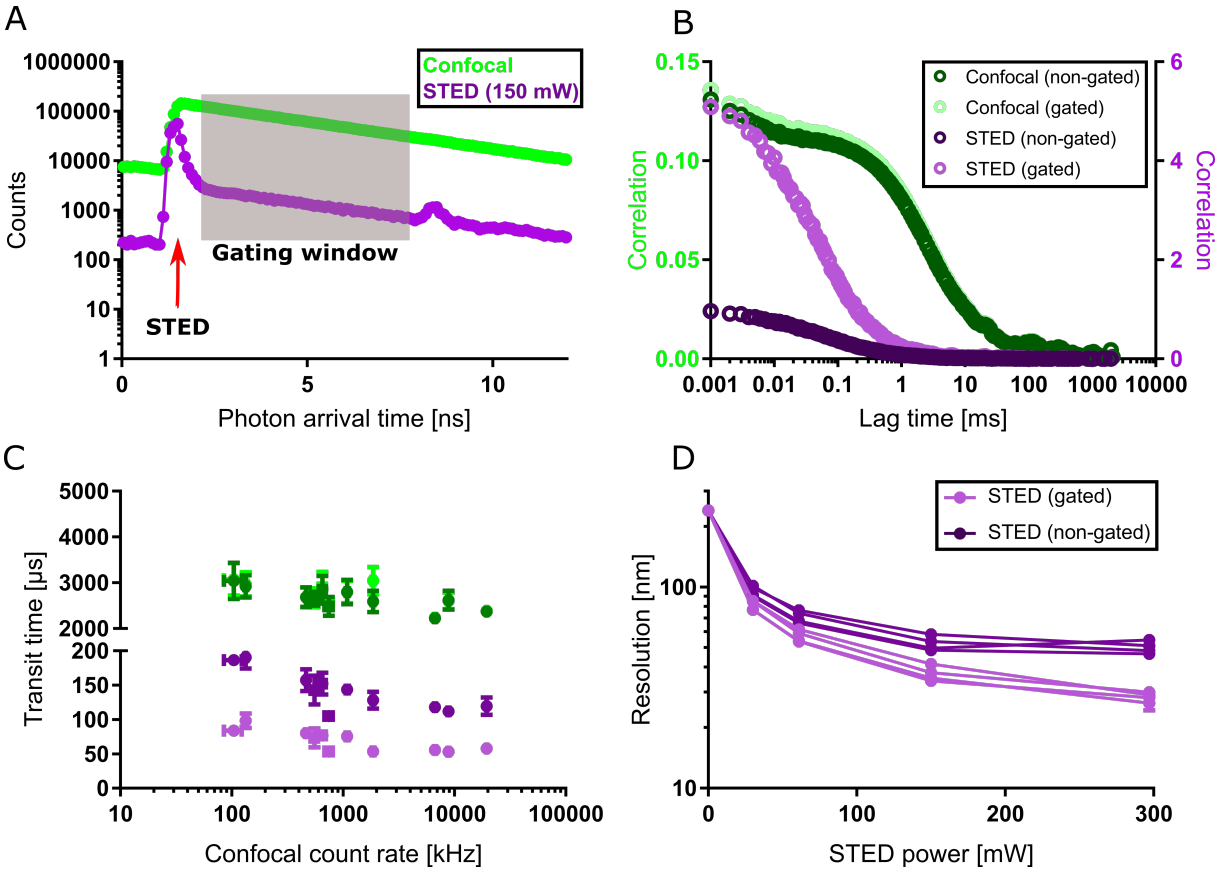


Figure 12: Time-tagged acquisition allows gating of STED-FCS data. **A**: TCSPC histogram of a STED-FCS measurement of KK114-DPPE diffusing in a DOPC SLB acquired in confocal (green) and STED (150 mW, magenta). The grey area indicates the gating window (photons used for correlation = gated data). The red arrow points to the (micro-)time when the STED laser pulses. **B**: FCS curves in confocal (green) and STED (magenta) obtained by correlating all collected photons (non-gated, darker shades) or by photons from the gating window (gated, lighter shades). The confocal data are merely distinguishable while the STED curves are different. **C**: Transit times in confocal and STED obtained from FCS measurements on bilayers with different concentrations (see Figure 10) with and without post-processing by gating. Mean and standard deviations of at least three measurements are shown. **D**: Apparent STED resolution at different STED laser powers calculated from the transit times (gated and non-gated) in C. Gating improves the resolution at higher STED powers.

hardware correlator card and special APDs) also higher count rates than 1 MHz can be tolerated by the equipment [14], but this set-up does not allow for any post-processing or software correlation. The relationship between acquisition time and data quality as well as the time gating of STED-FCS data was only possible due to the microtime information. The crucial influence of the gating is depicted in Figure 12 using again SLBs.

Gating allows to select a microtime window from which photons are taken into account for correlation (Figure 12 A). This can, for example, be used to remove scattered excitation light, or in this case, to remove contribution from confocal background. Fluorescence depletion is a stochastic photophysical process and needs some time to take action. Expe-

rimental optimisation, meaning the time delay between excitation and STED pulse (red arrow, Figure 12 A), needs to be accurately tuned [14]. Even after perfect adjustment, post-processing can help to remove initial undepleted fluorescence, which causes the peak in the TCSPC histogram before the linear decay under STED illumination. Note that one peculiarity of the utilised Leica set-up was the bumb in the Time Correlated Single Photon Counting (TCSPC) curve around 8 ns photon arrival time. According to the technicians, this is caused by an internal reflection in the set-up and only occurs at low count rates. In confocal FCS measurements (solutions, cells or for lifetime determination), I did not notice a difference in fitting parameters with or without gating this bump. Nonetheless, for all STED-FCS data (especially at vey high STED powers, low photon counts) it was removed together with the initial confocal contribution (grey gating window in Figure 12 applied to all STED-FCS data). Correlating gated and non-gated FCS measurements did not influence the FCS curves in confocal mode (Figure 12 B), but in STED a huge change in amplitude was observed. The gated data have a higher amplitude (meaning less molecules) in the observation area, as the non-gated data contain a confocal contribution. The effect of gating is also reflected in the transit times (Figure 12 C). Due to removal the confocal contribution, the apparent observation spot is smaller and the transit times faster. As expected, no difference for the confocal transit times is observed. Note that the effect of gating on STED data was checked at a wide range of KK114-DPPE concentrations in SLBs (resulting as before in a wide range of confocal count rates) and the results were consistent even for high initial confocal counts. The standard deviation of the measurements in STED decreases, though, notably with higher probe concentration. As gating changes the transit times in STED, it is also expected to change the apparent resolution, which is illustrated in Figure 12 D.

The TCSPC information can not only be used for simple gating, but also for other advanced fluorescence fluctuation techniques like Fluorescence Lifetime Correlation Spectroscopy (FLCS) or pattern matching [215, 216]. Gated STED-FCS also allows the acquisition of multiple observation spot sizes at once, especially, when using continuous-wave depletion [181, 194, 217]. Undoubtedly, all these approaches would benefit from the use of higher acquisition count rates.

5.1.4 Summary high count rate FCS

In this Section, I used novel turn-key detection equipment designed for fast live cell FLIM to perform FCS experiments at high count rates. FCS, being a fluctuation based technique, may initially seem not to be suited for high acquisition photon fluxes or high concentrations, but turned out to be absolutely applicable. The presented data represent the basis for a route to and devised guidelines for high quality and reliable measurements. Even at high count rates it remains crucial to measure long enough for the correlation function to converge properly, which can be combatted by increasing molecular brightness [148, 214]. For the first time, FCS data in living cells expressing various levels of fluorescent protein could be obtained without a bias for dim cells. An immediate application would be high-throughput screens, which would in turn not rely on pre-selecting cells or adapting laser powers any more [218]. High confocal acquisition count rates have been shown to be beneficial for the data quality in STED-FCS and obtaining the data in time-tagged mode enabled crucial post-processing like gating. In the future, this will enable more sophisticated photon filtering or allow for linking diffusion properties with fluorescence lifetime of, for example, environment sensitive probes.

5.2 Nano-scale diffusion dynamics in an actin-free system

The cortical actin cytoskeleton is known to be a major regulator of membrane organisation and mobility of membrane components [5, 34, 219]. Many studies have been performed to elucidate the protein and lipid organisation in dependence of the actin cytoskeleton. Using SPT and STED-FCS confined diffusion and actin depended compartmentalisation have been observed [32, 36]. Also using STED-FCS, trapped diffusion, caused by short-lived nano-scale interactions, has been discovered and shown to depend on cholesterol content and the intact actin cytoskeleton [122, 159]. Yet, in all these studies either drug treatments on living cells or cell-attached membrane blebs have been used for the measurements. In both cases, the exact nature of the remaining cytoskeleton and/or cellular cellular state were unknown. For this Section of the Results, I performed point STED-FCS measurements on living cells, compared the diffusion behaviour of different lipids as well as GPI-APs and assessed the nano-scale diffusion behaviour, for the first time, in free-standing, cell-derived but actin-free, plasma membrane vesicles, GPMVs.

5.2.1 Diffusion in artificial and cell-derived vesicles

The actin cytoskeleton is a dense network close to the plasma membrane [219] and well known to be disintegrated in GPMVs [55]. CHO cells expressing a fluorescently labelled actin binding peptide (Lifeact-GFP) were imaged together with a membrane marker (Cell Mask Deep Red) to demonstrate cytoskeletal disassembly. Figure 13 A shows confocal images of the CHO cells and GPMVs derived thereof.

In the living cells, a dense assembly close to the membrane can be observed, where the Lifeact-GFP is incorporated into the actin cortex. The merge indicates clearly in yellow that actin cortex and membrane are basically an indistinguishable structure at this resolution. However, in the GPMVs the signal from the actin is homogeneously distributed, indicating the disintegration of the cytoskeleton (probably only monomeric actin is observed). To make sure no actin structure in the GPMVs has an influence on the diffusion behaviour, the vesicles were additionally treated with Latrunculin B (Figure 13 B) to additionally diminish actin polymerisation. The diffusion of the fluorescent lipid analog Atto647N-DPPE (PE) did not change upon treatment, implying that the

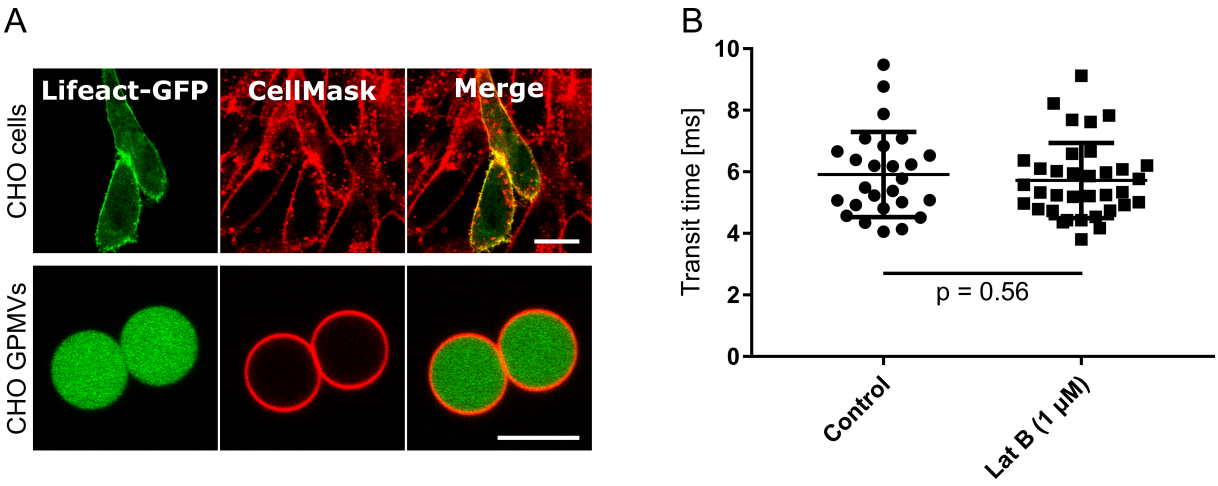


Figure 13: The actin cytoskeleton in GPMVs is disintegrated **A**: Confocal images of CHO cells (top) and GPMVs (bottom) expressing Lifeact-GFP to visualize free and cytoskeleton-bound actin. The membrane was labelled with Cell Mask Deep Red. The merge indicates an assembled actin network at the membrane in the cells but not in the vesicles. Scale bars are 10 µm. **B**: FCS measurements of Atto647N-DPPE (PE) in the bottom membrane of GPMVs with and without Latrunculin B treatment (1 µM final concentration). Each dot is a single FCS measurement from at least 10 different vesicles. The indicated p-value was obtained using an unpaired t-test. Mean and standard deviation are shown as bars.

GPMV production following the well-established protocol in [54] already yields "actin cytoskeleton free" vesicles.

Thus, the GPMVs seemed to be a suitable system to investigate the nano-scale diffusion behaviour of different lipids and GPI-APs in the plasma membrane context but without an organised actin cytoskeleton. The first practical issue to be solved was the specific and non-perturbing immobilisation of the vesicles, since the GPMVs on a glass cover slip move around. This represents not a problem for one confocal measurement, but immobilisation is strictly necessary for a dedicated STED-FCS study, where many repeats of the same vesicle had to be measured. GUVs can be embedded within agarose gels [220], which was not suitable for the GPMVs and caused them to burst. Thus, immobilisation on the cover slip was chosen as the preferred way. The final strategy is illustrated as a cartoon in Figure 14 A. The glass coverslip was first passivated with BSA and biotinylated BSA (common practise for GUVs which otherwise burst on the glass surface). The coated surface was then covered with streptavidin and the GPMVs, which previously incorporated biotinylated lipid (DSPE-PEG-Biotin), were dropped on this surface. The PEGylated lipid was used to increase the distance between surface and GPMV and to reduce potential interactions between probes and the coverslip.

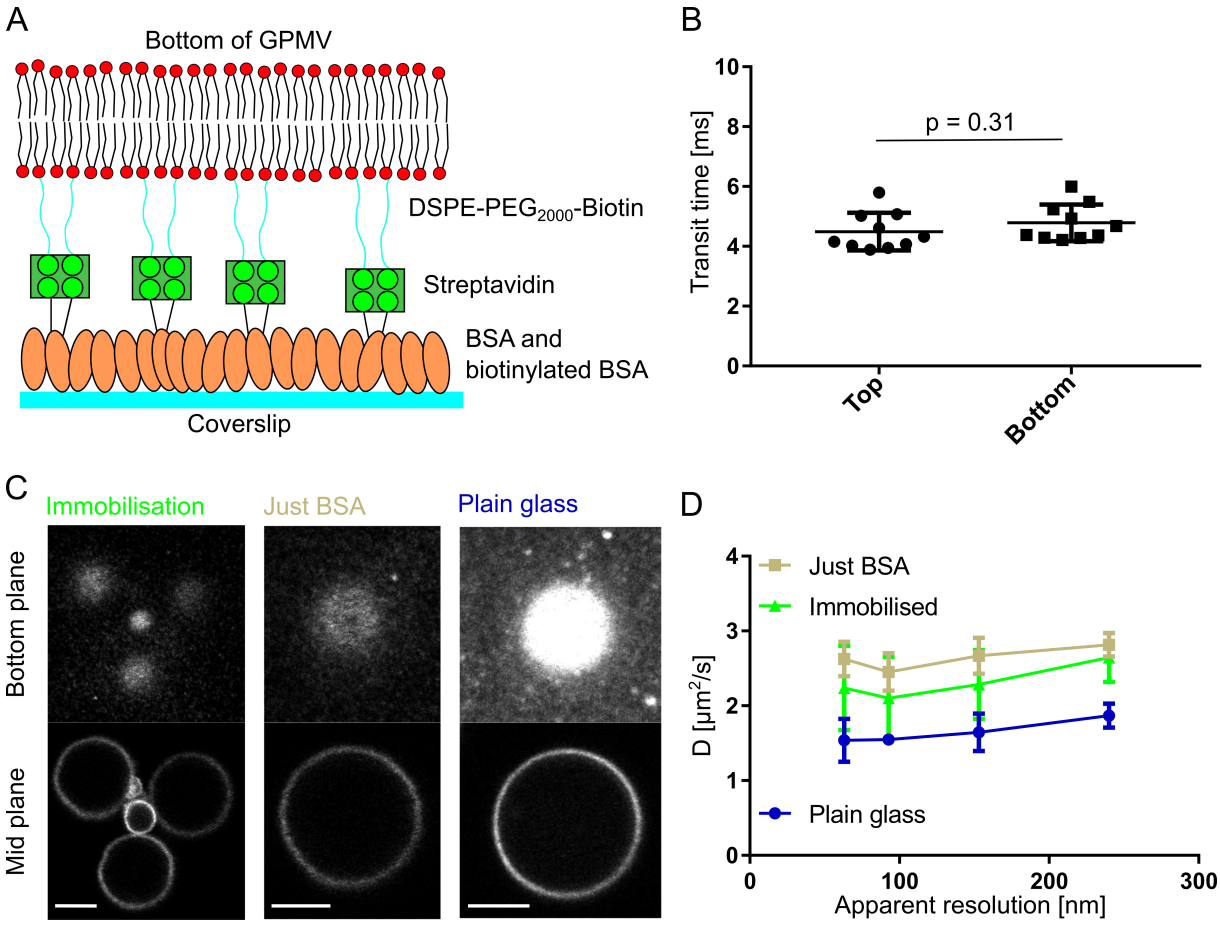


Figure 14: Immobilisation of GPMVs **A**: Cartoon illustrating the immobilisation strategy for GPMV measurements. **B**: FCS measurement of Atto647N-DPPE diffusion in the top and bottom membranes of immobilised GPMVs. Every dot represents the average of three measurements per GPMV. The indicated p-value was obtained using an unpaired t-test. **C**: Confocal images of Atto647N-DPPE labelled GPMVs immobilised as shown above (left), just on a BSA/BSA-biotin and streptavidin coated surface but without biotinylated lipid in the vesicle (middle) and on plain glass (right). The images in the top panels (bottom membranes) and bottom panels (mid planes) show the same dynamic range (with regards to intensities) for comparison, leading to strong image saturation in the case of plain glass. All scale bars are 5 µm. **D**: STED-FCS measurements of Atto647N-DPPE in the bottom membrane of GPMVs under the conditions as indicated by colour code and shown in Panel C. Every dot represents the average of >3 measurements at each STED laser power in at least 3 GPMVs with standard deviation as error bars.

To make sure that this is the case, the diffusion in top and bottom membranes of the immobilised GPMVs has been compared using confocal FCS (Figure 14 B). The obtained transit times are very similar, indicating the immobilisation strategy was indeed not perturbing the diffusion. Note that, by the time of the study, there were no set-ups available which could perform STED-FCS experiments in the top membrane reliably. For that a high-NA water-immersion objective, as more recently used for STED-FCS in Section 5.1.3, or adaptive optics to correct for the aberrations with an oil-immersion objective [184], could be used now and would be the preferred way to exclude surface-induced artefacts.

The immobilisation using a lipid with a long PEGylated linker, allows to measure at the same spot for an extended time and avoids surface interactions of the labelled probes. Figure 14 C shows bottom and mid planes of GPMVs on different surfaces. Immobilised GPMVs and GPMVs on the protein-coated coverslip show no sign of sticking of the probe to the surface, no interactions. In contrast, GPMVs on plain glass stick and the fluorescent probe accumulates (due to surface-sticking) at the bottom of the GPMVs. This changes the overall diffusion coefficient by about a factor of two, but does not influence the STED-FCS diffusion law (apparent diffusion coefficient versus apparent resolution, observation spot size d) for the PE probe (Figure 14 D). The diffusion mode in all conditions, as measured by STED-FCS, appears to be free.

Throughout this Section, I investigated the diffusion of different probes. The overall diffusion coefficients and diffusion behaviours seemed to arise mostly from interactions with other plasma membrane components or general plasma membrane properties (in cells and GPMVs) rather than from their chemical structures, since the diffusion times of DPPE, SM, GM1 and DOPE (all labelled with Atto647N) were similar in artificial vesicles (100 % DOPC GUVs, Figure 15 A).

Interestingly, when the probes are incorporated into different systems (GUVs, GPMVs or living cells), they all undergo comparable change in overall diffusion coefficient (Figure 15 B). The compositional complexity of GPMVs accounts for the difference between GUVs and the cell-derived vesicles. The influence of the actin cytoskeleton may account for the differences between cells and GPMVs. Note that also a cholesterol analog has been

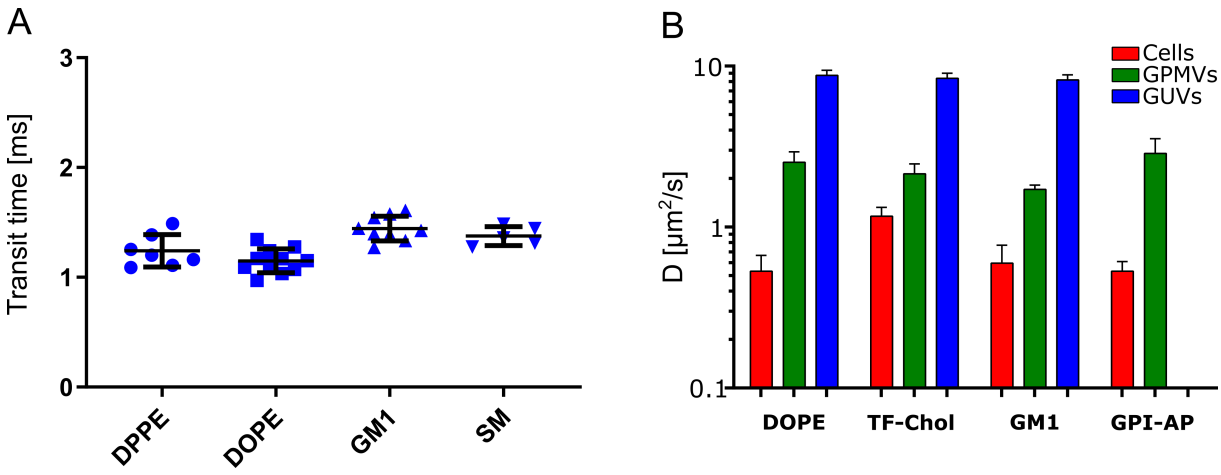


Figure 15: Diffusion of the investigated probes in artificial systems, GPMVs and cells. **A**: Confocal transit times of Atto647N labelled lipid analogs (DPPE, SM, DOPE and GM1) in the bottom membrane of 100 % DOPC GUVs. Every dot is a single measurement in a GUV. Bars are mean values and standard deviation. **B**: Diffusion coefficients of the probes measured by confocal FCS in GUVs (as in Panel A), GPMVs (immobilised) and basal plasma membrane of living PtK2 cells. In addition, to the probes in Panel A here also TopFluor-Cholesterol (TF-Chol) and GPI-AP (GPI-SNAP-KK114) have been included. Every bar represents at least 10 measurements. Error bars are standard deviations.

included (TF-Chol), which shows surprisingly fast diffusion in cells compared to the other probes. Even the outer membrane anchored GPI-AP (GPI-SNAP-KK114) has a lower diffusion coefficient. The fast diffusion of cholesterol may indicate reduced interactions with actin or differential positioning in the membrane, which may be mediated by fast relocation of the TF labelled cholesterol between the membrane leaflets by bobbing as recently described for tail-oxidised cholesterol in [221]. The fast diffusion of TF-Chol is revisited in Section 5.4.5 and further discussed in Section 6.2.

5.2.2 Diffusion in cells and GPMVs

The fluorescent lipid analogs PE (Atto647N-DPPE) and SM (Atto647N-sphingomyelin) have been investigated in the bottom membranes of Pkt2 cells by STED-FCS before and the actin cytoskeleton has been suggested to modulate their diffusion behaviour [122, 159].

These previous observations and hypothesis were confirmed using the same cell line and GPMVs derived therefrom (Figure 16). The phospholipid PE incorporated well into the plasma membrane of PtK2 cells (Figure 16 A) and STED-FCS revealed free diffusion with a diffusion coefficient of about 0.5 $\frac{\mu m^2}{s}$. The diffusion in GPMVs was also free but about 5 times faster (Figure 16 B). A convenient way to quickly assess the diffusion behaviour (free or not), is the ratio of the diffusion coefficients at a given STED power and in

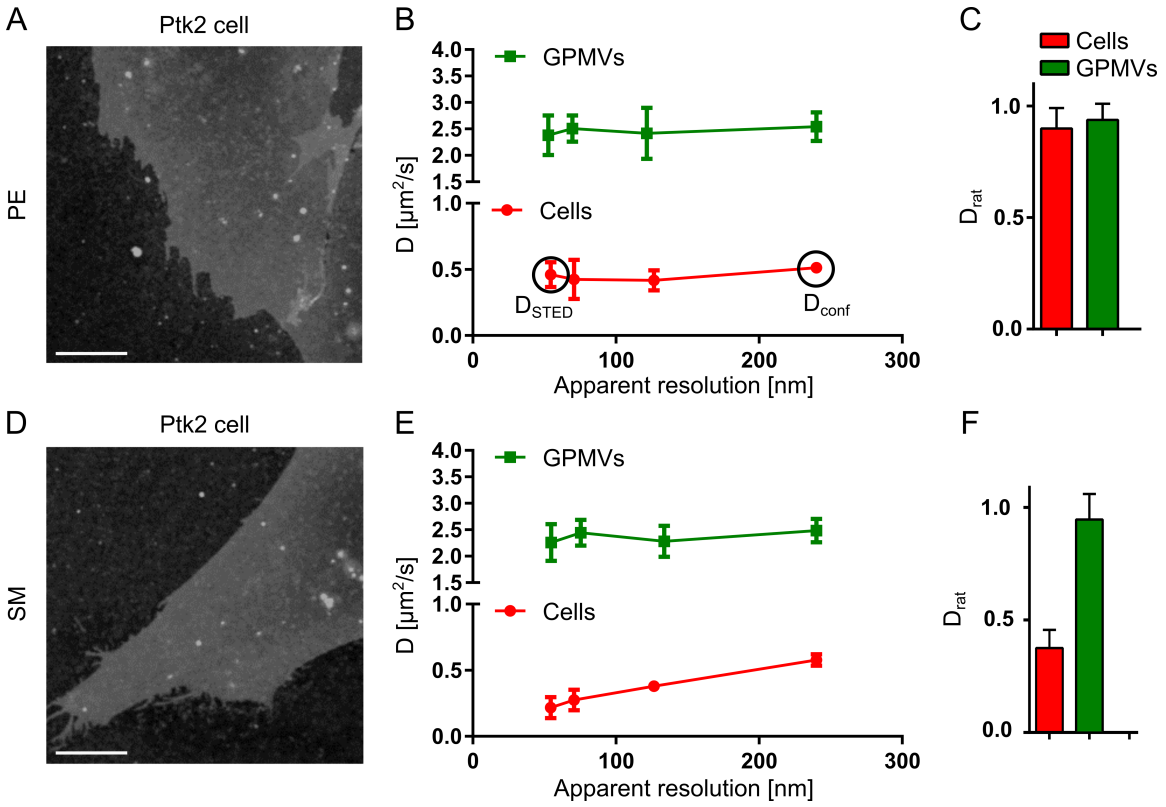


Figure 16: PE and SM diffusion in Ptk2 cells and GPMVs **A**: Confocal image of the basal membrane of a PtK2 cell labelled with Atto647N-DPPE (PE). Scale bar is 10 µm. **B**: STED-FCS diffusion law measurement for PE in Ptk2 cells (green) and GPMVs (red). The circles exemplify confocal and STED diffusion coefficients used for the D_{rat} calculations in Panels C, F and throughout this work. **C**: D_{rat}-values for DPPE in cells and GPMVs **D**: Confocal image of the basal membrane of a PtK2 cell labelled with Atto647N-SM (SM). Scale bar is 10 µm. **E**: STED-FCS diffusion law measurement for SM in Ptk2 cells (green) and GPMVs (red). **F**: D_{rat}-values for SM in cells and GPMVs. All STED-FCS measurements were performed on at least 10 cells/GPMVs and 3 repeats acquired at every STED power. Values indicate mean values and standard deviation between different cells.

confocal mode, the D_{rat}-value ($D_{rat} = D_{STED}/D_{confocal}$, around 1 for free diffusion, <1 for trapping or domain diffusion and >1 for confined/hop diffusion, Figure 16 B and C). Figure 16 D shows a confocal image of the basal membrane of a PtK2 cell labelled with SM, which visually does not appear very different from the membrane labelled with PE. Yet, measuring the STED-FCS diffusion law discloses pronounced hindered, trapped, diffusion of this lipid analog in living cells (Figure 16 E). The diffusion coefficient at confocal spot size has a similar value as compared to the one of PE, just slightly smaller, but it decreases to about 30 % of the initial value at smaller observation spot size. However, similarly to PE, the diffusion coefficient in the GPMVs is about 5 times faster than the confocal value and the diffusion mode is free diffusion, which can be easily seen when comparing the D_{rat}-values (Figure 16 F). These results suggest the heavy involvement of the actin cytoskeleton in the interactions causing the trapping of SM in live cells. The trapping of SM and the free diffusion of PE in live PtK2 cells serves as an experimental model system for different diffusion modes throughout this thesis.

Next, the diffusion behaviour of another (now unsaturated) phospholipid, DOPE, was determined in the live PtK2 cells and GPMVs. DOPE was an interesting choice, as this lipid has been used in the first, SPT based, studies revealing hop diffusion [33]. The confocal diffusion coefficient of DOPE in the plasma membrane of PtK2 cells was similar to the ones of PE and SM. The initial analysis of the STED-FCS measurements from DOPE indicated free diffusion but were very noisy. Analysing the data more carefully, revealed that, probably depending on location within the cell, two pools of diffusion modes existed: Population 1 showed hop and Population 2 free diffusion (Figure 17 A). For diffusion law measurements on immobilised GPMVs, this heterogeneity was absent, the diffusion coefficient about 5 times higher and the diffusion mode Brownian/free. These results are summarised in Figure 17 B by the D_{rat}-values. As indicated above, a possible explanation for observing two populations (with about 60 % free diffusion) might be spatial heterogeneity in the organisation and distribution of the cortical actin cytoskeleton, which is thought to cause hop diffusion (Figure 17 C). The actin cytoskeleton is not necessarily forming a homogeneous network across space, its density could vary. Thus a molecule may undergo hop diffusion (and strong confinement) in one part of the cell and

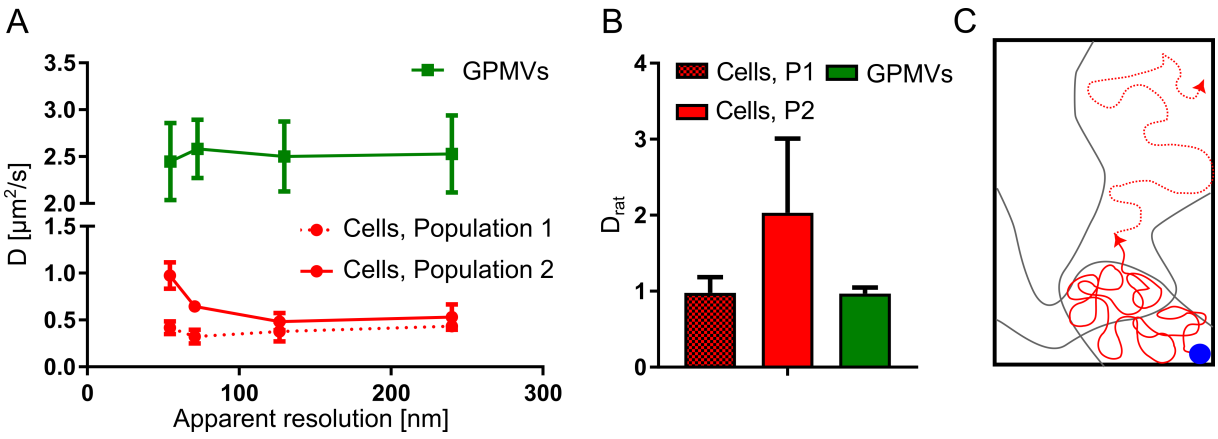


Figure 17: STED-FCS measurements of Atto647N-DOPE in PtK2 cells and GPMVs **A**: STED-FCS measurementes of Atto647N-DOPE (DOPE) shows two pools of diffusing species in living cells (confined diffusion (solid red line) and free diffusion (dashed red line)). The diffusion in GPMVs appears fast and free (green line). The populations were assigned by sorting the diffusion law data (STED power series) per location into free or hop diffusion based on the D_{rat}-values. Data from one cell but different locations could be included in both pools. **B**: D_{rat}-values for the two populations in cells and the GPMV measurements. **C**: Cartoon showing a possible explanation for two diffusing species in the cellular plasma membrane. The actin meshwork (solid grey lines) can be very dense in one part of the cell and influence (e.g. constrain) the diffusion of a molecule (blue dot) strongly (solid molecular track), whereas in other parts of the cell the meshwork can be wide and the diffusion appear free/Brownian (dashed molecular track). Values shown are mean values and standard deviation of at least three measurements per STED power in >10 cells.

diffuse freely in another. The free diffusion in the GPMVs would support this hypothesis. The importance of spatial information and how to spatially resolve diffusion modes, will be discussed in depth in the next part of the thesis (Section 5.3).

It is surprising that the Atto647N labelled lipid analogs, DPPE and DOPE, show such different diffusion characteristics at the nano-scale. However, the confocal diffusion coefficients in the cell membrane as well as in the GPMVs were similar. One hypothesis to explain this finding, is the influence of actin cytoskeleton anchored proteins (pickets). The unsaturation in the DOPE fatty acyl chains may facilitate protein-lipid interactions or increase the cross-section of the molecule.

As DOPE and DPPE only vary in the fatty acid chains and display very different nano-scale diffusion behaviours in the live cells, varying the headgroup may have a very strong influence as well. One class of lipids, namely glycolipids, are heavily involved in cellular signalling and cell-cell (cell-pathogen) recognition and have a very large (glycosylated headgroup). Some of them like GM1 are thought to cluster or form stable domains [122, 222, 223].

GM1 (labelled with Atto647N at the headgroup) was incorporated into the plasma membrane of PtK2 cells showing comparably fast internalisation (Figure 18 A). However, the STED-FCS diffusion laws in cells and GPMVs could be determined (Figure 18 B and C). The confocal diffusion coefficient in cells was slightly higher than for the other tested lipid analogs. However, the diffusion did not speed as up much in the GPMVs as compared to DPPE, SM or DOPE (only about 3 times). The diffusion behaviour in the cells did not quite resemble trapped diffusion, instead the diffusion law plot levelled off towards smaller observation spot sized, which is indicative of domain diffusion (see simulations in Section 5.2.3 below). Surprisingly, the domain-like diffusion behaviour persisted in the GPMVs, which is also represented in the D_{rat}-values (Figure 18 C). As the measurements in the GPMVs were challenging, the standard deviation quite large and the findings controversial, also other conditions were tested as controls. Figure 18 D shows a diffusion law measurement of GM1 in PtK2 GPMVs prepared with the alternative, supposedly less cross-linking, NEM method [54]. For comparison also DPPE, as free diffusion control, was measured in GPMVs from the same preparation. The domain-like diffusion behaviour for GM1 persisted. The same was observed for PFA/DTT GPMVs measured at 37 °C (Figure 18 E and D_{rat}-values in Figure 18 F). Note that measurements at 37 °C were more challenging, since the GPMVs start fluctuating considerably in axial direction, which may explain the big error bars and the rather noisy diffusion law plot for DPPE in Figure 18 E. These findings suggest that the actin cytoskeleton plays a less prominent role in the organisation of the glycolipid analog GM1-Atto647N.

Of similar interest as GM1 to signalling and outer cell membrane organisation are lipid-anchored proteins like GPI-APs. For these molecules a wide spectrum of different types of organisations ranging from freely diffusing over clustering to raft-association have been proposed [27, 28, 224]. The results from imaging and STED-FCS on two different GPI-AP (GPI-SNAP, an artifical GPI-anchored tag and LYPD6, a GPI-AP involved in Wnt signalling) are shown in Figure 19. The confocal images 19 A and D exemplify a broadly homogeneous distribution with some very bright but immobile spots (probably clusters). The mobile fraction was assessed by STED-FCS in cells and GPMVs. Note that the bright clusters were not present in the GPMVs, thus their appearance may depend on actin and

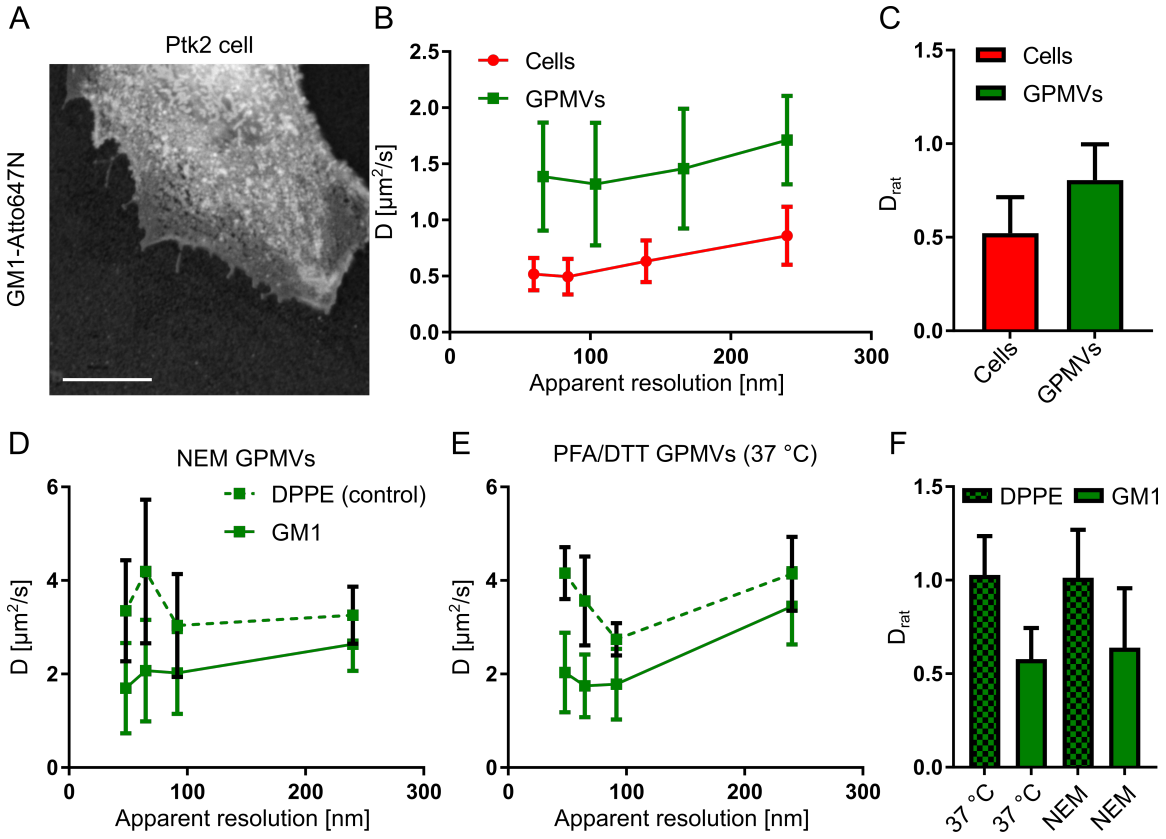


Figure 18: Hindered nano-scale diffusion of GM1 in cells and GPMVs **A**: Confocal image of the bottom membrane of a PtK2 cell labelled with Atto647N-GM1. Scale bar is 10 µm. **B**: STED-FCS diffusion law measurements of Atto647N-GM1 in bottom membranes of live PtK2 cells (red) and GPMVs (green). **C**: D_{rat}-values for cells and GPMVs from Panel B. **D**: STED-FCS diffusion law in PtK2 GPMVs produced with NEM (instead of the PFA/DTT method used for the data in Panels B and C). The dashed line indicates the diffusion of the phospholipid DPPE as a free diffusion control, the solid line is GM1. **E**: STED-FCS diffusion in PtK2 GPMVs at 37 °C for DPPE as free diffusion control (dashed green line) and GM1 (solid green line). **F**: D_{rat}-values for the measurements in D and E show the difference between the DPPE control (patterned) and GM1 (plain) in GPMVs. Data shown are mean values and standard deviation from at least three measurements per STED power in >10 cells or >3 vesicles.

energy-dependent processes. The diffusion law plot in the living cells resembles domain-like diffusion with similar confocal diffusion coefficients as the lipid analogs (Figure 19 B and E). In GPMVs the speed-up in diffusion is not as pronounced as for DPPE, SM or DOPE and more similar to GM1. However, the GPI-APs appear to be diffusing freely. In contrast to what may form the domains for GM1, the ones involved in the GPI-AP organisation seem to be dependent on the actin cytoskeleton. The diffusion of GPI-SNAP could not directly be measured in the GPMVs due to poor labelling efficiency. As an alternative, the diffusion law of GPI-RFP, detected with an anti-RFP nanobody (tagged with Atto647N), has been determined in the GPMVs. The same labelling strategy was then employed in cells and GPMVs for LYPD6. The results are summarised in the plots of the D_{rat}-values in Figure 19 C and F, where again DPPE was included in the GPMV measurements as a free diffusion control.

The findings on the GPI-AP organisation give a glance at the complexity of their spatio-temporal organisation, which will be elucidated in more detail in the next part of the thesis (see Section 5.3.2). At this point, it is worth noting that for all the lipid analogs and GPI-APs in the cell measurements, most likely, dynamics in the outer leaflet of the plasma membrane were observed. The flip-flop rates of the lipid analogs is probably slow to deliver them into the inner leaflet and the GPI-APs are inherently only found in the outer leaflet [122, 201, 225]. Measurement sessions on labelled cells were not longer than 1 h, but it cannot completely be ruled out that the lipid analogs reached the inner leaflet through trafficking pathways through the cell. However, the described effects of the cytoskeleton on the diffusion modes of the lipids, therefore, may imply interleaflet coupling [226] and a strong influence of cytoskeleton-anchored proteins [33, 227]

5.2.3 Monte Carlo simulations on diffusion modes investigated by STED-FCS

Simulations on diffusion modes and measurements with STED-FCS have been performed similarly as described before (e.g., [36, 203]). The simulations were crucial to the understanding and interpretation of the experimental results. Note that a noise-free system was used for the simulations and still large error bars were observed. Exemplary sets of simulation results are provided in Figure 20 (see Materials and Methods 4.12 for details

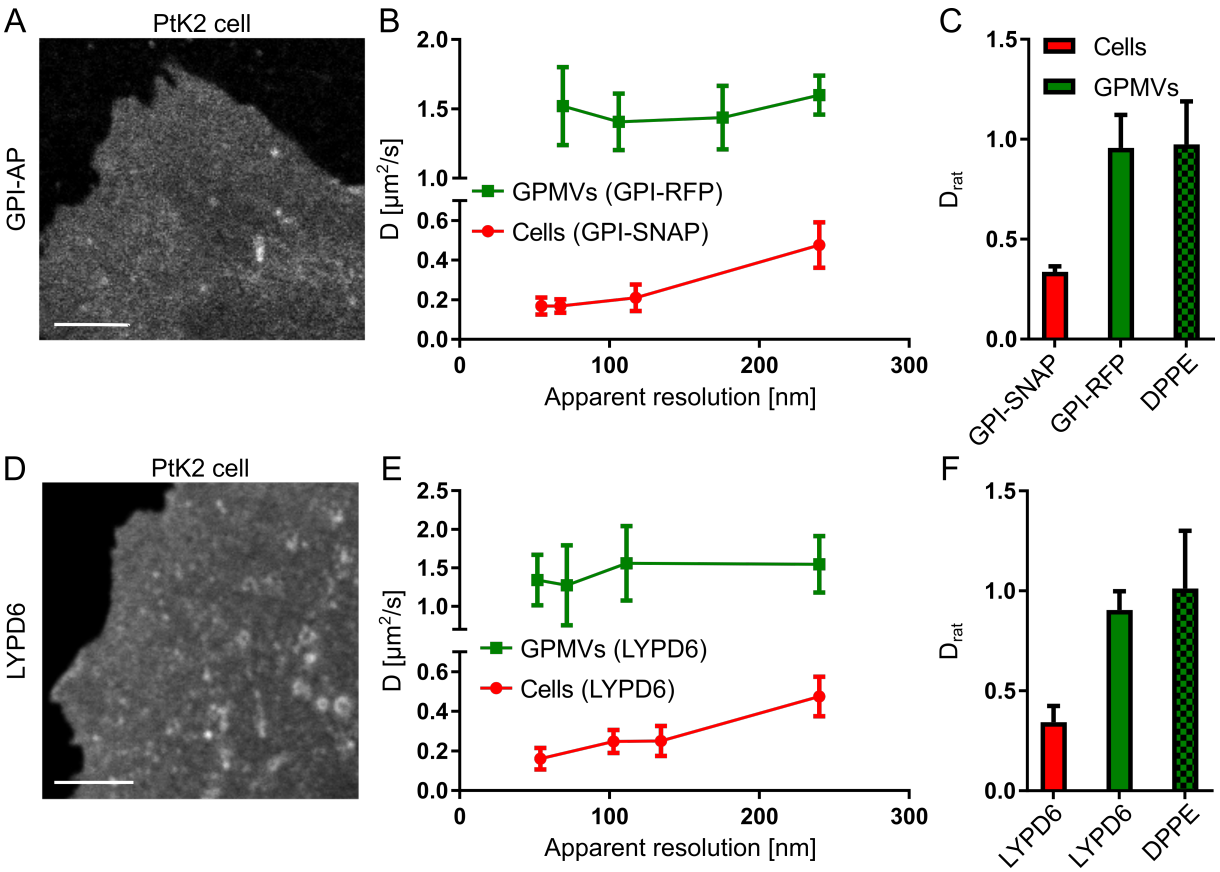


Figure 19: Nano-scale domain diffusion of GPI-APs in cells is abolished in GPMVs. **A**: Confocal image of the basal membrane of a PtK2 cell transfected with GPI-SNAP, which was labelled with KK114-Bg (SNAP substrate). Scale bar is 5 µm. **B**: STED-FCS of GPI-AP in PtK2 cells and GPMVs. Cells were labelled as in A but the diffusion in GPMVs was measured for GPI-RFP additionally tagged with anti-RFP nanobody labelled with Atto647N. **C**: D_{rat}-values for the diffusion law measurements in Panel B, additionally including a free diffusion control (DPPE in GPMVs, measured on the same day). **D**: Confocal image of the bottom membrane of a PtK2 cell transfected with LYPD6-mCherry (and additionally labelled with anti-RFP nanobody tagged with Atto647N). Scale bar is 5 µm. **E**: STED-FCS diffusion law measurements of LYPD6-mCherry tagged with anti-RFP nanobody (Atto647N labelled) in living PtK2 cells (red) and GPMVs (green). **F**: D_{rat}-values for the measurements in E additionally including a free diffusion control (DPPE in GPMVs, measured on the same day). All values shown are mean values and standard deviations for at least three measurements per STED power and >10 cells and GPMVs.

on simulation set-up and conditions).

The typical diffusion law plots for free, trapped and hop diffusion modes (as depicted in the cartoon in Figure 3) could be recovered by simulations (Figure 20 A). For this particular set of exemplary simulation parameters, already the confocal diffusion coefficients sampled from trapped (red) and hop (blue) diffusion deviate from the input diffusion coefficient of 1.0 $\frac{\mu m^2}{s}$ (free diffusion, green). Th effect of hindrance on the confocal diffusion coefficients does not necessarily need to be that pronounced, but it turned out that the introduction of spatially homo- or heterogeneous hindrance changes the confocal diffusion coefficients at least slightly. These simulations were initialised with a diffusion coefficient of 1.0 $\frac{\mu m^2}{s}$, however, for hop diffusion the diffusion law plot never reached this value (even at a small observation spot size of d = 50 nm). Experimentally, the hop diffusion of DOPE exceeded the diffusion coefficient found for the seemingly freely diffusing DPPE (compare Figure 17 A and Figure 16 B). This suggests that on very small scales DPPE may undergo some hindrance, which may affect the absolute values of the diffusion coefficients on all scales. The experimentally found final diffusion coefficient of DOPE rather resembles the one of Cholesterol, which has been suggested to be a fast and freely diffusing molecule in the membrane [228].

Figure 20 B summarises the results from Panel A in terms of D_{rat}-values. The diffusion behaviour of GM1 and GPI-AP in the live cells were initially controversial, since for the measurements at highest STED power often an increase in diffusion coefficient was observed (see, for example, Figure 18 B). This observation led to the initial hypothesis that a combination of hopping and trapping could cause such an effect. However, extensive simulations ruled that out. Interestingly, for the combination of these diffusion modes the trapping almost always overrules the hopping behaviour (Figure 20 C). The only simulation condition tested, which was able to resemble the experimentally observed diffusion law plots, was domain diffusion. To simulate this type of diffusion mode, small immobile areas were distributed across the simulation area. The the probe was allowed to diffuse in and out of these domains, but upon incorporation into a domain its diffusion coefficient was reduced (Figure 20 D). Importantly, the kink (or levelling off) in the diffusion law plot does not occur anywhere close to the domain size but well above it. These simulations

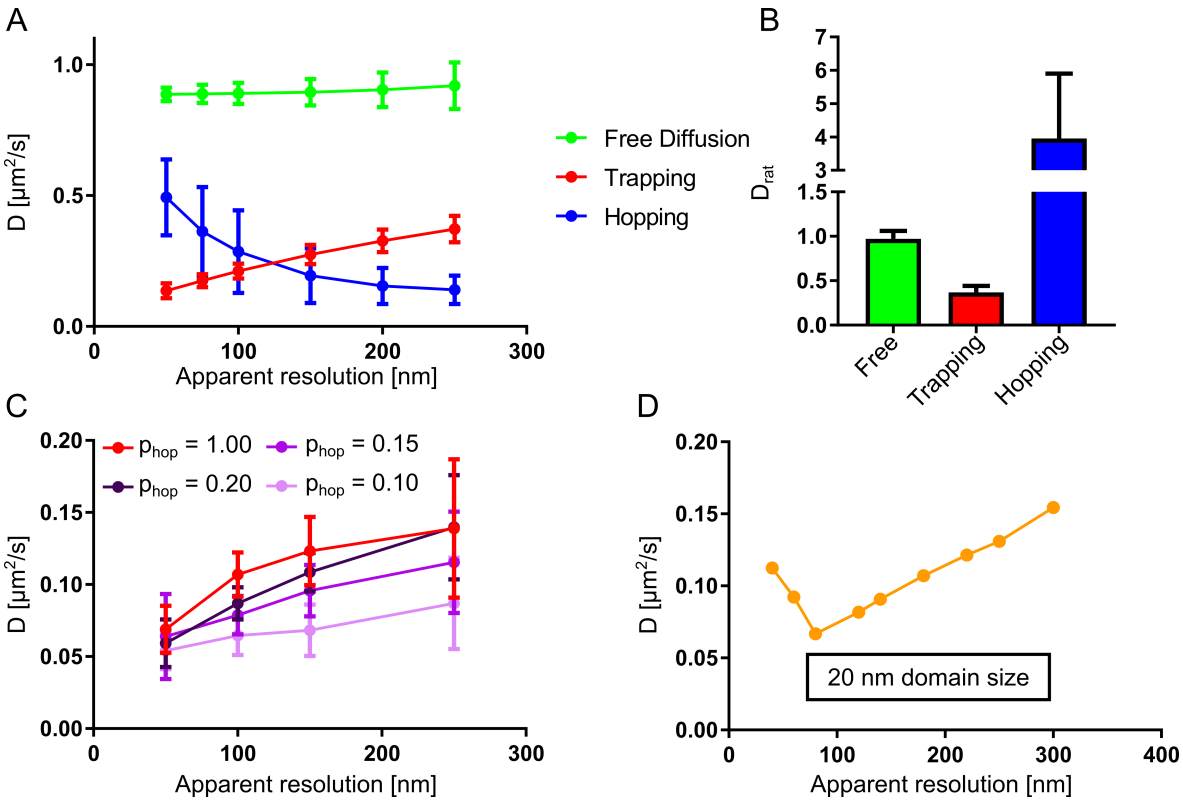


Figure 20: Simulated pSTED-FCS measurements on different diffusion modes. **A**: STED-FCS diffusion law measurements on exemplary data simulated for free diffusion (green), trapped diffusion (red), and hop diffusion (blue). Input diffusion coefficient was 1.0 $\frac{\mu m^2}{s}$. For trapping p_{trap} was 0.00005 and equal to p_{untrap}, for hopping Voronoi size was 110 nm and $p_{hop} = 0.05$ (see Materials and Methods Section 4.12 for details) **B**: D_{rat}-values for the simulated data in Panel A at FWHM of 50 nm for STED. **C**: STED-FCS diffusion law measurements of trapping alone (red) and in combination with hopping (magenta shades for varying hopping probabilities p_{hop} as indicated and fixed trapping probabilities $p_{trap_on} = p_{trap_off} = 0.00005$). The input diffusion coefficient was 0.4 $\frac{\mu m^2}{s}$. **D**: STED-FCS simulations on domain diffusion. 20 nm domains were distributed covering 50 % of the simulation area and the input diffusion coefficient 1.0 $\frac{\mu m^2}{s}$ reduced to a third once a molecule entered a domain. See Materials and Methods 4.12 for more details. The simulations on domain diffusion were performed in collaboration with Dr. Dominic Waithe.

were very helpful in interpreting the experimental results and were the starting point for many more simulations mostly on scanning FCS (see forthcoming Sections).

5.2.4 Summary nano-scale dynamics in cells and actin-free systems

The STED-FCS measurements on cells and GPMVs gave very detailed insights into the possible diffusion behaviours of various fluorescent lipid analogs and GPI-APs. The developed immobilisation protocol for the GPMVs allows long and reliable measurements in an equilibrated system, which does not seem to be perturbed by interactions with the surface of the coverslip. The influence of the actin cytoskeleton (and possibly other energy depen-

ded processes) on the diffusion coefficients and diffusion modes appeared overwhelming. Using the GPMVs, it came as a surprise that some hindrance remained for the ganglioside GM1 and no hindrance was observed for GPI-APs, which highlights the heterogeneous nature of plasma membrane organisation. The two diffusing pools of DOPE (hopping and free) as well as the actin-dependent domain-type diffusion of GPI-APs reveals the diffusional heterogeneity even within the membrane of one cell and poses challenges to accurately interpreting the data. The described measurements represent averages over many cells, locations and time points. In the next Chapter, a new approach to address these issues will be presented.

5.3 Spatially resolved diffusion modes: LIESS-FCS

Scanning STED-FCS (sSTED-FCS) allows to measure diffusion dynamics across a scanned line at given observation spot size, d (apparent resolution). However, it does not disclose the diffusion law in space *per se*, since for diffusion law measurements different spot sizes need to be acquired simultaneously. The principle, advantage and issues of sSTED-FCS are depicted in Figure 21. Scanning a line instead of measuring at a single spot may increases the amount of recorded data (i.e., the statistics). It may, for example, in one acquisition disclose differences in diffusion coefficients between two locations (e.g., two cells) and thus make use of spatial information (Figure 21 A).

In a standard sSTED-FCS experiment, though, confocal and STED recordings are acquired subsequently (Figure 21 B). This yields arrays of confocal and STED correlation curves, often plotted over space as a correlation carpet (Figure 21 C, D). The raw data are simply the intensity values at a given time along the scanned line, which is termed intensity carpet or xt-scan. Temporally correlating the intensity data at every spot (pixel) yields the correlation curves across space, from which spatially resolved dynamics can be calculated. Measurements with s(STED-)FCS are very convenient because they do not require dedicated equipment like a correlator card or TCSPC equipment. Intensity data from any LSM (equipped with a STED beam) can be collected and correlated [14, 148].

The sSTED-FCS approach has, for example, been used to show that SM (Atto647N-sphingomyelin) undergoes slowed-down diffusion at specific sites, which were termed hot-spots of trapping [166]. A big challenge with this type of measurements is that the data in confocal and at different STED powers are acquired subsequently, which means that, for example, cellular movement, reorganisation, or photodamage may only affect one measurement and not the other. This displays a potential source of artefacts. Acquiring the diffusion mode in one measurement using STED, has so far only been achieved employing custom TCSPC equipment [121] or CW-depletion and sophisticated gating schemes [194] in pSTED-FCS. These approaches do not provide any spatial information, require long acquisition times, and have not been performed on live cells. Hence, this Section deals with the issue of acquiring spatially resolved diffusion law data (STED and confoca mode across space at the same time) for the application in live cell measurements.

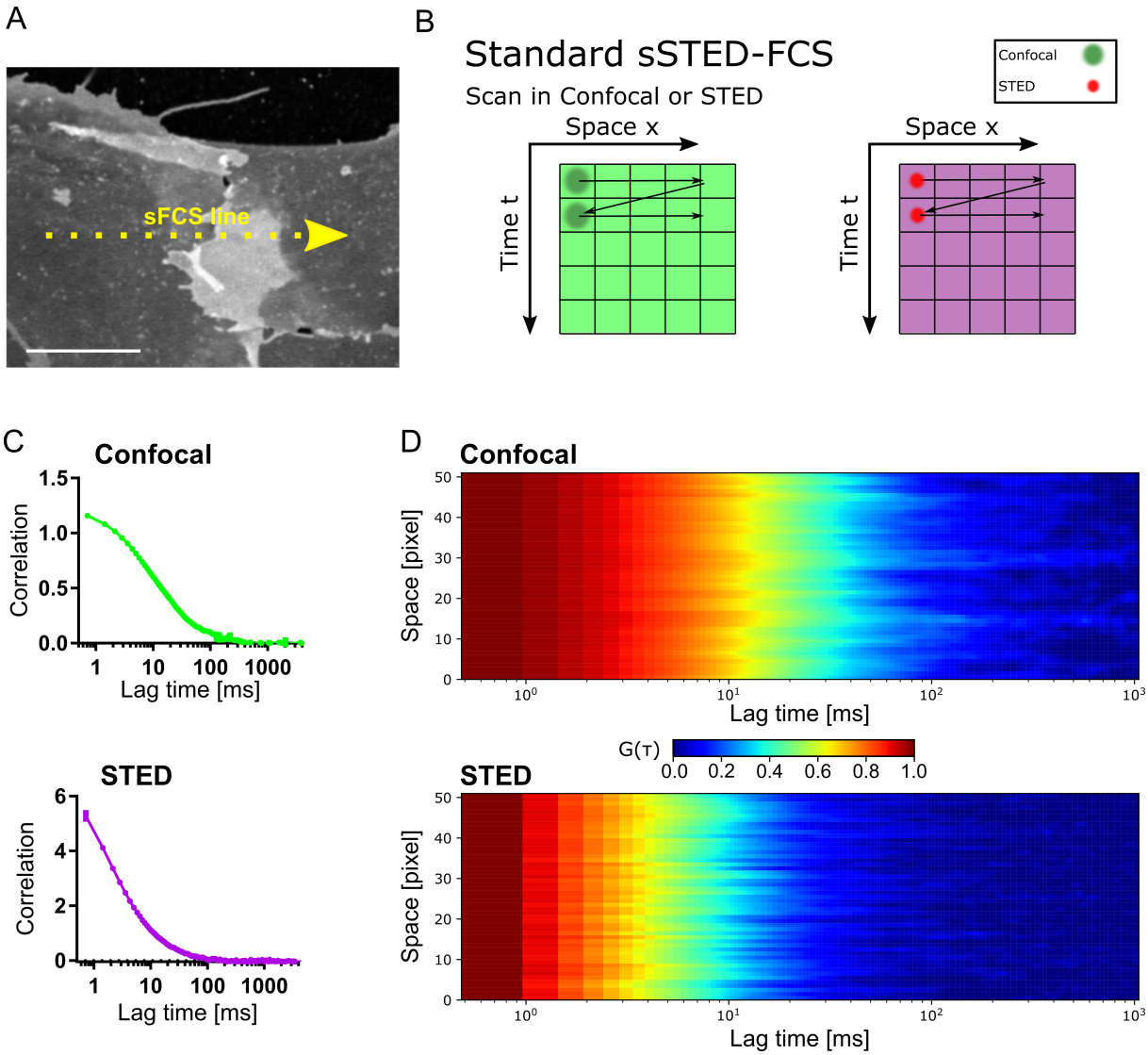


Figure 21: Scanning STED-FCS discloses local heterogeneities in diffusion. **A**: Confocal image of the bottom membrane of two Ptk2 cells labelled with KK114-PEG-Cholesterol. The dotted yellow line demonstrates a potential sFCS line and shows the advantage of obtaining spatial information (i.e., different diffusion coefficients in either of the cells). Scale bar is 10 µm. **B**: Acquisition scheme of a standard sSTED-FCS measurement. The same line is sampled over and over again which results in a xt measurement often termed intensity carpet. This measurement is either done using confocal excitation or including STED illumination. **C**: Correlation curves resulting from a simulated confocal (top, green) or STED (bottom, magenta) sFCS measurement. **D**: Correlation carpets resulting from a simulated confocal (top) or STED (bottom) sFCS measurement. For every point (pixel) along the line a single correlation curve is obtained disclosing the diffusion dynamics at that spot. The normalised correlation $G(\tau)$ is colour-coded blue to red. The confocal and STED data are not acquired at the same time.

5.3.1 Simultaneous acquisition of confocal and STED sFCS data

To readily disclose diffusion modes across space, the confocal and STED sFCS data need to be obtained at the same time. A first attempt to achieve this was binning of pixels, which is widely used in camera-based svFCS approaches (e.g. BimFCS [151, 152, 201, 229]). The idea of binning sSTED-FCS data is conceptualised schematically in Figure 22 A.

In a typical sSTED-FCS experiment the PSF is larger than the acquired pixel, ie., the location to which the intensity is allocated. By binning two or more adjacent pixels, the dimensions of the PSF should effectively increase. In line-scan mode (as compared to imaging mode with a camera) this should yield an elliptical effective observation spot, with a long axis (a) and a short axis (b) illustrated in Figure 22 A. The binning of simulated sSTED-FCS intensity data (xt-carpets) is exemplified in Figure 22 B. The intensity blurs in the direction of binning and the overall length of the carpet shortens, as always adjacent pixels are combined to a central one. The obtained intensity data can be temporally correlated and the resulting correlation curves fitted. This could for each binning yield the diffusion dynamics on different length scales.

The fitted transit times (and recalculated diffusion coefficients) were compared to a simulated sSTED-FCS experiment with supposedly the same, but isotropic, spot sizes (Figure 22 C, binned spot sizes based on the scheme in Figure 22 A). Increasing the PSF size notably elongates the trasit times for the sSTED-FCS simulations (Figure 22 C, blue). For the binned data (80 nm PSF binned into larger observation spots e.g. 160 nm or 240 nm, Figure 22 C, orange) the transit times barely change. The observed diffusion time seemed to be dominated by molecules passing through the short axis (b) of the elliptical observation area. To combat this effect, the correlation curves were fitted using a model accounting for an elliptical observation spot (and the transit time along the short axis fixed). This approach (red dots in Figure 22 C) yielded longer, although more scattered, values of the fitted transit time. As free diffusion was simulated, the diffusion law plot should result in a straight line. This is the case for the actual sSTED-FCS simulations. However, the corrected and uncorrected data from binning the 80 nm sSTED-FCS measurement did not recover this behaviour (Figure 22 D).

These simulations demonstrate that acquiring the data at different spot sizes is superior

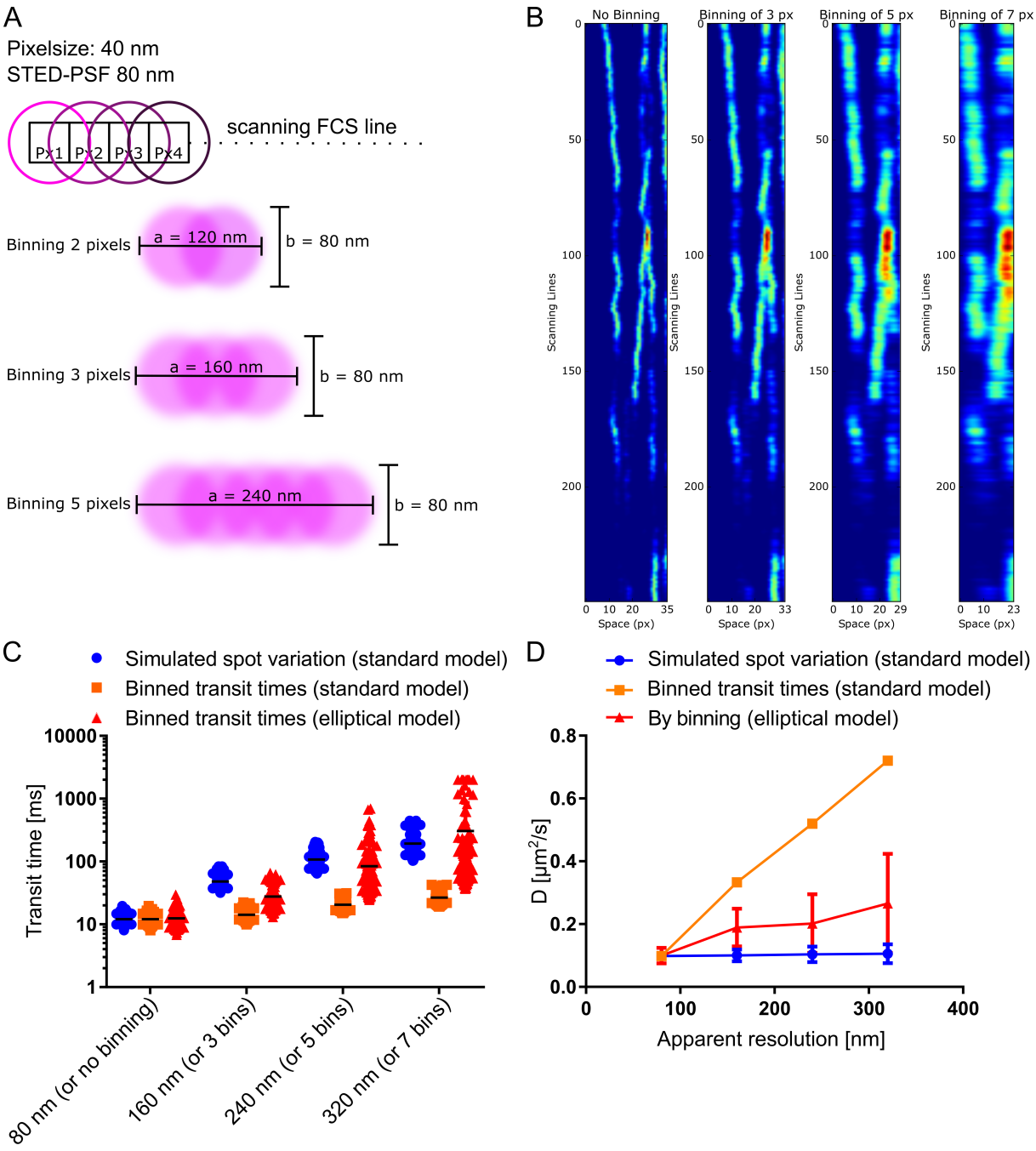


Figure 22: Binning of scanning STED-FCS data to obtain the diffusion law across space. **A**: Cartoon illustrating binning pixel (Px) from sSTED-FCS data to different length scales. Binning two or more symmetrical PSFs (approximated by a Gaussian disc in a 2D plane, magenta) results in elliptical observation spots with a short axis (b) and a long (varying) axis (a). **B**: Normalised intensity carpets (first 250 scanning lines, intensity is colour coded from 0.0 (blue) to 1.0 (red)) from simulated sSTED-FCS data (with a FWHM of 80 nm and a pixel size of 40 nm). The intensity values per pixel were binned into 1 pixel (no binning), 3 pixel, 5 pixel or 7 pixel resulting in FWHM (along the long axis a) of 80 nm, 160 nm, 240 nm and 320 nm, respectively. **C**: FCS transit times from actually varying the simulated observation spot (blue) or binning the 80 nm sSTED-FCS data into larger (asymmetrical) observation spots (orange: Fitted with a standard PSF model, red: Fitted with an elliptical PSF model) from 5 sSTED-FCS simulations (2 kHz scanning frequency, 0.1 $\frac{\mu m^2}{s}$ input diffusion coefficient). Black bars denote averages. **D**: STED-FCS diffusion law plots recalculated from the transit time data in Panel C. The diffusion coefficient obtained from actually varying the FWHM (blue) is constant, indicating free diffusion, whereas the diffusion coefficients from binning (with both fitting approaches, orange or red) overestimate the diffusion coefficients. Averages and standard deviations are shown.

to post-processing STED data in sFCS. The reason for that is the asymmetric observation spot and the averaging nature of FCS: It measures transits through the observation spot and these are dominated by many fast transits through the short b-axis of the elliptical PSF from binned sFCS data, which skews the average transit time towards shorter average values.

As an alternative to binning, confocal and STED data could be acquired alternatingly. By the time the project started, the available microscope(s) were not capable of switching quickly STED and confocal excitation (e.g., every pulse or pixel), but could switch line-wise in an image. Thus, line interleaved excitation scanning STED-FCS (LIESS-FCS) was developed. The LIESS-FCS principle is illustrated in Figure 23 A.

During acquisition, the intensity data are sorted in two sFCS channels (STED and confocal mode, respectively). Correlating these intensity data, with half of the acquisition scanning frequency, yields STED and confocal correlation curves (Figure 23 B), quasi-simultaneously, at the same locations across space (Figure 23 C and D; for every pixel in the correlation carpets a conventional and a super-resolved correlation curve has been obtained). As the confocal and STED recordings are now spatio-temporally linked, the diffusion mode can be calculated across space in the form of D_{rat}-values (Figure 23 E). The data shown here (Figure 23 B-F), represent simulated LIESS-FCS measurements for free diffusion and demonstrate, how the diffusion behaviour can be recovered across space. From all the calculated D_{rat}-values along the scanned line, also an average behaviour can be reported in the form of a D_{rat} histogram, which most likely represents the average obtained in pSTED-FCS. A simulated example is given in Figure 23 F. However, it is crucial that the line time (inverse scanning frequency) is significantly shorter than the transit time of the probe in confocal and STED mode. This is the case for any sFCS experiment and imposes the temporal resolution limit of the technique.

The LIESS-FCS principle seemed to work on simulated data. Thus, measurements on simple model systems were performed and compared to standard sSTED-FCS recordings. This is only possible in a spatially homogenous system, where free diffusion can be assumed, e.g., in an SLB. Thus, measurements were performed on the same SLBs containing 50 mol% DOPC and 50 mol% cholesterol labelled with a fluorescent lipid analog (KK114-

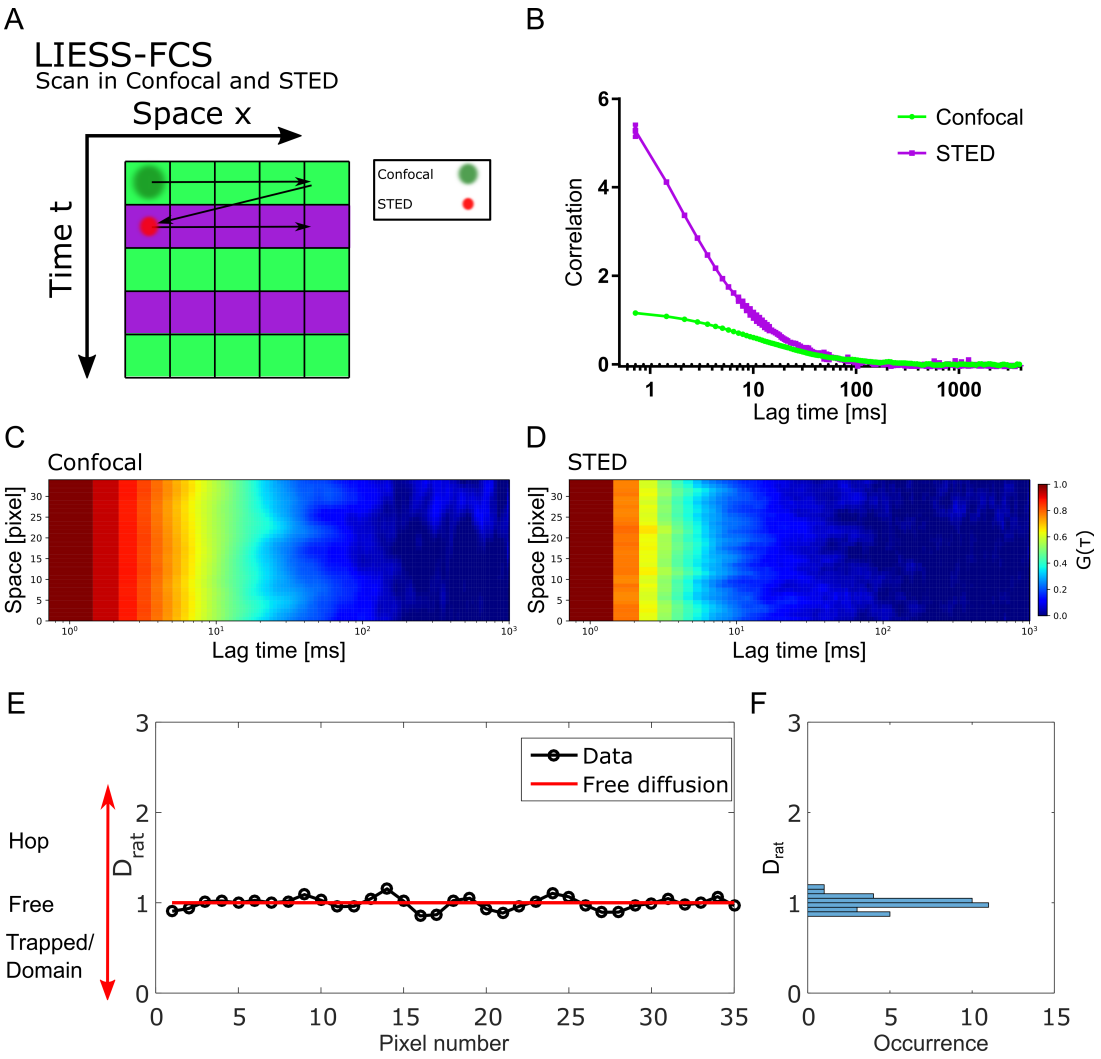


Figure 23: Line interleaved excitation scanning STED-FCS (LIESS-FCS) for diffusion mode imaging. **A**: Cartoon explaining the principle of LIESS-FCS. Every line the excitation is switched from confocal (green) to STED (magenta), obtaining conventional and super-resolved intensity data quasi-simultaneously. **B**: Simultaneously acquired confocal (green) and STED (magenta) FCS curves from simulated data. **C, D**: sFCS correlation carpets obtained from a simulation and sampled with LIESS-FCS for 40 s with PSFs of 240 nm (confocal) and 100 nm (STED) resulting in a confocal (C) and a STED measurement (D). The normalised correlation $G(\tau)$ is colour coded as indicated. **E**: D_{rat} plot across space from the simulated data in Panel C and D. The D_{rat}-values are obtained from the confocal and STED curves at every pixel, which is only possible as the data are acquired quasi-simultaneously. A D_{rat}-value around 1 indicates free diffusion, whereas $D_{rat}<1$ or $D_{rat}>1$ indicates hindered trapped or hop diffusion, respectively. **F**: Histogram of the D_{rat}-values for this LIESS-FCS measurement.

DPPE). Correlation carpets in confocal and STED obtained with standard sSTED-FCS (Figure 24 A) and LIESS-FCS (Figure 24 B) display no notable spatial heterogeneity. The sSTED-FCS measurement was acquired with similar scanning frequency (2780 Hz) as the LIESS-FCS measurement, where the frequency was halved during the analysis. However, the signal-to-noise, the noise in the carpets, is comparable. Also the fitted transit times obtained with both methods in confocal and STED are not significantly different or follow any trend (Figure 24 C). A first experimental LIESS-FCS plot (i.e., D_{rat}-values across space) for an SLB is shown in Figure 24 D together with the D_{rat}-histogram. The plot discloses free diffusion, as expected, but shows larger variation around $D_{rat} = 1$ compared to the simulated data, which seemed to be largely due to experimental noise and acquisition time issues (see below and Figure 25).

The data, reported throughout this Section, employ spot sizes of about 100 nm in STED. Of course, using higher depletion laser powers smaller spot sizes can be obtained, but the influences of noise and acquisition time get worse. Additionally, the expected transit times need to be considered. To calibrate the spot sizes SLBs (composed of DOPC/Chol) were used. Even at high concentrations of cholesterol the transit times of a fluorescent probe will be very short at small (STED) spot sizes. As mentioned above, in s(STED-)FCS the temporal resolution is given by the scanning speed, which defines the minimum lag time (correlation time). Measured transit times should be well above this minimum lag time.

The influence of noise in experimental versus simulated data and the influence of acquisition time were investigated more systematically, and helped choosing the acquisition parameters for forthcoming measurements. The ability of recovering free diffusion accurately is assessed for different acquisition times in Figure 25. For simulated data, in the absence of noise such as out of focus light or shot noise, the D_{rat} across space plots deviate strongly from $D_{rat} = 1$ for short acquisition times (e.g., 10 seconds). The plot gets smoother with longer acquisition times (Figure 25 left panels). The same behaviour was observed for experimental data on SLBs (Figure 25 right panels). Despite higher photon count rates, longer acquisition times were needed to accurately recover homogeneous free diffusion across space. For the evaluation of fast cellular processes this poses a challenge, but is inherent to any fluorescence fluctuation based method. One needs to sample

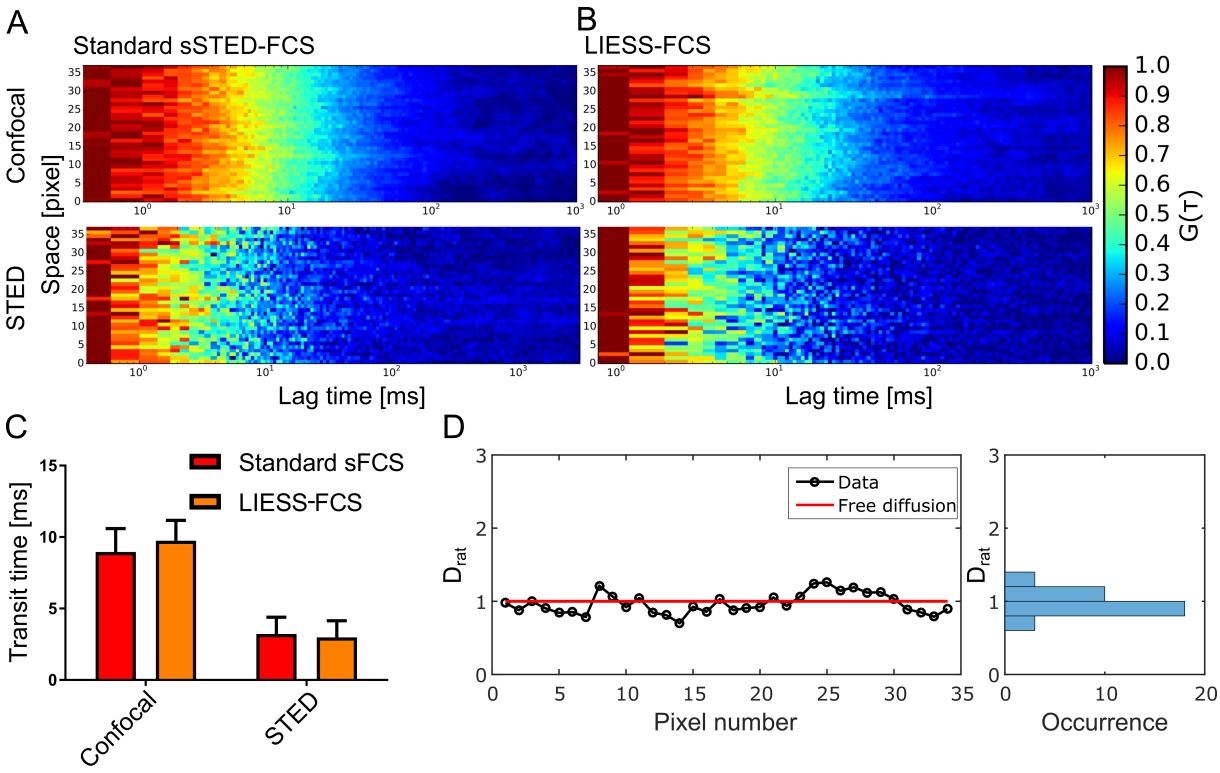


Figure 24: Performance of LIESS-FCS compared to standard sSTED-FCS on SLBs, composed of DOPC and Cholesterol (50 mol% each) and doped with KK114-DPPE. **A, B**: Confocal and STED correlation carpets acquired on an SLB with either standard sSTED-FCS Panel A or LIESS-FCS Panel B. Measurement time was 150 s. Normalised correlation $G(\tau)$ is colour coded as indicated. **C**: Comparison of the fitted transit times from standard sFCS (red) and LIESS-FCS (orange) in confocal and STED mode (average transit times and standard deviations from two independent measurements, 72 curves in total). **D**: Plot of D_{rat}-values from the SLB measurement in Panel B over space (left) and as histogram (on the right). D_{rat}-values around 1.0 indicates free diffusion.

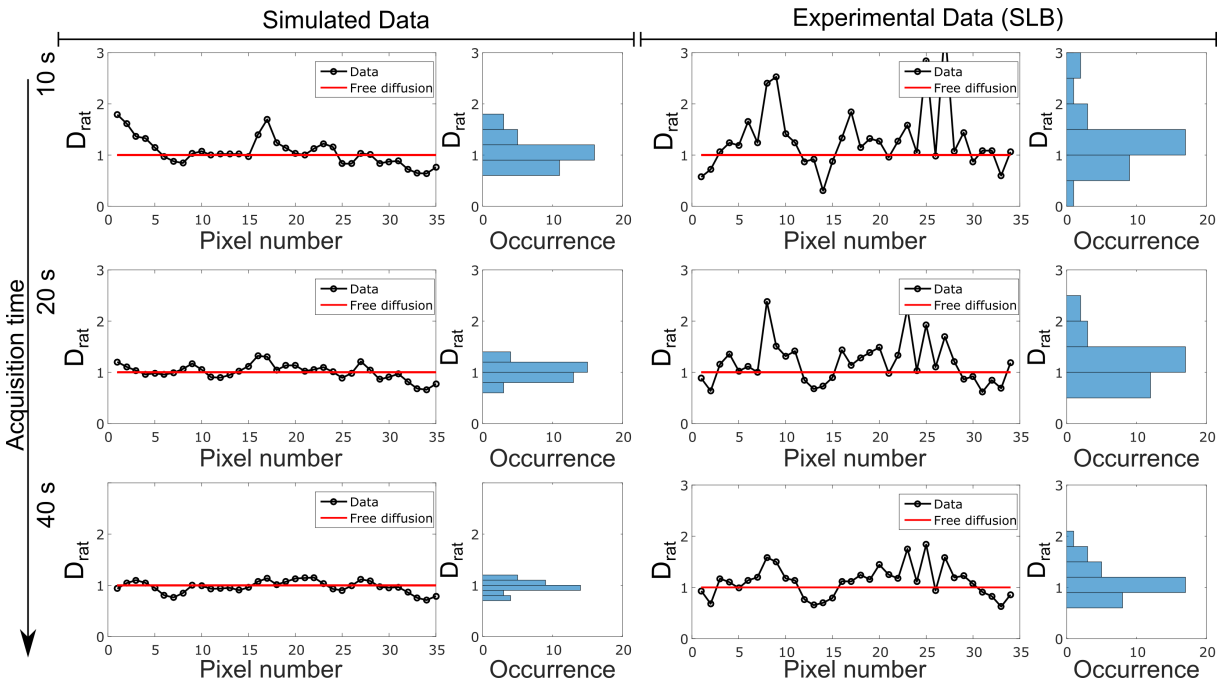


Figure 25: The effect of acquisition time on D_{rat}-plots in simulated (left) and experimental data (right). The Monte Carlo simulations were performed in accordance with the experimental data (1400 Hz and 1.36 µm scan, for details see Materials and Methods Section 4.12). The experimental data were acquired on an SLB (DOPC/Cholesterol 50 mol% each and doped with KK114-DPPE) with varying acquisition times. For both data sets the signal-to-noise, represented as smoothness of the D_{rat} fluctuations around 1 either for free diffusion across space (left panels) or from the average histogram (right panels), improve with longer acquisition times.

over enough events to be able to obtain a meaningful average. Therefore, calibration measurements on SLBs to determine the spot sizes were >120 s long.

5.3.2 LIESS-FCS measurements in living cells

As LIESS-FCS has been demonstrated to work on model systems, next the diffusion in the cellular plasma membrane was investigated using the above-explained optimised acquisition settings. From the previous Sections, the diffusion behaviours of Atto647N-DPPE, KK114-PEG-Cholesterol and Atto647N -SM are known and have been characterised in detail. Thus, first proof of principle LIESS-FCS experiments on the basal plasma membrane of PtK2 cells labelled with these probes were acquired and analysed. First, the freely diffusing probes, PE and KK114-PEG-Cholesterol, were investigated. Figure 26 A - C show LIESS-FCS correlation carpets as well as the D_{rat}-values across space and D_{rat} histogram for KK114-PEG-Cholesterol. The carpets as well as the LIESS-plot indicate no spatial heterogeneity for KK114-PEG-Cholesterol and free diffusion, D_{rat}-values around 1.0. However, some of the D_{rat}-values could be attributed to small local hindrance but

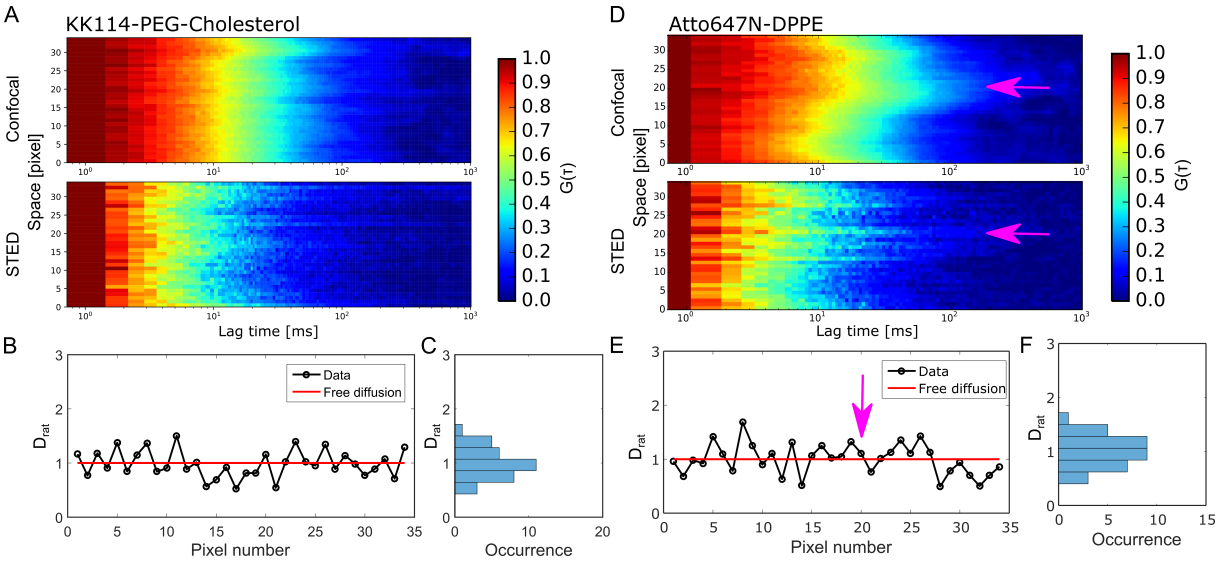


Figure 26: LIESS-FCS on freely diffusing molecules in live PtK2 cells. **A-C**: LIESS-FCS measurement on the basal membrane of PtK2 cells stained with KK114-PEG-Cholesterol. **D-F**: LIESS-FCS measurement on the basal membrane of PtK2 cells stained with Atto647N-DPPE. **A, D**: Confocal and STED (d = 100 nm) correlation carpets acquired quasi-simultaneously with LIESS-FCS (1.36 µm scan acquired for 120 s). **B,E**: D_{rat}-values over space for KK114-PEG-Cholesterol and Atto647N-DPPE, respectively. **C,F**: D_{rat}-histograms from the single scans for KK114-PEG-Cholesterol and Atto647N-DPPE, respectively. The pink arrows for Atto647N-DPPE indicate elongations in transit time but free diffusion revealed by the D_{rat} plot.

may just result from noise.

The same analysis was performed for Atto647N-DPPE, which is also expected to diffuse freely. In this case, the correlation carpets (Figure 26 D) show some spatial heterogeneity (pruple arrows) but are overall smooth. The D_{rat}-values across space as well as the histogram thereof (Figure 26 E and F, respectively) appear similar to the KK114-PEG-Cholesterol data, disclosing free diffusion. This example of DPPE is interesting, as in the confocal and STED carpet some heterogeneity is apparent (i.e., elongation towards longer correlation times). The D_{rat}-value indicates free diffusion at this spot, which in a classical sSTED-FCS measurement might have been mistaken for a trapping site (purple arrow in Figure 26 E). The inhomogeneity may just be membrane topology or cellular movement.

LIESS-FCS could well disclose free diffusion behaviour. Next, trapping was investigated. Atto647N-SM has been used as a model system for hindered trapped diffusion. Its pronounced trapping behaviour has been characterised in the previous Section as well as in the literature [122, 166]. An exemplary LIESS-FCS measurement (correlation carpets and D_{rat} plots) is shown in Figure 27 A-C. The confocal correlation carpet appears almost homogeneous, whereas in the STED correlation carpet pronounced spikes (i.e., shifts to-

wards longer correlation time) at specific locations appear, which have been described before as hot-spots of interactions [166]. The D_{rat} over space plot and the histogram imply that the hindrance of SM may be a combination of very strong interactions (very low D_{rat}-values, almost immobile, see magenta numbers in Figure 27 A and B) and some weaker interactions, together resulting in two peaks in the histogram (Figure 27 C). It has to be noted that the acquisition times to observe these spikes need to be relatively short (30 - 45 s), otherwise they seem to average out. The short acquisition times, though, yield to a decrease in signal-to-noise ratio and cause some artefacts (noise peaks of very high D_{rat}-values). This is a similar behaviour as observed during the evaluation of the influence of the acquisition time on LIESS-FCS performance (Figure 25), where too short acquisition times also predominantly caused a shift towards higher D_{rat}-values. The transient nature of the slow-down sites is depicted in Figure 27 D-L, where a long measurement was cropped into 30 s acquisition times. The sites of very low D_{rat}-values do not stay at the same locations, but seem to move or assemble and disassemble constantly, which explains the necessity for rather short acquisition times or dividing longer ones. The timescale of the assembly/disassembly seems to be about 10 to 30 s, which is far from diffusion timescales, but is in the range of actin cytoskeleton reorganisation [35]. This goes along with the finding from the previous Section and literature that the trapping of SM is actin dependent [122, 159]. To decipher the trapping dynamics in detail, better signal-to-noise and faster sampling is required, which could be obtained by performing sSTED-FCS using a fast resonance scanner [230] or higher acquisition count rates, as indicated in Section 5.1 for pFCS.

Finally, the organisation of GPI-APs in the plasma membrane of living PtK2 cells was investigated using LIESS-FCS. In the previous Section, domain diffusion behaviour of GPI-APs was revealed using pSTED-FCS in great temporal detail, but no information on the spatial heterogeneity could be obtained. In light of the measurements on the lipid analogs, LIESS-FCS seemed suitable to disclose a potential unique spatial organisation of GPI-AP. The investigation was only focussed on the mobile part of GPI-AP population, bright (immobile) clusters were avoided during the acquisitions. Figure 28 A shows the apparent homogeneous labelling of the plasma membrane by GPI-SNAP (labelled with

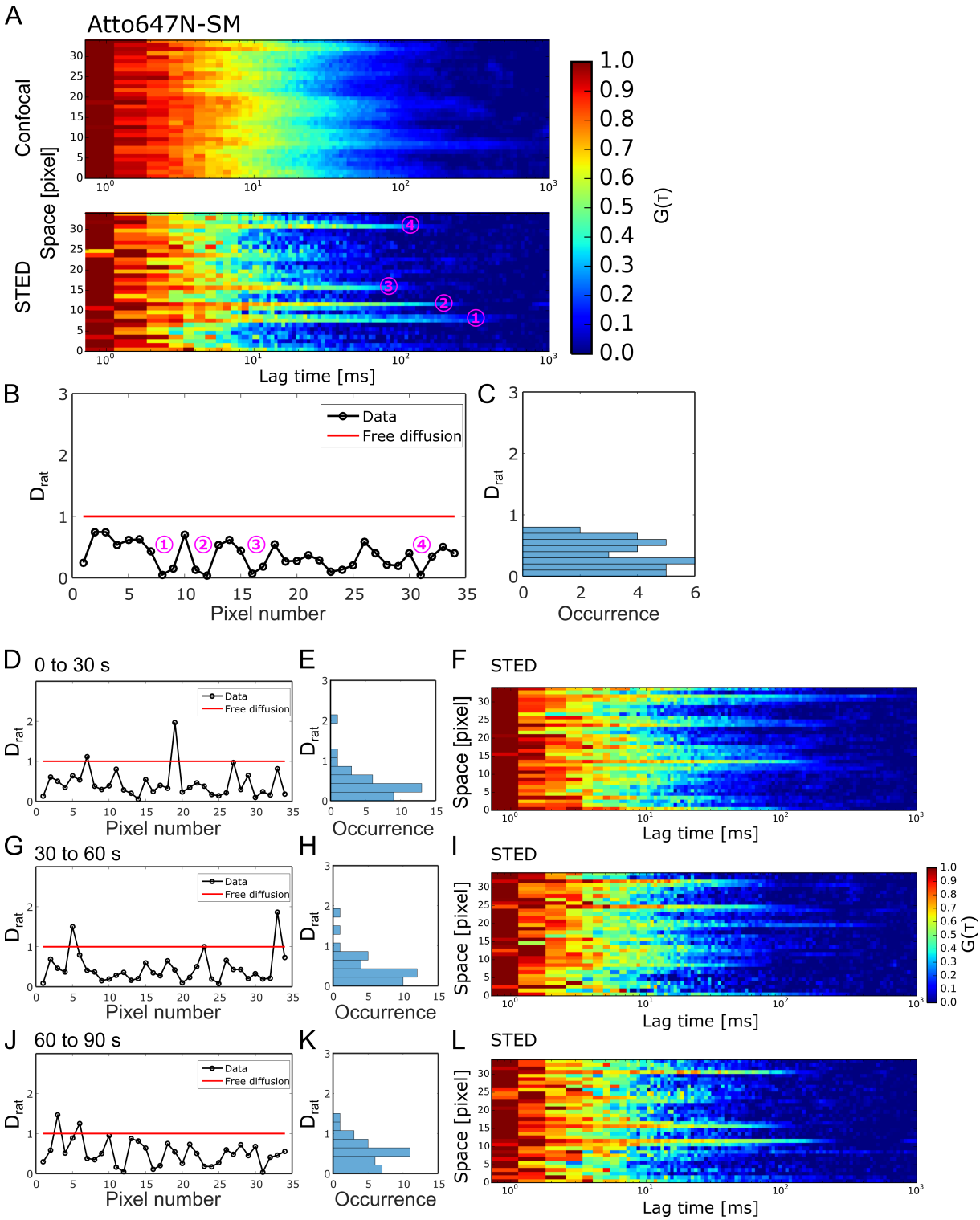


Figure 27: LIESS-FCS measurements on Atto647N-SM diffusion in Ptk2 live cell basal membrane. **A**: LIESS-FCS correlation carpets in confocal and STED (d = 100 nm). **B**: D_{rat}-values over space for the carpets in Panel A. The pink numbers indicate sites of slowed-down diffusion in the STED carpet and corresponding low D_{rat}-values in the plot across space. **C**: D_{rat}-histogram from the measurement in Panel A. (1.36 µm scan acquired for 120 s). **D-L**: Temporal evolution of the trapping sites for SM measured with LIESS-FCS for 30 s intervals. The sites of very low D_{rat} are not spatially constant. D_{rat}-values across space **D,G,J**, corresponding D_{rat}-histograms **E,H,K**, and STED correlation carpets **F,I,L** are shown. Normalised correlation $G(\tau)$ is colour coded as indicated.

KK114-Bg). A few immobile clusters appear across the cell. The correlation carpets in confocal and STED (Figure 28 B) display some spatial heterogeneity in diffusion, which is better assessed by plotting the D_{rat}-values over space. Figure 28 C-J give four examples of different diffusion modes for GPI-SNAP. The most interesting one is plotted in Panels C and D. In this measurement (i.e., in this area of a cell) GPI-SNAP shows a combination of trapping, hopping and free diffusion (in one area smaller than 2 µm given the length of the sFCS line). The occurrence of different types of diffusion of GPI-SNAP at different locations or in different cells was confirmed with more measurements.

Using only one label, it is difficult to elucidate the reason of the differential organisation of GPI-APs. A future project using LIESS-FCS would involve a second label to confirm the presence of certain other structures of interest. The second channel does not necessarily need to be correlated; intensity would provide enough information. One could label cytoskeletal components, use a polarity-sensitive probe, or fluorescently tag possible interaction partners like glycolipids or specific receptors. Such a reference label would enable to more systematically map the spatial distribution of diffusion modes. These are ongoing efforts in the laboratory.

LIESS-FCS enabled to decipher the spatial heterogeneity of the GPI-AP diffusional organisation and revealed an overwhelming complexity. A straightforward way to get an impression of the average diffusion behaviour in a population of cells (or locations) is to histogram the D_{rat}-values from multiple LIESS-FCS measurements (Figure 28 K). Compared to a free diffusion control such as KK114-PEG-Cholesterol (Figure 28 L, see also Figure 26 A-C) a clear shift towards lower D_{rat}-values is observed. The average D_{rat}-values then match up with the pSTED-FCS measurements obtained earlier (see Figure 19 C, F). Thus, LIESS-FCS provides single-cell (single location) and population resolution on the diffusion behaviour. The organisation of GPI-APs has been discussed very heatedly and the reports are rather controversial and even contradicting [224, 231–233]. Possible mechanisms of organisation include homo- and hetero-clustering [233, 234], domain formation or raft incorporation (thus cholesterol and sphingomyelin dependent organisation) [26, 31, 235], and confinement by the actin cytoskeleton [232, 236]. In my view, the modes of organisation of these molecules are not mutually exclusive (i.e., clustering does not

exclude that a proportion of molecules associates as monomers with nano-scale domains) and the findings may just be a matter of how exactly organisation is probed. For example, it is worth noting that by diffusion measurements no local induction of membrane order, as would be expected for raft incorporation, has been observed around GPI-AP inserted by micro-patterning into the plasma membrane of living cells [231]. This is very interesting since the L_o-preference of GPI-APs in GPMVs is well-known and has along with the affinity for DRMs been used to suggest raft-association of GPI-APs [26, 235]. The discrepancy may result from differing GPI-AP constructs or cellular states. Furthermore, it is widely appreciated that local changes in molecular order in the plasma membrane of live cells will be rather minor and are very difficult to detect [5, 51, 237] Thus, the varying reports on mechanisms of organisation may result from varying experimental techniques with different sensitivities, for instance, FCS or FRET, where FCS only reports on mobile particles and FRET only resolves length scales $<$10 nm. The imaging (and FRET studies) suggest immobile actin dependent clusters [233, 234], yet in this work, and also previously, the mobile pool of GPI-APs has been shown to depend on the actin cytoskeleton as well [232]. An additional complicating factor may be the cell types studied (e.g., adherent or suspension), which could show different organisations [31, 224]. A comparative study carefully assessing different GPI-APs in multiple cell types using the available toolkit of fluorescence techniques will help to decipher the GPI-AP organisation in the future. The results presented in this Section, along with the results on the actin cytoskeleton dependent organisation (pSTED-FCS on GPMVs and cells, see Section 5.2.2, Figure 19), add a new piece to the puzzle and allow to clearly appreciate the local heterogeneity in the mobile pool of GPI-APs even within one cell and demonstrates the variability from cell to cell.

5.3.3 Summary LIESS-FCS for Drat imaging

This Section was dedicated to spatially resolving diffusion modes and disclosing possible heterogeneities in space. It is very reassuring that the pSTED-FCS and the spatially resolved LIESS-FCS data give similar results, but provide also complementary insights. pSTED-FCS reveals more detail on the exact nature of the diffusion law (e.g., trapping

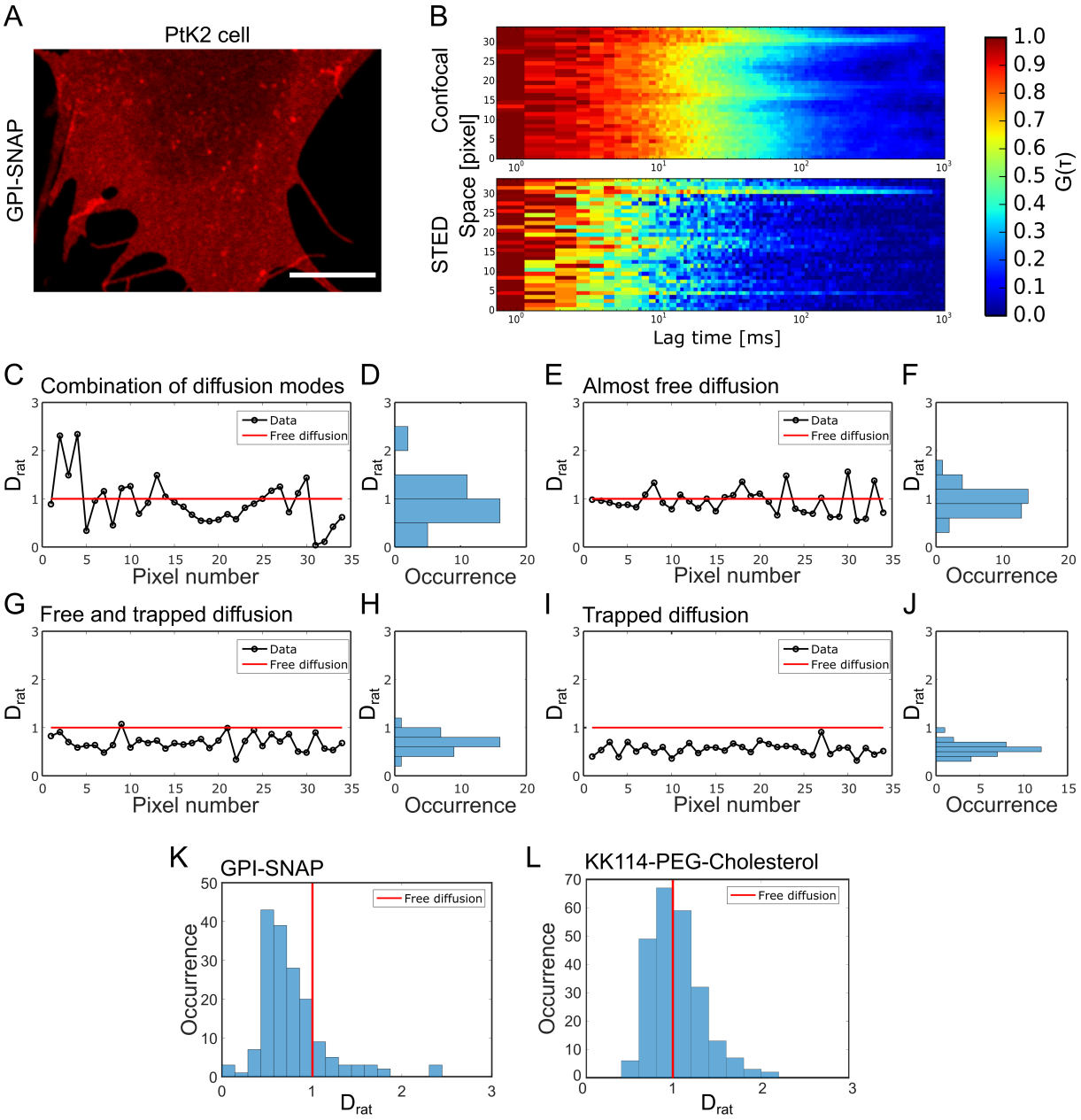


Figure 28: LIESS-FCS reveals diffusional heterogeneity of GPI-APs in space. All measurements were performed on PtK2 cells transfected with GPI-SNAP and labelled with KK114-Bg (SNAP ligand). **A**: Confocal image of the bottom membrane of a labelled PtK2 cell. Scale bar is 10 µm. **B**: Confocal and STED (d = 100 nm) LIESS-FCS correlation carpets. Normalised correlation $G(\tau)$ is colour coded as indicated. **C-J**: LIESS-FCS measurements with D_{rat}-values over space plot (left) and D_{rat}-histogram (right) in four different cells. They represent examples of different diffusion modes, or their combination, across space as labelled. **K**: Histogram of D_{rat}-values from five different LIESS-FCS measurements (red line indicating D_{rat}-value of 1, free diffusion). **L**: Histogram of D_{rat}-values from seven different LIESS-FCS measurements of the free diffusion control, KK114-PEG-Cholesterol (compare Figure 26). The red line indicates D_{rat}-value of 1, free diffusion.

versus domain diffusion), due to the higher temporal resolution compared to scanning based methods. However, the spatial and statistical information from sSTED-FCS measurements prove very useful. Both methods are based on STED microscopy, which can pose a technical limitation to many labs and introduces limitations in labelling. Best STED-FCS performance is obtained with organic far-red emitting dyes like KK114 (commercially available as Abberior STAR Red) or Atto647N, which need to be delivered efficiently to the molecule of interest [14]. Additionally, in STED microscopy the light dose is quite high and may introduce phototoxicity artefacts, which are at least in sSTED-FCS and LIESS-FCS combatted by the fast beam scanning [118, 166]. The next Section will deal with the described issues and introduce a technique based on confocal sFCS (possible on any LSM) to reveal hindrances in diffusion.

5.4 Statistical analysis of confocal sFCS reveals hindered diffusion

A few techniques only can reveal nano-scale diffusion dynamics, and usually require sophisticated equipment. This Section is dedicated to the development and application of a technique using confocal sFCS and its inherent statistics to reveal hindered diffusion dynamics.

The previous Sections described, how super-resolution STED microscopy and spectroscopy can be used to precisely, either with high temporal or spatial resolution, decipher hindered diffusion modes, for example, trapping, domain incorporation or confined (hop) diffusion. Only a limited number of other methods are capable of providing comparable insights, but these are based on plasmonic materials or invasive near-field scanning [169, 171]. Using standard illumination schemes (like widefield or TIRF), only the iMSD analysis can claim for short lag times to obtain sub-diffraction information on the diffusion modes (see [160, 162] and Section 2.2.4). However, the accessible spatio-temporal timescales are still limited by the camera acquisition rates, which could be overcome by fast beam scanning and a smaller field of view [158, 187].

In confocal pFCS, PE and SM, which display the experimental model system for free and hindered trapped diffusion, show a slight difference in diffusion coefficients. The marginally slower diffusion of SM is caused by the trapping events [122]. The simulations on pSTED-FCS also suggested that the introduction of any hindrance causes a decrease in diffusion coefficient (see Figure 20 A). These changes in confocal diffusion may not be obvious from a single pFCS measurement, but taking more data, i.e., getting enough statistics, should allow to obtain further information on the underlying diffusion behaviour of the probes. The scheme in Figure 29 illustrates the envisaged strategy of measuring sFCS in the basal membrane plane: Acquiring large data sets, ignoring any spatial information, correlating the data to gain a multitude of curves and analysing the histograms of the fitted transit times. Any deviations from the expected shape of the distributions would reveal underlying hindered diffusion dynamics.

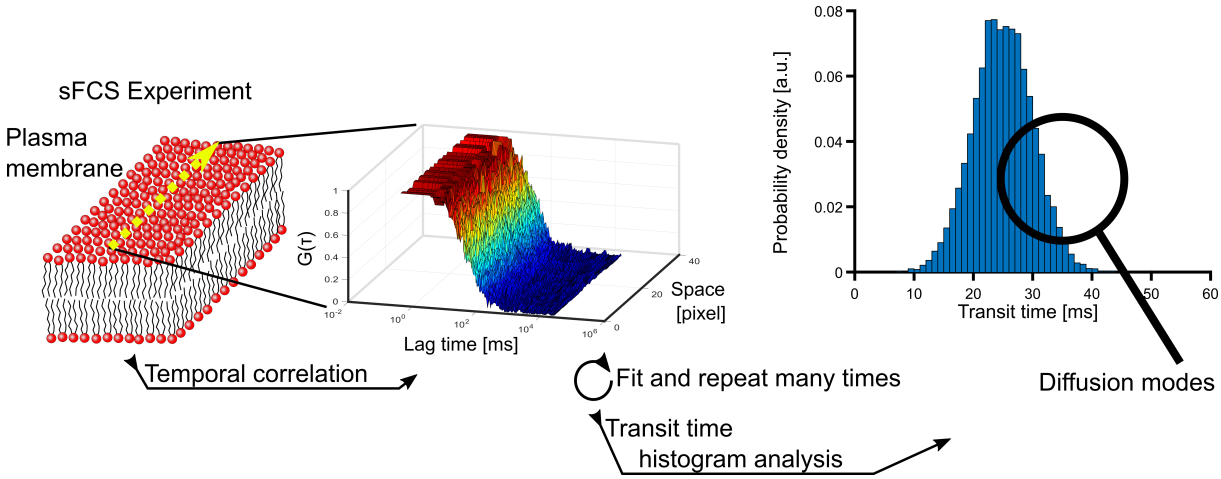


Figure 29: Scheme of the envisioned analysis strategy. A standard sFCS experiment (scanning a line in confocal mode across the membrane, yellow dotted arrow) yields a whole array of correlation curves and respective fitting parameters. Repeating the acquisition many times and creating histograms from the resulting parameters, allows insights into the diffusion behaviour on the population level.

5.4.1 Simulations and sFCS data on free diffusion

The shapes of the transit time histograms were expected to be symmetric (Gaussian) distributions for sFCS experiments on freely diffusing molecules (as depicted in the cartoon in Figure 29). However, experimentally non-symmetric shapes of distributions were observed. To understand the nature of the asymmetric distributions, large sets of Monte Carlo simulations were performed and analysed (in collaboration with Dominic Waithe). Freely moving molecules with varying input transit times were simulated and sampled at different scanning frequencies (Figure 30). Histogramming the resulting transit times yielded, surprisingly, broad and asymmetric distributions, which seemed symmetric on a logarithmic scale (Figure 30 A). Increasing scanning frequency and increasing diffusion coefficient (decreasing transit time plotted) resulted in sharper and more symmetric peaks. The simulations suggested an inherent sampling bias of sFCS, causing the skew and the non-normality of the distributions. The fact that the transit time values can only be positive, that the logarithmic representations appear normally distributed and that the signal-to-noise as well as the fitting error for the single curves increases with the transit time (compare Figure 30 B and C) suggests that the transit time histograms of freely diffusing molecules are lognormally distributed [148, 205]. The lognormal function is a well-known probability distribution function. It is similar to a Normal distribution (Gaussian) and is as well characterised by only two parameters μ and σ. For a Gaus-

sian distribution these parameters are known as the mean and standard deviation. For a lognormal function they are, unfortunately, more difficult to interpret. In sFCS, the increased, non-symmetric error, or bias, of the longer transit times is what causes the skew of the data in linear space and thus the lognormal nature of the data. Therefore, a tail in a transit time distribution does not necessarily report on non-Brownian diffusion or a slow sub-population and is just a property of the (scanning-)FCS measurement.

Accepting the lognormal nature of the transit time histogram data, allowed to develop a fitting approach to precisely recover the distribution parameters μ and σ. For a freely diffusing molecule μ is closely related to the average transit time ($\tau_D = \exp(\mu)$). As the analytical forms of the lognormal probability distribution function are known, the data fitting approach depicted in Figure 31 A was developed for accurate value recovery from experimental data. First, the transit times were histogrammed cumulatively and fitted with the respective cumulative lognormal probability distribution function. Empirically, the cumulative representation was found be very sensitive to deviations. Second, the fitting parameters (μ and σ) from the first fit were taken as input parameters to fit the logarithm of the input data (the so-called logarithmic representation, which should be normally distributed), and only a small variations of 10 - 30 % of the fitting parameters were allowed. Finally, the conventional (so-called linear) representation of the data was fitted with the lognormal function and strong constraints imposed, using the fitted values from the previous representations. Thus, two free fitting parameters were determined with these three fits. Comparing the output from the three fits allows to give an apparent error (standard deviation for the μ-value), which was usually in the range of 10 %. Note that for all cases the respective fit (linear, logarithmic or cumulative) is plotted and not the average of the fits. The residuals indicate that the lognormal probability distribution function represents the simulated histogram well (in this case simulated data of free diffusion sampled with 2018 Hz).

Fitting the large set of simulations from above, allowed to examine the performance of the fitting approach to recover the input value. Figure 31 B shows a scatter plot of simulated input against fitted, output, transit time (meaning recovered from fitting the three representations, exponential μ-value). Over a wide range of transit times and

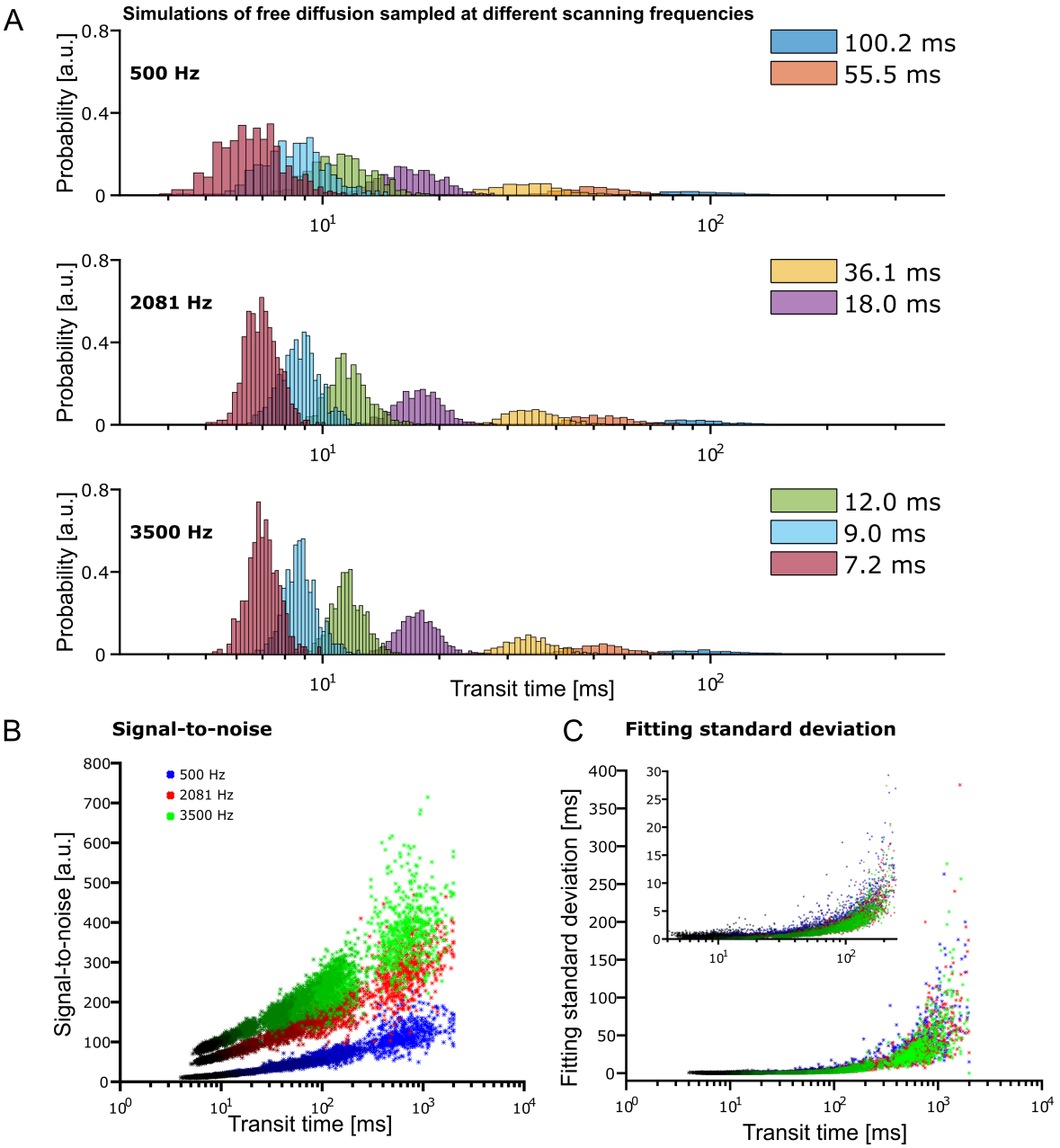


Figure 30: Simulated sFCS data on free diffusion. **A**: Transit time histograms obtained following the strategy in Figure 29. The symmetry, skew, and broadness of the distributions depends on sampling frequency and input transit time. Seven different transit times were simulated (colour coded as indicated), sampled for 30 seconds with sFCS (10 carpets per condition). **B**: Fitting the correlation curves, using the bootstrapping method, also allows to estimate a signal-to-noise value (low being good, high being bad) [148]. **C**: The same fitting approach also yields an approximation of the standard deviations of the transit times. The different shades indicate the different sets of input transit times and the colour indicates the different scanning frequencies: Green = 3500 Hz, red = 2081 Hz and blue 500 Hz.

Table 2: Overview of the simulated diffusion coefficients, D, and corresponding transit times, τ_D, given a simulated observation spot with a FWHM of 200 nm

D $[\frac{\mu m^2}{s}]$	0.01	0.05	0.07	0.13	0.2	0.4	0.6	0.8	1.0
τ_D [ms]	721.3	144.3	100.2	55.5	36.1	18.0	12.0	9.0	7.2

scanning frequencies the correct values could be captured. To get a better grasp on the performance, a value recovery measure was used (see Materials and Methods Section 4.13, where zero means perfect recovery of the input value). The plot of value recovery against different input transit times at three scanning frequencies (Figure 31 C) demonstrates a reasonable performance for the scanning frequencies above 500 Hz and transit times below 1000 ms. The scanning frequency is limiting the minimum lag time and thus, the temporal resolution for fast diffusing molecules. The higher scanning frequencies are beneficial for longer transit times, due to better sampling, but it seems that the value recovery is mostly limited by the overall maximum correlation time. This lag time is given by the acquisition time and dominates (or i.e., limits) the convergence of the single FCS curves (so-called duration noise [148]). Nonetheless, the simulated transit times (or rather diffusion coefficients ranging from 0.01 to 1 $\frac{\mu m^2}{s}$, see Table 2) as well as the scanning frequencies of 500 to 3500 Hz, cover most of the relevant timescale for diffusion in membranes, as well as typical technical specifications of commercially available LSMs.

Next, the analysis was used for "real", experimental, data. As a simple model system for free Brownian motion the diffusion of a fluorescent lipid within SLBs of different compositions was measured. A typical confocal image of an SLB is given in Figure 32 A, which shows a homogeneous bilayer aside from a few vesicular structures, which were avoided for measurements. The fast diffusion of KK114-DPPE in a bilayer, composed of DOPC only, and the comparably slower diffusion within a bilayer, additionally containing cholesterol, could be well described with a lognormal fit in the cumulative (Figure 32 B) and linear (Figure 32 C) representations. The transit time histograms will from now on often be presented in this reduced/simplified representation in which only the midpoint of the bins are plotted to facilitate visual assessment the fitting quality.

The lognormal fit seems to work well for the diffusion data in the bilayers. It is worth mentioning that these type of measurements do not require any special hardware, such as a correlator card on the microscope, and can be readily analysed by software correlation

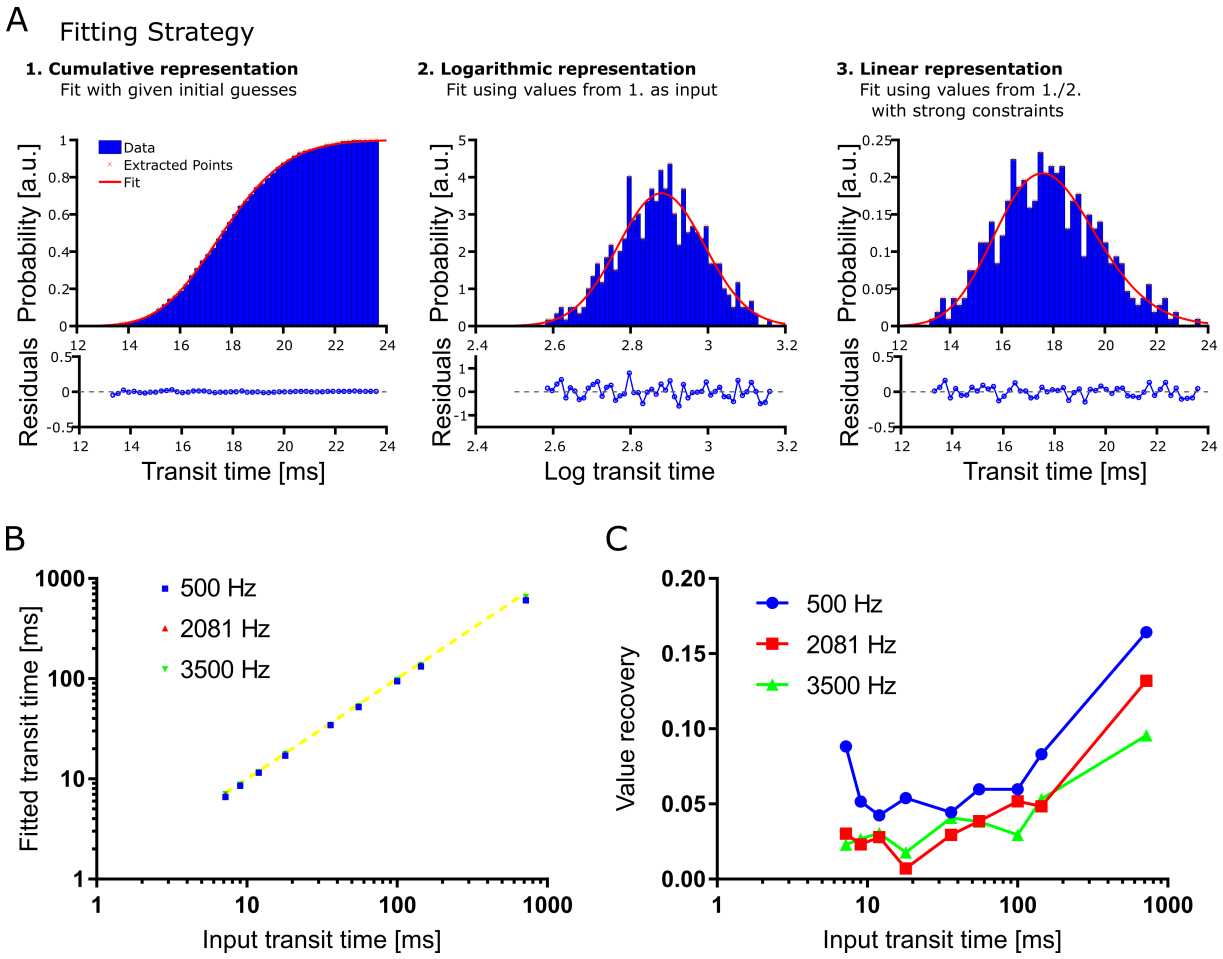


Figure 31: Lognormal fitting strategy and performance. **A**: The employed fitting strategy for freely diffusing molecules exploits three representation of the lognormal function and is demonstrated on simulated data. First the data are histogrammed (blue) and fitted (red) to the midpoints of the bins (orange crosses) in the cumulative representation, then the logarithmic data are histogrammed (obtaining a Gaussian-shaped distribution) and finally, the data are histogrammed and fitted in the linear representation. The normalised residuals (plotted at the bottom) give a first, qualitative, impression of fitting quality. **B**: Scatter plot of recovered transit times from fitting the histograms of the simulated data in Figure 30 A. The yellow line indicates a linear relation ship (i.e., perfect recovery) and is plotted for guidance. **C**: Value recovery (quality measure, see Materials and Methods section 4.13) against input transit time.

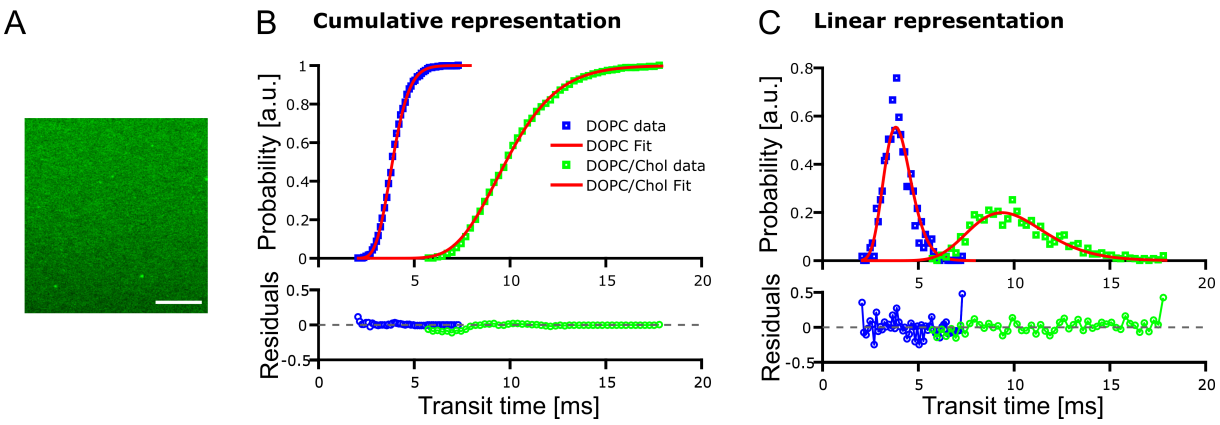


Figure 32: Fitting sFCS diffusion data obtained from measurements on SLBs (either pure DOPC or 50 mol% DOPC / 50 mol% cholesterol, both doped with KK114-DPPE). **A**: Confocal image of a 100 mol% DOPC SLB. Scale bar is 5 µm, which is also about the length of the sFCS line. **B**: Fitting the cumulative histograms (reduced representations) for sFCS data from both membrane compositions. The fit (red) recovers the curve for DOPC (blue) and the mixture with cholesterol (green) accurately. **C**: Fitting the linear histograms (reduced representations) for both SLBs.

of xt-images. That should enable a larger community of researchers to perform diffusion measurements.

5.4.2 Statistical analysis allows for the disclosure of hindered diffusion

The previous paragraphs introduced the analysis scheme for sFCS data on freely diffusing molecules. To exemplify the performance of the pipeline to distinguish between hindered (trapped) and free (Brownian) diffusion, the now well-established cellular model system, the diffusion of SM and PE in the plasma membrane of PtK2 cells, was used. The cumulative and linear representations, in the simplified/reduced form, as well as the corresponding fits with the lognormal models, of an exemplary measurement (i.e, histogram of the sFCS transit times extracted from measurements on >10 different cells) of DPPE diffusion are shown in Figure 33 A and B. The lognormal distribution describes the data in both cases well (according to the normalised residuals plotted in the bottom Panels of Figure 33 A and B). The diffusion data from sFCS measurements on SM were analysed in the same way (Figure 33 C and D). In this case, the lognormal models do not represent the data as well. Especially in the cumulative representation, the residuals display systematic deviations indicating the use of an inappropriate model. The histogram analysis of confocal sFCS data allowed to disclose a difference in the diffusion of PE and SM, which is hardly captured with a single pFCS or sFCS measurement, but has been

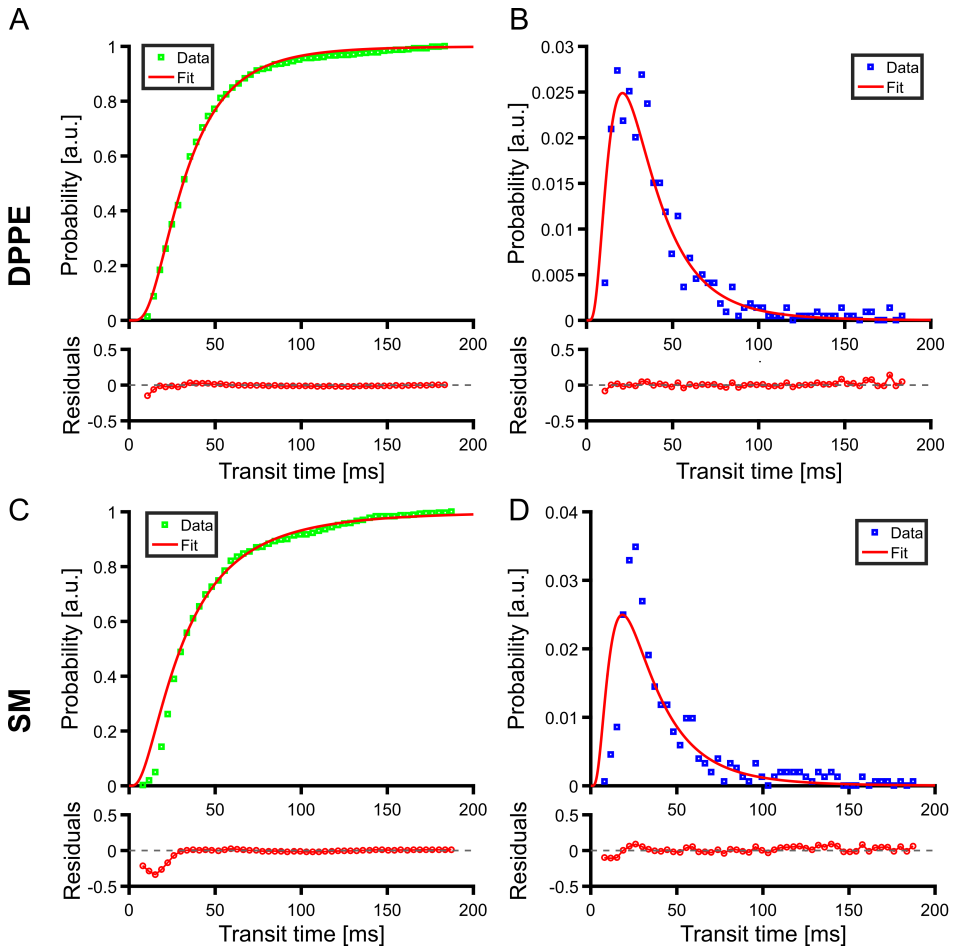


Figure 33: Fitting histograms obtained from sFCS experiments on the bottom membrane of live PtK2 cells at 37 °C labelled with Atto647N-DPPE (DPPE, upper panel) or Atto647N-SM (SM, lower panel) using the developed lognormal approach. **A**: Cumulative fit and histogram for DPPE. **B**: Linear fit and histogram for DPPE. **C**: Cumulative fit and histogram for SM. **D**: Linear fit and histogram for SM. The residuals (red lines plotted under the fitted histograms) represent a qualitative measure for fitting performance. Random fluctuations around zero indicate good fitting, systematic deviations indicate bad fitting, usage of a wrong fitting model.

established before using super-resolution STED-FCS recordings.

Given the results on SM, simulations on trapped diffusion sampled by sFCS were performed to extract the transit times for histogram analysis. Figure 34 A illustrates the employed trapping algorithm (transient complex formation), wherein a molecule at every time step can be trapped or free (and switch between these states with a given probability $p_{trap_on} = p_{trap_off}$). The trapped molecules were virtually immobile (see Materials and Methods section 4.12 for details). A parameter estimation for the trapping/untrapping probability is shown in Figure 34 B. The input diffusion coefficient (confocal, free diffusion coefficient) was 0.8 $\frac{\mu m^2}{s}$. The introduction of hindrance ($p_{trap_on} = p_{trap_off} \neq 0$) reduces the confocal diffusion coefficient notably, but does not automatically cause pronounced trapping, as would be apparent from a low D_{rat}-value (only small trapping probabilities

result in a drop of the D_{rat}-value). Given the parameter estimation, for all simulated trapping data values of $p_{trap_on} = p_{trap_off} \leq 0.001$ have been used, if not stated otherwise. The transient hold of a population of molecules, exploiting statistics from a large number of individual sFCS measurements, should result in a a second (slowly) diffusing component in the histogram analysis.

Trapped diffusion and sampling with sFCS have been simulated for >10 measurements and the resulting transit times were extracted for histogram analysis. Figure 34 C outlines the analysis of the trapped diffusion data in the three representations by fitting a lognormal function as before. Even for this case, with only slight trapping, some deviations from the longnormal fit can be observed. To better describe the data a double lognormal model (dlogN in accordance to single lognormal, slogN) has been employed. It displays the combination of two independent lognormal functions, representing the different timescales, and was fitted in the three representations to the data (Figure 34 D). The gain in fitting quality can be assessed using the Goodness of Fit parameter, which indicates the improvements in all representations, when using the double lognormal model.

The standard for trapped diffusion, experimentally, is the diffusion of SM in PtK2 cells. As described above, the single lognormal model fails in representing the diffusion data of SM accurately. Figure 34 E shows the (reduced) three representation for the SM data again, but fitted with the double lognormal model for trapped diffusion. In all cases, the fits seem to describe the data more convincingly. In the logarithmic representation one can even appreciate the separation of a another timescale as a second, smaller peak. In the linear representation the second component manifests in a larger extent of the skew, which has been indicated for SM before [166].

With these two models and the fitting pipeline at disposal, free and hindered (trapped) diffusion dynamics in the cellular membrane can be readily disclosed without the need for super-resolution microscopy. A problem remains: When is a lognormal fit good enough or when is it justified to choose the more complicated model? As famously depicted a few years ago, an elephant can be fitted with four to five free parameters [238]. Thus, the next Section deals with unbiased model selection.

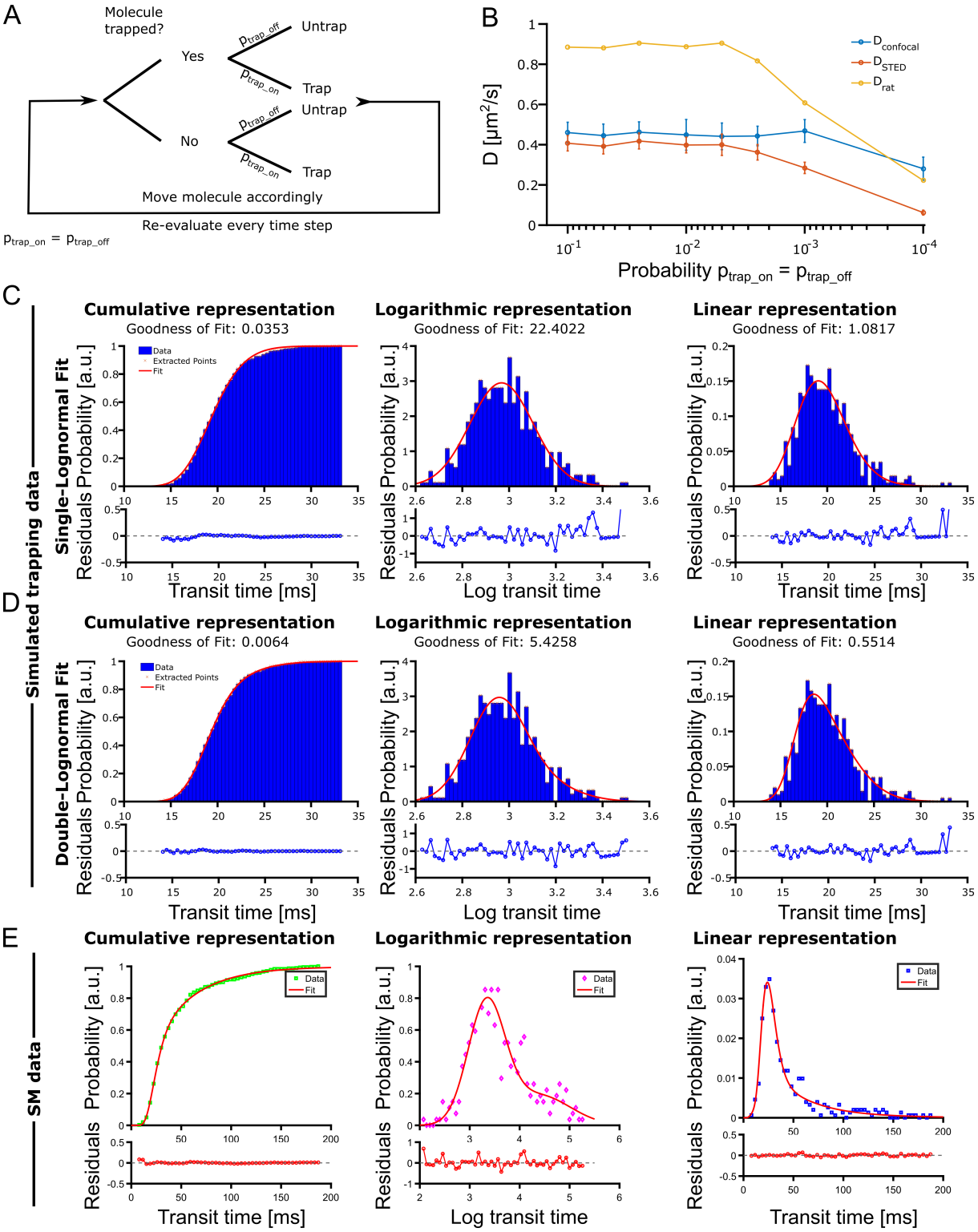


Figure 34: sFCS simulations and experimental data on trapped diffusion can be described with a double lognormal model (dlogN, two component model). **A**: Visualisation of the employed trapping model (same as for pFCS simulations). **B**: Parameter estimation for trapping probability p_{trap_on} and p_{trap_off} by measuring sSTED-FCS (d(confocal) = 240 nm, d(STED) = 80 nm). $D_{rat} < 1$ indicating trapping. **C**: Histogram fitting (cumulative, logarithmic and linear representations) for simulated data with mild trapping ($p_{trap_on} = p_{trap_off} = 0.001$). The normalised residuals, plotted in the bottom panels, indicating (poor) qualitative fitting performance. **D**: Same data as in Panel C but fitted with a double lognormal model Goodness of Fit parameters (top of the plots) represent the fitting quality as given by the residuals in a single value (see Materials and Methods Section 4.13.2). **E**: Experimental sFCS data on SM fitted with a two component (double lognormal) model for hindered trapped diffusion (see Figure 33 for single lognormal fits).

5.4.3 Model selection with Maximum Likelihood Estimation

Model selection is always a challenge when fitting data. The single FCS curves resulting from the sFCS measurements have, thus far, been fitted with the simplest model possible Of course, given sufficient signal-to-noise, one could also select different models.

For identifying hindered trapped diffusion in the histogram analysis, the Bayesian Information Criterion (BIC) was used to facilitate model selection. The fitting (in the three representations) was completely uncoupled from the model selection, to reduce bias from binning and normalisation. Consequently, the BIC was not calculated from the residuals, but rahter obtained from a Maximum Likelihood Estimation (MLE). Noteworthy, the BIC calculation applies a penalty for a higher number of free fitting parameters. Meaning, when data can be fitted equally well with two different models, the one with fewer free parameters would be preferred. From the BIC the Relative Likelihood value (RL value) was calculated, which is 1 for the most likely model (see Materials and Methods Section 4.13 for details).

The model selection process is exemplified in Figure 35 A and B for simulated single lognormal and double lognormal data, respectively. The data were generated by randomly sampling from the probability distribution functions and then analysed with the MLE routine. Figure 35 A shows an example of single lognormal data and the MLE for Gaussian, single lognormal and double lognormal models. The normal distribution (Gauss, orange line in Figure 35 A) does not fit the data. Both lognormal models describe the data equally well (slogN, yellow line, and dlogN, dashed purple line, in Figure 35 A), but due to the higher number of free parameters in the more complicated model, the RL values (i.e., the model selection) suggest the single lognormal model as most likely (RL value = 1). In contrast, the data generated from the double lognormal probability distribution function is described better with the more complicated model and the model selection favours clearly the double lognormal model (RL value = 1 for dLogN, Figure 35 B). The second component is apparent as pronounced broadening of the tail of the distribution. The MLE also yields "fitting parameters" (so-called estimators $\hat{\mu}$ and $\hat{\sigma}$) for the μ and σ values. They should be close to the values from the fitting procedure and can serve as values for initialisation and quality control.

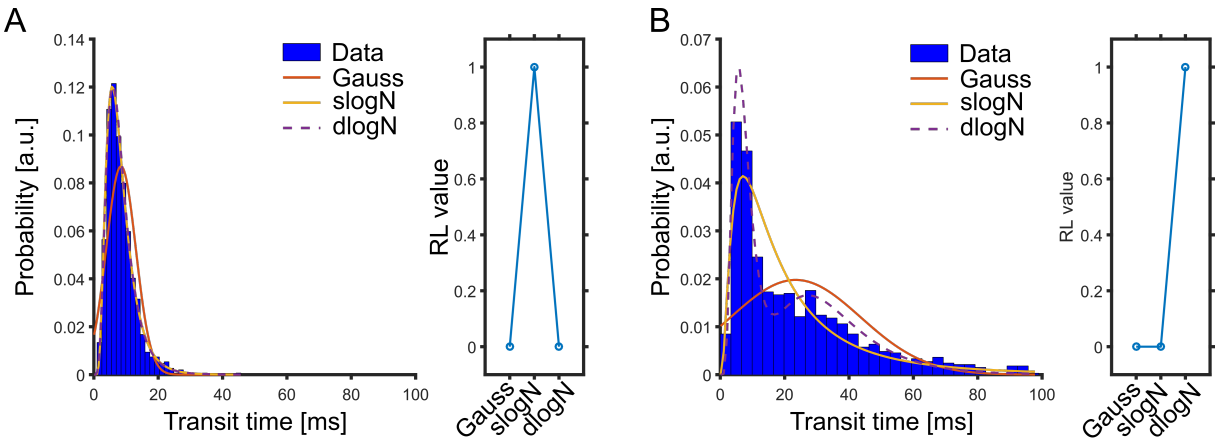


Figure 35: Calculating the relative likelihood (RL) value for model selection. **A**: Linear representation of random data generated from a single lognormal distribution function with $\mu = 2.0$ and $\sigma = 0.5$. The data were approximated using MLE with a Gauss (orange line), single lognormal (yellow line) and double lognormal (dashed purple line) model. An RL value of 1 represents the most likely model given the data. Notably, the normal (Gaussian) probability distribution function was included as well but does not fit the data. **B**: Linear representation and MLE of random data generated from a double lognormal probability distribution function (with $\mu_1 = 2.0$, $\sigma_1 = 0.5$, $\mu_2 = 3.5$, $\sigma_2 = 0.5$ and B = 0.5). The RL values indicate that the double lognormal model represents the data best.

The model selection seemed to work robustly on simulated data, thus all the experimental data from the previous Section were evaluated with this method. Figure 36 shows the model selection for the SLBs and the live cell data. For the SLBs with and without cholesterol (Figure 36 A) the distributions do not appear skewed, but the model selections clearly suggest the single lognormal model (over Gaussian serving as random data control). Thus, free diffusion in the model membranes was confirmed.

The same procedure was applied to the sFCS data on PE and SM diffusing in the plasma membrane of Ptk2 cells (Figure 36 B). For the phospholipid single lognormal, free diffusion, is identified as most likely model, whereas for the sphingolipid hindered diffusion is favoured. Together with the fitting strategy of the three representations, these results suggest that it is possible to reliably identify hindered diffusion based on large confocal sFCS data sets. Obviously, to decipher the diffusion modes in more detail (e.g., trapping versus domain incorporation), STED-FCS is still the method of choice.

5.4.4 Applications of the sFCS analysis pipeline

Confocal sFCS (and the statistical analysis) can readily be applied to any dye or fluorescent protein, as long as it is bright enough to obtain sFCS data. It can, for example,

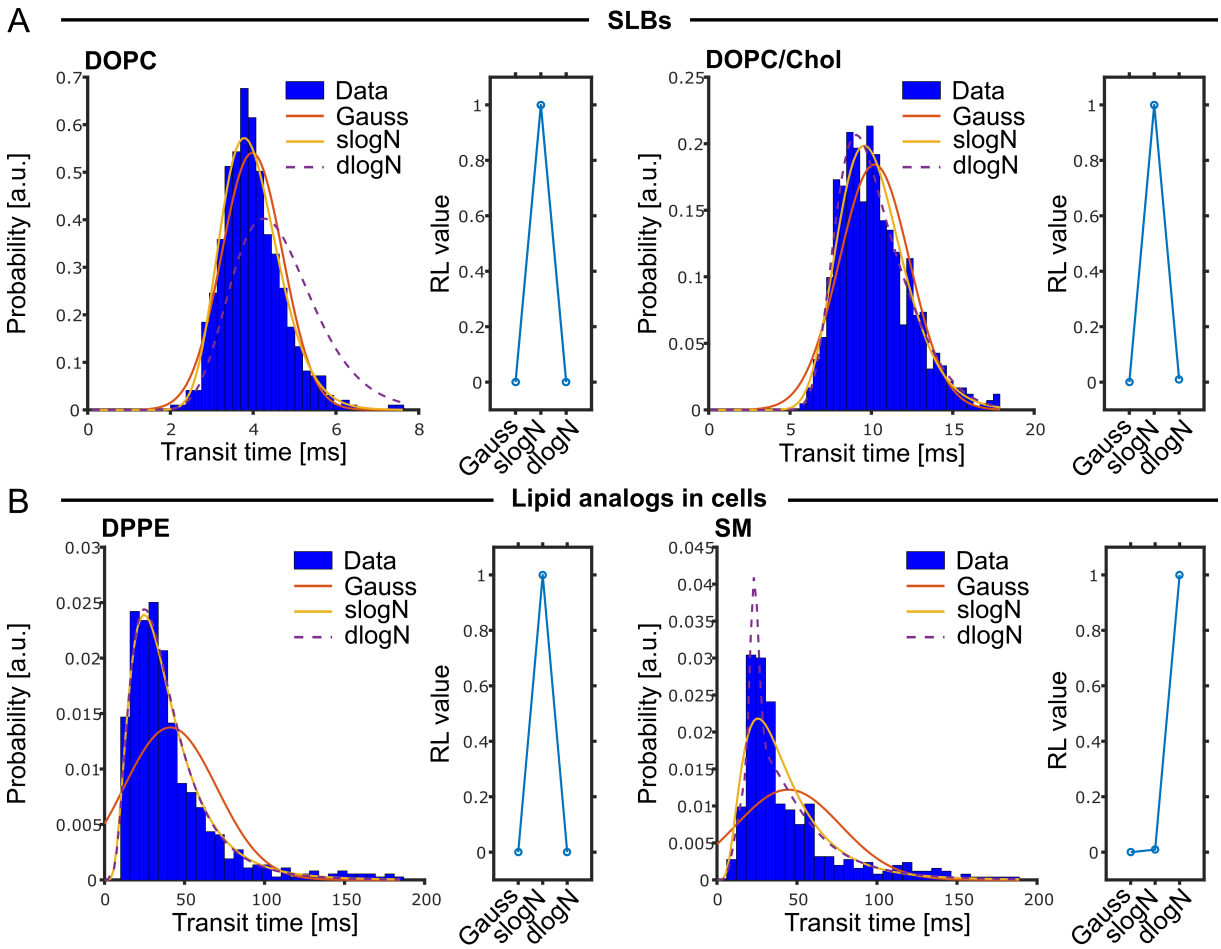


Figure 36: Calculating the most likely model for the aforementioned samples. **A**: Model selection for sFCS measurements on SLBs composed of DOPC (100 %, left, or plus 50 mol% cholesterol, right). In both cases, the free diffusion model (single lognorm, slogN) is the most likely (determined by an RL value of 1). Compare to the fits in Figure 32. **B**: Model selection for sFCS measurements on lipid analogs in PtK2 cell plasma membranes (compare fits in Figure 33 and Figure 34). Free diffusion is indicated by favouring the slogN model. Hindered, trapped diffusion indicated by favouring the dlogN model.

be used to complement findings from STED-FCS experiments. A few such examples of applications will be given in this Section to validate previous results. The workflow was always similar and highlights the applicability of the method to various systems of different complexities. First, sFCS recordings in multiple cells (>10) were acquired, the sFCS data were fitted, subjected to model selection, and the sFCS transit time histogram analysed statistically with the most likely model. This allowed to disclose diffusion modes and to obtain the diffusion timescale(s).

As a first example the diffusion of GPI-APs is revisited. In Section 5.2.2 (see Figure 19) and Section 5.3.2 (see Figure 28) their diffusion was investigated with an artificial GPI-AP, GPI- SNAP (labelled with KK114-Bg), and an actual GPI-AP, GPI-LYPD6-mCherry, which needed to be labelled with an Atto647N-tagged nanobody to enable depletion for STED-FCS. For the sFCS measurements and the statistical analysis, instead, a GPI-anchored eGFP was used. The resulting transit times were histogrammed and analysed with the pipeline presented in the previous Section. First, model selection using MLE was performed, then the three representations were fitted.

Figure 37 A shows the model selection for sFCS data on GPI-eGFP diffusion in the basal membrane of PtK2 cells at 37°C. The RL value suggests the use of a hindered diffusion model. Thus, the data were fitted with the double lognormal model. In Figure 37 B and C the cumulative and linear representations and fits are plotted, respectively. The residuals for the double lognormal fit (red) are given in the bottom panels and for comparison the residuals from a fit with a single lognormal is included as well (magenta residuals). From the fits or fitting residuals the deviation from free diffusion is not obvious, which demonstrates the strength of the independent model selection process (compare the magenta residuals in Figure 37 B and C). The observed hindrance and comparably fast diffusion of the GPI-AP is in accordance with the previously presented data (see for example Figure 15 B and Figure 19 and [201, 232]).

Reusing the approach from Section 5.2.2, also the diffusion mode in actin-free GPMVs was evaluated by statistical analysis of sFCS data. In contrast to the STED-FCS measurements, which were performed with an oil-immersion objective, the sFCS measurements in this Section employ a high-NA water-immersion objective and thus were not limited

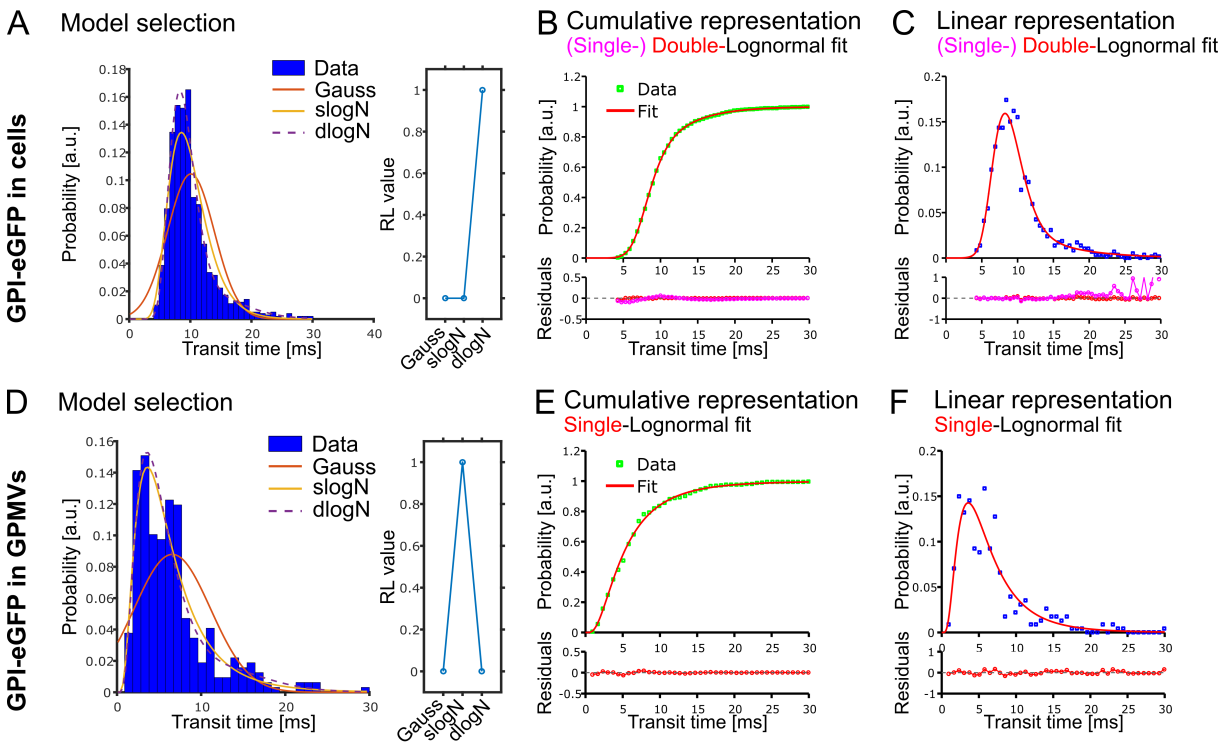


Figure 37: Statistical analysis of sFCS data in live PtK2 cells transfected with GPI-eGFP (upper panel) and in GPMVs derived thereof (lower panel). **A**: Model selection based on MLE and RL value for diffusion of GPI-eGFP in the basal membrane of living PtK2 cells at 37 °C. **B**: Fitting the cumulative representation with single lognormal model (magenta residuals) and double lognormal model (red residuals, preferred model according to RL value). **C**: Fitting the linear representation with single lognormal model (magenta residuals) and double lognormal model (red residuals, preferred model according to RL value). **D**: Model selection based on MLE and RL value for data recorded in the top membrane of immobilised GPMVs produced from Ptk2 cells transfected with GPI-eGFP. **E**: Fitting the cumulative representation with single lognormal model (red residuals, preferred model according to RL value). **F**: Fitting the linear representation with single lognormal model (red residuals, preferred mocel according to RL value).

to the basal plane of the GPMVs. Figure 37 D shows the model selection for GPI-eGFP diffusion data in the top membrane of PtK2 GPMVs suggesting free diffusion. The fitting of the different representations is presented in Figure 37 E and F. The free, but compared with lipid analogs slow diffusion in the GPMVs (diffusion coefficient of 1.5 $\frac{\mu m^2}{s}$), is again in accordance with the STED-FCS data from before (Figure 19). With sFCS and the statistical analysis pipeline, the free diffusion of GPI-AP in GPMVs versus the hindered diffusion in the live cell membrane could be confirmed independently of STED nanoscopy .

STED-FCS, employing Atto647N as a label for a variety of lipids, has revealed a large heterogeneity in the plasma membrane of living cells [14, 122, 159]. Using the exact same lipid analogs, the diffusion behaviours of, for example, PE and SM, have been confirmed

with other sophisticated techniques like NSOM-FCS or plasmonic nanoantennas [169, 171]. However, Atto647N is known to be a very hydrophobic and sticky dye, which changes also the phase partitioning behaviour of the probed lipid [51, 168]. Thus, now not limited by the compatibility of a dye with STED, the diffusion behaviour of the standard sample, PE and SM in the basal plasma membrane, were investigated for probes tagged with the bright and green emitting fluorophore TopFluor (TF, also termed Bodipy). Figure 38 A shows the model selection and Figure 38 B and C the respective fits for TF-DPPE diffusion data in the basal membrane of CHO cells. The diffusion of this lipid analog was in accordance with the Atto647N based data identified as diffusing freely in the plasma membrane of CHO cells. Furthermore, the model selection (Figure 38 D) and the respective fits (Figure 38 E and F) suggest that TF-SM undergoes a different type of diffusion behaviour. The hindered, trapped diffusion model describes the data well, also in accordance with the Atto647N based data. TF-SM seems to undergo nano-scale interactions in the cellular plasma membrane. This is a good example of demonstrating probe independent behaviour. The free and trapped diffusion of the two lipids seems to be independent of the dye. It should be stressed again that the statistical analysis cannot reveal the same detail as dedicated STED experiments, but it can surely provide complementary insights.

The diffusion of GM1 in immobilised GPMVs displays another example of revisiting STED-FCS data from before. In cells, it has been shown that GM1 undergoes domain type diffusion (see section 5.2.2 and [159]). Furthermore, in GPMVs some hindrance in diffusion remained for GM1, different from all other investigated probes (see Figure 18). GM1 has a large headgroup (multiple sugars in addition to the dye, Atto647N) and the diffusion law has been measured in the bottom membrane of immobilised GPMVs. The reason for that was the requirement of the oil-immersion STED objective at the time. Interactions with the coverslip could not be ruled out entirely as a reason for the observed hindrance in diffusion. Thus, it was an interesting control to revisit its diffusion behaviour in the top membrane of PtK2 GPMVs, which were immobilised in the very same way, but measured by confocal sFCS with a water-immersion objective far away from the coverslip surface.

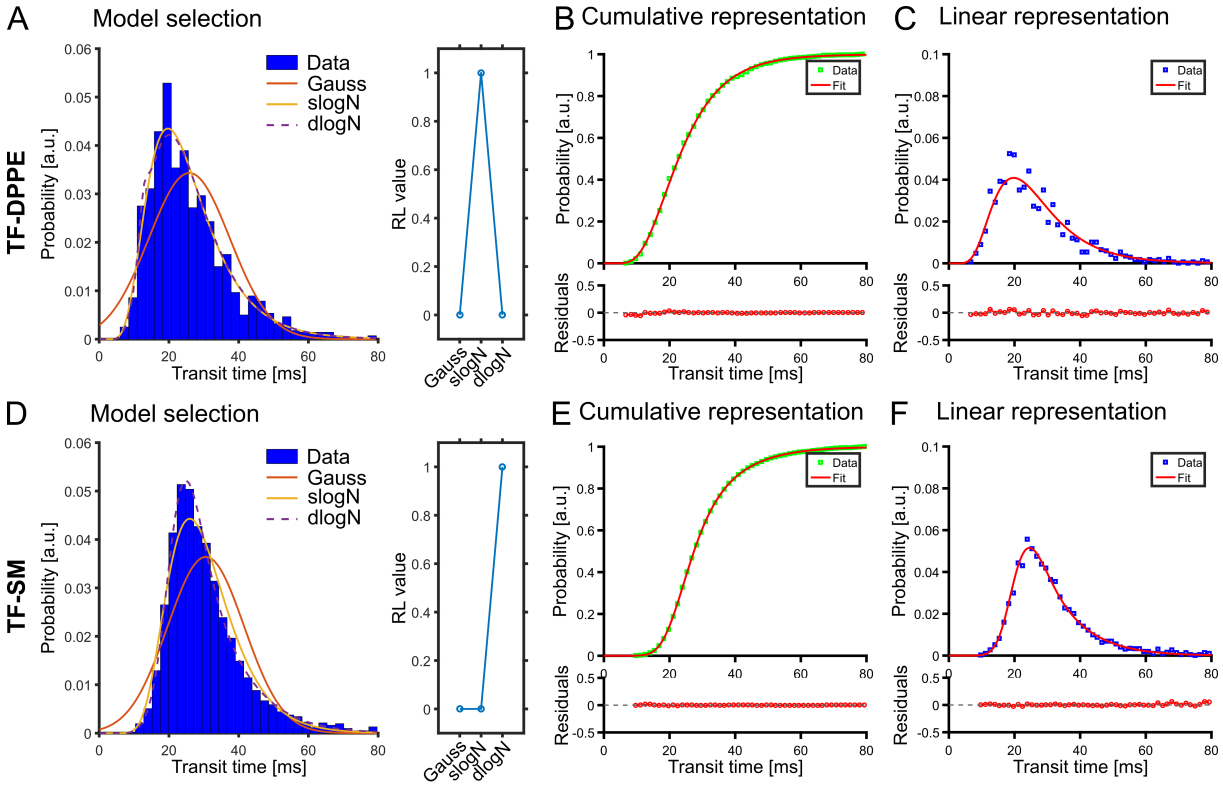


Figure 38: Statistical analysis of sFCS data acquired on the bottom membranes of live PtK2 cells labelled with TopFluor (TF) lipid analogs (upper panel TF-PE, lower panel TF-SM). **A**: Model selection based on MLE and RL value for the TF-DPPE live cell sFCS data. **B**: Fitting the cumulative representation (green) with single lognormal model (red line and residuals, preferred model according to RL value). **C**: Fitting the linear representation (blue) with single lognormal model (red line and residuals, preferred model according to RL value). **D**: Model selection based on MLE and RL value for TF-SM diffusing in the basal membrane of live PtK2 cells. **E**: Fitting the cumulative representation (green) with double lognormal model (red line and residuals, preferred model according to RL value). **F**: Fitting the linear representation (blue) with double lognormal model (red line and residuals, preferred model according to RL value). Shown are pooled data from three independent experiments (on different days).

As before, Atto647N-DPPE (DPPE or PE) in Ptk2 GPMVs has been used as a control for free diffusion. Figure 39 A and B are confocal images of the mid plane and top plane of an exemplary GPMV labelled with Atto647N-DPPE. The fluorescence in the mid plane is not homogeneous due to a polarisation effect (photoselection) of the employed microscope [54]. The intensity is very homogeneous in the top plane of the GPMV. Acquiring sFCS data for multiple GPMVs allows for the calculation of the transit time histograms, and model selection suggests free diffusion of DPPE (Figure 39 C). Notably, in this case there is a small probability that the double lognormal model could fit the data, too (elevated point in the RL plot). This could be due to focussing issues (as even the immobilised GPMVs wiggle in axial direction, which caused difficulties for the comparably long sFCS acquisitions).

Confocal images of mid and top plane of PtK2 GPMVs labelled with GM1 are shown in Figure 39 D and F, and display the same photoselection effect in the equatorial plane and apparent homogeneous distribution of the dye in the top membrane. Nonetheless, when performing the analysis of large sFCS data sets, the model selection suggests that GM1 undergoes some hindrances in the GPMVs, which confirms the findings from STED-FCS. However, the sFCS analysis cannot discriminate between domain incorporation and trapping, it only reveals hindrance The GM1 data were taken in the top membrane, therefore, excluding any effects or artefacts from the probe interacting with the coverslip surface.

This Section demonstrates the power of the sFCS analysis, since it does not require special dyes (as STED) and has no requirement for specific optics or objectives (given that they are high-grade enough to perform FCS experiments). It also allows for a straightforward comparison of the data obtained with different dyes.

5.4.5 Further considerations for sFCS experiments

The presented statistical analysis can be of great value for the identification of hindered diffusion, but also for sFCS experiments, in general, to determine diffusion times accurately. Measuring changes in the diffusion across samples or conditions is wide-spread practise. Yet, evaluating differences and indicating a statistical significance can be chal-

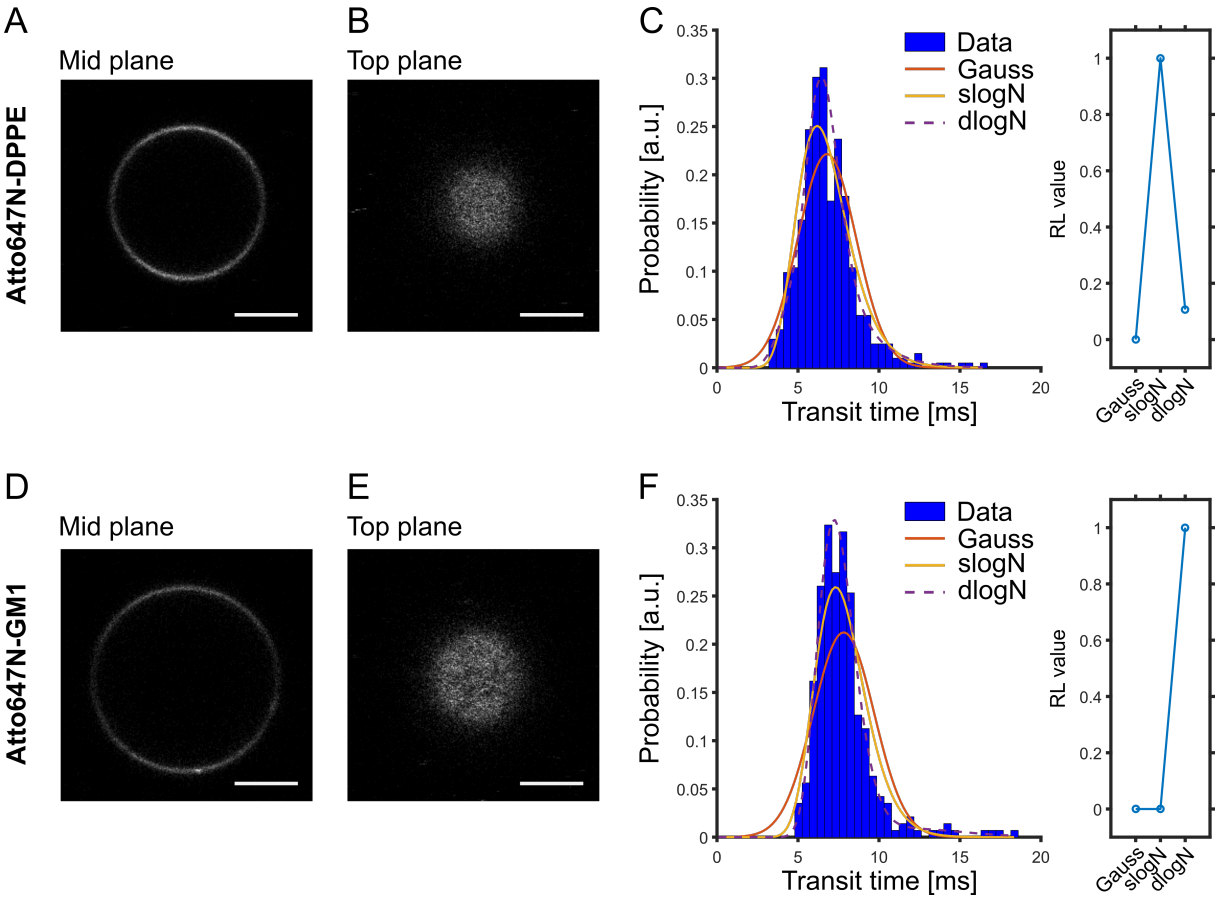


Figure 39: Statistical analysis of sFCS data on DPPE (top panel) and GM1 (bottom panel) in the top membrane of immobilised PtK2 GPMVs. Both lipid analogs were headgroup labelled with Atto647N. **A**: Confocal image of the mid plane of a GPMV labelled with DPPE. **B**: Confocal image of the top plane of a GPMV labelled with DPPE. **C**: Model selection with MLE reveals free diffusion (slogN as most likely model) for DPPE diffusion in the top membrane of PtK2 GPMVs. **D**: Confocal image of the mid plane of a GPMV labelled with GM1. **E**: Confocal image of the top plane of a GPMV labelled with GM1. **F**: Model selection with MLE reveals hindered diffusion (dlogN as most likely model) for GM1 diffusion in the top membrane of PtK2 GPMVs. All scale bars are 5 µm.

lenging due to the non-normal distribution of the data, meaning that the usage of a standard t-test is not appropriate. The Kolmogorov–Smirnov test allows for the unbiased (it makes no assumption on underlying distribution) assessment, but can be problematic due to the large sample size in sFCS experiments, since it could overestimate noise as significant differences between samples. A way to circumvent that could be to perform the statistical analysis for three or more sets of individual data recordings (e.g., from different days), and compare the fitted parameters (μ and σ) using standard statistics (i.e., t-test, see an example in Section 5.5.2 , Figure 48 F).

Assessing a mixture of two types of diffusion with sFCS is possible, but care needs to be taken in interpretation. The observed processes need to separate well in time. The trapping (transient halts) causes a very pronounced slow-down and the apparent diffusion coefficient (calculable from the μ_2-value) does not necessarily have a physical meaning. For two freely diffusing components, which are close in diffusion coefficient, the statistical analysis does not disclose a second population. This limitation is exemplified in Figure 40. Free diffusion of particles with a diffusion coefficient of 0.3 $\frac{\mu m^2}{s}$ and 0.07 $\frac{\mu m^2}{s}$ (24 ms and 103 ms transit time, respectively, given a FWHM of 200 nm) has been simulated. The relative abundance of the fast component was changed from 0.7 (Figure 40 A) to 0.5 (Figure 40 B). The histogram shifts according to more molecules diffusing slower, but the shape remains lognormal. In both cases, the model selection suggests free diffusion. The raw sFCS curves were fitted with a one component model as the sFCS carpet and the curves do not require the use of a more complicated model, given that the residuals show no systematic deviations (Figure 40 C and D). It is a well known issue in FCS that diffusion coefficients need to be orders of magnitude apart to allow distinction [126]. For these type of problems sFCS is probably not suited, as also the signal-to-noise of the single curves is worse than in pFCS. This is just caused by less photons at every single pixel in comparison to a pFCS measurement with the same acquisition time. This phenomenon has been discussed in depth in Section 5.1.1. The acquisition time for the sFCS measurements could, of course, be increased, but is often limited by the manufacturer of the LSM. Thus, for this type of question or separation of diffusion timescales a long pFCS measurement (and fit of the correlation curve with a two-component model) seems more suitable.

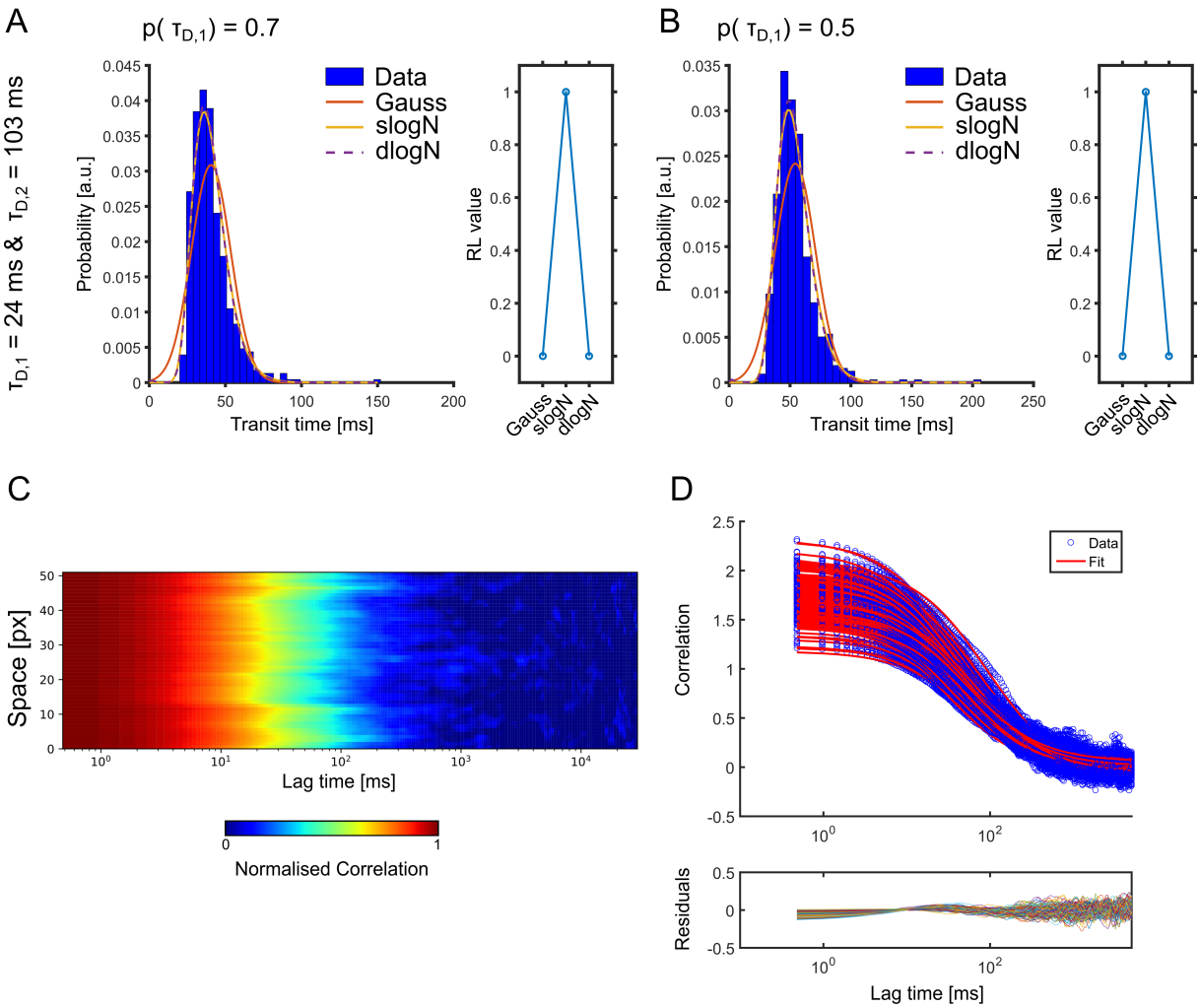


Figure 40: Statistical analysis of simulated sFCS data sets with two populations of freely diffusing molecules at a ratio of p = 0.7 or 0.5 (upper panel, input transit times of 24 ms and 103 ms, as diffusion coefficients 0.3 $\frac{\mu m^2}{s}$ and 0.07 $\frac{\mu m^2}{s}$, respectively). **A**: Model selection (MLE) for simulated data with a fraction of p = 0.7 fast diffusing molecules (23 ms). Most likely model is free diffusion, median transit time is shifted to 36.6 ms. **B**: Model selection (MLE) for simulated data with a fraction of p = 0.5 fast diffusing molecules (23 ms). Most likely model is free diffusion, median transit time is shifted to 50.5 ms. **C**: Exemplary correlation carpet with p = 0.5. Normalised correlation colour coded as indicated. **D**: Correlation curves (blue circles) and FCS fits using a single component model and respective residuals (below).

Another mechanism, which may cause sufficient separation in time of diffusive processes, is the so-called confined or hop diffusion. It is a result of molecules being constrained within a meshwork. The long range diffusion shows pronounced slow-downs, but inside the meshwork the diffusion is fast. As the cellular meshworks (like the actin cytoskeleton, which is most likely responsible for the hop diffusion, see section 5.2.2 and [36]) are not homogeneous in space, sFCS could gather enough data to reveal a fast diffusing population. In confocal sFCS experiments that would only work given that the mesh size is not too far below the diffraction limit. To evaluate if sFCS and the histogram analysis can in principle reveal hop diffusion, Monte Carlo simulations were employed. Random meshes were generated using Voronoi transformed random seeds and particles allowed to diffuse within the given mesh (characterised by the mesh size parameter L). When hitting a boundary, the particles were only allowed to pass on to another compartment with a certain probability of p_{hop}, otherwise they reside in the same compartment. Figure 41 A illustrates a spatial hop map with a small fraction of molecular trajectory in a typical simulation set-up. As mentioned before the presence and detectability of hopping depends on the parameters L and p_{hop}. Hence, a parameter estimation with sSTED-FCS was performed to find a suitable combination. As expected from previous simulations, the obtained confocal diffusion coefficients (Figure 41 B) drop with the introduction of hindrance (for a hopping probability of 1 and varying mesh size they stay constant around the input parameter of 0.2 $\frac{\mu m^2}{s}$). The simulated data were sampled in LIESS-FCS mode to also calculate the average D_{rat}-values given in Figure 41 C. Strikingly, the parameter estimation revealed only a narrow range in which hoping could be observed with sSTED-FCS. For too low p_{hop} and very small L, the D_{rat}-values indicate trapping. This could be explained by the fact that very small compartments, which the molecules cannot leave, can act as a domains or in extreme cases as a sites of trapping. After selection of promising parameters (red dot indicated in Figure 41 C) dedicated, longer sFCS measurements were simulated. Some single FCS curves showed a long and a short component in the autocorrelation decay and were, consequently, fitted with a two-component model. Hence, the data pre-processing needed to be adapted and was different from the data presented before (see Materials and Methods Section 4.13; briefly a contribution of a second component in the ACF fits

was allowed). Histogramming the pooled data revealed an additional short component. To describe the hop diffusion data histogram statistically, a combination of the lognormal probability distribution function and the exponential probability distribution function was used (and abbreviated logNExp). The MLE model selection and the fitting in the three representations were implemented as before and demonstrated that the trapping model (dlogN) could not describe the data, whereas the new dlogNExp model describes the data well and allows for the identification of hopping (Figure 41 D and E). The dlogNExp approach is admittedly preliminary and needs more investigation, especially in the presence of experimental noise or using a dynamic meshwork (allowing for actin turnover). However, overall, these simulations indicate the potential of the expansion of the presented statistical analysis of transit times to another diffusion mode.

Performing sFCS measurements and extracting the diffusion dynamics can yield further insights into the membrane organisation. However, fluctuation data from sFCS recordings provide an additional variety of complementary information such as the number of particles, the anomaly factor or the brightness (interchangeably used with counts per molecule, cpm). These other parameters can easily be calculated from the same data and could be included in the statistical analysis to add more details.

A first attempt to include the cpms into the analysis is presented in Figure 42 for the comparison of TopFluor (TF) labelled phospholipid (PE) and cholesterol. Figure 42 A shows the linear transit time histograms from sFCS measurements of both probes in the plasma membrane of CHO cells. The histogram for TF-cholesterol is shifted to the left, indicating faster diffusion compared to TF-DPPE, which may be surprising as both molecules should experience the same membrane environment. Additionally, cholesterol is bigger or bulkier in its structure (note that data from pFCS have been presented in Figure 15 and fast diffusion of cholesterol has been reported before [228]). The cause of the difference in diffusion could be manifold. For example, the molecules could have affinities for different membrane environments or have differential localisation within the membrane plane. To rule out an effect of membrane composition, the cell diffusion data could be compared to model systems. By extracting and histogramming the brightness (cpm) from the sFCS measurements an interesting observation occurred. Despite cholesterol and PE

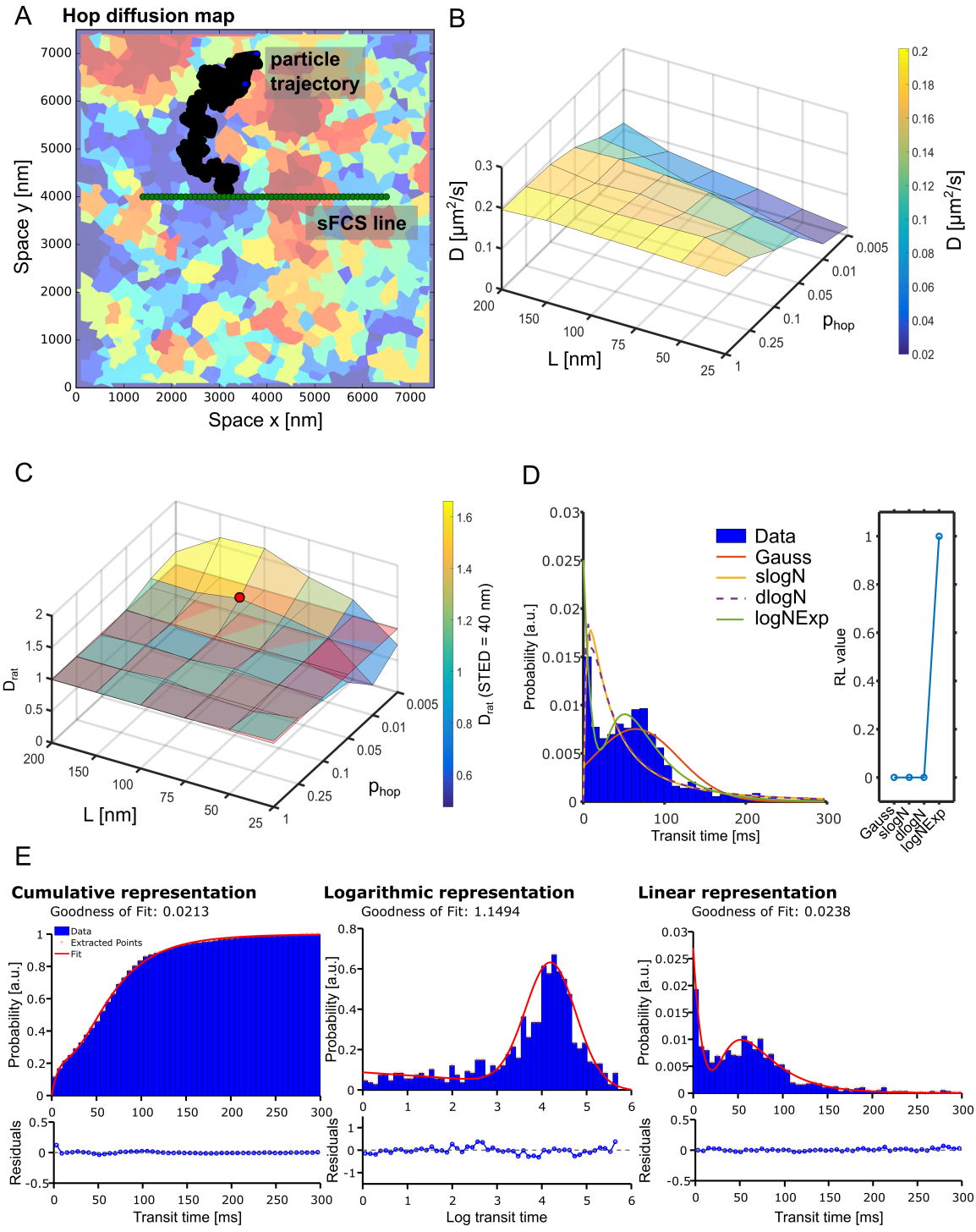


Figure 41: Statistical analysis of sFCS data on hindered hop diffusion. **A**: Simulated hop diffusion map (coloured areas) with short exemplary track (black) and sFCS line in green. **B**: sFCS diffusion coefficient in confocal mode for a parameter estimation of the hopping probability p_{hop} and the mesh size parameter L (4 simulated carpets per condition, 30 s sampling time, input diffusion coefficient was 0.2 $\frac{\mu m^2}{s}$). **C**: Parameter estimation from Panel B but showing the change in D_{rat}-value for STED (FWHM = 40 nm) . The red plane indicates $D_{rat} = 1$, free diffusion. The red dot indicates the parameters used to simulate 10 measurements with 45 seconds acquisition time. **D**: MLE and model selection via RL value including the new model for hindered hop diffusion (combination of lognormal and exponential probability distribution functions, logNExp). **E**: Fitting the three representations of the simulated data with the logNExp model.

being labelled with the same dye, cholesterol yields a much broader distribution of cpms, suggesting that a proportion of molecules emits more photons than others (Figure 42 B). This could be a hint that the orientation of the dyes is very different for PE and cholesterol, meaning that the location of the molecules could differ. This is very interesting, since the dye in both cases should be buried within the hydrophobic core of the membrane, as DPPE is labelled at the acyl chain. A possible explanation may be flipping of the orientation of TF-Chol. In one case the dye could be exposed to the hydrophobic core (similar to TF-DPPE) in the other case it could be exposed to the hydrophilic surrounding medium, which may change its emission properties. The energetic costs for burying the dye or the hydroxyl-group of cholesterol within the bilayer may be similar. Alternatively, such a change of local environment for the dye could also be explained by the bobbing mechanism, where cholesterol shifts up and down the bilayer without reorientation of the whole molecule [221]. Higher brightness may of course result from oligomerisation, but that would be counter intuitive with a faster diffusion.

To check if the fast diffusion is an effect of the cellular plasma membrane environment, the same analysis on transit times and brightness has been performed on SLBs and GUVs (Figure 42 C, D and E, F respectively). The faster diffusion of cholesterol compared to DPPE seems to prevail in the model systems, meaning it is not caused by the cellular environment (i.e., plasma membrane composition, interactions with proteins etc.). The differences in brightness distribution also remain unchanged. Reassuringly, the brightnesses between the different systems line up, excluding environment effects on the cpms (e.g., salt or pH dependence of the quantum yield). It should be noted that the diffusion of cholesterol in GUVs (containing 50 mol% of cholesterol) was found to be very fast and almost at the temporal resolution limit of sFCS. The analysis of sFCS fitting parameters such as number of molecules, brightness and transit time could be combined. The comparison between TF-DPPE and TF-Cholesterol gives only one example, which demonstrates the power of a potential extended histogram analysis.

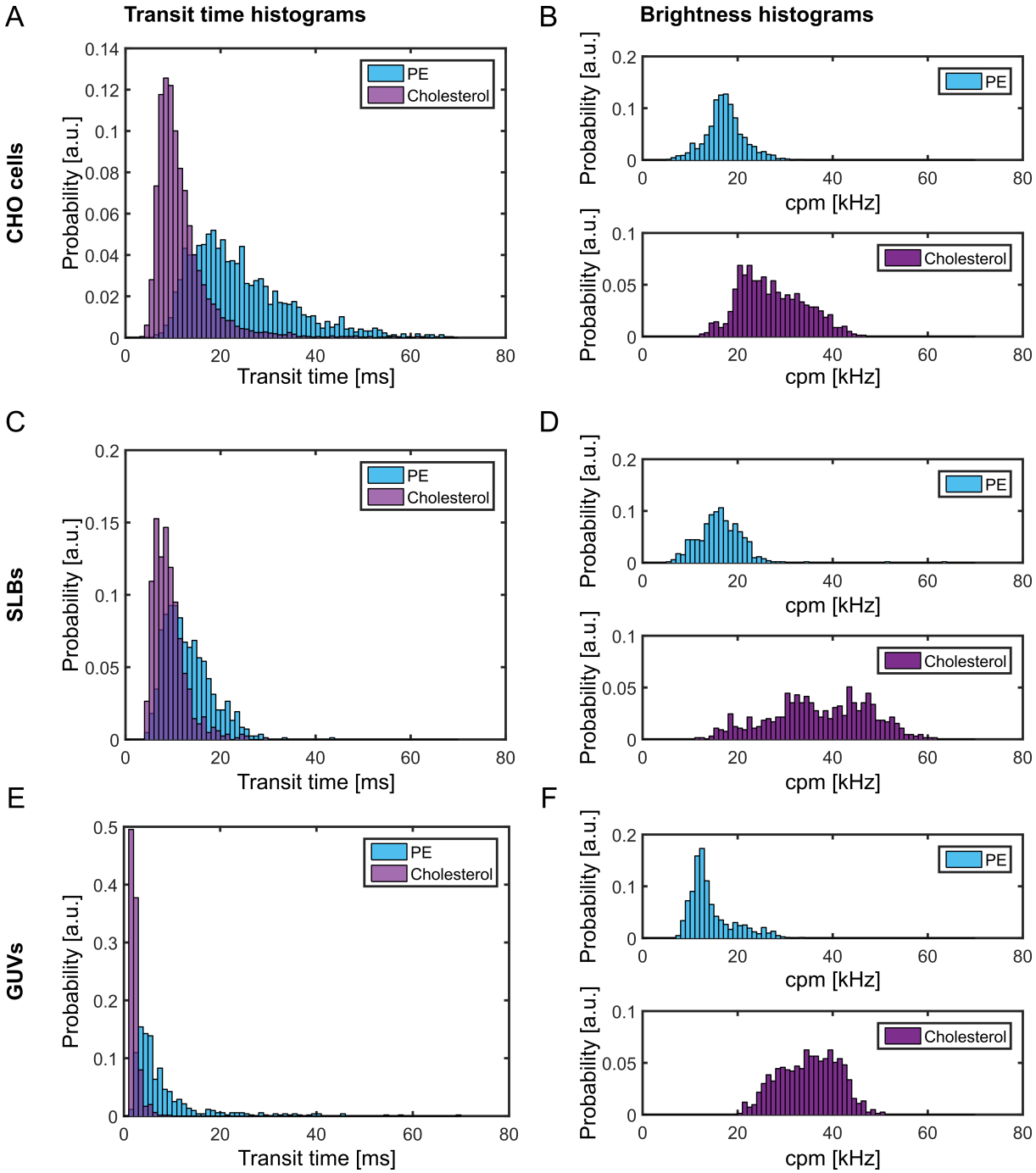


Figure 42: Expanding the histogram analysis to include brightness (counts per molecule, cpm) for the comparison of the organisation of TF-DPPE (PE, blue) and TF-Cholesterol (Cholesterol, magenta) in the basal membrane of CHO cells, SLBs (DOPC with 50 mol% cholesterol) and GUVs (DOPC with 50 mol% cholesterol). **A**: Linear transit time histograms of TF-Cholesterol and TF-DPPE diffusing in the basal membrane of CHO cells. **B**: Counts per molecule (brightness) histogram for TF-DPPE (top) and TF-Cholesterol (bottom). The cpm are obtained from the same sFCS measurement. **C**: Linear transit time histogram of TF-Cholesterol and TF-DPPE diffusing in an artificial membrane, SLB. **D**: Counts per molecule (brightness) histograms in SLBs for DPPE (top) and Cholesterol (bottom) . **E**: Linear transit time histogram of TF-Cholesterol and TF-DPPE diffusing in the bottom membrane of GUVs. **F**: Counts per molecule (brightness) histogram for the sFCS data on TF-DPPE and TF-Cholesterol in GUVs.

5.4.6 Summary sFCS statistical analysis

The developed statistical analysis of sFCS data, including the model selection and fitting in three representations, enables the precise disclosure of the average diffusion time for a freely diffusing molecule and allows to reveal hindrance in diffusion. The combination with the analysis of other parameters such as molecular brightness is promising. The sFCS analysis allowed to confirm the diffusion modes for SM and PE using a different label, validated the free diffusion of GPI-AP in GPMVs and disclosed the hindered diffusion of GM1 in the top membrane of GPMVs. Thus, it served convincingly as complementary approach to STED-FCS using only a standard LSM and elaborate data analysis. More work needs to be done to understand mathematically the origin of the lognormal appearance of the tranist time histograms. A comprehensive mathematical model would allow to give a physical meaning to the σ parameter and would be especially convenient for the analysis of hindered diffusion, where currently the fitting parameters are very difficult to interpret. This is ongoing work and considering sFCS experiments as a special case of the multiplicative central limit theorem, seems a promising approach [239]. Once the closed forms of the distributions would be derived, one should be able to extract further information from the sFCS measurements.

5.5 Applications in immune signalling

Investigating the organisation of the plasma membrane is a demanding task. The previous Sections added new tools and approaches to facilitate more advanced and detailed measurements and microscopy studies. In the final part of the Results, I present some preliminary applications to T cells and immune signalling. Such measurements are technically challenging due to the high sensitivity of T cells to their environment and their constant reshaping of the actin cytoskeleton [76, 240]. However, elucidating membrane dynamics in T cells will improve our understanding of the adaptive immune system. The GPMVs, LIESS-FCS and the statistical analysis of sFCS data were used as a remedy with the overall aim to shine a new light on the organisation of the Src-kinase Lck comparing resting and activating T cells. Lck is the main kinase of T cells and plays a crucial role in T-cell activation [9]. Yet, its nano-scale distribution and diffusion dynamics remain unclear. The existence of Lck clusters, their increase upon activation and the raft association of Lck as well as possible functional implications have been proposed. Pre-organisation and activity of Lck in the resting state is heavily debated and may also reflect that commonly used conditions for studying the resting state are actually inducing activation [12, 83, 84, 240].

In this study, a hydrogel suspension method is presented and was used as resting condition throughout and contrasted with anti-TCR antibody-coated coverslips as activating condition. Additionally, GPMVs were used to differentiate active from passive processes as well as to add a thermodynamic equilibrium state to the analysis. This Section exemplifies, how my developed techniques introduced throughout the Results chapter, can help elucidate the dynamic organisation of Lck, how this organisation may report on change in cellular state and how biological complexity can drive method development.

5.5.1 The quest for a resting state

The definition of what a resting cell is depends of course on the definition of activation. In this work, TCR triggering visualised as calcium signalling and changes in morphology (such as cell spreading) are considered as markers of activation. Cells interacting with an antibody (OKT3) coated surface of a coverslip served as condition for activating state [240]. The T cells (suspension cells) were dropped on the surface and measured for the

first minutes of interaction with the surface (i.e., while undergoing activation). OKT3 is an antibody binding the CD3 protein complex of the TCR and causing T-cell activation [241]. Traditionally, PLL-coated surfaces are used as inert/non-activating surfaces (not only in Immunology, but also all across cell biology), but it has recently been reported that PLL-coated coverslips cause T-cell triggering (and change the diffusion dynamics) [240, 242]. These studies suggest that suspending the cells in a hydrogel (away from any surface) would keep them in a resting state, which would be in accordance with the kinetic segregation model for T-cell activation, where a surface can result in ligand-independent TCR triggering (see [13, 64] and Section 2.1.3).

The preparation of cell-hydrogel suspension samples and the investigation by microscopy are challenging due to the chemical nature of the hydrogel and the steady slow sinking of the cells through the gel. Measuring the diffusion dynamics in T cells would be more convenient on a surface (in a still and stationary system). Adherent cells like CHO or Ptk2 cells, which were used earlier, were easier to handle compared to the suspension cells. Additionally, the micron-thick gel may introduce different sorts of optical aberrations due to air bubbles, inhomogeneities or optical properties of the material. Thus, many alternative resting states were assessed and are briefly outlined here. T-cell activation was routinely checked using calcium signalling as a reporter on TCR triggering. Based on the fluorescence increase of a calcium sensitive dye (Fluo4) activation can be inferred. In addition, cell morphology (spreading) was utilised as an indicator of the cellular state (compare Figure 43 A and B as examples). For all tested surfaces such as coating the coverslip with PLL, BSA, PEG, lipid bilayers or fibronectin, initial calcium flashing when the cells approached the surface or shortly after was observed. Also commercially available coverslips coated with a thin hydrogel layer caused the cells to activate.

As surfaces seemed to cause the artefactual activation of T cells, more biophysical approaches were considered. An acousto-optical levitation (provided by LUMICKS) and optical tweezing (provided by Ionovation) were tested. The trial with the optical tweezers poses as an example for all the tested conditions (such as surfaces or acousto-optical levitation) in which T cells would activate (Figure 43). However, T-cell spreading (like on the coverslip surfaces, Figure 43 A) was not observed when trapping either Jurkat or

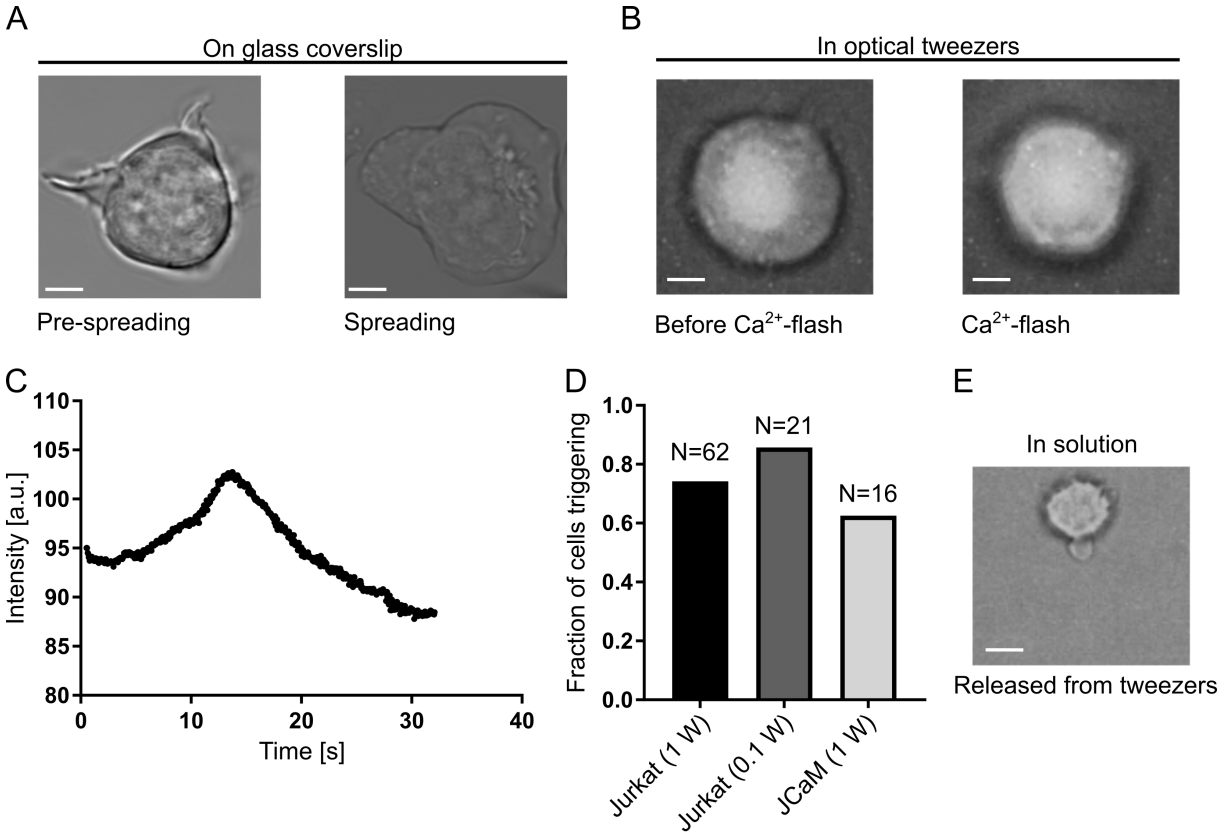


Figure 43: Morphology and calcium imaging as markers of T-cell activation in the context of optical tweezing. **A**: Bright-field image of a JCaM T cell activating on a glass coverslip. Before activation (left) the cell shows a round shape. During activation (right) the cell undergoes pronounced morphological changes and shows spreading. All scale bars are 5 µm. **B**: Bright-field images overlaid with Fluo4 signal for calcium imaging of a Jurkat T cell immobilised with optical tweezers. The cell only shows weak fluorescence right after trapping (left), but the fluorescence intensity increases a few seconds later (right) indicating calcium release and thus triggering. **C**: Exemplary intensity trace for calcium release in a Jurkat T cell immobilised using optical tweezers. The intensity rises after about 10 s in the trap revealing triggering. **D**: Quantification of the preliminary optical tweezing experiments. Jurkat cells (at different trapping laser powers) and JCaM T cells activate (calcium flash) upon trapping with the infrared laser. The numbers indicate individual cells from multiple experiments over the course of three days. **E**: Bright-field image of a Jurkat T cell released from the optical trap after 220 s. The cell clearly shows blebbing as a sign of apoptosis which might indicate phototoxicity of the optical trap.

JCaM cells in optical tweezers (Figure 43 B). Jurkat cells represent a model for standard T cells, whereas JCaM cells are lacking Lck and were initially chosen as a negative control and as a system for reconstitution with Lck-eGFP. This strategy enabled to match the expression levels of Lck-eGFP with the endogenous expression levels in wild type Jurkat cells. For both cell types only seconds after activating the tweezer laser, calcium release was observed, indicating triggering and activation. An exemplary time trace for a Jurkat cell is plotted in Figure 43 C. The intensity change arises from the fluorogenic dye Fluo4 binding to intracellular calcium. The calcium levels were sustained for a few seconds and then dropped beyond background levels, which can be attributed to bleaching or leaking of the dye. Jurkat and JCaM T cells were tested for calcium triggering upon variation in trapping laser power. However, in all tested conditions a calcium response in a considerable fraction of the cells was observed. (Figure 43 D). It is noteworthy that a lot of cells did not seem to survive the optical tweezing procedure. Figure 43 E shows a cell released from the optical trap floating in the surrounding medium. The shape of the cell is ill-defined and it blebbed off a large vesicle. These are signs of apoptosis and demonstrate that the use of the optical tweezers to keep the live T cells stationary is without further optimisation not appropriate. To assess this more in detail a dye indicating DNA damage or apoptosis could be used. A possible explanation for the reaction may be heating up of the cell as temperature increases of about 1.45 °C/100 mW infrared laser power have been reported [243]. In any case, optical tweezing as an alternative method to keep the T cells in a resting state was dismissed. To investigate these cells in a resting state the hydrogel remained the method of choice.

5.5.2 Elucidating diffusion dynamics in T cells

Measuring and understanding Lck diffusion dynamics in resting and activating T cells may help to shine a new light on the organising principles of this crucial molecule. Initially, pFCS and pSTED-FCS measurements were intended to provide further insights, but for this type of study labelling of Lck with an organic dye would be crucial. For this purpose Lck was tagged with a SNAP-tag and visualised with the cell-permeable Silicon-Rhodamine (SiR) fluorophore tagged with a SNAP-ligand (SiR-Bg, Figure 44 A). SiR was

the preferred dye, as to the best of my knowledge, it is the best live-cell-permeable dye available compatible with STED-FCS (and far-red depletion). Imaging JCaM cells with reconstituted Lck-SNAP (labelled with SiR) revealed a large fraction of the dye bound to Lck in the cytoplasm (or free dye which could not be removed by washing). Comparing the intensities between cytoplasm and membrane gave barely any contrast (Figure 44 B). This resulted in a problem when performing pSTED-FCS experiments, as the not-depleted background fluorescence from molecules in the cytoplasm in 2D-STED-FCS greatly reduces the amplitude and the signal-to-noise of the autocorrelation curves [163, 182, 184]. Furthermore, the confocal FCS curves in Figure 44 C exemplify the complicated dynamics, high variability and noise in the Lck-SNAP measurements. They also give a notion for the complex dynamics and the resulting difficulties in choosing models as well as the high number of fitting parameters involved. The curves require a fit accounting for at least three timescales (triplet state, fast 3D diffusion and slower 2D diffusion). Additional variability in the curves seemed to be a result of the exact position of the recording within the cell. To systematically assess changes in such a system turned out to be extremely challenging. To overcome these issues, sFCS was employed. Loss in temporal resolution proved beneficial for these measurements, as fast dynamics (such as the cytoplasmic fraction or the triplet state) were not captured by sFCS. Also sFCS was only minimally affected by background fluorescence since it mainly affects shorter lag times.

As a proof of principle experiment for measurements on super-resolved dynamics on immune cells, the diffusion mode of KK114-PEG-Cholesterol in the plasma membrane of T cells spreading on PLL-coated coverslips was determined. The previously developed LIESS-FCS approach was applied to JCaM cells labelled with the cholesterol analog. Fast spreading of the cell could be observed, and the plasma membrane labelling worked comparably well to the adherent cells described earlier (Figure 45 A). LIESS-FCS measurements were performed and revealed free diffusion of this probe in the plasma membrane of a cell activating on a PLL-coated surface (see exemplary LIESS-FCS plot in Figure 45 B and C).

The LIESS-FCS measurements were enabled by the bright and photo-stable organic dye KK114. Data of similar quality could not be obtained for Lck-SNAP (using SiR)

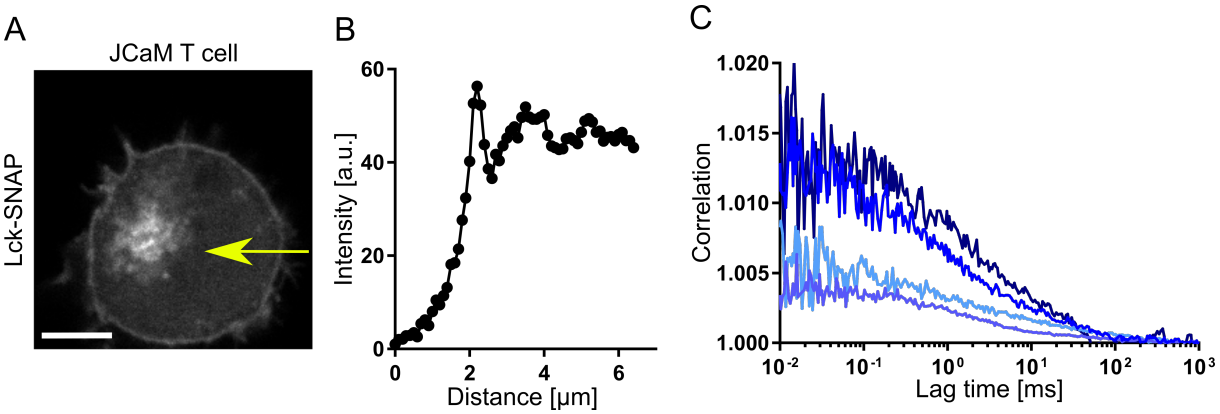


Figure 44: Labelling and FCS measurements of Lck-SNAP (tagged with SiR). **A**: Confocal image of a JCaM T cell with reconstituted Lck-SNAP, which was labelled with cell permeable SiR-Bg. The yellow arrow indicates the section for the line profile in Panel B. Scale bar is 5 µm. **B**: Line profile on the yellow arrow in Panel A. **C**: Exemplary pFCS curves (confocal) of Lck-SNAP labelled with SiR (bottom membrane of a JCaM cell spreading on PLL-coated coverslip). The curves show varying amplitudes and signal-to-noise ratios depending on labelling efficiency and expression levels. The autocorrelation decays show at least three timescales (e.g., triplet state, cytoplasmic and membrane diffusion).

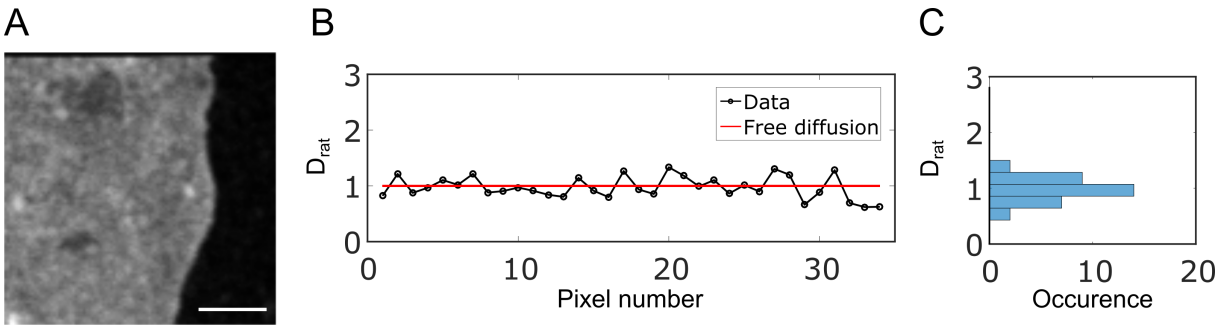


Figure 45: LIESS-FCS on JCaM T cells labelled with KK114-PEG-Cholesterol. **A**: Confocal image of the basal membrane of a JCaM T cell spreading on a PLL-coated coverslip. Besides from a few internalised vesicles the fluorescence appears homogeneous. Note that the JCaM T cell was reconstituted with Lck-eGFP (not shown). Scale bar is 2.5 µm. **B**: LIESS-FCS measurement of KK114-PEG-Cholesterol in JCaM plasma membrane. D_{rat}-values over space. **C**: D_{rat}-histogram for the measurement in Panel B. Measurements were acquired at 1.4 kHz per channel, for 120 s.

neither in the resting nor activating conditions probably due to inferior labelling efficiency and comparably poor performance of SiR. The LIESS-FCS measurements using an oil-immersion objective on T cells on a PLL coated coverslip worked well, but, as outlined above, PLL could not be used as resting condition. For the hydrogel suspension a STED microscope equipped with suitable water-immersion objective was required, which was not available by the time of the study.

To measure the diffusion dynamics of Lck in resting and activating conditions, these caveats were overcome by employing the statistical analysis of sFCS data. Measurements of Lck-eGFP in JCaM T cells suspended in hydrogel could be recorded using a conventional LSM and a water-immersion objective. The cells were measured >10 µm above the coverslip. Already by imaging, morphological differences between the activating (OKT3-coated surface) and resting (hydrogel suspension) condition could be observed. The cells in the suspension experience contact with any stiff surface and appeared not flat but rather round (Figure 46 A, compare also with the round cells in the optical tweezers Figure 43 B). For JCaM and Jurkat cells in culture, i.e., in the culture flask, healthy cells often show an aggregated phenotype. As the tissue culture condition is considered resting, it is reassuring that the same phenotype was also found for cells suspended in hydrogel (Figure 46 B). For no other tested condition such a phenotype has been observed. Usually, when cells interact with a surface they spread (and activate) as previously indicated in Figure 43 A and Figure 46 C. The Lck-eGFP molecule distributed visually almost homogeneously in the membrane. Due to the morphological differences between the resting and activating state (Figure 46 A, B and C) it can be appreciated that just imaging is not sufficient to shed light on the Lck organisation and heterogeneity.

Following the procedure presented in the previous Results section, sFCS data were recorded for Lck-eGFP in the live cell membrane in resting and activating condition. The data were first subjected to model selection and then fitted with the most likely model. The MLE suggested a single lognormal distribution, i.e., free diffusion, as the best model for diffusion data of Lck-eGFP in JCaM cells suspended in hydrogel (Figure 46 D). The data were fitted accordingly (cumulative and logarithmic representation shown in Figure 46 E and F). The fit yielded a μ-value of 3.9 resulting in an average transit time of 47.5 ms

(±1.5 ms, corresponding to a diffusion coefficient of about 0.15 $\frac{\mu m^2}{s}$ at 37 °C), which is surprisingly slow for a freely diffusing lipid-anchored molecule (compare for example with the GPI-AP diffusion in Figure 15 or Figure 37).

The sFCS analysis was performed for data acquired on JCaM cells with reconstituted Lck-eGFP activating on OKT3-coated coverslips. The model selection procedure (Figure 46 G) suggested a hindered diffusion model (double lognormal, trapping, as in simulations and experiments on trapped diffusion; Figure 34). Figure 46 H and I show the respective fits in cumulative and logarithmic representations also highlighting the trapping, which suggests a population of Lck-eGFP undergoing transient binding and unbinding events. However, the overall Lck-eGFP dynamics in activating cells appeared shifted towards faster diffusion (smaller transit times). The slow (but free) diffusion in the hydrogel (i.e., resting) scenario may arise for topological reasons as the membrane is not flat in suspended cells (Figure 46 A). Diffusion on membrane ruffles and other 3D structures may cause an apparent slow-down, but should still be identified as free diffusion by sFCS. Overall, these results illustrate very different dynamics of Lck for the two different cellular states: In the resting cells Lck seems to undergo free, but slow diffusion, in the activating cells Lck shows fast, but trapped, diffusion, which indicates interactions.

As mentioned above, PLL-coated surfaces do not serve as a resting state condition [240]. Accordingly, JCaM cells with reconstituted Lck-eGFP spread and activate in this condition (see Figure 47 A). The cells appeared morphologically similar to the cells on OKT3, but seemed more flat and stronger attached to the coverslip. Interestingly, Lck-eGFP molecules in the bottom of T-cell GPMVs got stuck on PLL-coated surfaces (compare green localised dots in Figure 47 B). This effect has been used to crudely immobilise GPMVs, but influenced the diffusion dynamics in the bottom membrane. Figure 47 C shows pFCS measurements on supposedly freely diffusing lipid (Atto488-DOPE) in the bottom and top membranes of T cells and GPMVs. Pronounced shifts towards longer transit times, slower diffusion, in the bottom membrane measurements can be observed. For the specific immobilisation protocol developed in Section 5.2.1 such an effect on bottom membrane diffusion was not observed (see Figure 14 B). This exemplifies, how PLL-coated surfaces could influence diffusion dynamics in living systems as well as in thermodynamically

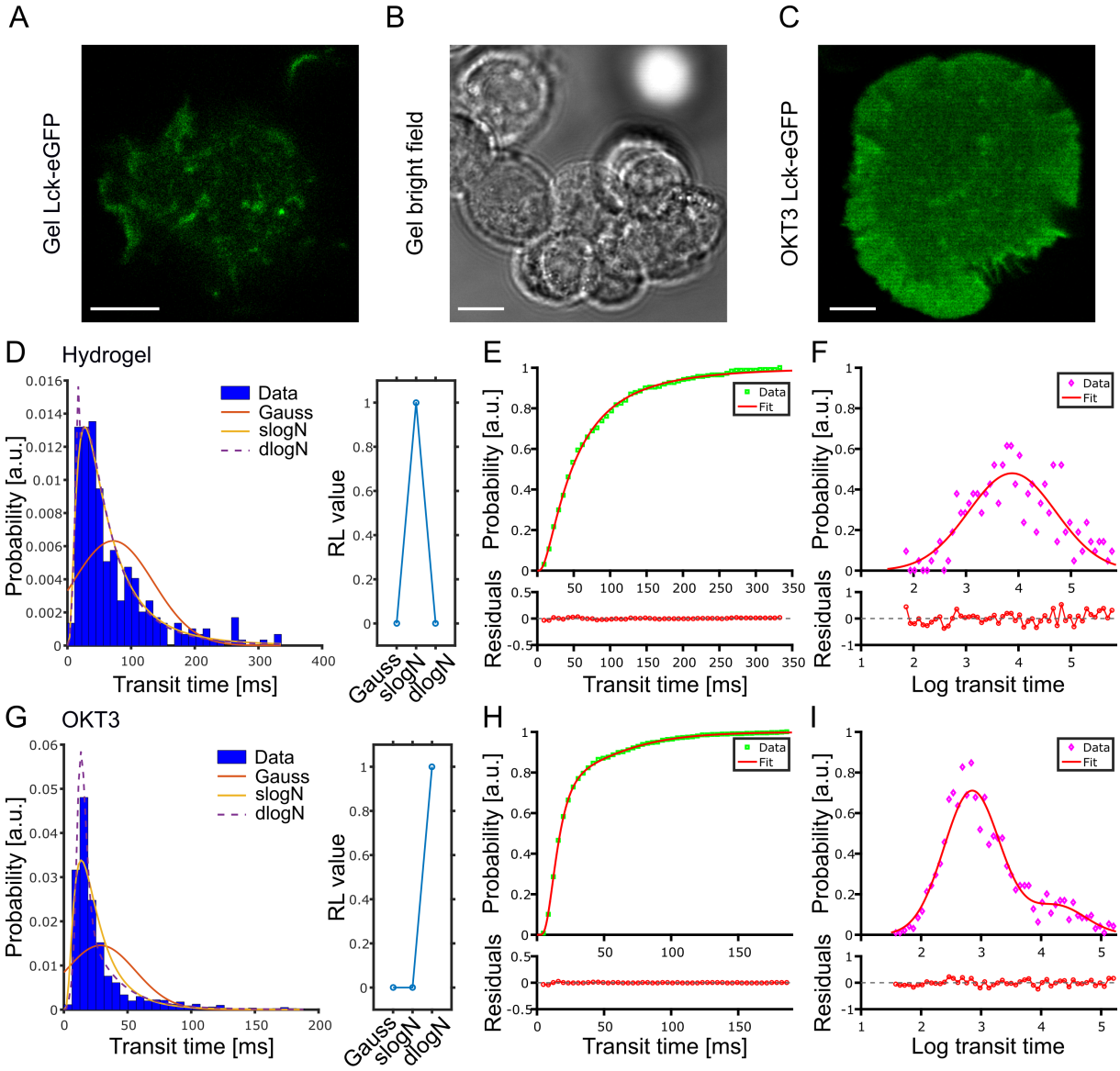


Figure 46: Imaging and sFCS of JCaM T cells reconstituted with Lck-eGFP in resting (hydrogel) and activating (OKT3-coated coverslip) condition. **A**: Confocal image of the bottom membrane of a JCaM T cell suspended in hydrogel. **B**: Bright-field image of T cells suspended in hydrogel forming a tissue culture like cell cluster. **C**: Confocal image of the bottom membrane of a JCaM cell with reconstituted Lck-eGFP spreading on an OKT3-coated coverslip. **D**: Model selection for sFCS data obtained from Lck-eGFP JCaM cells suspended in hydrogel. The single lognormal (free diffusion) model is the most likely model. **E**: Single lognormal fit in the cumulative representation and **F**: Single lognormal fit in the logarithmic representation for Lck-eGFP data in hydrogel. The sFCS measurements reveal free but slow diffusion. **G**: Model selection for sFCS data obtained from Lck-eGFP JCaM cells activating and spreading on OKT3-coated coverslips. The double lognormal (hindered, trapped diffusion) model is the most likely model for the data. **H**: Double lognormal fit in the cumulative representation and **I**: Double lognormal fit in the logarithmic representation for Lck-eGFP data from cells spreading on OKT3 coated coverslip. All scale bars are 5 µm. The data are representative for three independently prepared JCaM Lck-eGFP cell lines and >3 experiments for each condition (pooling >750 sFCS curves for the histogram analysis).

equilibrated systems.

sFCS data from JCaM cells (reconstituted with Lck-eGFP) were recorded on the PLL-coated coverslips and analysed as before. Model selection and linear representation of the data are presented in Figure 47 D. The best fit was obtained by the double lognormal model indicating hindered diffusion. The respective fits for cumulative and logarithmic representation are shown in Figure 47 E and F. Comparing the data to the resting and activating Lck-eGFP diffusion data in Figure 46 D-F and G-I, respectively, implies that the diffusion dynamics on PLL are more similar to the OKT3 data (activated) than to the hydrogel data (resting, see also Table 3). Interestingly, the diffusion mode could be used as a readout for cell activation. The overall diffusion of Lck-eGFP in the living cells on PLL was not considerably slower than on OKT3-coated coverslips (compare Figure 47 D-F and 46 G-I and Table 3). The PLL induced slowed-down diffusion in the bottom versus the top membrane given in Figure 47 C for the lipid analog did not occur for Lck-eGFP, which displayed similar diffusion timescales on OKT3- and PLL-coated surfaces. The reason for that was probably the location of the dye in the membrane. The lipid analog with the hydrophilic Atto488 dye got most likely only incorporated into the outer leaflet of the plasma membrane, whereas Lck is only attached to the inner leaflet. The charged PLL surface only interacted with the outer leaflet, which may imply that the Lck-eGFP dynamics seem to be more influenced by the cellular state of activation. Additionally, the sFCS measurements were much longer than the pFCS measurements in Figure 47 C. Thus passively immobilised molecules (as illustrated in Figure 47 B for Lck-eGFP stuck at the bottom of the GPMV) would likely be photobleached and excluded from the analysis.

To get a better understanding of the difference in dynamics of Lck between activating and resting state also the thermodynamic equilibrium state of the membrane was considered. To this end, T-cell GPMVs were prepared. The standard protocol was modified for working with the suspension cells (see [54, 186] and Materials and Methods section 4.4). The amount of GPMVs per preparation could be optimised, but only a small number of fluorescent Lck-eGFP molecules got incorporated into the vesicles generated from JCaM cells. For this reason most GPMV data were generated from Jurkat Lck-eGFP GPMVs, which yielded the highest number of molecules in the vesicular membrane. In Figure 48

Table 3: Overview of the sFCS fit results of Lck-eGFP in JCaM cells and Jurkat GPMVs. The lognormal fitting procedure yields the μ-values from which transit times ($\tau_{D,1/2}$) and the respective diffusion coefficients ($D_{1,2}$) can be calculated. Note that the diffusion coefficients and the transit times in the cases of hindered diffusion cannot straightforwardly be interpreted and are given for completeness only.

Cells					
Sample	Free Diffusion?	μ_1 ($\tau_{D,1}$ [ms])	D_1 [$\mu m^2/s$]	μ_2 ($\tau_{D,2}$ [ms])	D_2 [$\mu m^2/s$]
Hydrogel	Yes	3.9 (47.5)	0.15	NA	NA
OKT3	No	4.1 (61.3)	0.12	2.7 (15.6)	0.46
PLL	No	4.1 (61.7)	0.12	3.0 (19.6)	0.39
GPMVs					
Sample	Free Diffusion?	μ_1 ($\tau_{D,1}$ [ms])	D_1 [$\mu m^2/s$]	μ_2 ($\tau_{D,2}$ [ms])	D_2 [$\mu m^2/s$]
NEM	Yes	1.8 (6.2)	1.2	NA	NA
DTT	Yes	1.1 (3.1)	2.3	NA	NA

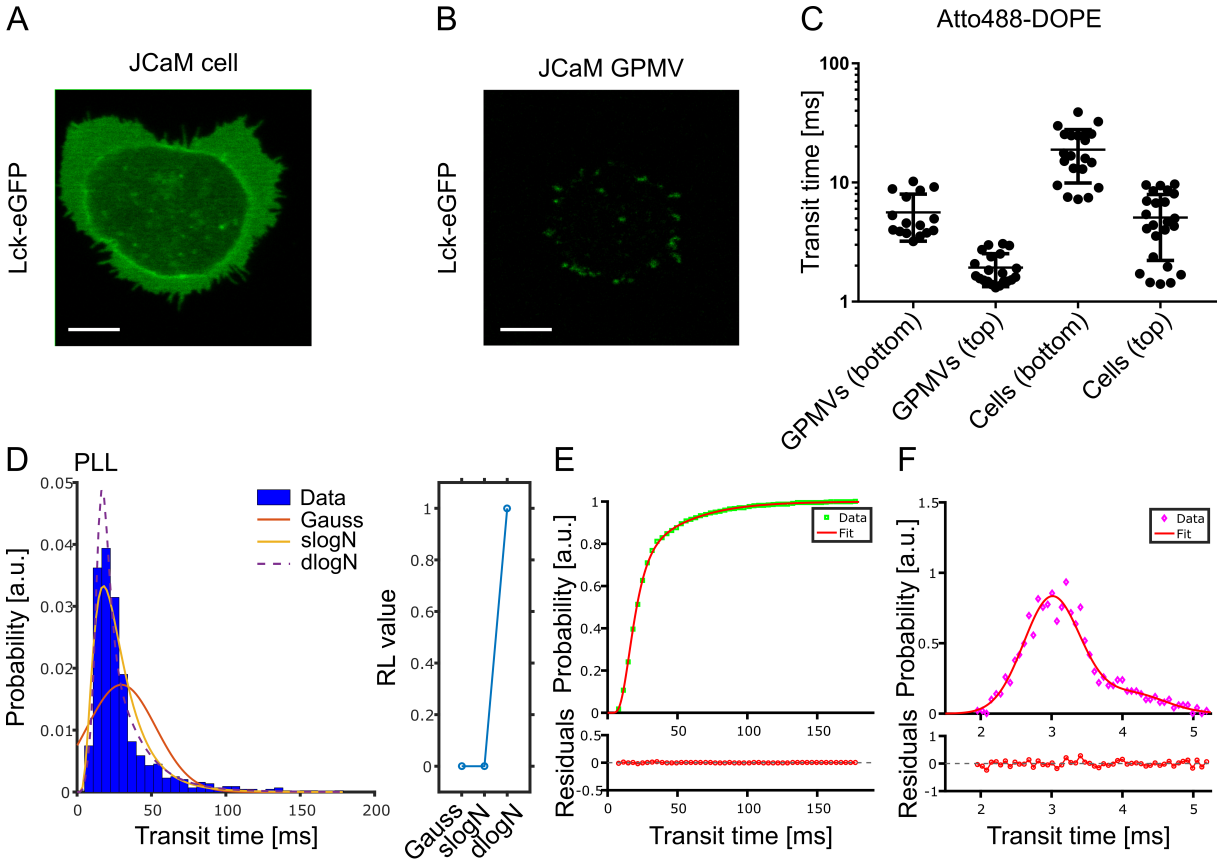


Figure 47: Diffusion dynamics of Lck are influenced by PLL. **A**: Confocal images of the bottom membrane of a Lck-eGFP JCaM cell showing spreading on a PLL-coated coverslip. **B**: Confocal image of the bottom membrane of a GPMV produced from Lck-eGFP JCaM cells. The green dots are Lck-eGFP molecules apparently stuck to the surface. All scale bars are 5 µm **C**: Point-FCS measurements of the lipid analog Atto488-DOPE in top and bottom membrane of JCaM cells and GPMVs on PLL. Standard deviation and data mean are shown. Every dot represents the measurement per cell or GPMV. **D**: Model selection for sFCS measurements taken in the bottom membrane of JCaM cells reconstituted with Lck-eGFP spreading on a PLL-coated coverslip. The double lognormal (hindered diffusion model) is suggested as most likely. **E**: Cumulative fit of the double lognormal model to the sFCS data in Panel D. **F**: Logarithmic fit and representation (double lognormal) of the data in Panel D and E. Representative sFCS analysis from three independently prepared Lck-eGFP cell lines. Pooled sFCS measurements from >10 cells.

A-D confocal images of Lck-eGFP GPMVs as well as GPMVs labelled with a lipid analog control (namely, Atto488-DOPE) are shown. The GPMVs from cells expressing Lck-eGFP (Figure 48 A and C) exhibit only very low fluorescence intensity from the Lck-eGFP in the membrane (although still more compared to JCaM GPMVs).

sFCS measurements were performed in the top membrane of immobilised GPMVs (using the developed BSA-biotin strategy, see Figure 14, section 5.2.1) and were subjected to the statistical analysis pipeline. The model selection for four exemplary sFCS measurement is presented in Figure 49. All probes seemed to diffuse freely but with varying transit times. The Jurkat Lck-eGFP GPMVs were prepared with two different methods (NEM and DTT, wherein DTT is a reducing agent). Interestingly, the diffusion of Lck in GPMVs prepared with NEM was much slower compared to the GPMVs prepared with DTT (Figure 48 E). The preparation method had no comparable influence on the lipid analog diffusion (Figure 48 F). The transit times recalculated from the distribution fitting are compared in Figure 48 F, where every dot represents the result from one sFCS histogram analysis (>250 FCS curves from multiple vesicles per preparation day). This analysis approach may be more intuitive than just comparing the histograms of free diffusion visually (as discussed more in section 5.4.5). All measurements were performed at 37 °C, which makes the slow diffusion (roughly two-fold slower than a lipid) of Lck-eGFP in NEM GPMVs even more interesting. The Lck-eGFP diffusion data from the GPMV measurements are presented alongside the data of the JCaM cells in Table 3.

The Atto488-DOPE control excluded that the membrane compositions between both preparation methods changed and influenced the overall diffusion (which has already been reported previously for adherent cell derived GPMVs [164]). A possible explanation for the different behaviours could be the influence of the lipidations of Lck, which could be partially removed by the DTT chemical, which is a highly reducing agent. In its membrane bound, native state Lck is post-transcriptionally modified by palmitoylation on two cysteines and additionally by myristoylation [244]. The palmitoyl-modification(s) could contribute to slow-downs due to interactions with lipid domains or other molecules. The myristoylation of Lck should not be affected by the treatment with DTT and has been reported to be sufficient for targetting Lck to the membrane in T cells [244]. Notably,

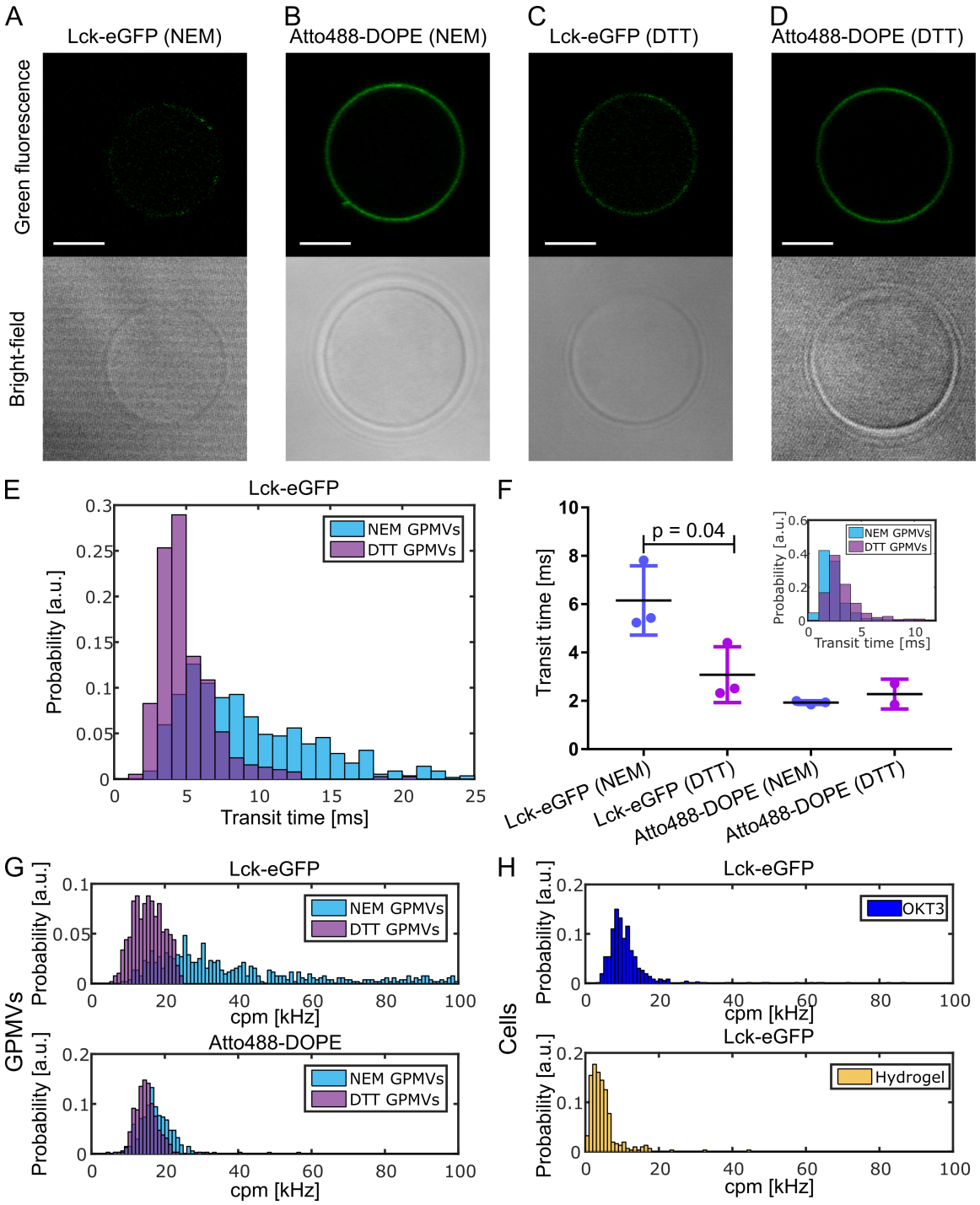


Figure 48: Lck dynamic organisation at thermodynamic equilibrium. Jurkat Lck-eGFP GPMVs prepared with either the NEM or DTT method. Confocal (green, top panels) and bright-field (bottom panels) images of **A**: Lck-eGFP prepared with NEM, **B**: Atto488-DOPE labelled GPMV prepared with NEM, **C**: Lck-eGFP GPMV prepared with DTT and **D**: Atto488-DOPE labelled GPMV prepared with DTT. All scale bars are 5 µm. **E**: Exemplary transit time histograms of Lck-eGFP for NEM (blue) and DTT (magenta). **F**: Quantification of sFCS data on Lck-eGFP and Atto488-DOPE diffusion (inset exemplary sFCS histogram for the lipid control) in top membranes of Jurkat GPMVs. Every dot represents one histogram fit ($>$ 250 single FCS measurements). Three independent sFCS experiments (only two for Atto488-DOPE in DTT-GPMVs) were performed and statistically analysed. Standard deviation and mean are shown. p-value was obtained from an unpaired t-test. **G**: Exemplary brightness histograms for Lck-eGFP and Atto488-DOPE in GPMVs. **H**: Exemplary brightness histograms for JCaM cells expressing Lck-eGFP in activating (OKT3, blue) and resting (hydrogel, yellow) conditions.

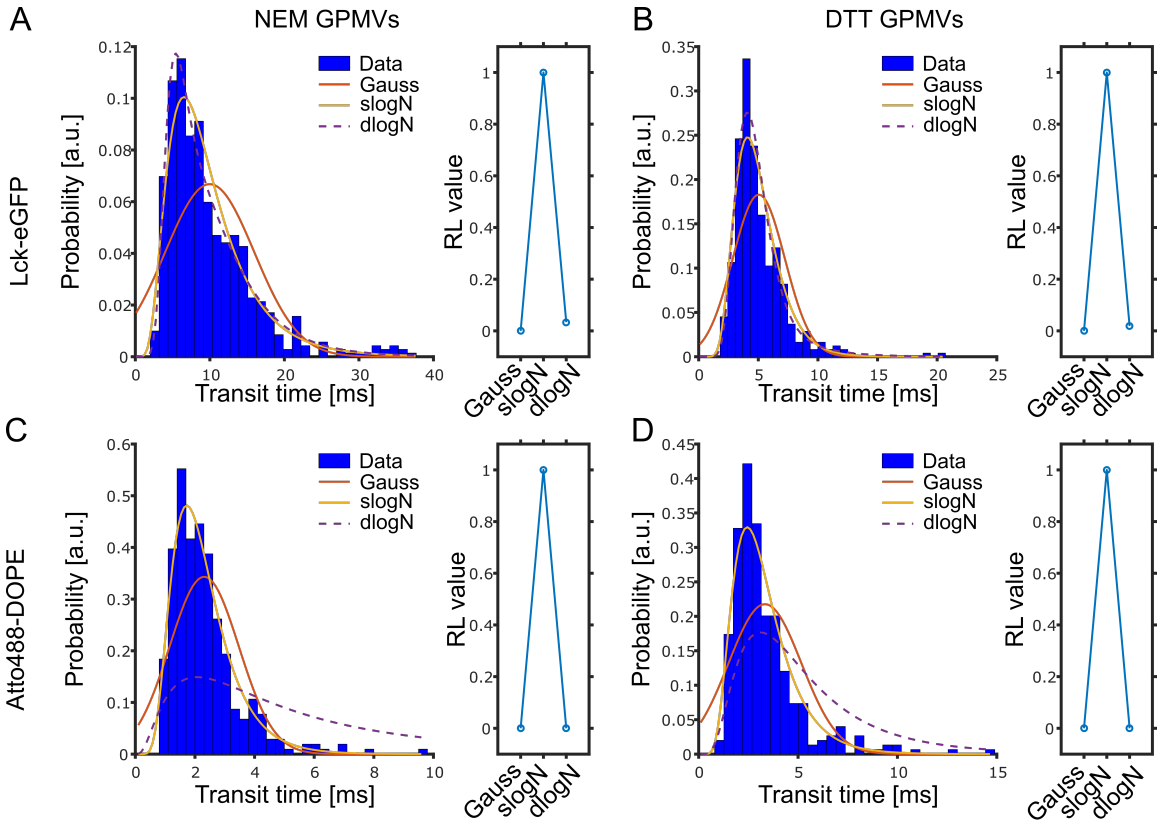


Figure 49: Maximum likelihood estimation and model selection for Lck-eGFP and Atto488-DOPE diffusing in the top membrane of GPMVs derived from Jurkat cells. **A**: Lck-eGFP in NEM GPMVs . **B**: Lck-eGFP in DTT GPMVs. **C**: Atto488-DOPE NEM GPMVs. **D**: Atto488-DOPE in DTT GPMVs. For all conditions the RL value suggests free diffusion as most likely model.

it has been proposed that at least one palmitoylation is necessary for the activity of Lck [80]. To check if the measured diffusion dynamics arose from single molecules or clusters, the molecular brightness was taken into account. Figure 48 G shows the cpm histograms for Lck-eGFP and Atto488-DOPE in both conditions. For the lipid analog a symmetrical peak for both GPMV preparation methods was observed as well as for Lck-eGFP in DTT GPMVs. In contrast, the histogram for Lck-eGFP diffusing in NEM vesicles had a long tail and was shifted towards higher brightness, which could indicate oligomerisation or domain incorporation in this thermodynamic equilibrium state of the plasma membrane.

Given these results the sFCS data for Lck-eGFP in the JCaM cells were revisited and the molecular brightness analysed (Figure 48 H). On the activating surface coated with OKT3 a single peak was observed indicating one population of relatively bright diffusing molecules. For the data in hydrogel also one population was obtained, but it has much lower brightness. The reason for that could be the optical properties of the hydrogel and the distance from the coverslip. Additionally, the excitation and emission light had to traverse multiple layers of cells residing at different heights within the hydrogel matrix. All of that could have caused a drop in signal-to-noise ratio and brightness.

Furthermore, the diffusion and brightness information derived from the sFCS data could be used in a combined analysis and presented as scatter plots or bivariate histograms (Figure 50). This could provide further insights into the molecular organisation. Clusters or domains, causing slow diffusion and incorporating more than one fluorescently tagged molecule, should result in a correlation between transit time and brightness. Confined molecules in a domain or compartmentalised region should cause an apparent slowed down diffusion but no change in brightness. This approach was explored on the data on Atto488-DOPE in the GPMVs as well as on Lck-eGFP in GPMVs and JCaM cells (Figure 50). Atto488-DOPE in GPMVs served as control for monomeric free diffusion. The bivariate histogramming uncovers a single population in both conditions (Figure 50 A and B). However, the distribution for Lck-eGFP from the NEM preparation showed a broadening of the peak compared to the DTT-derived GPMVs (Figure 50 C and D). The transit time versus brightness plot for Lck-eGFP in DTT GPMVs appeared similar to the lipid controls, probably representing a freely diffusing monomer. The data on

Lck-eGFP in the NEM GPMVs were much noisier and less conclusive. A slight, positive correlation between transit times and cpms might be present implying a small degree of clustering or domain formation. In a similar manner, also the diffusion data on Lck-eGFP in resting (hydrogel suspended cells) and activating (cells spreading on OKT3 coated coverslip) condition were investigated using the bivariate histogram approach. The low brightness of Lck-eGFP as well as the comparably slow diffusion were apparent in the resting (hydrogel) condition, but no bright and slow clusters were observed (Figure 50 E). The histogram for the activating condition showed a clear population of bright and fast molecules, but also no indication of bright and slow clusters in agreement with the statistical analysis (Figure 50 F). As discussed in section 5.4.5, including more FCS fitting parameters in the statistical analysis and maybe even implementing global fits may offer new robust routes to the analysis of molecular organisation.

The arising picture would be that at undisturbed equilibrium condition (lipidated, NEM GPMVs) Lck diffuses freely but slowly (compared to lipids or GPI-AP in GPMVs; see Section 5.2.1, Figure 14 B, D or Figure 15), implying it might be sequestered into a domain. In the resting cells, slow and free diffusion has been found. Upon T-cell activation, the Lck dynamics speed up and undergo trapping, suggesting that the molecule might be released from a domain and starts interactions. Comparing the molecular brightness on the surfaces with the hydrogel might yield some insights into oligomeric state. To overcome the putative loss in fluorescence signal induced by the hydrogel, a reference fluorophore could be introduced to the measuremnets for normalisation of the brightness. The biological implications of these results will be discussed further on in Section 6.2.

5.5.3 Summary dynamics in T cells

This Section showed some examples of how to use the advanced optical methodologies and techniques developed in earlier Sections in the context of immune cells and signalling. The difficulty of measuring dynamics in the resting state arose from the complicated experimental execution and the complex biology of the T cells compared to the previously employed planar model systems (i.e., adherent cells). The field needs to move further towards exploring nano-scale organisation in more physiological settings than on a coverslip

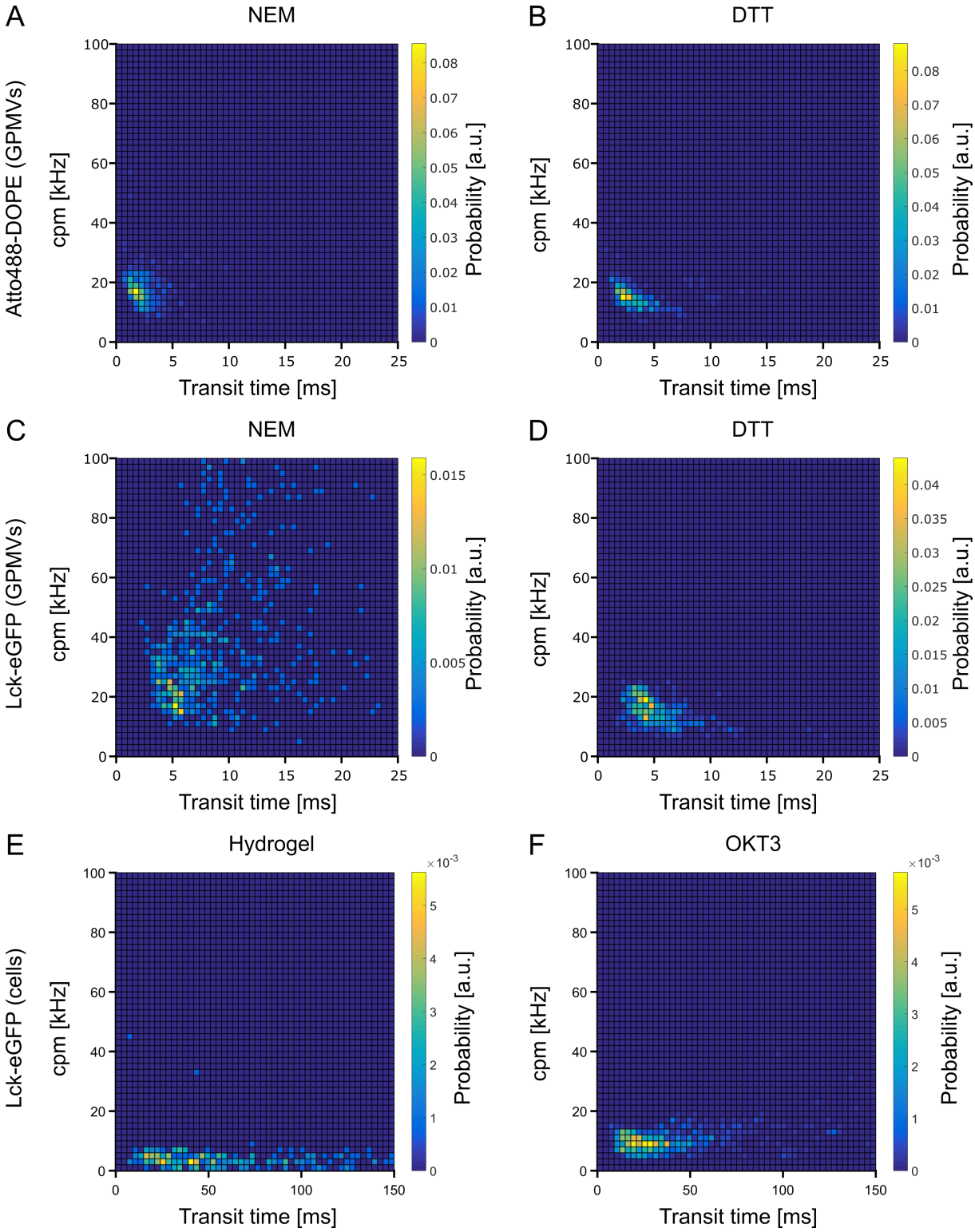


Figure 50: Bivariate histograms of the transit times and brightnesses (given as cpm) from the sFCS data on Atto488-DOPE in JCaM GPMVs and Lck-eGFP in JCaM GPMVs and cells. **A**: Atto488-DOPE sFCS transit time versus brightness (cpm) for GPMVs prepared with NEM and DTT (**B**). **C**: Lck-eGFP sFCS transit time versus brightness (cpm) for GPMVs prepared with NEM and DTT (**D**). **E**: Lck-eGFP sFCS transit time versus brightness (cpm) for molecules diffusing in JCaM cells either suspended in hydrogel or activating on OKT3-coated coverslips (**F**). >250 sFCS curves were analysed per condition.

and moreover appreciate the unsuspected sensitivity of T cells towards surfaces.

Using the best system for resting T cells at hand, the dynamics of Lck were demonstrated to be different (slow and free diffusion) from the dynamics in activated cells (fast but hindered diffusion). Together with the GPMV data (thermodynamic equilibrium) it can be concluded that the diffusion dynamics of Lck in T cells could be used as indicator of cellular state and that Lck might be sequestered in the resting state and is getting mobilised during activation. Nevertheless, many more experiments are necessary to fully decipher the underlying organisation. The developed techniques and approaches could be translated to T cells and especially the combined analysis of transit time and brightness could be of great value in future studies.

6 Discussion and Future Work

The findings were discussed individually and in detail in the respective part of the Results Chapter. In this Chapter, therefore, I will only present a broad general discussion. In the first part, I will fit the developed techniques into the context of other methods for measurements on diffusion dynamics in living systems and in a second part, I will focus on the biological findings of this work discussing the results on the organisation of lipids, GPI-APs and Lck in the plasma membrane. Additionally, I will suggest future directions and discuss how the presented methods as well as biological findings could be improved further.

6.1 Novel techniques to investigate diffusion dynamics

In the first part of the Results, FCS experiments at high-count rates have been evaluated. Using novel detection equipment, typical fluctuation experiments could be performed outside the standard count rate regime. Traditionally, FCS is considered a single molecule technique [245], but the only obvious limitations to FCS, given the averaging nature of technique, are the acquisition time and the molecular brightness of the probe, not the total number of molecules in focus (i.e., concentrations). Until recently, the accurate time-tagging of photons has been a technical restrain. I strongly believe the ease-of-use as well as the applicability of FCS to biological systems improved greatly with the latest commercial equipment. The presented data represent a versatile guideline for future users from the beginner to the expert level. However, the analysis has only been performed on a limited number of dyes (including only one fluorescent proteins) and could be extended in future work to find the new experimental limitations which will supposedly be the photophysics and photochemistry of the fluorophores or even the temporal resolution of fluorescence itself. The possibility of FCS at high count rates and the potential benefits have been considered before, but were difficult to implement [210, 211, 246]. The advantages of high concentrations of probes for STED-FCS measurements are obvious, yet until now, no assessment had been performed. Improvements in data quality will allow to perform more sophisticated experiments in living cells, tissues and even organisms. The improved signal quality should allow to draw conclusions from fewer measurements with

a similarly high confidence than conventionally in model systems. Nonetheless, a major issue with measurements in live cell tissue and organisms are optical aberrations, which need to be considered and corrected for [184]. The accurate time-tagging at high photon count rates will enable to perform lifetime based methods such as multi-colour FLIM in living cells much faster. This will additionally allow more sophisticated approaches such as Metal Induced Energy Transfer (MIET) or FLCS to be used by a broader community and to be easier performed in biological systems, which is an appealing future perspectives [215, 247].

In the second Section of the Results, GPMVs were introduced as actin-free plasma membrane mimics. pSTED-FCS has been used to characterise the nano-scale diffusion behaviour of different fluorescent lipid analogs and GPI-APs. The diffusion law measurements yielded robust and detailed insights into the diffusional heterogeneity of the plasma membrane (the biological implications will be discussed below, Section 6.2). Only very few other methods can resolve dynamics truly beyond the diffraction limit. Near-field methods like NSOM-FCS or optical nano-antennas represent alternatives to STED-FCS, but they (at least straightforwardly) only yield one additional length scale, are difficult to implement, and may be rather invasive [169, 171]. In STED-FCS the observation spot can flexibly be tuned to different length scales by varying the laser power, which is available on every commercial STED microscope, and became more robust in combination with the high-count rate detectors.

However, the data obtained from pSTED-FCS need to be interpreted with care. Hindered and free diffusion can straightforwardly be distinguished, but beyond that, the interpretation relies on exact knowledge about the diffusion modes. For this work, it was crucial to simulate FCS measurements under realistic experimental conditions at different prescribed diffusion modes like trapping or hopping and study the effective outcome when sampled at different spot sizes with (STED-)FCS. The most important results were that for all the combinations of hopping and trapping tested, the trapping overruled the hopping (no increase or levelling off of the diffusion law plot) and that for the domain diffusion the apparent kink is not on the order of the domain size. Not many dedicated STED-FCS studies on experimental data validated by simulations have been published

before [36, 122, 176, 203]. Nonetheless, simulations and experiments on svFCS have been performed extensively [154–157, 165]. An important consideration for future studies and simulations is the movement of domains or trapping sites as well as the assembly and disassembly of the confinement meshwork. It has, for example, been indicated that moving domains are very difficult to detect by svFCS and even STED-FCS [165]. Also the simulations in this work only assumed immobile domains, which does not necessarily reflect the biological reality.

The third part of the Results described the extension of STED-FCS in particular sSTED-FCS to measure the diffusion modes across space. LIESS-FCS provides a significant improvement in terms of spatial information and statistics compared to pSTED-FCS, but sacrifices, in turn, temporal resolution and details on the diffusion modes. It has been used to explore GPI-AP diffusional heterogeneity and to confirm SM trapping in spatially dynamic sites [166]. Major shortcoming of the technique seems to be the long acquisition time. In future studies the new detection equipment and knowledge on high count rate FCS could advance LIESS-FCS further to more biological applicability. Of course, the interleaved excitation scheme could be combined with other (STED-)FCS variants like RICS, pulsed-interleaved excitation and combined with functional probes (e.g., for observing local lipid ordering) [121, 179, 248]. However, at this time, sFCS seems to provide the best compromise in terms of scanning speed, line length and temporal resolution (compared to image correlation based approaches) for studying comparably fast diffusing lipids and lipid-anchored proteins at physiological temperature. The next logical step for the further development of LIESS-FCS would be to introduce a second colour. For example, distinct structures of interest or interaction partners could be labelled (like cytoskeletal components or receptors), membrane polarity or viscosity indicators could be used or calcium flux(es) could be visualised simultaneously. The second channel could just be a marker for cellular state or the presence of another molecule or structure and does not necessarily need to be correlated. These are ongoing efforts in the research group. A more challenging addition would be to actually correlate the intensity rerecorded in the second channel yielding (s)STED-FCCS, which so far has not been achieved. The advantage would be the possibility to observe fast and transient interactions of molecules in cross-

correlation manner, in addition to just observing the diffusion dynamics of two molecules at a time [249, 250]. In my opinion, the biggest obstacle for the robust implementation of STED-FCCS is the spectral cross-talk between channels and available fluorophores. Especially, when observing short lived interactions this needs to be accounted for. Using a pulse interleaved excitation/depletion scheme, supported by sophisticated photon filtering or pattern matching approaches, may make it possible in the near future [121, 217].

MINFLUX is a more recent technique which could in combination with SPT provide similar insights into the diffusion dynamics as STED-FCS [123, 124]. It is going to be very exciting to see the first diffusion data on SM or GPI-AP as well as data on hop diffusion in PtK2 cells resolved with this technique. Unfortunately, no commercially implementation is available at this time and only one set-up exits so far. However, this may change over the course of the next years as commercialisation of the technique has been initiated and MINFLUX may not remain a method restricted to a few expert users.

Using standard optics and equipment, camera-based FCS or iMSD have become popular choices to determine diffusion behaviours, dynamic heterogeneity and interactions [160, 161, 251]. These techniques have a multitude of advantages like the simple equipment or the compatibility with fluorescent proteins, but do not access the super-resolution regime. However, they use fast acquisition and spatial correlation, so that short lag times may provide sub-diffraction information [162]. An advantage is the large field of view which allows for building a diffusion map across the whole cell or cell membrane. The ideal scenario would be to assess the diffusion dynamics all across space at high spatio-temporal resolution but for now compromises need to be made.

To implement an alternative for the camera based acquisition using a LSM and resolving fast diffusion in membranes as well as hindrance in diffusion the statistical analysis of sFCS has been developed and introduced in the fourth part of the Results. This pipeline discards any spatial information for the sake of obtaining statistics and to be able to allow insights into nano-scale diffusion dynamics on the population level. Statistics in FCS have often been assessed for single measurements in regard to photons, acquisition time, standard deviation or signal-to-noise ratio [209, 212, 213, 252, 253], but interestingly statistics in terms of a multitude of curves and measurements fall short (with a few exceptions [148,

214]). The skewed nature of large sFCS measurements was a major finding and allowed the assessment of free versus hindered diffusion. The approach displays a complementary technique to STED-FCS as it can be used with probes, which may not be applicable to super-resolved recordings. Future work will enable a better understanding of the origin of the lognormal as well as the double lognormal probability distribution functions. It would be ideal to obtain analytical forms from mathematical modelling to describe the sFCS process (model diffusion dynamics and measurement) for free and hindered diffusion dynamics. This would allow to assess accuracy or standard deviations of sFCS recordings precisely and to extract more information especially from the hindered diffusion data (interpretation of the two μ and σ values is very challenging). This in turn could yield information on trapping times, interacting populations and other dynamics. Combining the statistical analysis with STED may also yield additional insights, especially in the case of hop diffusion and is currently being explored. The presented data demonstrate that extracting other parameters than the transit time can be beneficial. Future analysis should include brightness and the average number of molecules in the observation volume to get a better understanding of the dynamics.

A significant advantage of acquiring s(STED-)FCS data over standard p(STED-)FCS data is the flexibility. The intensity fluctuations are conveniently stored in xt-images and can be analysed in many ways. The data are readily usable for spatio-temporal correlation analysis, which can provide additional diffusional information to, for instance, characterise the observation spot or volume and yield an internal calibration [167, 168]. The observation spot size or PSF can be a big concern as the resolution is often only calibrated at the start of the measurement session. Self-calibrated methods could prove very versatile, specifically when measuring in slightly different conditions than used for calibration (e.g., curved cell membrane as sample versus perfectly flat SLB as calibration). A remedy may be the implementation of a pseudo two-focus FCS approach by quickly scanning two lines with a known displacement subsequently [254–256] or to use a deformable mirror to perform fast z-scan FCS in imaging mode [90, 257, 258].

Other ways to obtain more information from the sFCS data is to reanalyse them with pair-correlation, which yields information on obstacles, in the diffusion path [178, 259]

or Number and Brightness analysis that gives insights about oligomerisation [260, 261]. The analysis code for most of these alternative methods is open-source available and can be used on the xt-images (.tiff-files from any microscope) [262]. The acquired sFCS data may thus display a very versatile and rich resource and all these analysis methods could be paired with one another to gain the most from the data, maximising the output from any biological experiment.

The bio-imaging community already proposed the idea of a data repository (see "Image Data Resource" idr.openmicroscopy.org), where researchers can access and reanalyse published data sets for example in co-localisation studies. Bringing in the (s)FCS community could provide a great resource with well-documented data to, for example, trial and benchmark new analysis code with, to compare the results with previously published ones or to just have reference data sets for free diffusion, trapping or oligomerisation.

Overall, the developed techniques to assess dynamics on the nano-scale represent a step forward in bringing easy-to-use and robust fluctuation measurements to living cells. The next challenge would be the application of these quantitative methods to even more complex biological systems like organoids, cell tissues or whole organisms. This progress is already being made for super-resolution imaging [263, 264] and I believe it will also happen for the dynamic methods described throughout this work. All this will help to decipher the mysteries of membrane organisation and their physiological relevance.

6.2 Deciphering the diffusion dynamics in the plasma membrane of living cells

This work discusses many different diffusion dynamics, which show the considerable complexity of diffusional organisation and heterogeneity in the plasma membrane of living cells. In this section, I highlight and discuss the most important findings and try to fit them in the context of the current literature.

The influence of the cortical actin cytoskeleton on the diffusion dynamics in the plasma membrane has been pointed out before (see for example [33, 159, 232]), yet the assessment of diffusion dynamics has so far only been achieved in artificial systems (with limited lipid composition but without cortical actin cytoskeleton) or in cells under actin-depleting drug

treatments. In this thesis, it was shown how the actin cytoskeleton seems to control the trapping and hopping of molecules by comparing diffusion modes in live cells and cytoskeleton-free GPMVs. It would be very interesting to dial in cytoskeleton with varying complexity (different mesh sizes and concentrations adapter proteins) to decipher the details and the influence of specific actin structures like asters or stars [34, 265]. A system like that could be used in synthetic biology as well, building a minimal cell or measuring the passive interaction or uptake of compounds by the immobilised vesicles [60].

The GPMVs seem to represent a valuable and versatile system for studies exclusively on the plasma membrane (no cytoskeleton). A limitation of this system is that at least some of the membrane asymmetry is lost during vesicle preparation [54, 55, 266]. Proteins are unlikely to flip, but the leaflet specific membrane composition with regard to the lipid species may not be exactly the same as in the plasma membrane of a living cell. Furthermore, for the formation of GPMVs the cells are treated with vesiculating chemicals like in this case PFA/DTT, which may induce cross-linking of certain membrane components [54]. For that reason, control measurements with NEM-derived GPMVs as an alternative preparation method are advisable, but unfortunately due to the lower vesicle yield more challenging. Both preparation methods result in cleavage of the cytoskeleton from the membrane, but how exactly the GPMV formation occurs remains unknown [53, 54].

Throughout the thesis, the free diffusion of the phospholipid PE (DPPE) and the trapping of SM have been used as experimental model systems for different diffusion modes, which has proven itself very useful. However, it is surprising that the measured diffusion coefficients of the hopping DOPE exceeds the ones of DPPE at small spot sizes in the STED-FCS diffusion law plots, which may indicate some unresolved hindrance and may for example originate from very short-lived interactions. The discovery of two populations of diffusing DOPE, hopping and free diffusion, was very interesting and lets us appreciate that the membrane dynamics are difficult to describe with a single parameter or model across space [7, 33].

The presence of the cytoskeleton (pinned transmembrane proteins) changes the fluidity of the membrane more towards a gel like phase which changes in the membrane derived

vesicles [38] and is the possible reason for the observed large speed-up in diffusion coefficients of the lipids. The GPMV approach displays a more robust actin-free model than living cells treated with drugs like Latruncullin B or CK666, but the observed changes in diffusion behaviour are in line with previously described data [36, 122, 159].

Most studied molecules undergo free diffusion in the GPMVs, with the exception of the GM1 analog which seems to undergo hindered diffusion in the vesicles as well as in the cells. GM1 domains have been observed before and the labelled probes have been suggested to undergo domain-like diffusion in structures of sub-diffraction size even in artificial model membrane systems [19, 223, 267]. The results on GM1 in the cell derived vesicles extend these observation to physiologically more relevant membrane compositions. GM1 is due to its receptor function for cholera toxin and its physiological implication in Alzheimer's disease an interesting molecule to investigate [268, 269]. The choice of ipid analogs to study for this work was initially limited by availability and applicability (compatibility with STED). In future studies, it would be very interesting to include different gangliosides, phosphatidylinositol-phosphates or different ceramides to better characterise the origin, function and physiological relevance of domain diffusion and trapping, which supposedly does not originate from the phase partitioning behaviour [14, 51].

The organisation of GPI-APs remains under heated debate and various, sometimes opposing, organisations such as random distribution (no particular organisation), cluster formation, or domain incorporation among others have been proposed [31, 34, 224, 270]. The presented findings validate that GPI-APs undergo hindered diffusion in living cells. Using LIESS-FCS it became clear that the organisation is spatially very heterogeneous, what may explain the different opinions in the literature. Different GPI-APs were measured (GPI-SNAP, GPI-eGFP, GPI-RFP and LYPD6-mCherry) using different approaches and the results were consistent within this work. Yet, a comprehensive comparison (based on the signal sequence and the attached lipid anchor at best confirmed with mass spectrometry data) remains to be performed. This goes along with the choice of lipid analogs and highlights that the focus of this work was the method development, where it is important to stress that all the performed FCS experiments may miss very slowly moving or immobile particles. Clusters or bright spots of GPI-AP which are immobile

on the measurement timescale have been observed. To get a full understanding of the organisation a combination of approaches should be pursued and experiments with for example FRAP or SPT could be included. That said, some information on immobile particles could be extracted from the sFCS data using the initial seconds of photobleaching which were usually discarded for the analysis [148].

It is also very interesting,, that the outer leaflet anchored GPI-APs seem to be influenced by the actin cytoskeleton which implies a role of actin anchored trans-membrane proteins or strong interleaflet coupling [226, 227]. The speed up in diffusion when the GPI-APs are incorporated into the GPMVs is less than for the lipids which could be a result of size or charge (STED-FCS measurements were performed at the bottom of immobilised GPMVs). The effect was similar for GM1, but in that case the reduced diffusion coefficient can be attributed to remaining domain diffusion and interactions.

In this work, the diffusion of different cholesterol analogs, namely KK114-PEG-Cholesterol and TopFluor(TF)-Cholesterol, were investigated. These two analogs have very different properties. Due to the large hydrophilic linker, the PEGylated version cannot flip and its phase partitioning behaviour is distorted (it does not have a preference for the cholesterol-rich ordered phase) [166, 190, 271]. Nonetheless, it displays an excellent probe for plasma membrane labelling, shows a similar diffusion coefficient to the studied lipid analogs (aside from GM1) and free diffusion. It has been observed before by SPT that cholesterol diffuses comparably fast [228]. Thus, this PEG-probe represents another valuable model for free diffusion (for example as a control in STED-FCS experiments also due to its high labelling efficiency for the plasma membrane), but is most likely not representative for the native behaviour of cholesterol. Using TF-Cholesterol the fast diffusion could be confirmed and extended as the observation holds in living cells and model membrane systems (SLBs and GUVs). The analysis of the brightness indicates that the location or orientation of the dye on the probe is very different from the control lipid (TF-DPPE). The broad distribution may indicate different positioning (flipping or interleaflet location) of the probe. The question of the orientation in the lipid bilayer could, for example, be addressed with polarised light measuring fluorescence anisotropy [272]. However, it remains puzzling that a molecule known to stiffen membranes (i.e., increases the viscosity) and suggested to

interact with many proteins diffuses so fast [4, 15, 228, 273].

For the most part of the thesis the membrane was assumed to be perfectly flat (two-dimensional structure) and very close to the cover slip. This assumption seems fair for the adherent cells, but could be more problematic in the case of the T cells which constantly interact with the surface, ruffle and change flatness. The ruffling could be picked up by correlative techniques, but has not been observed either due to mismatching time scales or too strong interaction between plasma membrane and OKT3/PLL-coated coverslips. The topology may also cause orientation artefacts in the analysis of the molecular brightness. Dyes were assumed to be freely rotating and excitation light was assumed to exciting all orientations equally well, but if there was a preferred orientation of the fluorescent reporter that may cause artefacts [214, 274]. If the membrane was bent away from the coverslip, this would increase the transit time of a molecule through an assumed two dimensional observation spot which may mimic a trapping site. A remedy to this issue is the developed LIESS-FCS technique, but artefacts or misinterpretation cannot be completely ruled out. It remains debatable how three dimensional the plasma membrane actually is and to date only very few methods exists to visualise membrane topology or even dynamics in z on the relevant length scales (due to the axial resolution limit). MIET or variable angle TIRF microscopy indicated that the membrane can be quite far away from the cover slip ($>$50 nm, strongly depending on cell line) and the distance can vary even within one cell which indicates differences in topology and curvature [247, 275]. The topology is a challenging issue, which may be resolved in simple systems like adherent cells but poses a serious challenge for the study of membrane dynamics in vivo.

The last part of the thesis revisited the widely discussed organisation of the Src kinase Lck in resting and activating T cells. Similarly to the GPI-APs, where multiple types of organisation like clustering, domain incorporation or spatial randomness have been suggested, Lck is traditionally considered clustered and a raft-marker [81, 83–85, 276, 277]. The conflicting findings may result from the use of different cell lines and the definition of resting and activating state. Using calcium flux as indicator of triggering, the specific or non-specific T-cell activation on many supposedly resting surfaces has been demonstrated [240]. In accordance, within this work no surface could be identified that would not result

in activation. Therefore, the hydrogel suspension has been adapted as resting state. The use of the hydrogel suspension is experimentally challenging, but remained the only option. In this condition, specifically, the above discussed topology plays a crucial role. The cells appear curved, round and active which makes interpretation of the observed, surprisingly slow, diffusion difficult. That may just originate from the diffusion along the lateral direction. Free diffusion for the resting state has been observed, whereas for the activated cell trapping has been found. The trapping could mean that Lck engages another molecule and stays immobile for a while. Reduced mobility of Lck upon activation has been reported before, but was always compared to coated coverslips (mostly PLL) as resting state [82, 278, 279]. Interestingly, the diffusion of TCR and CD45 have been found to be rather fast inside the hydrogel [242]. This can be explained by the fact that both molecules are transmembrane proteins and interactions with any surface will result in a slow diffusion and the diffusion in hydrogel will then appear fast in comparison. This is different for Lck which is only anchored to the inner leaflet of the plasma membrane and thus shows rather high mobility even on PLL coated surfaces. It should be noted that Lck is known to interact with various transmembrane proteins most importantly CD4 (in a zinc mediated manner, see below), which could cause a certain extend of transmembrane protein like features [12, 62, 81, 280]. The overall fast dynamics of Lck-eGFP on PLL coated coverslips allow to hypothesise that only a small fraction of the molecules may be stably interacting with a transmembrane protein, but also highlights the re-occurring problem of the correlative approaches being insensitive for immobile molecules. It cannot be ruled out that some fraction of Lck molecules is moving extremely slow (or not at all) and is not represented in the analysis.

The question of (pre-)clustering of Lck in the resting state remained and is due to the topology (and the optical properties of the gel) difficult to answer. Thus, T-cell GPMVs were used as an "ultimate resting state" model (i.e, thermodynamic equilibrium). Using gentle preparation of Jurkat Lck-eGFP GPMVs (with the NEM method) yielded surprisingly slow diffusion of Lck (as compared to a lipid control) and a broad distribution of molecular brightnesses. The GPMV preparation with DTT increased mobility and reduced brightness. This may indicate the possibility of lipidation dependent clustering or

domain incorporation of Lck at thermodynamic equilibrium. In T cells the myristylation of Lck (which should not be influenced by the DTT treatment) has been shown to be sufficient for membrane localisation of the molecules [244]. An alternative or complementary explanation would be the disruption of a protein-protein interaction like Lck and CD4 which in this case mediated by cysteine residues (and zinc ions) [280]. DTT may affect their binding and cause an apparent speeding up in diffusion, but does not explain changes in molecular brightness unless the binding changes the fluorophore orientation. It should be noted that PFA was added to both preparation methods to increase the GPMV yield [186]. The PFA may have some cross-linking effect, but should influence both preparations equally [54] and the diffusion of the lipid control showed no unexpected behaviour.

The statistical analysis of the Lck-eGFP data in GPMVs suggested free diffusion of the molecule, but may not be sensitive enough to pick up very small domains. Additionally, it may also not detect molecules permanently incorporated into domains. They may appear as slowly and freely diffusing entities. If Lck diffused in a stable domain in the NEM case, it should appear as a slow but dim complex. For the case of transient incorporation of multiple molecules into one domain structure or cluster a clear correlation of transit time and brightness should be observed. Alternatively, the molecule could be transiently slowed down by domain incorporation which should not change the brightness. Unfortunately, the data are too noisy and thus rather inconclusive, but imply a clear difference between NEM and DTT prepared GPMVs. So far this does not prove or reject the possibility of clustering upon activation in the cells. The diffusion mode measurements in the cells point towards an increase in mobility of Lck upon T-cell activation and the initiation of trapping events (short-lived transient interactions, halts in the diffusion path). The analysis of the brightness did not suggest any mobile (bright) clusters in the activated or resting state. Comparison of the brightnesses turned out to be challenging due to the different measurement conditions (surface versus hydrogel). A solution to this issue could be to use a second dye. Either an unaffected control as internal standard or an interaction partner which may change upon activation. Again the co-receptor CD4 (as mentioned above), which is also a lipidated molecule and Lck phosphorylates the TCR, may be a good

candidate [62, 81]. Interaction studies with Fluorescence Cross-Correlation Spectroscopy (FCCS) in living cells may offer new avenues to decipher Lck functional organisation and would be in GPMVs prepared with either NEM or DTT very interesting to understand the difference in diffusion and brightness of Lck-eGFP. To ultimately answer the question of clustering Number and Brightness analysis in activated and resting state (both in gel with comparable optical properties and soluble OKT3 for activation) could be performed [260]. The presented preliminary data are the basis for forthcoming experiments to shed light on the changes in T-cell membrane heterogeneity upon activation. Unravelling the membrane complexity could yield new approaches for therapy in autoimmune diseases or cancer.

7 Conclusions

Measuring diffusion to investigate the live cell membrane organisation has turned out to be a fruitful and exciting journey that has led to the development of several new technologies and novel biophysical insights.
Briefly, I have achieved:

- The assessment of FCS and STED-FCS at high fluorophore concentrations and high photon count rates to enable measurements in systems exhibiting highly variable intensities, for example, due to protein expression.

- The acquisition of super-resolved diffusion measurements of lipids and proteins in cellular and model membranes to investigate the influence of the actin cytoskeleton on molecular diffusion.

- The development of LIESS-FCS representing an advanced modality of STED-FCS where confocal and STED measurements are performed quasi-simultaneously at multiple locations.

- The development of a statistical analysis pipeline that enables diffusion mode measurements on a conventional confocal microscope.

- The revelation of new insights into the organisation of Lck in the T-cell membrane.

The use of a fluctuation based technique like FCS at high probe concentrations and high count rates where intensity variations are largely absent, might appear initially unreasonable, but should be possible given the high molecular brightness of available fluorophores. Reassuringly, FCS turns out to be quite feasible in this intensity regime, thus allowing for more flexible and less biased confocal measurements and paving the way for more sophisticated super-resolved STED-FCS acquisitions in living systems. The ease-of-use and the robustness of the tested equipment as well as the established protocols will make (STED-)FCS accessible to a wider community.

The actin cytoskeleton is known to influence the organisation of the cellular plasma membrane, yet this has not been tested in models where cellular complexity is retained but cortical actin is absent. The GPMVs provided the perfect platform for such a study.

Free diffusion was observed for almost all probes in the GPMVs and the diffusion coefficients were consistently higher than in the live cells. Interestingly, only the glycolipid analog GM1 retained some hindered diffusion in the vesicles. In this part of the work, highly detailed insights into the nano-scale diffusion behaviour could be obtained by using pSTED-FCS.

The spatial heterogeneous diffusion of GPI-APs sparked the idea of and showed the necessity for spatially resolved diffusion mode measurements. Introducing LIESS-FCS, where confocal and STED measurements are acquired quasi-simultaneously, allowed for the first time to spatially resolve the diffusion modes of molecules beyond the diffraction limit. Admittedly, the spatial and temporal resolution (and the field of view) could be further improved, but in its current form LIESS-FCS represents an important step towards a super-resolved diffusion mode map of the cellular plasma membrane.

Not every laboratory has access to the expertise or has the required equipment to perform STED-FCS experiments. In this case, the statistical analysis of sFCS data represents a good alternative yielding valuable first insights. Of course, it cannot replace dedicated STED-FCS measurements, but it gives complementary information with standard fluorophores and can be used to pre-screen which conditions could be interesting to explore with STED nanoscopy.

The aforementioned scenario occurred for the biological example of the resting T cells in this thesis. The oil-immersion STED microscope available at that time was not appropriate to perform super-resolved STED-FCS measurements in live T cell in the hydrogel suspension. Hence, the versatile alternative of the statistical sFCS analysis came into play. Together with the use of activating surfaces and GPMVs this yielded new perspectives on the organisation of Lck.

Overall, this work adds a few puzzle pieces to the mystery of membrane organisation, provides versatile and broadly applicable additions to the toolkit for the investigation of diffusion dynamics, and highlights the complexity and heterogeneity of living systems.

References

[1] Singer, S. and Nicolson, G. *The fluid mosaic model of the structure of cell membranes.* Science, 175(4023):720–731, 1972.

[2] Nicolson, G. L. *The Fluid—Mosaic Model of Membrane Structure: Still relevant to understanding the structure, function and dynamics of biological membranes after more than 40years.* Biochimica et Biophysica Acta - Biomembranes, 1838(6):1451–1466, 2014.

[3] Semrau, S. and Schmidt, T. *Membrane heterogeneity – from lipid domains to curvature effects.* Soft Matter, 5(17):3174, 2009.

[4] Marrink, S. J., et al. *Computational Modeling of Realistic Cell Membranes.* Chemical Reviews, 119(9):6184–6226, 2019.

[5] Sezgin, E., et al. *The mystery of membrane organization: composition, regulation and roles of lipid rafts.* Nature Reviews Molecular Cell Biology, 18(6):361–374, 2017.

[6] Jacobson, K., et al. *The Lateral Organization and Mobility of Plasma Membrane Components.* Cell, 177(4):806–819, 2019.

[7] Bernardino de la Serna, J., et al. *There Is No Simple Model of the Plasma Membrane Organization.* Frontiers in Cell and Developmental Biology, 4(September):1–17, 2016.

[8] Goñi, F. M. *"Rafts": a nickname for putative transient nanodomains.* Chemistry and Physics of Lipids, 2018.

[9] Murphy, K. *Janeway's Immunobiology.* Garland Science, 8 edition edition, 2008.

[10] Wu, W., et al. *Regulation of T cell signalling by membrane lipids.* Nature Reviews Immunology, 2016.

[11] Rossboth, B., et al. *TCRs are randomly distributed on the plasma membrane of resting antigen-experienced T cells.* Nature Immunology, 1, 2018.

[12] Rossy, J., et al. *How does the kinase Lck phosphorylate the T cell receptor? Spatial organization as a regulatory mechanism.* Frontiers in Immunology, 3(JUN):1–6, 2012.

[13] Shannon, M. and Owen, D. M. *Bridging the Nanoscopy-Immunology Gap.* Frontiers in Physics, 6(January):1–8, 2019.

[14] Sezgin, E., et al. *Measuring nanoscale diffusion dynamics in cellular membranes with super-resolution STED–FCS.* Nature Protocols, 14(4):1054–1083, 2019.

[15] Reddy, a. S., et al. *Effect of membrane tension on the physical properties of DOPC lipid bilayer membrane.* Biochimica et Biophysica Acta - Biomembranes, 1818(9):2271–2281, 2012.

[16] Tristram-Nagle, S., et al. *Structure and interactions of fully hydrated dioleoylphosphatidylcholine bilayers.* Biophysical journal, 75(2):917–925, 1998.

[17] Schrauwers, A. and Poolman, B. *Synthetische Biologie.* Springer Berlin Heidelberg, Berlin, Heidelberg, 2013.

[18] Bretscher, M. S. *Membrane structure: some general principles.* Science (New York, N.Y.), 181(4100):622–9, 1973.

[19] Cebecauer, M., et al. *Membrane Lipid Nanodomains.* Chemical Reviews, 118(23):11259–11297, 2018.

[20] Yu, J., et al. *Selective solubilization of proteins from red blood cell membranes by protein perturbants.* Journal of Supramolecular Structure, 1(3):220–232, 1973.

[21] Sezgin, E. and Schwille, P. *Model membrane platforms to study protein-membrane interactions.* Molecular Membrane Biology, 29(5):144–154, 2012.

[22] McConnell, H. M., et al. *Periodic structures in lipid monolayer phase transitions.* Proceedings of the National Academy of Sciences of the United States of America, 81(10):3249–53, 1984.

[23] Tamm, L. K. and McConnell, H. M. *Supported phospholipid bilayers.* Biophysical Journal, 47(1):105–113, 1985.

[24] Jacobson, K., et al. *Lipid rafts: at a crossroad between cell biology and physics.* Nature Cell Biology, 9(1):7–14, 2007.

[25] Lommerse, P. H. M., et al. *Single-molecule diffusion reveals similar mobility for the Lck, H-ras, and K-ras membrane anchors.* Biophysical journal, 91(3):1090–1097, 2006.

[26] Levental, I., et al. *Palmitoylation regulates raft affinity for the majority of integral raft proteins.* Proceedings of the National Academy of Sciences, 107(51):22050–22054, 2010.

[27] Özhan, G., et al. *Lypd6 Enhances Wnt/β-Catenin Signaling by Promoting Lrp6 Phosphorylation in Raft Plasma Membrane Domains.* Developmental Cell, 26(4):331–345, 2013.

[28] van Zanten, T. S., et al. *Hotspots of GPI-anchored proteins and integrin nanoclusters function as nucleation sites for cell adhesion.* Proceedings of the National Academy of Sciences of the United States of America, 106(44):18557–18562, 2009.

[29] Rissanen, S., et al. *Phase Partitioning of GM1 and Its Bodipy-Labeled Analog Determine Their Different Binding to Cholera Toxin.* Frontiers in Physiology, 8(May):252, 2017.

[30] Komura, N., et al. *Raft-based interactions of gangliosides with a GPI-anchored receptor.* Nature Chemical Biology, 12(6):402–410, 2016.

[31] Sevcsik, E. and Schütz, G. J. *With or without rafts? Alternative views on cell membranes.* BioEssays, 38(2):129–139, 2016.

[32] Fujiwara, T., et al. *Phospholipids undergo hop diffusion in compartmentalized cell membrane.* The Journal of cell biology, 157(6):1071–81, 2002.

[33] Kusumi, A., et al. *Paradigm Shift of the Plasma Membrane Concept from the Two-Dimensional Continuum Fluid to the Partitioned Fluid: High-Speed Single-Molecule Tracking of Membrane Molecules.* Annual Review of Biophysics and Biomolecular Structure, 34(1):351–378, 2005.

[34] Köster, D. V. and Mayor, S. *Cortical actin and the plasma membrane: inextricably intertwined.* Current Opinion in Cell Biology, 38:81–89, 2016.

[35] Fritzsche, M., et al. *Actin kinetics shapes cortical network structure and mechanics.* Science Advances, 2(4):e1501337, 2016.

[36] Andrade, D. M., et al. *Cortical actin networks induce spatio-temporal confinement of phospholipids in the plasma membrane – a minimally invasive investigation by STED-FCS.* Scientific Reports, 5(May):11454, 2015.

[37] Yeagle, P. L. *Lipid regulation of cell membrane structure and function.* The FASEB Journal, 3(7):1833–1842, 1989.

[38] Shi, Z., et al. *Cell Membranes Resist Flow.* Cell, 175(7):1769–1779.e13, 2018.

[39] Duncan, A. L., et al. *Protein crowding and lipid complexity influence the nanoscale dynamic organization of ion channels in cell membranes.* Scientific Reports, 7(1):16647, 2017.

[40] Duncan, A. L., et al. *Lipid-Dependent Regulation of Ion Channels and G Protein–Coupled Receptors: Insights from Structures and Simulations.* Annual Review of Pharmacology and Toxicology, 60(1):annurev–pharmtox–010919–023411, 2020.

[41] Baird, D. and Tanford, C. *Ben Franklin Stilled the Waves: An Informal History of Pouring Oil on Water, with Reflections on the ups and Downs of Scientific Life in General.*, volume 77. Oxford University Press, 2006.

[42] Milo, R. and Phillips, R. *Cell biology by the numbers.*

[43] Langmuir, I. *The constitution and fundamental properties of solids and liquids. II. Liquids.* Journal of the American Chemical Society, 39(9):1848–1906, 1917.

[44] Bangham, A. D. and Horne, R. W. *Negative staining of phospholipids and their structural modification by surface-active agents as observed in the electron microscope.* Journal of Molecular Biology, 8(5):660–668, 1964.

[45] Diao, J., et al. *A single vesicle-vesicle fusion assay for in vitro studies of SNAREs and accessory proteins.* Nature Protocols, 7(6):921–934, 2012.

[46] Lind, T. K. and Cárdenas, M. *Understanding the formation of supported lipid bilayers via vesicle fusion—A case that exemplifies the need for the complementary method approach (Review).* Biointerphases, 11(2):020801, 2016.

[47] Honigmann, A., et al. *STED microscopy detects and quantifies liquid phase separation in lipid membranes using a new far-red emitting fluorescent phosphoglycerolipid analogue.* Faraday Discuss., 161:77–89, 2013.

[48] Richter, R. P. and Brisson, A. R. *Following the formation of supported lipid bilayers on mica: a study combining AFM, QCM-D, and ellipsometry.* Biophysical journal, 88(5):3422–3433, 2005.

[49] Zhang, L. and Granick, S. *Lipid diffusion compared in outer and inner leaflets of planar supported bilayers.* Journal of Chemical Physics, 123(21), 2005.

[50] Angelova, M. I. and Dimitrov, D. S. *Liposome electroformation.* Faraday Discussions of the Chemical Society, 81:303–311, 1986.

[51] Sezgin, E., et al. *Partitioning, diffusion, and ligand binding of raft lipid analogs in model and cellular plasma membranes.* Biochimica et biophysica acta, 1818(7):1777–84, 2012.

[52] Veatch, S. L. and Keller, S. L. *Separation of Liquid Phases in Giant Vesicles of Ternary Mixtures of Phospholipids and Cholesterol.* Biophysical Journal, 85(5):3074–3083, 2003.

[53] Scott, R. *Plasma membrane vesiculation: a new technique for isolation of plasma membranes.* Science, 194(4266):743–745, 1976.

[54] Sezgin, E., et al. *Elucidating membrane structure and protein behavior using giant plasma membrane vesicles.* Nature protocols, 7(6):1042–51, 2012.

[55] Baumgart, T., et al. *Large-scale fluid/fluid phase separation of proteins and lipids in giant plasma membrane vesicles.* Proceedings of the National Academy of Sciences, 104(9):3165–3170, 2007.

[56] Hafeman, D. G., et al. *Specific antibody-dependent interactions between macrophages and lipid haptens in planar lipid monolayers.* Proceedings of the National Academy of Sciences, 78(7):4552–4556, 1981.

[57] Groves, J. T. and Dustin, M. L. *Supported planar bilayers in studies on immune cell adhesion and communication.* Journal of Immunological Methods, 278(1-2):19–32, 2003.

[58] Su, X., et al. *Phase separation of signaling molecules promotes T cell receptor signal transduction.* Science, 352(6285):595–599, 2016.

[59] Jenkins, E., et al. *Reconstitution of immune cell interactions in free-standing membranes.* Journal of Cell Science, 132(4):jcs219709, 2019.

[60] Ganzinger, K. A. and Schwille, P. *More from less – bottom-up reconstitution of cell biology.* Journal of Cell Science, 132(4):jcs227488, 2019.

[61] Jain, S., et al. *Lipid Based Vesicular Drug Delivery Systems.* Advances in Pharmaceutics, 2014(i):1–12, 2014.

[62] Grakoui, A. *The Immunological Synapse: A Molecular Machine Controlling T Cell Activation.* Science, 285(5425):221–227, 1999.

[63] Fooksman, D. R., et al. *Functional Anatomy of T Cell Activation and Synapse Formation.* Annual Review of Immunology, 28(1):79–105, 2010.

[64] Davis, S. J. and van der Merwe, P. A. *The kinetic-segregation model: TCR triggering and beyond.* Nature immunology, 7(8):803–809, 2006.

[65] Chang, V. T., et al. *Initiation of T cell signaling by CD45 segregation at 'close contacts'.* Nature immunology, 17(5):574–82, 2016.

[66] James, J. R. and Vale, R. D. *Biophysical mechanism of T-cell receptor triggering in a reconstituted system.* Nature, 487(7405):64–69, 2012.

[67] Cooper, J. A. and Qian, H. *A Mechanism for Src Kinase-Dependent Signaling by Noncatalytic Receptors.* Biochemistry, 47(21):5681–5688, 2008.

[68] Xavier, R., et al. *Membrane compartmentation is required for efficient T cell activation.* Immunity, 8(6):723–732, 1998.

[69] Viola, A., et al. *T lymphocyte costimulation mediated by reorganization of membrane microdomains.* Science, 283(5402):680–682, 1999.

[70] Simons, K. and Toomre, D. *Lipid rafts and signal transduction.* Nature reviews. Molecular cell biology, 1(1):31–39, 2000.

[71] Levin, S. E. and Weiss, A. *Twisting tails exposed: Figure 1.* The Journal of Experimental Medicine, 201(4):489–492, 2005.

[72] Minguet, S., et al. *Full Activation of the T Cell Receptor Requires Both Clustering and Conformational Changes at CD3.* Immunity, 26(1):43–54, 2007.

[73] Xu, C., et al. *Regulation of T Cell Receptor Activation by Dynamic Membrane Binding of the CD3e Cytoplasmic Tyrosine-Based Motif.* Cell, 135(4):702–713, 2008.

[74] Fernandes, R. A., et al. *What Controls T Cell Receptor Phosphorylation?* Cell, 142(5):668–669, 2010.

[75] Kumari, S., et al. *T cell antigen receptor activation and actin cytoskeleton remodeling.* Biochimica et biophysica acta, 1838(2):546–56, 2014.

[76] Fritzsche, M., et al. *Cytoskeletal actin dynamics shape a ramifying actin network underpinning immunological synapse formation.* Science Advances, 3(6):e1603032, 2017.

[77] Colin-York, H., et al. *Cytoskeletal Control of Antigen-Dependent T Cell Activation.* Cell Reports, 26(12):3369–3379.e5, 2019.

[78] Yasuda, K., et al. *Serine 6 of Lck Tyrosine Kinase: A Critical Site for Lck Myristoylation, Membrane Localization, and Function in T Lymphocytes.* The Journal of Immunology, 165(6):3226–3231, 2000.

[79] Sheng, R., et al. *Lipids regulate Lck protein activity through their interactions with the Lck Src homology 2 domain.* Journal of Biological Chemistry, 291(34):17639–17650, 2016.

[80] Yurchak, L. K. and Sefton, B. M. *Palmitoylation of either Cys-3 or Cys-5 is required for the biological activity of the Lck tyrosine protein kinase.* Molecular and cellular biology, 15(12):6914–22, 1995.

[81] Irles, C., et al. *Plasma membrane subdomain partitioning of Lck in primary human T lymphocytes.* Canadian Journal of Physiology and Pharmacology, 88(4):487–496, 2010.

[82] Ma, Y., et al. *Measuring membrane association and protein diffusion within membranes with supercritical angle fluorescence microscopy.* Biomedical Optics Express, 7(4):1561, 2016.

[83] Rossy, J. J. J. J. J. J., et al. *Conformational states of the kinase Lck regulate clustering in early T cell signaling.* Nature immunology, 14(1):82–89, 2012.

[84] Baumgart, F., et al. *Varying label density allows artifact-free analysis of membrane-protein nanoclusters.* Nature Methods, 2(May):0–10, 2016.

[85] Ventimiglia, L. N. and Alonso, M. *The role of membrane rafts in Lck transport, regulation and signalling in T-cells.* Biochemical Journal, 454(2):169–179, 2013.

[86] Liu, T.-l., et al. *Observing the cell in its native state: Imaging subcellular dynamics in multicellular organisms.* Science, 1392(April), 2018.

[87] Hell, S. W., et al. *The 2015 super-resolution microscopy roadmap.* Journal of Physics D: Applied Physics, 48(44):443001, 2015.

[88] Clausen, M. P., et al. *Pathways to optical STED microscopy.* NanoBioImaging, 1(1), 2014.

[89] Eggeling, C. *Super-resolution optical microscopy of lipid plasma membrane dynamics.* Essays In Biochemistry, 57(1):69–80, 2015.

[90] Vangindertael, J., et al. *Methods and Applications in Fluorescence - An introduction to optical super-resolution microscopy for the adventurous biologist.* Methods and Applications in Fluorescence, 6(2):55, 2018.

[91] Abbe, E. *Beitraege zur Theorie des Mikroskops und der mikroskopischen Wahrnehmung.* Archiv für Mikroskopische Anatomie, 9(1):413–418, 1873.

[92] Sezgin, E., et al. *Super-resolution optical microscopy for studying membrane structure and dynamics.* Journal of Physics: Condensed Matter, 273001(27):273001, 2017.

[93] Eggeling, C., et al. *Lens-based fluorescence nanoscopy.* Quarterly Reviews of Biophysics, 48(02):178–243, 2015.

[94] Jradi, F. M. and Lavis, L. D. *Photosensitive fluorophores for single-molecule localization microscopy.* ACS Chemical Biology, page acschembio.9b00197, 2019.

[95] Nicovich, P. R., et al. *Turning single-molecule localization microscopy into a quantitative bioanalytical tool.* Nature Protocols, 12(3):453–461, 2017.

[96] Sharonov, A. and Hochstrasser, R. M. *Wide-field subdiffraction imaging by accumulated binding of diffusing probes.* Proceedings of the National Academy of Sciences, 103(50):18911–18916, 2006.

[97] Schnitzbauer, J., et al. *Super-resolution microscopy with DNA-PAINT.* Nature Protocols, 12(6):1198–1228, 2017.

[98] Pereira, P. M., et al. *Fix Your Membrane Receptor Imaging: Actin Cytoskeleton and CD4 Membrane Organization Disruption by Chemical Fixation.* Frontiers in Immunology, 10(April):675, 2019.

[99] Shroff, H., et al. *Live-cell photoactivated localization microscopy of nanoscale adhesion dynamics.* Nature Methods, 5(5):417–423, 2008.

[100] Griffié, J., et al. *Dynamic Bayesian Cluster Analysis of Live-Cell Single Molecule Localization Microscopy Datasets.* Small Methods, 2(9):1800008, 2018.

[101] Gustafsson, M. G. *Surpassing the lateral resolution limit by a factor of two using structured illumination microscopy.* Journal of Microscopy, 198(2):82–87, 2000.

[102] York, A. G., et al. *Resolution doubling in live, multicellular organisms via multifocal structured illumination microscopy.* Nature Methods, 9(7):749–754, 2012.

[103] Müller, C. B. and Enderlein, J. *Image scanning microscopy.* Physical Review Letters, 104(19):1–4, 2010.

[104] Halász, H., et al. *Live cell superresolution-structured illumination microscopy imaging analysis of the intercellular transport of microvesicles and costimulatory proteins via nanotubes between immune cells.* Methods and Applications in Fluorescence, 6(4), 2018.

[105] Li, D., et al. *Extended-resolution structured illumination imaging of endocytic and cytoskeletal dynamics.* Science, 349(6251), 2015.

[106] Sage, D., et al. *Super-resolution fight club: assessment of 2D and 3D single-molecule localization microscopy software.* Nature Methods, 16(5):387–395, 2019.

[107] Schermelleh, L., et al. *Super-resolution microscopy demystified.* Nature Cell Biology, 21(1):72–84, 2019.

[108] Hell, S. W. and Wichmann, J. *Breaking the diffraction resolution limit by stimulated emission: stimulated-emission-depletion fluorescence microscopy.* Optics Letters, 19(11):780, 1994.

[109] Klar, T. A. and Hell, S. W. *Subdiffraction resolution in far-field fluorescence microscopy.* Optics letters, 24(14):954–6, 1999.

[110] Klar, T. A., et al. *Fluorescence microscopy with diffraction resolution barrier broken by stimulated emission.* Proceedings of the National Academy of Sciences of the United States of America, 97(15):8206–10, 2000.

[111] Vicidomini, G., et al. *STED super-resolved microscopy.* Nature Methods, 15(3):173–182, 2018.

[112] Galiani, S., et al. *Super resolution microscopy reveals compartmentalization of peroxisomal membrane proteins.* Journal of Biological Chemistry, 291(4):jbc.M116.734038, 2016.

[113] Han, K. Y., et al. *Three-Dimensional Stimulated Emission Depletion Microscopy of Nitrogen-Vacancy Centers in Diamond Using Continuous-Wave Light.* Nano Letters, 9(9):3323–3329, 2009.

[114] Sahl, S. J., et al. *Fluorescence nanoscopy in cell biology.* Nature Reviews Molecular Cell Biology, 18(11):685–701, 2017.

[115] Rankin, B. R., et al. *Nanoscopy in a living multicellular organism expressing GFP.* Biophysical Journal, 100(12):63–65, 2011.

[116] Sahl, S. J., et al. *Comment on "Extended-resolution structured illumination imaging of endocytic and cytoskeletal dynamics".* Science, 352(6285):527.1–527, 2016.

[117] Li, D. and Betzig, E. *Response to comment on "extended-resolution structured illumination imaging of endocytic and cytoskeletal dynamics".* Science, 352(6285):527, 2016.

[118] Kilian, N., et al. *Assessing photodamage in live-cell STED microscopy.* Nature Methods, 15(10):755–756, 2018.

[119] Wu, Y., et al. *Resonant Scanning with Large Field of View Reduces Photobleaching and Enhances Fluorescence Yield in STED Microscopy.* Scientific Reports, 5(September):1–12, 2015.

[120] Deng, S., et al. *Effects of donor and acceptor's fluorescence lifetimes on the method of applying Förster resonance energy transfer in STED microscopy.* Journal of Microscopy, 269(1):59–65, 2018.

[121] Koenig, M., et al. *ns-time resolution for multispecies STED-FLIM and artifact free STED-FCS.* volume 9712, page 97120T. International Society for Optics and Photonics, 2016.

[122] Eggeling, C., et al. *Direct observation of the nanoscale dynamics of membrane lipids in a living cell.* Nature, 457(7233):1159–62, 2009.

[123] Balzarotti, F., et al. *Nanometer resolution imaging and tracking of fluorescent molecules with minimal photon fluxes.* Science, 355(6325):606–612, 2017.

[124] Eilers, Y., et al. *MINFLUX monitors rapid molecular jumps with superior spatiotemporal resolution.* Proceedings of the National Academy of Sciences, 115(24):6117–6122, 2018.

[125] Fritzsche, M. and Charras, G. *Dissecting protein reaction dynamics in living cells by fluorescence recovery after photobleaching.* Nature Protocols, 10(5):660–680, 2015.

[126] Lackowicz, J. *Principles of Fluorescence Spectroscopy.* Springer US, Boston, MA, third edition, 2006.

[127] Macháň, R., et al. *On the Equivalence of FCS and FRAP: Simultaneous Lipid Membrane Measurements.* Biophysical Journal, 111(1):152–161, 2016.

[128] Pincet, F., et al. *FRAP to characterize molecular diffusion and interaction in various membrane environments.* PLoS ONE, 11(7):1–19, 2016.

[129] Manzo, C. and Garcia-Parajo, M. F. *A review of progress in single particle tracking: from methods to biophysical insights.* Reports on Progress in Physics, 78(12):124601, 2015.

[130] Reina, F., et al. *Complementary studies of lipid membrane dynamics using iSCAT and super-resolved fluorescence correlation spectroscopy.* Journal of Physics D: Applied Physics, 51(23), 2018.

[131] Lagerholm, B. C., et al. *Convergence of lateral dynamic measurements in the plasma membrane of live cells from single particle tracking and STED-FCS.* Journal of Physics D: Applied Physics, 50(6):063001, 2017.

[132] Sezgin, E. and Schwille, P. *Fluorescence Techniques to Study Lipid Dynamics.* Cold Spring Harbor Perspectives in Biology, 3(11):a009803–a009803, 2011.

[133] Ehrenberg, M. and Rigler, R. *Rotational brownian motion and fluorescence intensify fluctuations.* Chemical Physics, 4(3):390–401, 1974.

[134] Ehrenberg, M. and Rigler, R. *Fluorescence correlation spectroscopy applied to rotational diffusion of macromolecules.* Quarterly Reviews of Biophysics, 9(1):69–81, 1976.

[135] Magde, D., et al. *Thermodynamic Fluctuations in a Reacting System—Measurement by Fluorescence Correlation Spectroscopy.* Physical Review Letters, 29(11):705–708, 1972.

[136] Magde, D., et al. *Fluorescence correlation spectroscopy. II. An experimental realization.* Biopolymers, 13(1):29–61, 1974.

[137] Elson, E. L. *Fluorescence correlation spectroscopy: Past, present, future.* Biophysical Journal, 101(12):2855–2870, 2011.

[138] Di Bona, M., et al. *Measuring Mobility in Chromatin by Intensity-Sorted FCS.* Biophysical Journal, 116(6):987–999, 2019.

[139] Koppel, D. E., et al. *Dynamics of fluorescence marker concentration as a probe of mobility.* Biophysical Journal, 16(11):1315–1329, 1976.

[140] Kitamura, A. and Kinjo, M. *State-of-the-art fluorescence fluctuation-based spectroscopic techniques for the study of protein aggregation.* International Journal of Molecular Sciences, 19(4), 2018.

[141] Ruan, Q., et al. *Spatial-temporal studies of membrane dynamics: scanning fluorescence correlation spectroscopy (SFCS).* Biophysical Journal, 87(2):1260–1267, 2004.

[142] Ries, J., et al. *Accurate determination of membrane dynamics with line-scan FCS.* Biophysical Journal, 96(5):1999–2008, 2009.

[143] Petersen, N. O., et al. *Quantitation of membrane receptor distributions by image correlation spectroscopy: concept and application.* Biophysical Journal, 65(3):1135–1146, 1993.

[144] Hebert, B., et al. *Spatiotemporal image correlation spectroscopy (STICS) theory, verification, and application to protein velocity mapping in living CHO cells.* Biophysical journal, 88(5):3601–3614, 2005.

[145] Digman, M. A., et al. *Measuring fast dynamics in solutions and cells with a laser scanning microscope.* Biophysical Journal, 89(2):1317–1327, 2005.

[146] Digman, M. A., et al. *Fluctuation correlation spectroscopy with a laser-scanning microscope: Exploiting the hidden time structure.* Biophysical Journal, 88(5):L33–L36, 2005.

[147] Dunsing, V., et al. *Direct evidence of amyloid precursor–like protein 1 trans interactions in cell–cell adhesion platforms investigated via fluorescence fluctuation spectroscopy.* Molecular Biology of the Cell, 28(25):3609–3620, 2017.

[148] Waithe, D., et al. *Optimized processing and analysis of conventional confocal microscopy generated scanning FCS data.* Methods, 140-141:62–73, 2018.

[149] Schneider, F., et al. *Nanoscale Spatiotemporal Diffusion Modes Measured by Simultaneous Confocal and Stimulated Emission Depletion Nanoscopy Imaging.* Nano Letters, 18(7):4233–4240, 2018.

[150] Sankaran, J., et al. *Diffusion, transport, and cell membrane organization investigated by imaging fluorescence cross-correlation spectroscopy.* Biophysical Journal, 97(9):2630–2639, 2009.

[151] Bag, N., et al. *Calibration and limits of camera-based fluorescence correlation spectroscopy: A supported lipid bilayer study.* ChemPhysChem, 13(11):2784–2794, 2012.

[152] Jin, W., et al. *Quantifying spatial and temporal variations of the cell membrane ultra-structure by bimFCS.* Methods, 140-141:151–160, 2018.

[153] Wohland, T., et al. *Single Plane Illumination Fluorescence Correlation Spectroscopy (SPIM-FCS) probes inhomogeneous three-dimensional environments.* Optics Express, 18(10):10627, 2010.

[154] Wawrezinieck, L., et al. *Fluorescence Correlation Spectroscopy Diffusion Laws to Probe the Submicron Cell Membrane Organization.* Biophysical Journal, 89(6):4029–4042, 2005.

[155] Lenne, P.-F., et al. *Dynamic molecular confinement in the plasma membrane by microdomains and the cytoskeleton meshwork.* The EMBO Journal, 25(14):3245–3256, 2006.

[156] Ruprecht, V., et al. *Spot Variation Fluorescence Correlation Spectroscopy Allows for Superresolution Chronoscopy of Confinement Times in Membranes.* Biophysical Journal, 100(11):2839–2845, 2011.

[157] Favard, C., et al. *FCS diffusion laws in two-phase lipid membranes: Determination of domain mean size by experiments and Monte Carlo simulations.* Biophysical Journal, 100(5):1242–1251, 2011.

[158] Di Rienzo, C., et al. *From Fast Fluorescence Imaging to Molecular Diffusion Law on Live Cell Membranes in a Commercial Microscope.* Journal of Visualized Experiments, (92):1–12, 2014.

[159] Mueller, V., et al. *STED Nanoscopy Reveals Molecular Details of Cholesterol- and Cytoskeleton-Modulated Lipid Interactions in Living Cells.* Biophysical Journal, 101(7):1651–1660, 2011.

[160] Di Rienzo, C., et al. *Fast spatiotemporal correlation spectroscopy to determine protein lateral diffusion laws in live cell membranes.* Proceedings of the National Academy of Sciences, 110(30):12307–12312, 2013.

[161] Moens, P. D., et al. *Modes of Diffusion of Cholera Toxin Bound to GM1 on Live Cell Membrane by Image Mean Square Displacement Analysis.* Biophysical Journal, 108(6):1448–1458, 2015.

[162] Di Rienzo, C., et al. *Spatiotemporal Fluctuation Analysis: A Powerful Tool for the Future Nanoscopy of Molecular Processes.* Biophysical Journal, 111(4):679–685, 2016.

[163] Kastrup, L., et al. *Fluorescence Fluctuation Spectroscopy in Subdiffraction Focal Volumes.* Physical Review Letters, 94(17):178104, 2005.

[164] Schneider, F., et al. *Diffusion of lipids and GPI-anchored proteins in actin-free plasma membrane vesicles measured by STED-FCS.* Molecular Biology of the Cell, 28(11):1507–1518, 2017.

[165] Šachl, R., et al. *Fluorescence correlation spectroscopy diffusion laws in the presence of moving nanodomains.* Journal of Physics D: Applied Physics, 49(11):114002, 2016.

[166] Honigmann, A., et al. *Scanning STED-FCS reveals spatiotemporal heterogeneity of lipid interaction in the plasma membrane of living cells.* Nature Communications, 5(9):5412, 2014.

[167] Maraspini, R., et al. *Circle scanning STED fluorescence correlation spectroscopy to quantify membrane dynamics and compartmentalization.* Methods, 140-141:188–197, 2017.

[168] Benda, A., et al. *Self-Calibrated Line-Scan STED-FCS to Quantify Lipid Dynamics in Model and Cell Membranes.* Biophysical Journal, 108(3):596–609, 2015.

[169] Manzo, C., et al. *Nanoscale Fluorescence Correlation Spectroscopy on Intact Living Cell Membranes with NSOM Probes.* Biophysical Journal, 100(2):L8–L10, 2011.

[170] Winkler, P. M., et al. *Transient Nanoscopic Phase Separation in Biological Lipid Membranes Resolved by Planar Plasmonic Antennas.* ACS Nano, page acsnano.7b03177, 2017.

[171] Regmi, R., et al. *Planar Optical Nanoantennas Resolve Cholesterol-Dependent Nanoscale Heterogeneities in the Plasma Membrane of Living Cells.* Nano Letters, 17(10):6295–6302, 2017.

[172] Chojnacki, J., et al. *Envelope glycoprotein mobility on HIV-1 particles depends on the virus maturation state.* Nature Communications, 8(1):545, 2017.

[173] Urbančič, I., et al. *Lipid Composition but not Curvature Is the Determinant Factor for the Low Molecular Mobility Observed on the Membrane of Virus-Like Vesicles.* Viruses, 10(8):415, 2018.

[174] Guzmán, C., et al. *The efficacy of raf kinase recruitment to the GTPase H-ras depends on H-ras membrane conformer-specific nanoclustering.* Journal of Biological Chemistry, 289(14):9519–9533, 2014.

[175] Sarangi, N. K., et al. *Complex dynamics at the nanoscale in simple biomembranes.* Scientific Reports, 7(1):11173, 2017.

[176] Sarangi, N. K., et al. *Unraveling complex nanoscale lipid dynamics in simple model biomembranes: Insights from fluorescence correlation spectroscopy in super-resolution stimulated emission depletion mode.* Methods, 140-141:198–211, 2017.

[177] Sarangi, N. K., et al. *Super-resolution Stimulated Emission Depletion-Fluorescence Correlation Spectroscopy Reveals Nanoscale Membrane Reorganization Induced by Pore-Forming Proteins.* Langmuir, 32(37):9649–9657, 2016.

[178] Bianchini, P., et al. *Nanoscale protein diffusion by STED-based pair correlation analysis.* PLoS ONE, 9(6), 2014.

[179] Hedde, P. N., et al. *Stimulated emission depletion-based raster image correlation spectroscopy reveals biomolecular dynamics in live cells.* Nature Communications, 4(May):1–8, 2013.

[180] Leutenegger, M., et al. *Fluorescence correlation spectroscopy with a total internal reflection fluorescence STED microscope (TIRF-STED-FCS).* Optics Express, 20(5):5243, 2012.

[181] Lanzanò, L., et al. *Measurement of nanoscale three-dimensional diffusion in the interior of living cells by STED-FCS.* Nature Communications, 8(1):65, 2017.

[182] Wang, R., et al. *A straightforward STED-background corrected fitting model for unbiased STED-FCS analyses.* Methods, 140-141:212–222, 2018.

[183] Sozanski, K., et al. *Quantitative fluorescence correlation spectroscopy in three-dimensional systems under stimulated emission depletion conditions.* Optica, 4(8):982, 2017.

[184] Barbotin, A., et al. *Adaptive optics allows STED-FCS measurements in the cytoplasm of living cells.* Optics Express, 27(16):23378, 2019.

[185] Zhou, Y., et al. *Bile acids modulate signaling by functional perturbation of plasma membrane domains.* Journal of Biological Chemistry, 288(50):35660–35670, 2013.

[186] Koller, T., et al. *Rituximab capping triggers intracellular reorganization of B cells.* Matters, pages 1–7, 2017.

[187] Schneider, F., et al. *Statistical Analysis of Scanning Fluorescence Correlation Spectroscopy Data Differentiates Free from Hindered Diffusion.* ACS Nano, 12(8):8540–8546, 2018.

[188] Konrad, A., et al. *Revealing the radiative and non-radiative relaxation rates of the fluorescent dye Atto488 in a λ/2 Fabry–Pérot-resonator by spectral and time resolved measurements.* Nanoscale, 8(30):14541–14547, 2016.

[189] Wurm, C. a., et al. *Novel red fluorophores with superior performance in STED microscopy.* Optical Nanoscopy, 1(1):7, 2012.

[190] Pinkwart, K., et al. *Nanoscale dynamics of cholesterol in the cell membrane.* Journal of Biological Chemistry, page jbc.RA119.009683, 2019.

[191] Cavallo, G., et al. *Preparation and characterization of four new variously deacetylated lysogangliosides, breakdown products of GM1.* Carbohydrate Research, 248(C):251–265, 1993.

[192] Weissig, V., editor. *Liposomes Methods and Protocols Volume 2: Biological Membrane Models*, volume 606 of *Methods in Molecular Biology.* Humana Press, Totowa, NJ, 2 edition, 2010.

[193] Simonsen, A. C. and Bagatolli, L. a. *Structure of spin-coated lipid films and domain formation in supported membranes formed by hydration.* Langmuir, 20(22):9720–9728, 2004.

[194] Clausen, M. P., et al. *A straightforward approach for gated STED-FCS to investigate lipid membrane dynamics.* Methods, 88:67–75, 2015.

[195] Rueden, C. T., et al. *ImageJ2: ImageJ for the next generation of scientific image data.* BMC Bioinformatics, 18(1):529, 2017.

[196] Schneider, C. A., et al. *NIH Image to ImageJ: 25 years of image analysis.* Nature Methods, 9(7):671–675, 2012.

[197] Schindelin, J., et al. *Fiji: an open-source platform for biological-image analysis.* Nature Methods, 9(7):676–682, 2012.

[198] Fritzsche, M., et al. *CalQuo: automated, simultaneous single-cell and population-level quantification of global intracellular Ca2+ responses.* Scientific reports, 5(October):16487, 2015.

[199] Lee, A. M., et al. *CalQuo 2 : Automated Fourier-space, population-level quantification of global intracellular calcium responses.* Scientific Reports, 7(1):5416, 2017.

[200] Waithe, D., et al. *FoCuS-point: software for STED fluorescence correlation and time-gated single photon counting.* Bioinformatics, 32(6):958–960, 2016.

[201] Huang, H., et al. *Effect of receptor dimerization on membrane lipid raft structure continuously quantified on single cells by camera based fluorescence correlation spectroscopy.* PLoS ONE, 10(3):1–18, 2015.

[202] Mueller, V., et al. *FCS in STED microscopy: studying the nanoscale of lipid membrane dynamics.* Methods in enzymology, 519:1–38, 2013.

[203] Ringemann, C., et al. *Exploring single-molecule dynamics with fluorescence nanoscopy.* New Journal of Physics, 11(10):103054, 2009.

[204] Wahl, M., et al. *Fast calculation of fluorescence correlation data with asynchronous time-correlated single-photon counting.* Optics express, 11(26):3583–3591, 2003.

[205] Limpert, E., et al. *Log-normal Distributions across the Sciences: Keys and Clues.* BioScience, 51(5):341, 2006.

[206] Ginos, B. F. *Parameter Estimation for the Lognormal Distribution.* Ph.D. thesis, Brigham Young University, 2009.

[207] Burnham, K. P. and Anderson, D. R. *Multimodel inference: Understanding AIC and BIC in model selection.* Sociological Methods and Research, 33(2):261–304, 2004.

[208] Schwarz, G. *Estimating the Dimension of a Model.* The Annals of Statistics, 6(2):461–464, 1978.

[209] Kask, P., et al. *Statistical accuracy in fluorescence fluctuation experiments.* European Biophysics Journal, 25(3):163–169, 1997.

[210] Kinkhabwala, A. A., et al. *Fluorescence correlation spectroscopy at high concentrations using gold bowtie nanoantennas.* Chemical Physics, 406:3–8, 2012.

[211] Laurence, T. A., et al. *Fluorescence correlation spectroscopy at micromolar concentrations without optical nanoconfinement.* Journal of Physical Chemistry B, 118(32):9662–9667, 2014.

[212] Koppel, D. E. *Statistical accuracy in fluorescence correlation spectroscopy.* Physical Review A, 10(6):1938–1945, 1974.

[213] Wohland, T., et al. *The Standard Deviation in Fluorescence Correlation Spectroscopy.* Biophys. J., 80(6):2987–2999, 2001.

[214] Ries, J. and Schwille, P. *New concepts for fluorescence correlation spectroscopy on membranes.* Physical Chemistry Chemical Physics, 10(24):3487, 2008.

[215] Kapusta, P., et al. *Fluorescence lifetime correlation spectroscopy (FLCS): Concepts, applications and outlook.* International Journal of Molecular Sciences, 13(10):12890–12910, 2012.

[216] Ghosh, A., et al. *Fluorescence lifetime correlation spectroscopy: Basics and applications.* Methods, 140-141:32–39, 2018.

[217] Vicidomini, G., et al. *STED-FLCS: An Advanced Tool to Reveal Spatiotemporal Heterogeneity of Molecular Membrane Dynamics.* Nano Letters, 15(9):5912–5918, 2015.

[218] Wachsmuth, M., et al. *High-throughput fluorescence correlation spectroscopy enables analysis of proteome dynamics in living cells.* Nature Biotechnology, 33(4):384–389, 2015.

[219] Clausen, M. P., et al. *Dissecting the actin cortex density and membrane-cortex distance in living cells by super-resolution microscopy.* Journal of Physics D: Applied Physics, 50(6):064002, 2017.

[220] Lira, R. B., et al. *Posing for a picture: Vesicle immobilization in agarose gel.* Scientific Reports, 6(1):25254, 2016.

[221] Kulig, W., et al. *Bobbing of Oxysterols: Molecular Mechanism for Translocation of Tail-Oxidized Sterols through Biological Membranes.* Journal of Physical Chemistry Letters, 9(5):1118–1123, 2018.

[222] Yuan, C. and Johnston, L. J. *Atomic Force Microscopy Studies of Ganglioside GM1 Domains in Phosphatidylcholine and Phosphatidylcholine/Cholesterol Bilayers.* Biophysical Journal, 81(2):1059–1069, 2001.

[223] Šachl, R., et al. *On multivalent receptor activity of GM1 in cholesterol containing membranes.* Biochimica et biophysica acta, 1853(4):850–7, 2015.

[224] Lebreton, S., et al. *Organization of GPI-anchored proteins at the cell surface and its physiopathological relevance*, 2018.

[225] Kułakowska, A., et al. *Fluorescence lifetime tuning-a novel approach to study flip-flop kinetics in supported phospholipid bilayers.* Journal of Fluorescence, 20(2):563–569, 2010.

[226] Fujimoto, T. and Parmryd, I. *Interleaflet Coupling, Pinning, and Leaflet Asymmetry—Major Players in Plasma Membrane Nanodomain Formation.* Frontiers in Cell and Developmental Biology, 4(JAN):1–12, 2017.

[227] Freeman, S. A., et al. *Transmembrane Pickets Connect Cyto- and Pericellular Skeletons Forming Barriers to Receptor Engagement.* Cell, 172(1-2):305–317.e10, 2018.

[228] Hiramoto-Yamaki, N., et al. *Ultrafast Diffusion of a Fluorescent Cholesterol Analog in Compartmentalized Plasma Membranes.* Traffic, 15(6):583–612, 2014.

[229] Krieger, J. W., et al. *Imaging fluorescence (cross-) correlation spectroscopy in live cells and organisms.* Nature Protocols, 10(12):1948–1974, 2015.

[230] Wu, Y., et al. *Resonant-scanning dual-color STED microscopy with ultrafast photon counting: A concise guide.* Methods, 88:48–56, 2015.

[231] Sevcsik, E., et al. *GPI-anchored proteins do not reside in ordered domains in the live cell plasma membrane.* Nature Communications, 6:6969, 2015.

[232] Saha, S., et al. *Diffusion of GPI-anchored proteins is influenced by the activity of dynamic cortical actin.* Molecular Biology of the Cell, 26(22):4033–4045, 2015.

[233] Mayor, S., et al. *GPI-anchored proteins are organized in submicron domains at the cell surface.* Nature, 394(6695):798–801, 1998.

[234] Goswami, D., et al. *Nanoclusters of GPI-Anchored Proteins Are Formed by Cortical Actin-Driven Activity.* Cell, 135(6):1085–1097, 2008.

[235] Legler, D. F., et al. *Differential insertion of GPI-anchored GFPs into lipid rafts of live cells.* The FASEB Journal, 19(1):73–75, 2005.

[236] Gowrishankar, K., et al. *Active remodeling of cortical actin regulates spatiotemporal organization of cell surface molecules.* Cell, 149(6):1353–1367, 2012.

[237] Sezgin, E., et al. *Polarity-Sensitive Probes for Superresolution Stimulated Emission Depletion Microscopy.* Biophysical Journal, 113(6):1321–1330, 2017.

[238] Mayer, J., et al. *Drawing an elephant with four complex parameters.* American Journal of Physics, 78(6):648, 2010.

[239] Limpert, E. and Stahel, W. A. *Problems with Using the Normal Distribution – and Ways to Improve Quality and Efficiency of Data Analysis.* PLoS ONE, 6(7):e21403, 2011.

[240] Santos, A. M., et al. *Capturing resting T cells: the perils of PLL.* Nature Immunology, 19(3):203–205, 2018.

[241] Norman, D. J. *Mechanisms of Action and Overview of OKT3.* Therapeutic Drug Monitoring, 17(6):615–620, 1995.

[242] Ponjavic, A., et al. *Single-Molecule Light-Sheet Imaging of Suspended T Cells.* Biophysical Journal, 114(9):2200–2211, 2018.

[243] Liu, Y., et al. *Evidence for localized cell heating induced by infrared optical tweezers.* Biophysical Journal, 68(5):2137–2144, 1995.

[244] Akimzhanov, A. M., et al. *Rapid and transient palmitoylation of the tyrosine kinase Lck mediates Fas signaling.* Proceedings of the National Academy of Sciences of the United States of America, 112(38):11876–11880, 2015.

[245] Schwille, P., et al. *Fluorescence correlation spectroscopy with single-molecule sensitivity on cell and model membranes.* Cytometry, 36(3):176–182, 1999.

[246] Schaub, E. *High countrate real-time FCS using F2Cor.* Optics Express, 21(20):23543, 2013.

[247] Chizhik, A. I., et al. *Metal-induced energy transfer for live cell nanoscopy.* Nature Photonics, 8(2):124–127, 2014.

[248] Bosch-fortea, M., et al. *The ciliary membrane of polarized epithelial cells stems from a midbody remnant-associated membrane patch with condensed nanodomains.* bioRxiv, pages 1–29, 2019.

[249] Bacia, K. and Schwille, P. *Practical guidelines for dual-color fluorescence cross-correlation spectroscopy.* Nature Protocols, 2(11):2842–2856, 2007.

[250] Sadaie, W., et al. *Quantitative In Vivo Fluorescence Cross-Correlation Analyses Highlight the Importance of Competitive Effects in the Regulation of Protein-Protein Interactions.* Molecular and Cellular Biology, 34(17):3272–3290, 2014.

[251] Sankaran, J., et al. *Accuracy and precision in camera-based fluorescence correlation spectroscopy measurements.* Analytical Chemistry, 85(8):3948–3954, 2013.

[252] Saffarian, S. and Elson, E. L. *Statistical analysis of fluorescence correlation spectroscopy: The standard deviation and bias.* Biophysical Journal, 84(3):2030–2042, 2003.

[253] Qian, H. *On the statistics of fluorescence correlation spectroscopy.* Biophysical Chemistry, 38(1-2):49–57, 1990.

[254] Dertinger, T., et al. *Two-focus fluorescence correlation spectroscopy: A new tool for accurate and absolute diffusion measurements.* ChemPhysChem, 8(3):433–443, 2007.

[255] Dörlich, R. M., et al. *Dual-color dual-focus line-scanning FCS for quantitative analysis of receptor-ligand interactions in living specimens.* Scientific reports, 5(May):10149, 2015.

[256] Unsay, J. D., et al. *Scanning Fluorescence Correlation Spectroscopy for Quantification of the Dynamics and Interactions in Tube Organelles of Living Cells.* ChemPhysChem, 19(23):1–7, 2018.

[257] Steinberger, T., et al. *Z-scan fluorescence correlation spectroscopy as a tool for diffusion measurements in planar lipid membranes.* Methods in molecular biology (Clifton, N.J.), 1076:617–34, 2014.

[258] Humpolícková, J., et al. *Probing diffusion laws within cellular membranes by Z-scan fluorescence correlation spectroscopy.* Biophysical journal, 91(3):L23–L25, 2006.

[259] Digman, M. A. and Gratton, E. *Imaging barriers to diffusion by pair correlation functions.* Biophysical Journal, 97(2):665–673, 2009.

[260] Cutrale, F., et al. *Using enhanced number and brightness to measure protein oligomerization dynamics in live cells.* Nature Protocols, 14(2):616–638, 2019.

[261] Digman, M. A., et al. *Mapping the number of molecules and brightness in the laser scanning microscope.* Biophysical Journal, 94(6):2320–2332, 2008.

[262] Schrimpf, W., et al. *PAM: A Framework for Integrated Analysis of Imaging, Single-Molecule, and Ensemble Fluorescence Data.* Biophysical Journal, 114(7):1518–1528, 2018.

[263] Follain, G., et al. *Seeing is believing - multi-scale spatio-temporal imaging towards in vivo cell biology.* Journal of Cell Science, 130(1):23–38, 2017.

[264] Dekkers, J. F., et al. *High-resolution 3D imaging of fixed and cleared organoids.* Nature Protocols, 14(6):1756–1771, 2019.

[265] Fritzsche, M., et al. *Self-organizing actin patterns shape membrane architecture but not cell mechanics.* Nature Communications, 8:14347, 2017.

[266] Steinkühler, J., et al. *Mechanical properties of plasma membrane vesicles correlate with lipid order and viscosity and depend on cell density.* Communications Biology, 2(8):1–18, 2019.

[267] Suzuki, K. G., et al. *Development of new ganglioside probes and unraveling of raft domain structure by single-molecule imaging.* Biochimica et Biophysica Acta (BBA) - General Subjects, (July):0–1, 2017.

[268] Amaro, M., et al. *GM 1 Ganglioside Inhibits β-Amyloid Oligomerization Induced by Sphingomyelin.* Angewandte Chemie International Edition, 55(32):9411–9415, 2016.

[269] Yanagisawa, K. *GM1 ganglioside and Alzheimer's disease.* Glycoconjugate Journal, 32(3-4):87–91, 2015.

[270] Fülöp, G., et al. *Determination of the Membrane Environment of CD59 in Living Cells.* 8(2), 2018.

[271] Sezgin, E., et al. *A comparative study on fluorescent cholesterol analogs as versatile cellular reporters.* Journal of Lipid Research, 57(2):299–309, 2016.

[272] Honigmann, A., et al. *Characterization of horizontal lipid bilayers as a model system to study lipid phase separation.* Biophysical Journal, 98(12):2886–2894, 2010.

[273] Hedger, G., et al. *Cholesterol Interaction Sites on the Transmembrane Domain of the Hedgehog Signal Transducer and Class F G Protein-Coupled Receptor Smoothened.* Structure, 27(3):549–559.e2, 2019.

[274] Milon, S., et al. *Factors influencing fluorescence correlation spectroscopy measurements on membranes: simulations and experiments.* Chemical Physics, 288(2-3):171–186, 2003.

[275] Cardoso Dos Santos, M., et al. *Topography of Cells Revealed by Variable-Angle Total Internal Reflection Fluorescence Microscopy.* Biophysical Journal, 111(6):1316–1327, 2016.

[276] Kapoor-Kaushik, N., et al. *Distinct Mechanisms Regulate Lck Spatial Organization in Activated T Cells.* Frontiers in Immunology, 7(MAR):1–12, 2016.

[277] Wennmalm, S. *Potentials and pitfalls of inverse fluorescence correlation spectroscopy.* Methods, 140-141:23–31, 2018.

[278] Ike, H., et al. *Mechanism of Lck recruitment to the T-cell receptor cluster as studied by single-molecule-fluorescence video imaging.* ChemPhysChem, 4(6):620–626, 2003.

[279] Douglass, A. D. and Vale, R. D. *Single-Molecule Microscopy Reveals Plasma Membrane Microdomains Created by Protein-Protein Networks that Exclude or Trap Signaling Molecules in T Cells.* Cell, 121(6):937–950, 2005.

[280] Kim, P. W. *A Zinc Clasp Structure Tethers Lck to T Cell Coreceptors CD4 and CD8.* Science, 301(5640):1725–1728, 2003.